INVESTIGATION OF CORRELATIONS BETWEEN MECHANICAL AND MICROSTRUCTURAL PROPERTIES OF HIGH PURITY POLYCRYSTALLINE NIOBIUM

By

Mengge Zhao

A THESIS

Submitted to
Michigan State University
in partial fulfillment of the requirements
for the degree of

Materials Science and Engineering–Master of Science

2015

ABSTRACT

INVESTIGATION OF CORRELATIONS BETWEEN MECHANICAL AND MICROSTRUCTURAL PROPERTIES OF HIGH PURITY POLYCRYSTALLINE NIOBIUM

By

Mengge Zhao

Superconducting radio frequency (SRF) cavities made from high purity niobium are commonly used in particle accelerators. An understanding of the relationship between mechanical and functional properties and the processing history is essential in order to manufacture cavities with uniform performance. The crystallographic texture and microstructure in polycrystalline sheet varies considerably and identifying its influence on properties is needed to achieve a better understanding of how to control properties of high purity niobium. Texture (preferred crystal orientations) strongly affects mechanical properties and formability of metals and alloys. Samples received from many lots of material from two companies, Tokyo Denkai and Ningxia, for building cavities for the Facility for Rare Isotopes were examined to identify relationships between these two properties. Texture of the undeformed niobium samples through thickness was measured using Orientation Imaging Microscopy^{TM} system (OIM). Texture was identified with pole figures (PF), orientation distribution function (ODF) and grain misorientation relationships. Stress-strain testing was done to identify ultimate tensile stress (UTS), elongation, 0.2% yield strength, and hardening rate. From tests on many lots, there was no clear trend between the mechanical and material properties in high purity niobium and correlations between various microstructural and mechanical properties showed significant scatter and few apparent correlations.

To my parents, who always love and support me without any doubt.

ACKNOWLEDGEMENTS

I sincerely thank my advisor Dr. Bieler, who always had time to answer questions. I also thank my graduate committee members Dr. Boelert and Dr. Eisenlohr for all the time and energy spent to evaluate my progress.

Thanks to Chris Compton at Facility for Rare Isotope Beams and Di Kang, who provided support and necessary results.

Last and certainly not least, I thank you all my fellow graduate students for their help, support, encouragement, instruction, and friendship, particularly, Di Kang, whose work set up this investigation.

TABLE OF CONTENTS

LIST OF TABLES

LIST OF FIGURES

KEY TO SYMBOLS AND ABBREVIATIONS

BCC	Body center cubic
BCP	Buffered Chemical Polishing
CSL	Coincident site lattice
EBSD	Electron Backscattered Diffraction
EDM	Electrical discharge machining
KAM	Kernel average misorientation
LAM	Local average misorientation
ND	Normal direction
ODF	Orientation distribution function
OIM	Orientation Imaging Microscopy
PF	Pole figures
SEM	Scanning electron microscope
SRF	Superconducting radio frequency
RD	Rolling direction
RRR	Residual resistivity ratio
TD	Transverse direction
TSL	TexSEM Laboratory
UTS	Ultimate tensile stress
ϕ_1,Φ,ϕ_2	Bunge Euler angle notation: phi one, phi, phi two

I. INTRODUCTION

Superconducting radio frequency (SRF) cavities have been used in applications requiring continuous wave or long-pulse accelerating fields above a few million volts per meter (MV/m) [1]. The important advantages for the usage of SRF cavities in accelerators are not only because it uses less energy but also because it can be shorter and thus imposes less disruption of the accelerated particles [1]. To achieve the best performance of an accelerator, the design and material choice of SRF cavities is critical. The shape of SRF cavities require a large beam hole, to reduce beam disruption and provide high quality beams, and multiple cavities are needed to construct a completed accelerator [1]. Figure 1 shows one example of a set of SRF cavities.

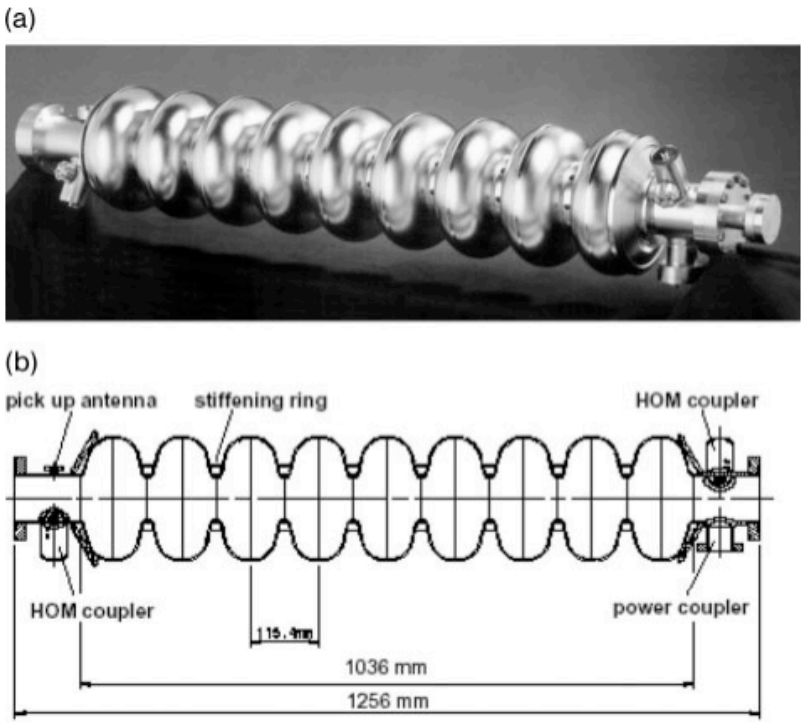

Figure 1: a) A 9-cell TESLA accelerating structure with one input power coupling port at one end and one high order mode coupler at each end. b) Layout of the components for the 9-cell TESLA-style structure. (Courtesy of DESY and ACCEL) [1].

Nowadays, high purity niobium is an ideal material to make SRF cavities for many reasons. First, high purity niobium provides a great magnetic field at low temperature and second, it is easy to machine at room temperature [2]. Niobium sheets can be ordered from many suppliers that meet established cavity specifications, for examples flatness, uniform grain size, near-complete recrystallization, high RRR values, and good surface quality [1]. The microstructure of niobium also has a large effect on the etching processes required to obtain a clean and smooth surface that is essential for high performance of accelerators [3]. However, the properties of the niobium sheets often show a large range of variability and exhibit random variations in properties.

It is well established that crystallographic texture is an inherent characteristic of metals produced by deformation processing and heat treatment, and has a significant influence on mechanical, physical as well as chemical properties of materials [4]. Some properties where the role of texture is well established are strength, ductility, modulus of elasticity, electrical conductivity, piezoelectricity, magnetic susceptibility, light refraction and wave propagation [4]. In general, there are relationships between the mechanical and material properties, which can provide useful information for improving a manufacturing process. For high purity niobium, these correlations are still not understood. As mechanical properties change thought out fabrication process, the correlation between mechanical properties and texture is useful to predict the mechanical properties of the final product, and in addition, to manufacture cavities with similar mechanical properties. Moreover, the large data set can support additional research, when encounter failures in SRF cavities.

II. LITERATURE SURVEY

Niobium, the material of choice for manufacturing superconducting radio frequency (SRF) cavities for particle accelerators, has a set of acceptance categories and criteria for use in fabricating accelerator cavities for the new Facility for Rare Isotope Beam (FRIB) at MSU [5]. This list includes chemical composition, surface finish, mechanical properties, metallurgical properties, and electrical properties. Additionally, specified dimensional tolerances, with tight control of thickness are also needed to meet fabrication requirements [5]. Electrical properties, are defined by the residual resistivity ratio (RRR), which is the resistivity of niobium at room temperature divided by resistivity at 4.2 K in the normal state [6]. It is useful to use RRR, because it also reflects the purity of niobium, since during the process of manufacturing the high purity niobium, interstitial impurities may be introduced into the final product, such as O, N, C and H. Table 1 below shows an example of some technical specifications of the niobium used in specific cavities [1].

Table 1: Technical specifications to niobium sheets for cavities [1].

Concentration of impurities in ppm (weight)				Mechanical properties	
Ta	≤500	H	≤2	RRR	≥300
W	≤70	N	≤10	Grain size	≈ 50 μm
Ti	≤50	O	≤10	Yield strength, $\sigma_{0.2}$	$50<\sigma_{0.2}<100$ N/mm^2 (MPa)
Fe	≤30	C	≤10	Tensile strength	>100 N/mm^2 (MPa)
Mo	≤50			Elongation at break	30%
Ni	≤30			Vickers hardness HV 10	≤60

Among all impurities, oxygen has the dominant effect because of the high affinity of niobium with oxygen, so the concentrations of oxygen should be kept below 10 ppm [7]. Even though the influence of hydrogen is not as significant, the concentration of hydrogen should be kept below 2 ppm in order to prevent hydride precipitation and degradation of the Q-value of the high RRR cavities under certain cool-down conditions [7].

The Q-value is the quality factor of RF cavities that describes the RF losses in the cavity. In other words, an RF cavity with a high Q-value uses RF power more efficiently compared to a low Q-value RF cavity [8]. This factor is defined as,

$$Q = \frac{\omega U}{P}$$

Where ω is the angular frequency (2πf), U is the cavity stored energy and P is the power dissipated in the walls per radian of the RF cycle [8]. In this equation, the maximum stored energy U in the cavity is determined by the cavity shape and volume. P is determined by the resistivity and magnetic permeability of the material of the inner wall of the cavity [8].

The acceptable concentration of tantalum is the highest compared with other impurities, as tantalum has the same number of electrons in the outer shells (and is below Nb on the periodic table) and also because it accompanies niobium in most ores and is hard to separate [7]. An impurity level of 500 ppm is normally harmless for cavity performance, since tantalum is a substitutional impurity and does not substantially affect the behavior of niobium [7]. However, whether there is a positive effect on the concentration of tantalum is still unclear. Other abundant substitutional impurities such as tungsten, titanium, molybdenum, iron and nickel usually have a concentration level less than 70 ppm.

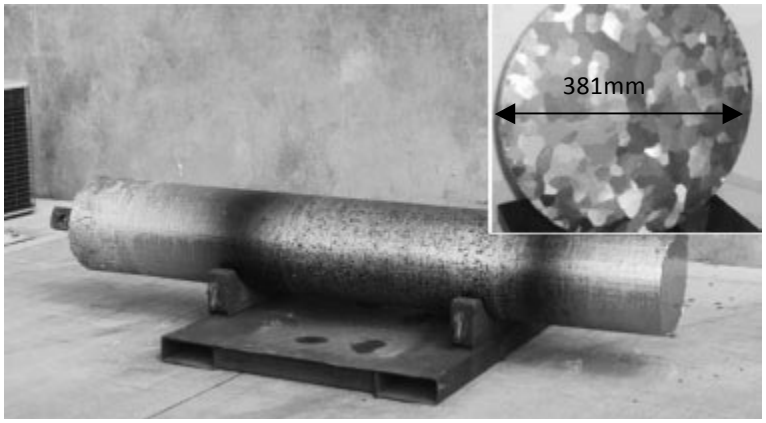

Figure 2: Finished electron-beam melted ingot (diameter 15 inch) from Wah Chang. Inset: Example of the grain structure of a standard ingot [1].

Starting from a large ingot, as shown in Figure 2 above, the method of fabrication of niobium sheets at Tokyo Denkai Company is shown as Figure 3 [1]. The manufacturing process consists of several stages, from forging, grinding, rolling, cleaning and annealing [1]. High RRR is normally obtained by electron beam melting the ingot several times [1]. For example, Tokyo Denkai melts the ingot six times to achieve a narrow spread in RRR between 295 and 370 [1]. Due to this repeated melting process, electron beam melting purification becomes the largest cost in the process [1].

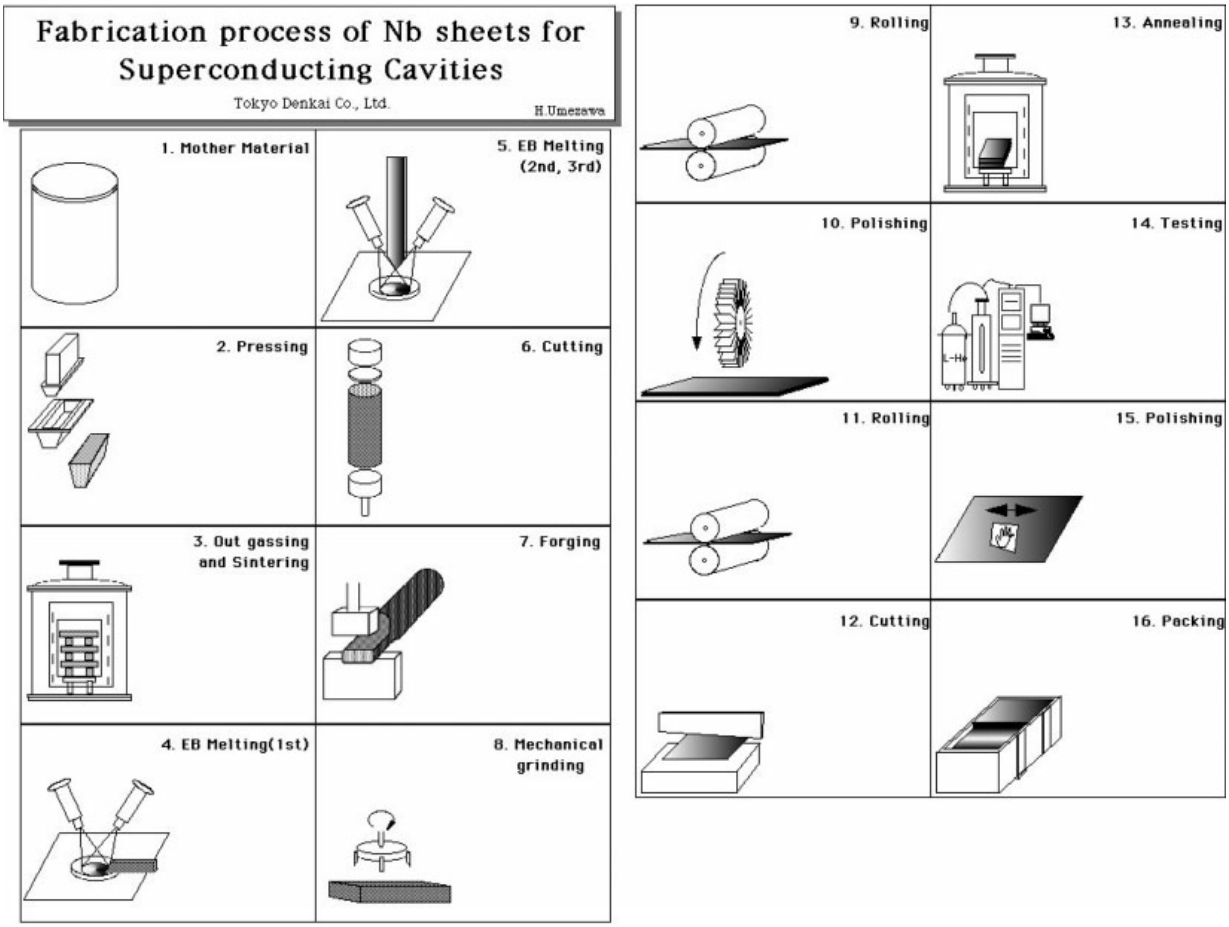

Figure 3: Stages in production of sheet from the ingot (Courtesy of Tokyo Denkai) [1].

Final annealing between 750°C and 800°C is essential to recrystallize the material [1]. This temperature and time must be chosen carefully in consideration of RRR, so that recrystallization will be nearly complete, but the temperature must not be too high in order to maintain a fine and uniform grain size (50μm) that provides the best forming properties [1]. Figure 4 below shows one example of fully and partially recrystallized sheet.

In deformation studies, recrystallization is the development of a new grain structure with low dislocation density, either during deformation or after deformation [9]. Grains with higher dislocation densities have higher stored energies than grains with low dislocation densities. Grains with low densities may consume grain with higher stored energies though grain boundary migration [9]. It is possible that grain growth is oriented, which is to say that for some reason, such as being a hard orientation with a lower dislocation density, grains with certain crystallographic orientations may grow faster than others [9]. Thus, the final texture may not be random and may reflect the oriented grain growth.

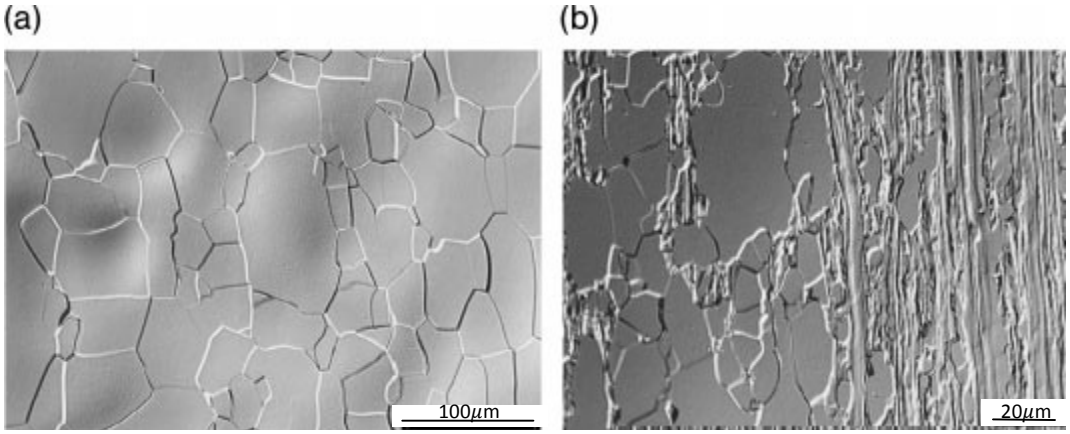

Figure 4: (a) Grain structure for fully recrystallized niobium sheet; scale bar is 100 μm. (b) SEM micrograph of niobium with incomplete recrystallization; scale bar is 20 μm. (Courtesy of DESY) [1].

Besides this long and expensive manufacturing process, there is another method used to produce cavities using large-crystal or single-crystal niobium to simplify the process, starting with sheets cut directly from the ingot by either wire electrical discharge machining (EDM) or diamond saw cutting [1]. Wire EDM provides a very smooth starting finish, but it is very slow, taking 1 day per sheet, diamond saw cutting is faster and has been proven successful, however, the overall cost advantage of large grain material is still unclear [1]. Figure 5 below shows an example of a large grain ingot with a large central, single crystal [1].

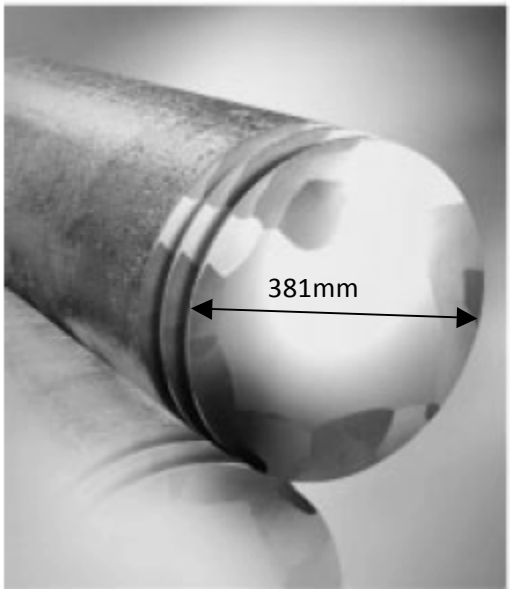

Figure 5: Large grain ingot from W.C. Heraeus [1].

To further analyze the correlations between processing and properties, a better understanding of the origins of material and mechanical properties of high purity niobium is desired. One microstructure based measurement that affects material properties is crystallographic texture. It has been known that preferred orientations, which is what texture of the material describes, governs various structural and mechanical properties of the material [4]. Texture can define the arrangement of building blocks in the polycrystalline material [4]. During the process of solidification, plastic deformation, annealing and phase transformation, different preferred orientation may develop [4]. Texture has been considered a significant feature to characterize material, since it has been known that microstructure plays an important role in showing the properties of materials, and the microstructure is a combination of morphology and orientation of the constituents [4]. Figure 6 shows an example of texture, which is illustrated by a set of pole figures (PF).

Ultimately, the study of texture is to develop materials with favorable properties. One typical example is the sheet metal used for deep drawing; the semi-isotropic characteristic is required in order to avoid undesirable ears [4]. The study of texture of niobium is necessary, since it can be used to develop material with favorable and reproducible properties, which is desired in the process of manufacturing uniform high purity niobium sheet.

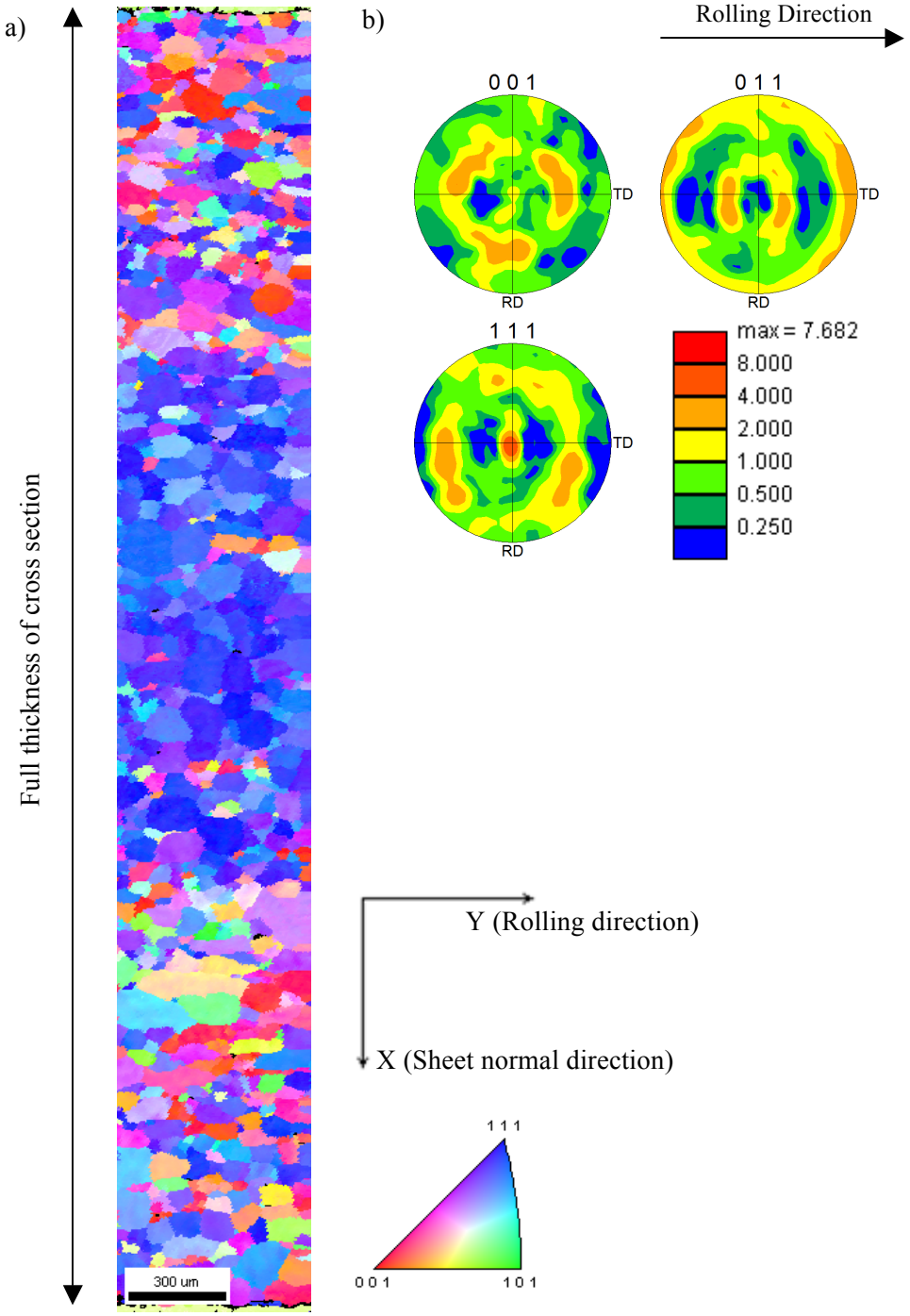

Figure 6: Example of a normal direction inverse pole figure map and correlated pole figures.

The components of a textured rolled material is normally represented by {hkl} [uvw], which means the {hkl} planes of these grains lie nearly parallel to the sheet plane and the [uvw] direction points nearly parallel to the rolling direction (RD) [4]. For rolled product, the directions associated with external shape is RD, the through-thickness direction is the direction normal to the rolling direction (ND) and the other direction is the transverse direction (TD). The overall texture $=\sum \lambda_i \{hkl\}_i < uvw >_i$, where λ_i is the weight factor which is introduced to allow for the relative intensities or strengths of the various components [4].

If the texture is less complex, it is possible to describe the texture by one or a few pole figures determined by the X-ray diffraction method [4], but to fully understand the texture and its relationship to microstructure, a better method is recommended, such as Scanning electron microscope (SEM) based Electron Backscattered Diffraction (EBSD), having a setup shown in Figure 7 below.

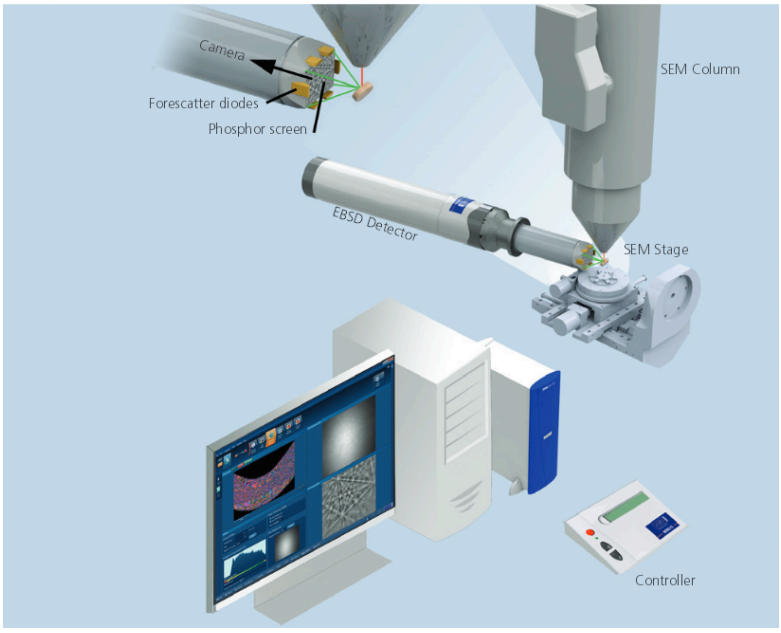

Figure 7: The principle components of an EBSD system [10].

SEM is more and more popular due to it is availability and not much background information is needed for the user to produce measurement of texture [4]. In the SEM-EBSD method, the interaction of the electron beam with the near-surface layer of the sample produces EBSD patterns [4]. A typical EBSD facility consists of the following parts: 1) Crystalline sample tilted to 70° from horizontal, by using SEM stage or a pretilted holder. 2) A phosphor screen, which is fluoresced by the electrons scattered from the sample. 3) A sensitive camera and optics for viewing the pattern formed on the phosphor screen. 4) An insertion mechanism that controls the position of the detector. 5) Electronics to control the SEM. 6) Computer to control the EBSD data acquisition, to collect and analyze the diffraction patterns. 7) Optional forward scatter diodes (FSD) mounted around the phosphor screen to generate microstructure images of the sample before collecting EBSD data [10]. The advantage of this method is that it is the only technique that provides localized texture information in a quantitative manner [4]. However, it can only be used with crystals with fairly low dislocation densities, and surface preparation is critical and the automatic indexing procedure is not always reliable [4].

In the TSL system, the default is Bunge Euler Angles, which identifies how to orient the crystal xyz axes in the external XYZ sample coordinate system. This is accomplished by a first rotation of $\phi_1$about the z-axis, then a rotation about Φ about the rotated x-axis, and then a rotation of ϕ_2 about the rotated z-axis. This is illustrated in Figure 8 below. To generate an orientation map, the simplest way is to map by plotting the three Euler Angles using an RGB color scheme. This map gives general information about orientation. However, one issue is that large differences in orientation do not always correspond to different colors on the scale, which can cause confusion when looking at orientation maps [10]. As a result, more methods have been developed to analyze the texture of material.

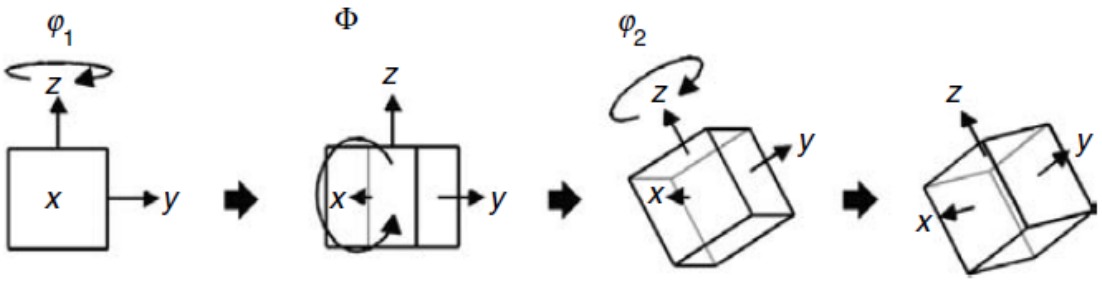

Figure 8: Euler angle rotations according to Bunge's convention [9].

With known orientations and area fractions from each grain, an orientation distribution exists that describes the entire data set. As this orientation distribution function (ODF) is a four dimensional set of data, a pole figure is a convenient two-dimensional projection of a 3 dimensional subset of the orientation distribution and represents the probability of finding a pole to a lattice plane (hkl) in a certain sample direction [9]. The pole figure shows the projected position of a particular set of crystallographic planes, where the poles have been identified on a unit sphere and projected onto a circular plot, typically with a stereographic projection [10]. A pole figure is useful to show the orientations of specific crystallographic planes and directions within a sample [10].

An inverse pole figure, plots sample directions in the crystallographic coordinate system [10]. For example, instead of plotting the <111> direction in terms of RD and ND in pole figure, an inverse pole figure plots the RD in terms of the crystal direction, i.e. within the [100], [110], and [111] fundamental triangle [10]. One advantage of inverse pole figure is that each orientation appears as single point in an inverse pole figure, where there may be many poles plotted from the same orientation in a pole figure, based on the crystal symmetry [10]. Due to the crystal symmetry, the complete inverse pole figure contains many areas where the information is repeated. For example, the cubic system has 24 equivalent sectors for the inverse pole figure that can be drawn, shown in Figure 9 below [10].

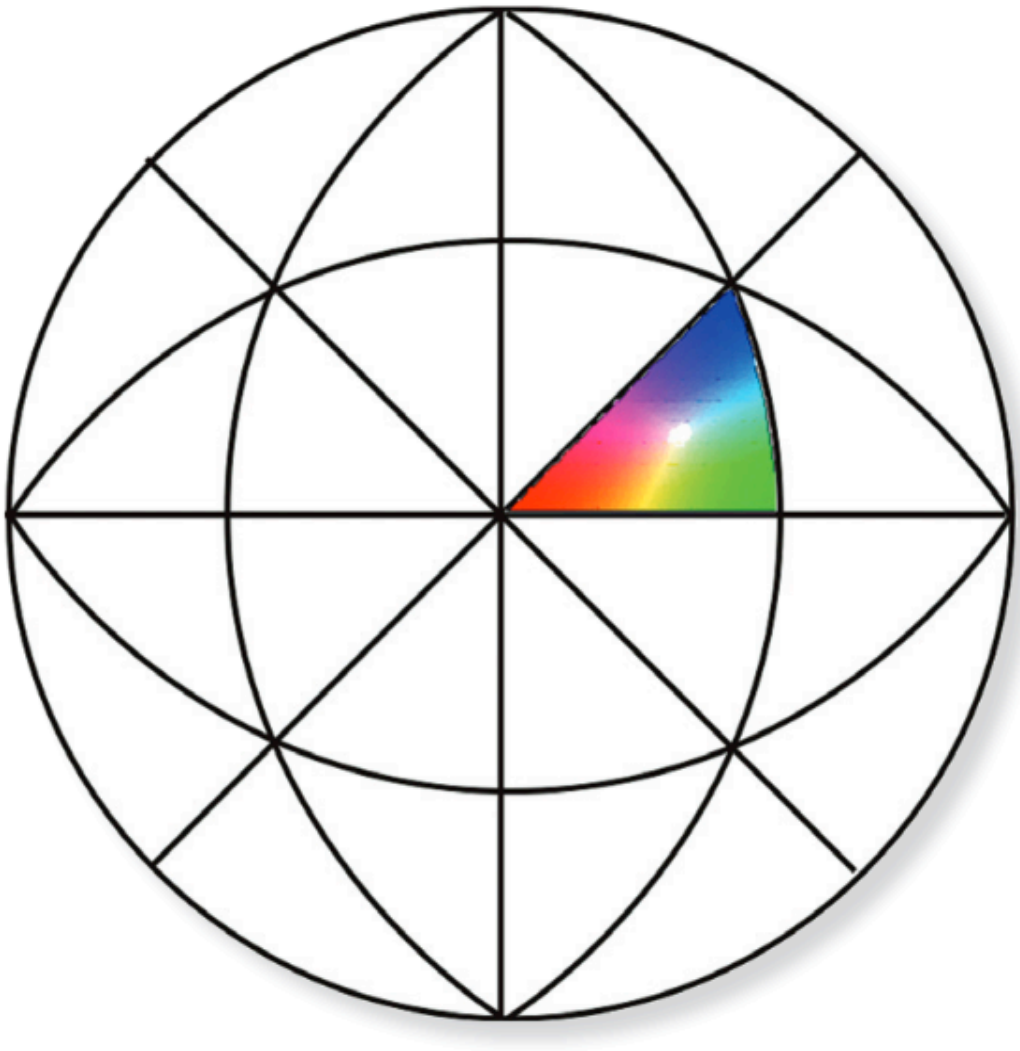

Figure 9: The 24 symmetrically equivalent regions in the (high) cubic inverse pole figure [10].

However, a pole figure is usually not enough to determine the true and complete texture if the crystallites possess more than one preferred (ideal) orientation [11]. Thus a plot of the ODF is also valuable [4]. Because this probability function is in 3 dimensions, the 3-dimensional volume is sliced and laid out as a series of 2-D plots at particular values of the third Euler angle. In polycrystals, a given orientation has an orientation probability for the three Euler angles used to describe an ODF [9]. The ODF describes the frequency of occurrence of particular orientations in a three-dimensional orientation space [4]. As each orientation can be described by a symmetric variant, all symmetric variants of each orientation are also plotted in the ODF.

One of the major texture components can be easily seen using an ODF, the fiber texture. The analyses of texture in body centered cubic (BCC) metals are mainly done in steel, especially in low and extra low carbon steel [4]. The major deformation texture components in deformation of BCC metals and alloys are the α-fiber {001} <110> to {111} <110>, and the γ-fiber {111} <110> to {111} <112>, which appears in the $\phi_2 = 45°$ section of ODF, shown as Figure 10 below. During the rolling process, different strain conditions will appear on the surface and center, because the shear on the surface activates slip systems that rotate crystals differently from the plane-strain compression in the center [12]. Due to these differences, the plane-strain compression typically causes {111} to be approximately parallel to the sheet ND in the middle, which is blue orientation in the color scale of TSL system [12]. Shear on the surface normally causes {001}||ND, which is the red orientation [12].

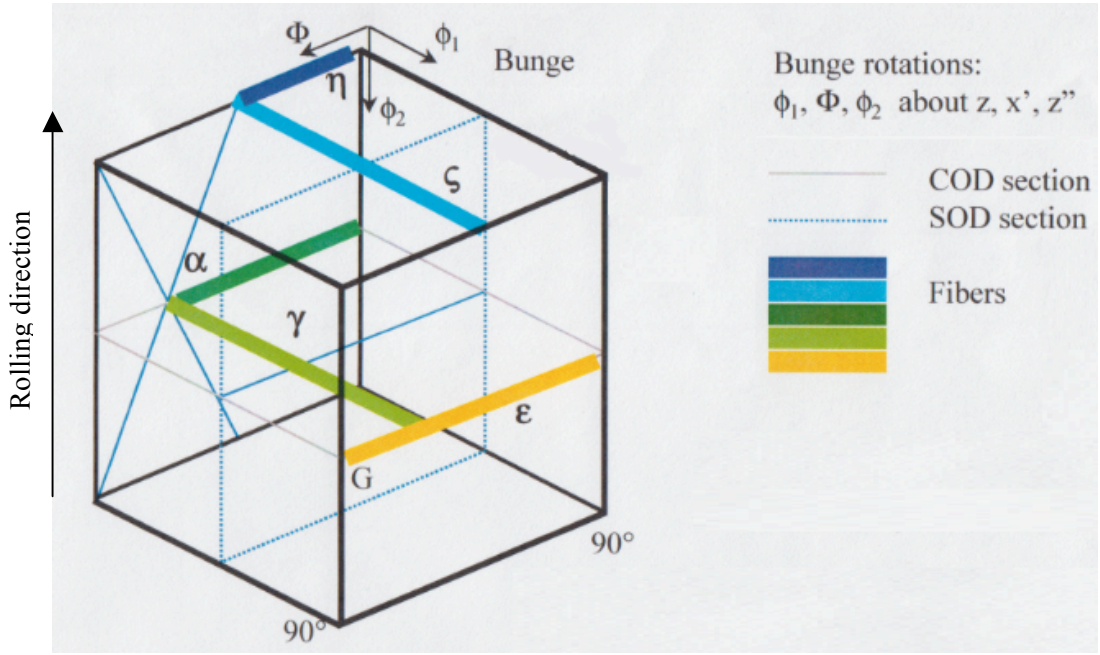

Figure 10: Common fibers for BCC deformation texture observed in Euler space. (Lecture notes of T.R. Bieler)

Misorientation is the measurement of the difference in orientation between two crystals. The misorientation is a relative measurement, which is with respect to some other orientation, so as a result, the choice of reference orientation is important [11]. There are many ways of quantifying and visualizing misorientation. The most basic measurement and visualization of misorientation is grain boundary mapping, they are determined as locations at which the scalar misorientation between adjacent pixels is greater than some critical vale [11]. However, if the misorientation is too small, the misorientation axis becomes more and more sensitive to measurements errors, and will result of lack of accurate information. As such, it is more difficult to precisely describe the nature of measured small angle boundaries [11].

Grain boundaries can be identified after measuring the misorientation between all pixel pairs. Coincident site lattice (CSL) boundaries are one of the types of grain boundaries that can be identified in EBSD analysis, and they typically have a significant impact on material properties. For

example, grain boundaries tend to decrease the electrical and thermal conductivity of the material [10]. CSL boundaries are boundaries that fulfill the coincident site lattice criteria whereby the two lattices share some of the lattice sites in a boundary, examples of CSL boundaries are shown below [10]. CSL boundaries are characterized by Σ, where Σ is the ratio of the number of atoms in a CSL unit cell compared to the number of atoms that reside in both lattices [10]. The CSL boundaries that are possible in cubic crystal structure are shown in the Table 2 below.

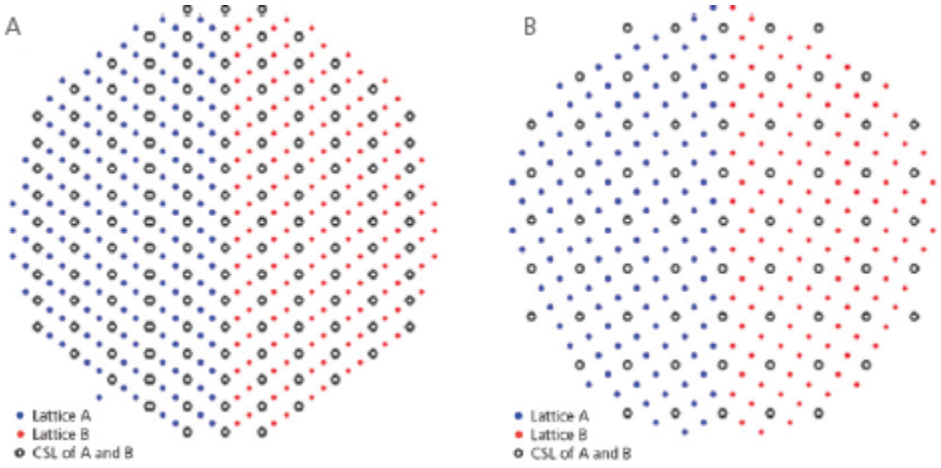

Figure 11: a) The sigma 3 boundary (twin boundary) is a 60° rotation about the [111] direction. b) The sigma 5 boundary is a 36° rotation about the [100] direction [10].

Table 2: CSL rotation table (TSL analysis software documentation).

Σ Type	Angle	Axis
1	0	1 1 1
3	60	1 1 1
5	36.86	1 0 0
7	38.21	1 1 1
9	38.94	1 1 0
11	50.47	1 1 0
13a	22.62	1 0 0
13b	27.79	1 1 1
15	48.19	2 1 0
17a	28.07	1 0 0
17b	61.92	2 2 1
19a	26.53	1 1 0
19b	46.83	1 1 1
21a	21.78	1 1 1
21b	44.41	2 1 1
23	40.45	3 1 1
25a	16.26	1 0 0
25b	51.68	3 3 1
27a	31.59	1 1 0
27b	35.43	2 1 0
29a	43.60	1 0 0
29b	46.40	2 2 1

Another misorientation map is the kernel average misorientation (KAM). The KAM is calculated as the average misorientation between a measurement point and a defined set of near neighbor points [13]. If the areas of the sample in which the very local misorientation is high, KAM is useful [11]. Early work shows that in a single crystal, a misorientation map based upon the average Euler angles for the grain works well [11]. The local average misorientation (LAM) is the average misorientation between each neighboring point pair within a set radius (of pixels) within a grain, when LAM is larger than 5°, it is not considered to be part of the same grain. [14]. Figure 12 below shows an illustration of these two misorientation analyses.

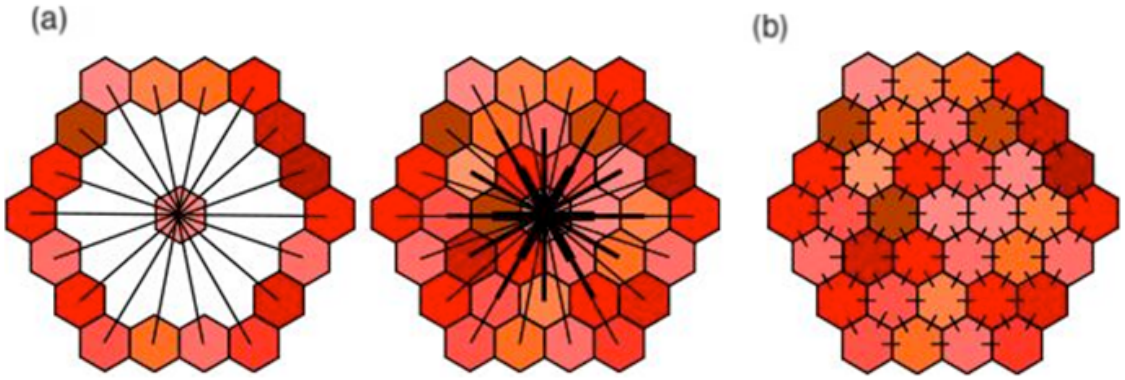

Figure 12: a) Kernel Average Misorientation b) Local Average Misorientation (TSL analysis software documentation).

From a stress-strain curve, much information can be observed, such as ultimate tensile strength, 0.2% yield strength, elongation and hardness. All of this information is important, as it reflects the manufacture process. As the cavity must withstand stresses induced by the differential pressure between the beam pipe vacuum and atmospheric pressure the strength must be large enough to resist plastic strain [1].

Even though niobium is an almost ideal material for manufacturing SRF cavities, it is still an element that has a large range of properties, and the correlations between material and mechanical properties are unknown. Identifying a trend between the properties of high purity niobium and cavity performance can help to manufacture sheet having specific texture or mechanical properties to build SRF cavities, in order to test and determine best performance. Consequently, additional work is needed on analyzing relationships between texture and stress-strain testing. From this data, plots to identify correlations can be made using scatter plot. (A scatter plot illustrates the relationship between two variables, which is a tool to visually determine whether there is a potential relationship between the two variables. Some examples of scatter plots are shown as Figure 13 below [15]).

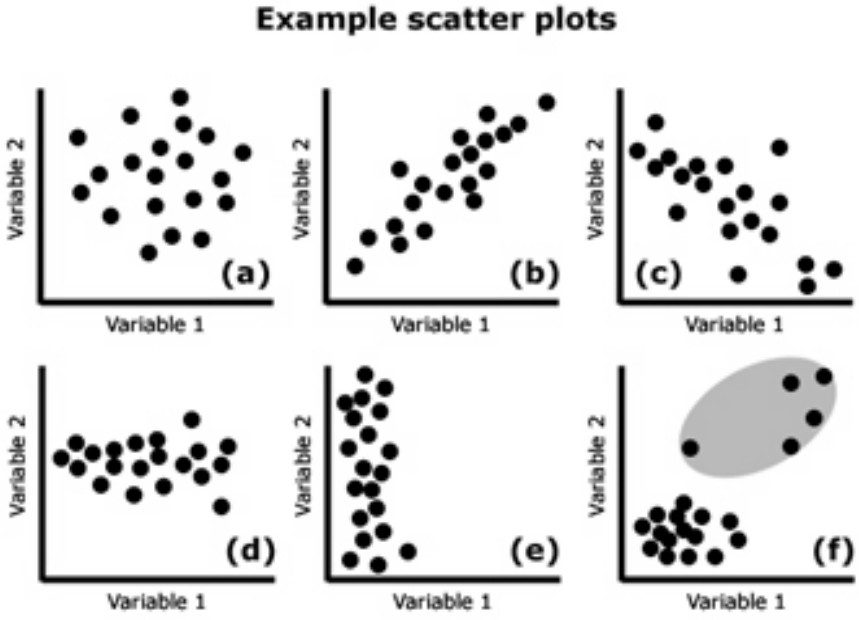

Figure 13: a) Shotgun scatter, with low correlation. b) Strong positive correlation. c) Strong negative correlation. d) and e) low correlation with very little change in one variable compared with the other. f) This scatter would generate a spurious high correlation because of the effect of the five points enclosed by the shaded area [15].

III. EXPERIMENTAL AND ANALYTICAL APPROACH

To study the mechanical and microstructural properties of high purity niobium, samples were cut from non-usable material area, an example of which is shown in Figure 14 [5]. The standard ATSM "dog-bone" sample was prepared by EDM machining for tensile tests, and a square sample was provided for OIM measurement of microstructure and texture on samples received from two companies, Tokyo Denkai and Ningxia. Because the tensile sample directions were different (due to the different unusable areas for materials ordered for different kinds of cavity structures), the tensile direction is not the same with respect to the rolling direction for the two lots of material. Furthermore, some of the strips from the Ningxia set were along the rolling direction, and others were along the transverse direction. An Instron 4302 universal testing machine was used to measure tensile behavior in experiments conducted by Di Kang. SEM-EBSD measurements were made on a Camscan 44FE emission scanning electron microscope, by Di Kang, with additional measurements made by the author to investigate the repeatability of measurements made on the same lot in different locations. Before measurements, etching of niobium in buffered chemical polish (BCP) were performed by Chris Compton at Chemical Etching Facility at National Superconducting Cyclotron Laboratory, in order to remove impurities and rough surface resulting from EDM cuts that reveal its interior surface. BCP consists of 2 parts of 85% phosphoric acid to 1 part of 49% hydrofluoric acid to 1 part of 70% nitric acid [16]. All the name of samples is the same as-received to keep track of the sources.

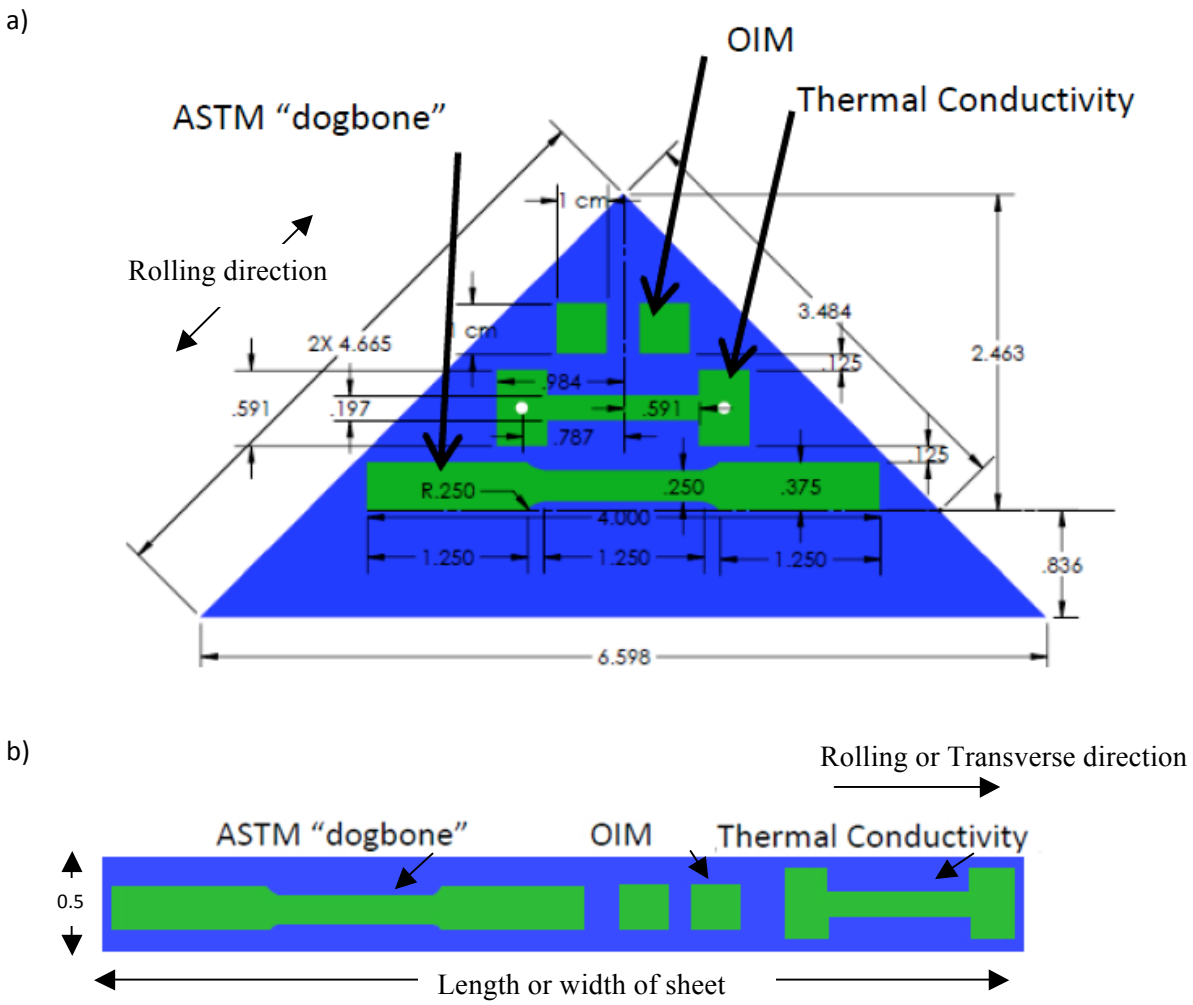

Figure 14: Concept of sample layout, cut from as-received niobium for use in acceptance testing. a) Tokyo Denkai. b) Ningxia (Unit: inch) [5].

A displacement rate of 5 mm/min was used for all received samples by Di Kang, then the samples were deformed to fracture [5]. The data were plotted as engineering stress vs. engineering strain. Elongation, UTS and 0.2% yield strength were recorded from each sample. The 0.2% yield strength is measured as follows: First, an offset line with slope equal to the elastic portion of the stress-strain curve is shifted by a strain of 0.002 to the right. Then the 0.2% yield strength is the stress corresponding to the intersection of the offset line and the stress-strain curve. The raw data output from stress-strain tests were filtered before calculating the hardening rate, due to high frequency noise. To achieve a smooth hardening rate curve, a 9-point smoothing was done on the original data, and hardening rate was identified at 10% and 25% elongation.

For each 1cm x 1cm square sample, SEM-EBSD was used to generate OIM data on the cross section using an EDAX/TSL system and in the thickness though the grip of the dog-bone samples. Since the edges of the dog-bones from Ningxia were affected by shear cut of the strip, a 3mm cut from the end of the dog-bone were performed to acquire a sample to measure OIM data on selected samples. Post processing software was then used to generate various measures of microstructure statistics, including texture file containing the ODF and PF, average grain size (diameter) and misorientation.

First, the data were given a "clean up" to remove erroneous pixels using grain dilation and grain CI standardization with a grain tolerance angle of 5 and a minimum grain size of 3 pixels. Then, only pixels with a confidence index larger than 0.1 were kept, to improve the reliability of displayed pixels. Due to the sample mounting orientation with respect to the sample rolling and normal directions, as well as placement in the microscope, the EBSD Euler angle data needed to be rotated around the rotated around specimen ND by 180°, then rotated about the specimen horizontal axis by 90°(labeled TD on pole figures), and then a final rotation about the sheet normal direction that depended on how the sample was cut from the sheet in order to obtain a standard coordinate system

for presenting texture data. After rotation, the orientation distribution function (ODF) was computed using a Harmonic series expansion with L= 16, HW =5, and an orientation map was generated using the quick IPF map (with the sample normal direction (001) as the IPF reference direction). The (001), (011), (111) PF and the ODF were constructed with a bin resolution of 5°. The ODF was computed with: ϕ_1 from 0° to 360°, Φ from 0° to 180°, ϕ_2 from 0° to 360°. As it was not possible to determine which way the rolling direction pointed on the square samples, final rotation around the new ND by ±45° or 90° was made to the Euler angle coordinate system so that PF have the shapes consistent with rolling, where the orientation spread directions are perpendicular to the (horizontal) rolling direction.

The ODF sections with ϕ_2 = 0° and ϕ_2 = 45° were used to texture illustrate fibers. From the exported ODF, a Matlab code was written to extract fiber data from the ODF. The ϕ_2 = 45° section was used to find the maximum value, average and standard derivation on the γ-fiber (Figure 10), where Φ is in the range of 45° to 65°.There are four columns in the raw data: ϕ_1, Φ, ϕ_2 , ODF intensity value. The step size of Bunge Euler angles is 5°. For example, the code below plots the $\phi_2 = 45°$ slice and extracts the gamma fiber information. A graph with ϕ_2 equals to 45° is illustrated in Figure 15 comparing the Matlab and TSL result of the same data set.

```
%% 45 degree
a45 = (ODF(:,3) ==45); %Find values when phi2 equals 45°
ph245 = ODF(a45,:);
ph245(:,3)=[];  % A matrix has phi1, phi and ODF intensity when phi2 equals 45°
%plot the 3D ODF
x = ph245(:,1);
y = ph245(:,2);
```

```
z = ph245(:,3);


figure
tri = delaunay(x,y);
trisurf(tri,x,y,z)
colormap jet
c = colorbar;
c.Label.String = 'ODF intensity';
%%set(gca, 'CLim', [0,16]);
xlabel('phi1')
xi = min(x);
xa = max(x);
xlim([xi xa])
set(gca,'XTick',[xi:45:xa])
ylabel('PHI')
zlabel('ODF')
title('At 45 degree phi2 ')
set(gcf,'Color',[1,1,1])


%%
%Find standard deviation, max, average along Gamma fiber
b55 = find(ph245(:,2) >=45 & ph245(:,2) <=65); %Find the gamma fiber band
ph255 = ph245(b55,:);
SD_G = std(ph255(:,3));
AVG_G = mean(ph255(:,3));
MAX_G = max(ph255(:,3));
BB = [SD_G, AVG_G, MAX_G] %Export standard deviation, maximum and average value
```

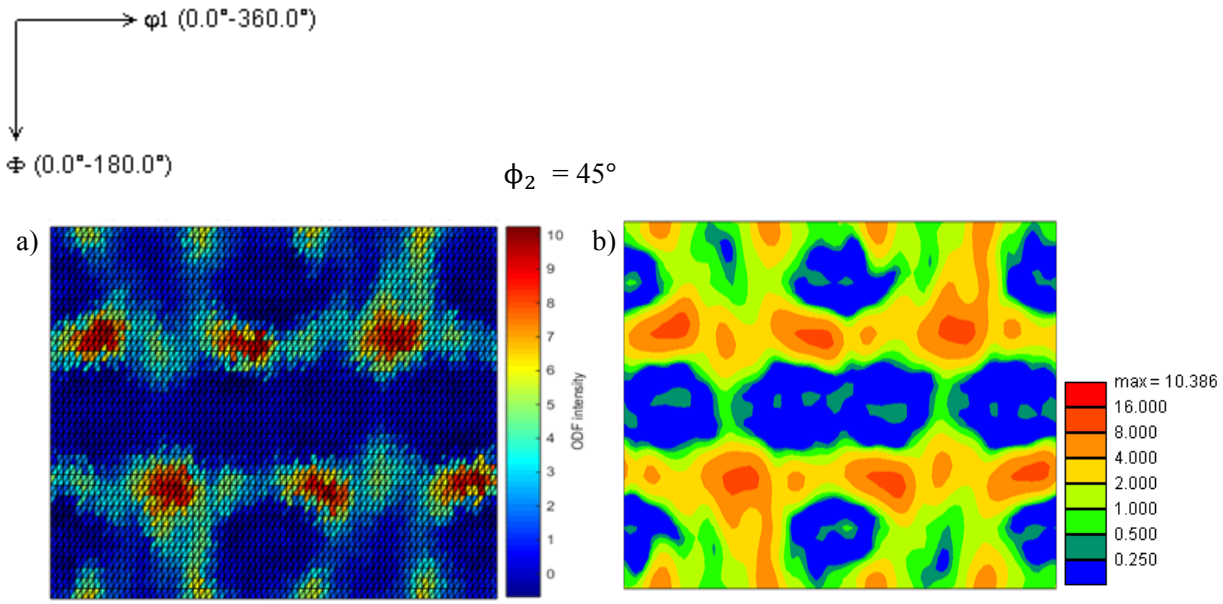

Figure 15: ODF plot from a) Matlab code and b) TSL, at $\phi_2 = 45°$ of Lot 4483 #35 with thickness of 3mm from Tokyo Denkai.

To compute a hard-soft contrast factor related to grain boundaries, a Matlab code written by Dr. Bieler was used and shown in Appendix B. In this code, [100] (soft) and [111] (hard) direction components of the crystal orientation were computed with respect to sample X, Y, Z directions for a pair of grains along each boundary. The product of $\max[100]_i$ * $\max[111]_j$ components in the Y direction for i,j = grains A,B, provides a measure of how well aligned two <111> and <100> crystal directions are for each grain pair; two values are possible, so the higher value was chosen. Each value was weighted by the length of the boundary. Thus, if there are more grain pairs with hard and soft orientations adjacent to each other, the contrast factor will be high. The maximum value will occur when a <111> in one grain and <100> in the other grain is aligned with Y, a value of 1. The minimum will be when both grains have <111> or <100> aligned with the Y axis, yielding a value of 0.577. This computation used the reconstructed boundary file and the grain file exported from TSL

analysis software. These files contain average orientation in degrees, as well as centroid position (x, y) in microns, and grain identify on either side of a grain boundary segment, and other quantities.

LAM and KAM data were exported from TSL system. A peak can be found in each of the curves and then plotted vs. mechanical properties. For both misorientation maps, the maximum misorientation is 3° and the number of bins is 75. CSL boundaries are calculated from $\sum$ type 1 to 29b, with tolerance = $\frac{K}{\sum^n}$, where K equals to 15 and n equals to 0.5.

These data were analyzed and compared to find the correlations between mechanical and microstructural properties of high purity niobium.

IV. RESULTS

1. Result of OIM square and dog-bone samples comparisons for consistency

For Tokyo Denkai samples, the IPF maps of the OIM square, left grip and right grip of dog-bone of Lot 4499 #74 with thickness 4mm are shown in Figure 16 below. All three IPF maps are relatively similar, with blue band in the middle and red band near the two surfaces. Figure 17 shows the PFs and ODF plots for ϕ_2 equals to 0° and 45° of this sample. In all three measurements, PFs are similar and the γ-fiber is not smooth, and the peak positions on γ-fiber are different.

Figure 18 shows the IPFs results of OIM squares and dog-bone samples of Lot 4482 #22, #35 and #55. In Figure 18, a) #55 and b) were rotated upside down by 180 ° due to the placement of the sample. The IPF maps are similar for OIM square and dogbone sample. The PFs in Figure 19 are almost the same for all three samples. Figure 20 is ODF plots for ϕ_2 equals to 0° and 45°, the shape are similar with a different peak positions on γ–fiber.

For Lot 4503 #114, Figure 21 shows the IPF maps of OIM square and dog-bone sample, the dog-bone sample were rotated by 180 ° due to the placement of the sample. The IPF maps are similar at bottom, but the dog-bone sample shows less red band at the other side. In Figure 22, the PFs and ODF plots for ϕ_2 equals to 0° and 45° for these two samples are almost the same.

Figure 23 shows the IPF maps of OIM square and dog-bone sample of Lot 4504 #117, #122. The IPF maps share a lot similarity. Figure 24-25 are PFs and ODF plots for ϕ_2 equals to 0° and 45°. The shapes of the PFs and ODF slices have some differences in peak positions, but are otherwise the same.

In general, measurements made on the same lots in different regions of provided material are nearly the same.

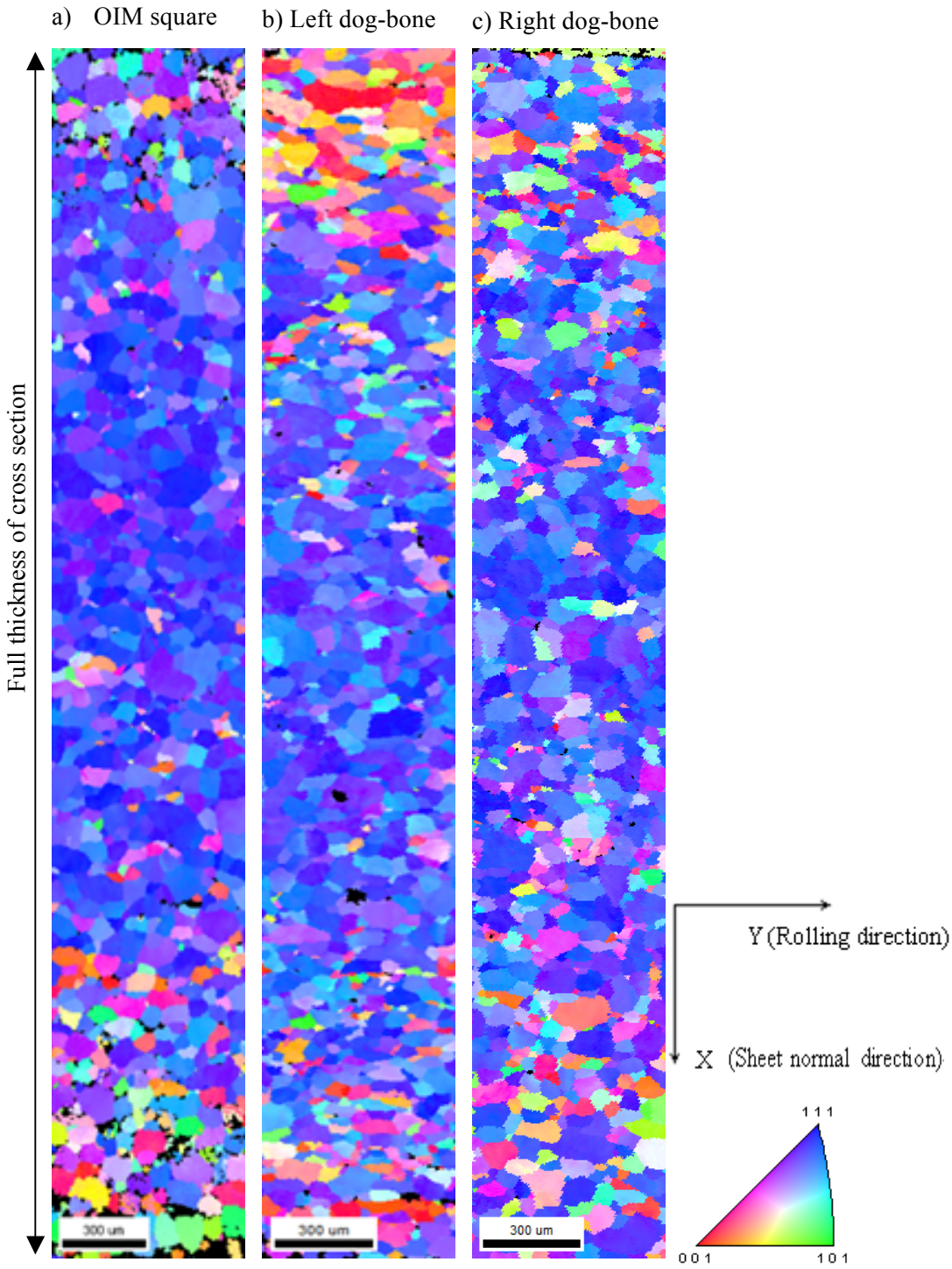

Figure 16: IPF maps of a) OIM square, b) Left grip of dog-bone and c) right grip of dog-bone of niobium sheet Lot 4499 #74 with thickness 4mm. (Tokyo Denkai)

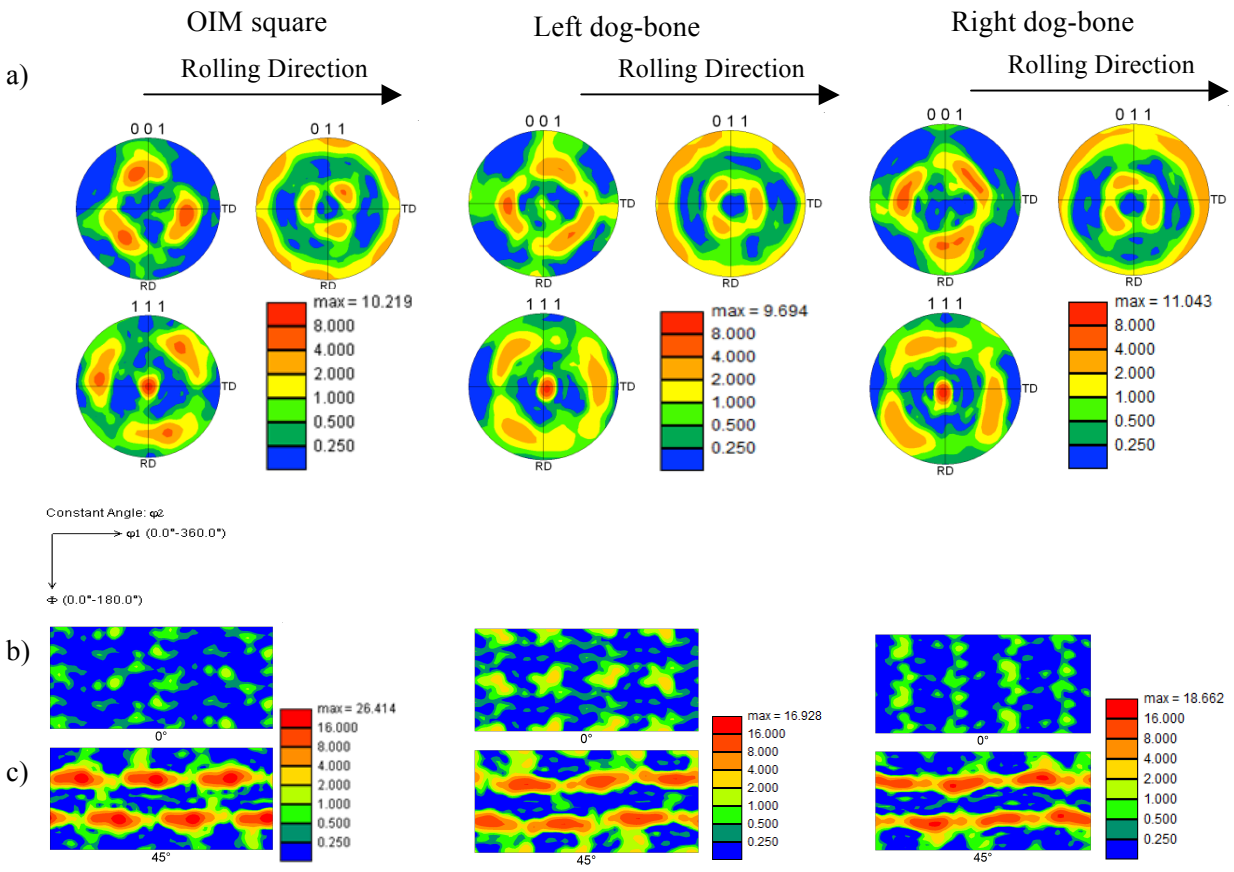

Figure 17: a) PFs and b) ODF plots of ϕ_2 equals 0° and c) 45° of OIM square, Left grip of dog-bone and right grip of dog-bone layer of niobium sheet Lot 4499 #74 with thickness 4mm. (Tokyo Denkai)

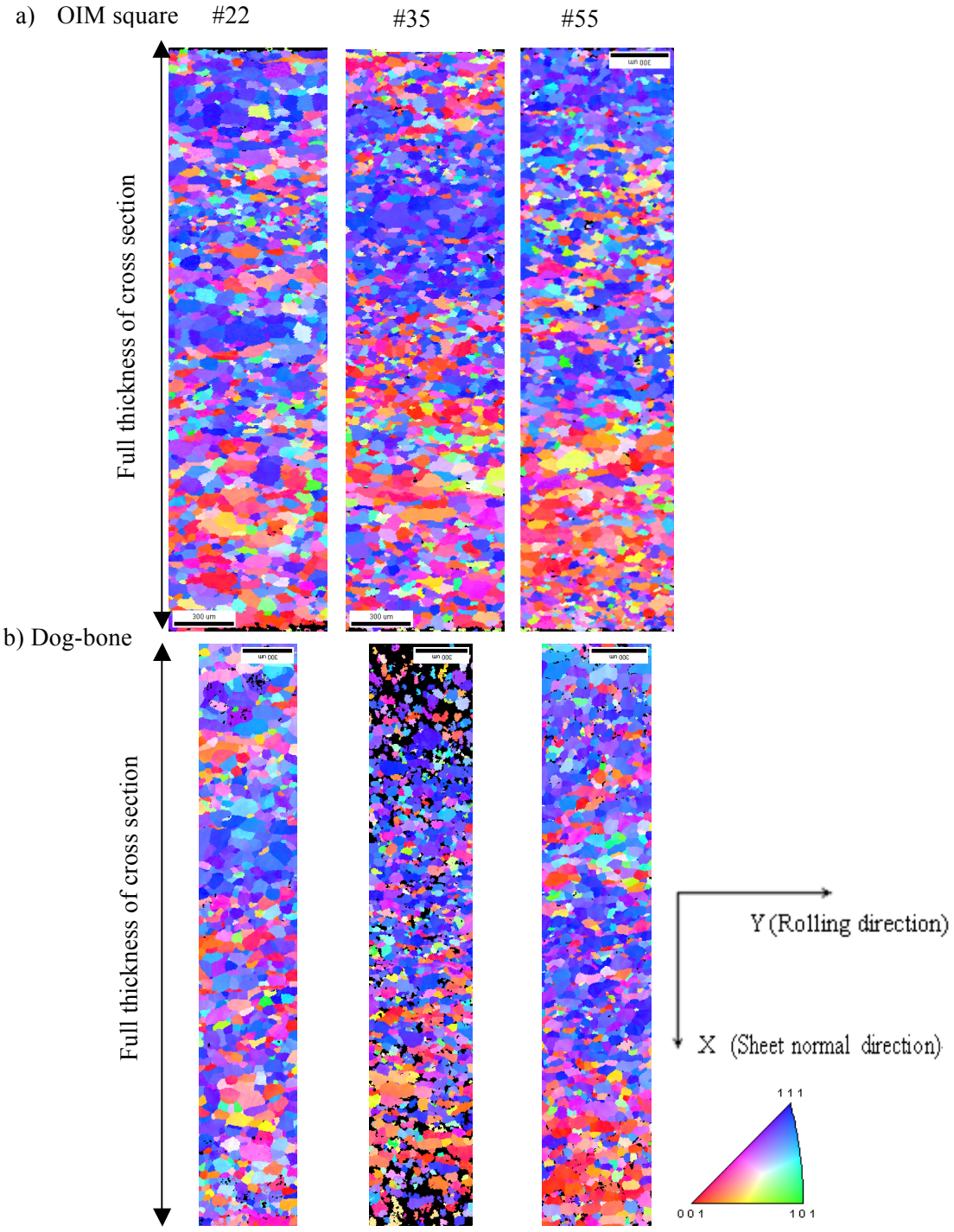

Figure 18: IPF maps of a) OIM square, b) Grip of dog-bone of niobium sheet Lot 4482 #22, #35, #55 with thickness 3mm. (Tokyo Denkai)

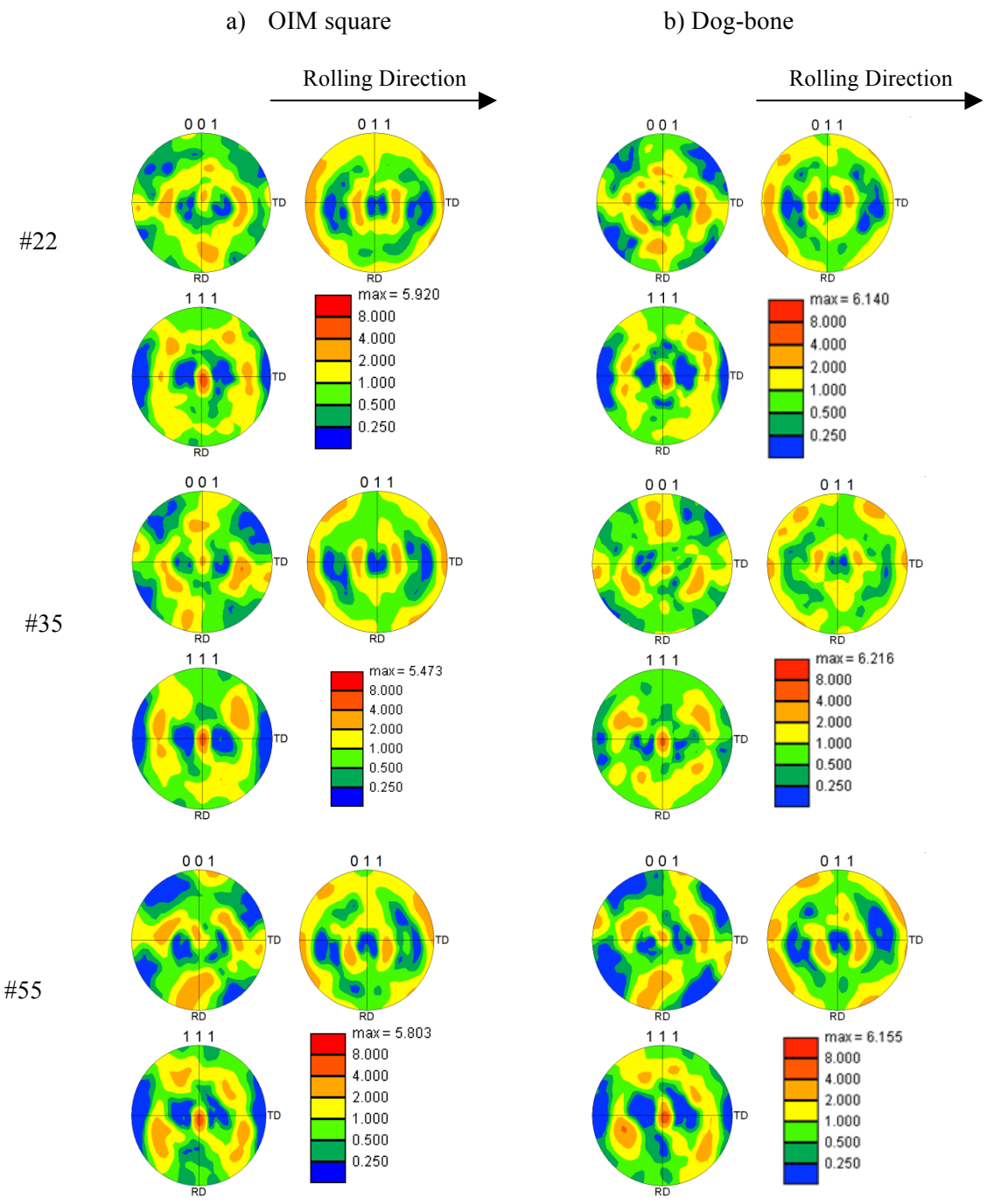

Figure 19: PFs of a) OIM square, b) Grip of dog-bone of niobium sheet Lot 4482 #22, #35, #55 with thickness 3mm. (Tokyo Denkai)

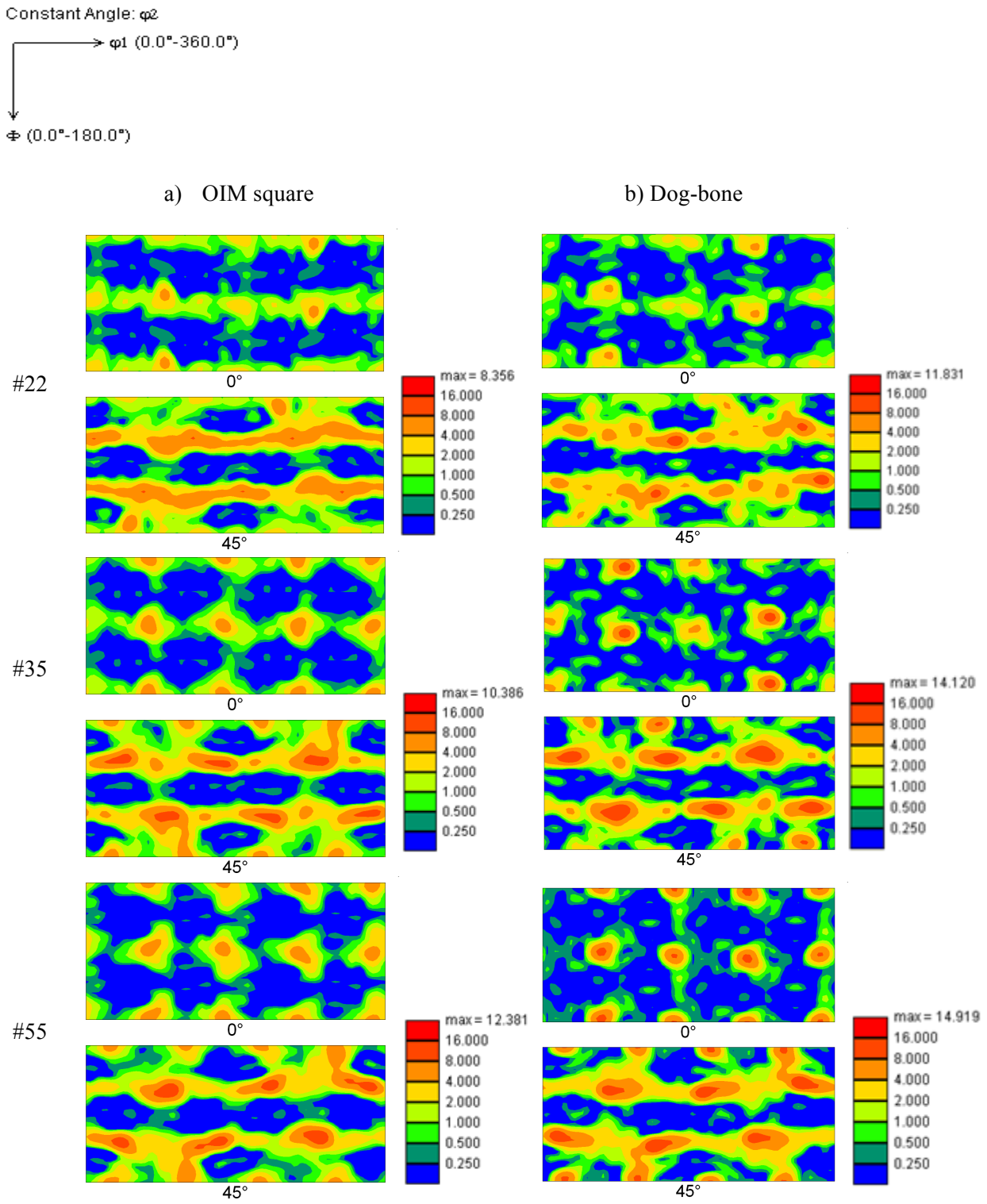

Figure 20: ODF plots of ϕ_2 equals 0° (top) and 45° (bottom) of a) OIM square, b) Grip of dog-bone of niobium sheet Lot 4482 #22, #35, #55 with thickness 3mm. (Tokyo Denkai)

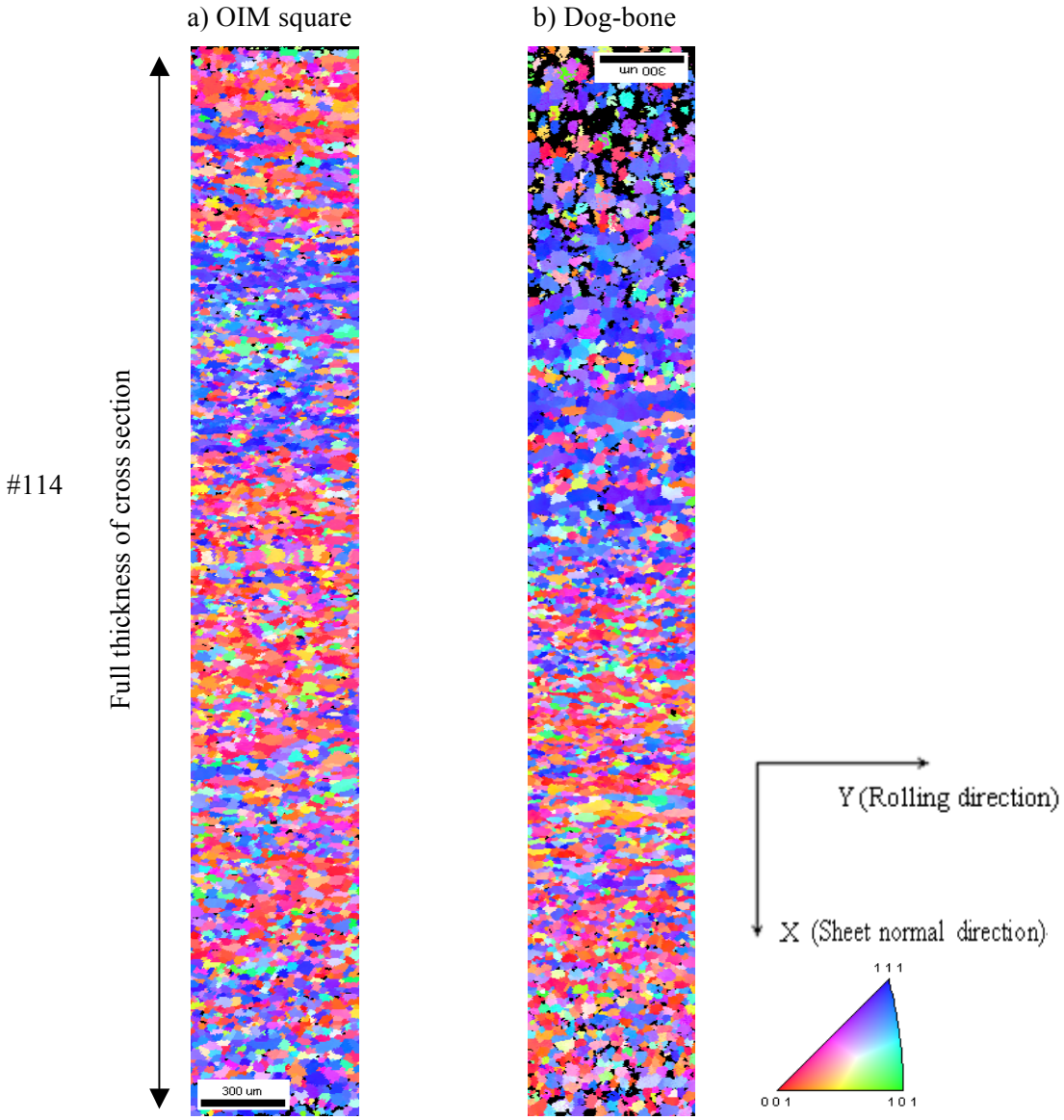

Figure 21: IPF maps of a) OIM square, b) Grip of dog-bone of niobium sheet Lot 4503 #114 with thickness 4mm. (Tokyo Denkai)

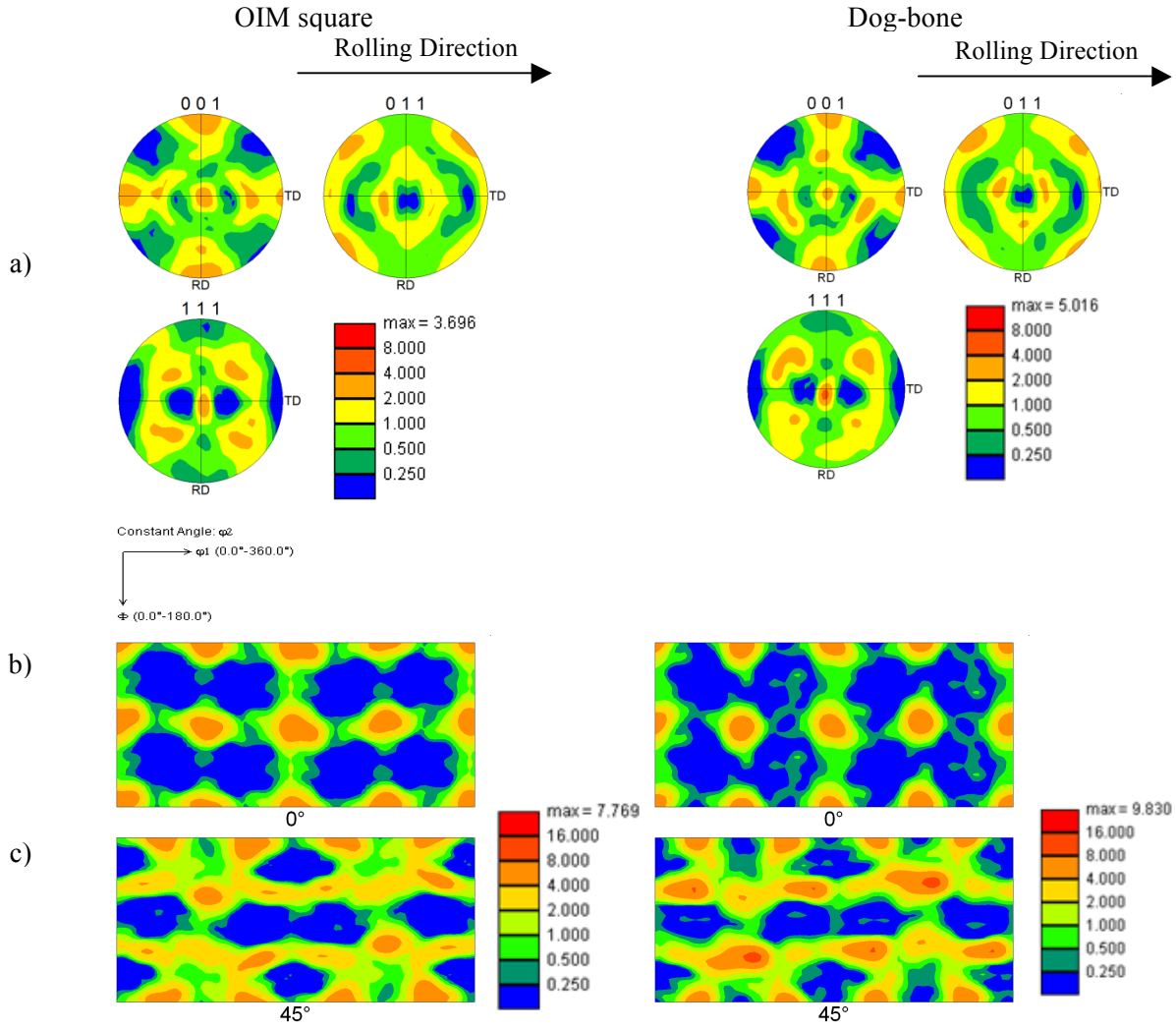

Figure 22: a) PFs, b) ODF plots of ϕ_2 equals 0° and c) 45° of OIM square and Grip of dog-bone of niobium sheet Lot 4503 #114 with thickness 4mm. (Tokyo Denkai)

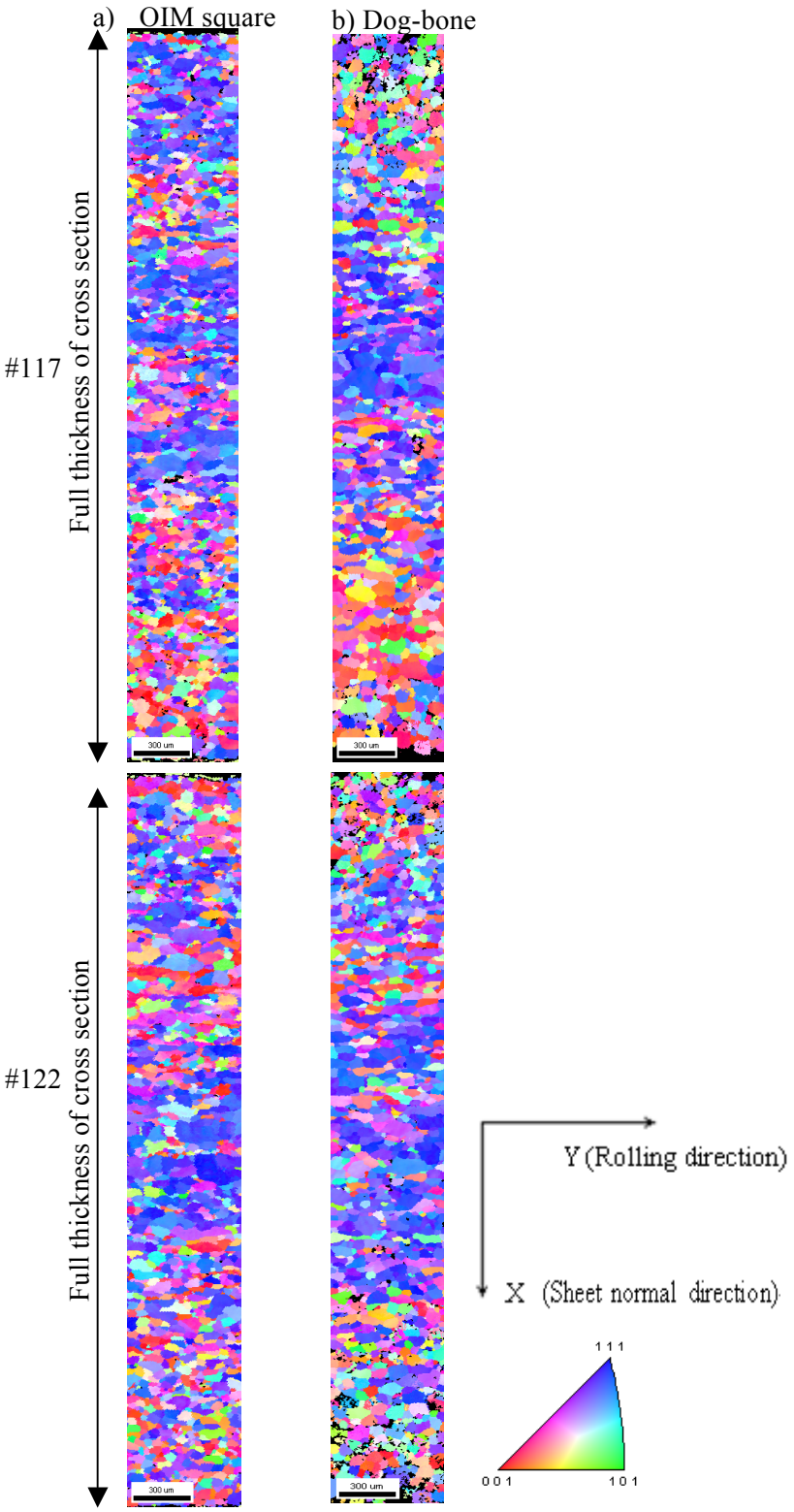

Figure 23: IPF maps of a) OIM square, b) Grip of dog-bone of niobium sheet Lot 4504 #117, #122 with thickness 4mm. (Tokyo Denkai)

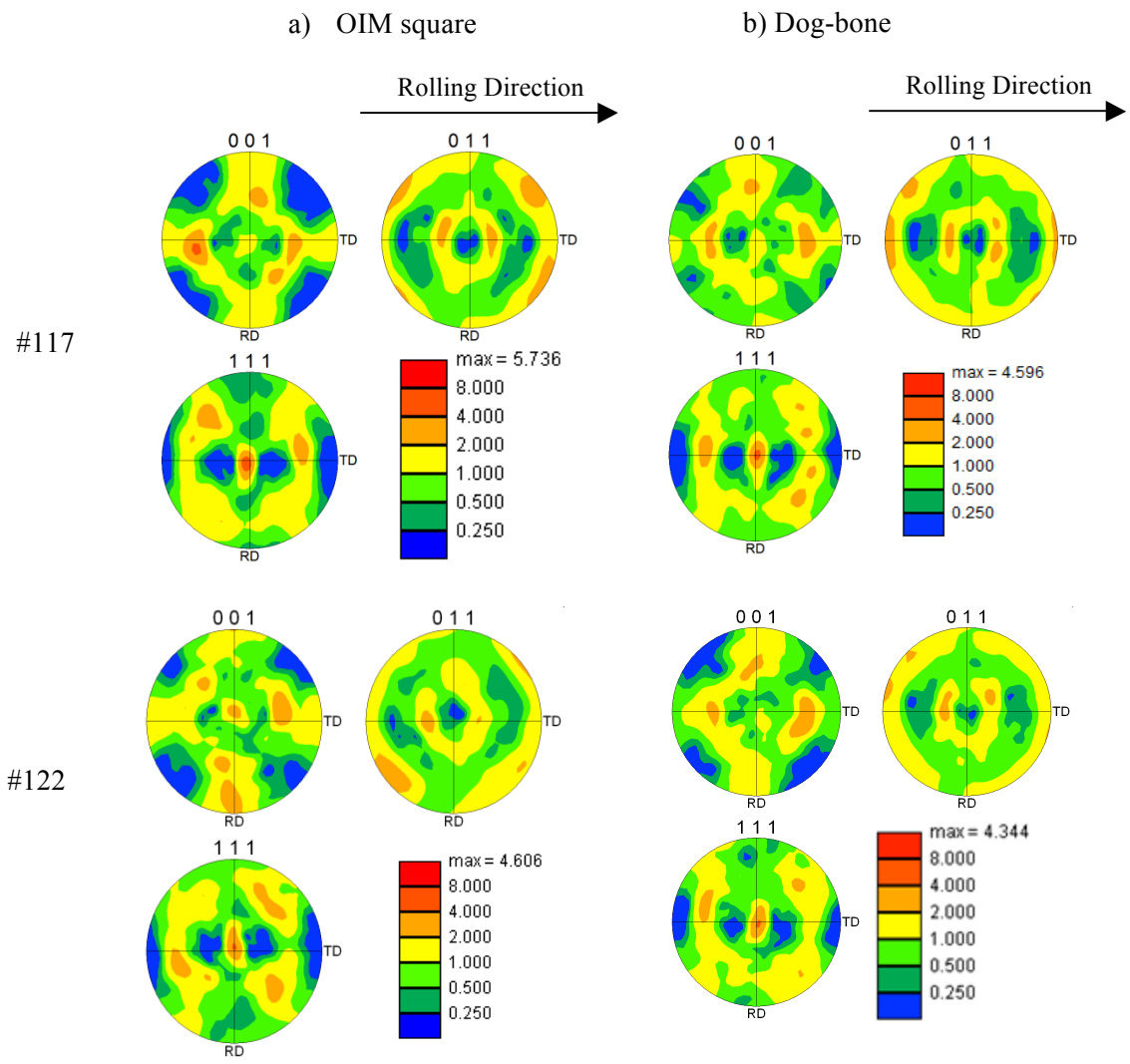

Figure 24: PFs of a) OIM square, b) Grip of dog-bone of niobium sheet Lot 4504 #117, #122 with thickness 4mm. (Tokyo Denkai)

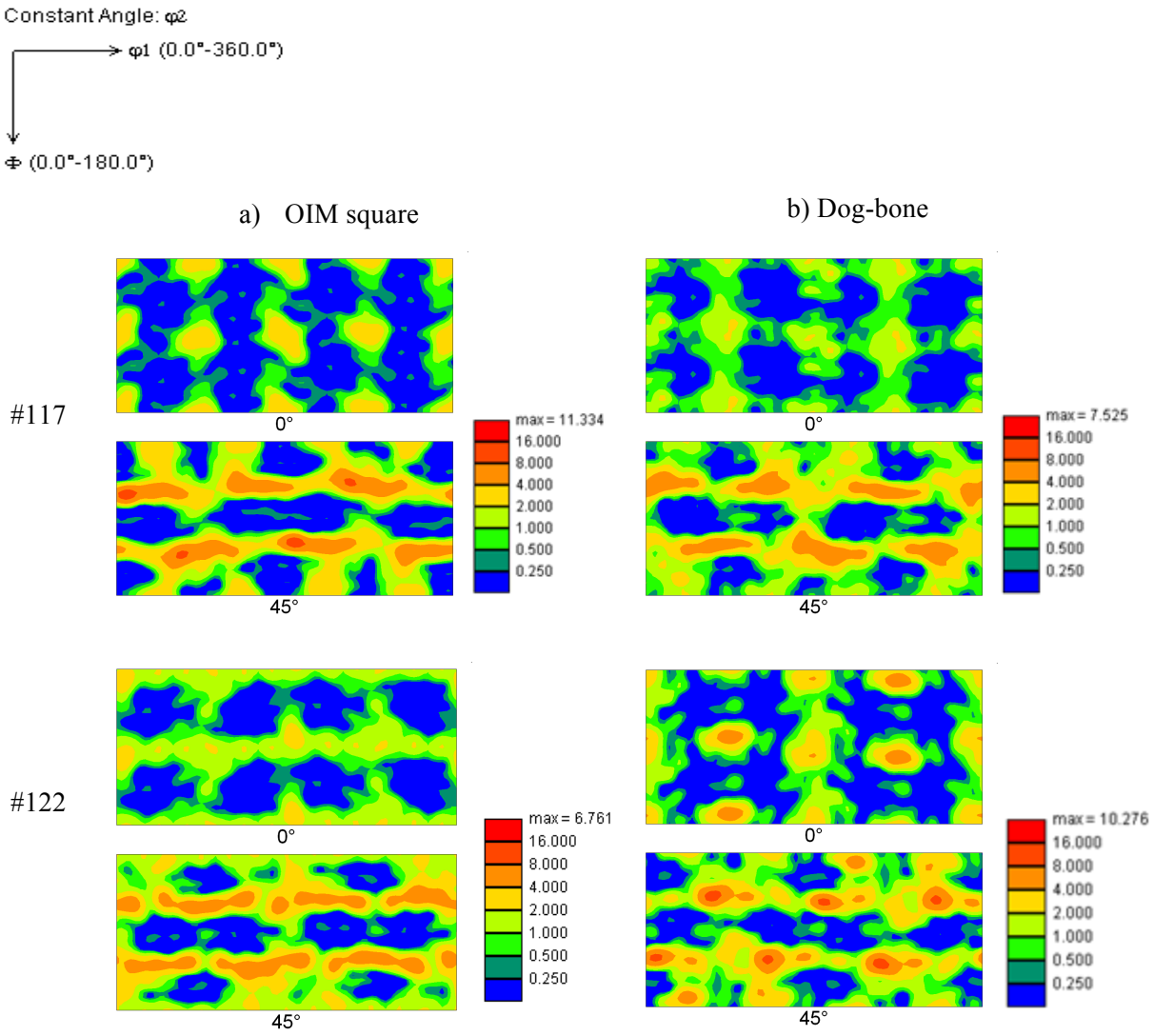

Figure 25: ODF plots of ϕ_2 equals 0° (top) and 45° (bottom) of a) OIM square, b) Grip of dog-bone of niobium sheet Lot 4504 #117, #122 with thickness 4mm. (Tokyo Denkai)

For Ningxia samples, Figure 26 below shows the IPF maps for OIM square and dog-bone samples of niobium sheet A-5 and A-26. The IPF maps show almost the same feature. Figure 27-38 are PFs and ODF plots for ϕ_2 equals to 0° and 45° of these samples. There are lots of similarities but the peak positions on the γ -fiber are different.

The IPF maps for OIM square and dog-bone sample of niobium sheet D-25 and D-27 are shown in Figure 29, which are similar, but more blue is shown in the dog-bone samples of D-25. Figure 30-31 are PFs and ODF plots for ϕ_2 equals to 0° and 45° of these samples. The PFs are relatively the same, and the ODF slices have similar shape.

For OIM square and dog-bone sample of niobium sheet E-37 and E-38, the IPF maps are shown as Figure 32. The IPF maps are similar for E-37, but dog-bone sample of E-38 has less red feature compares with OIM square. Figure 33-34 are PFs and ODF slices for ϕ_2 equals to 0° and 45° of these samples. The PF of dog-bone sample of E-38 is significantly different from the OIM square, where the ODF slices are similar with a different position of peak on ODF slice for E-38's OIM square, compare with E-38's dog-bone sample.

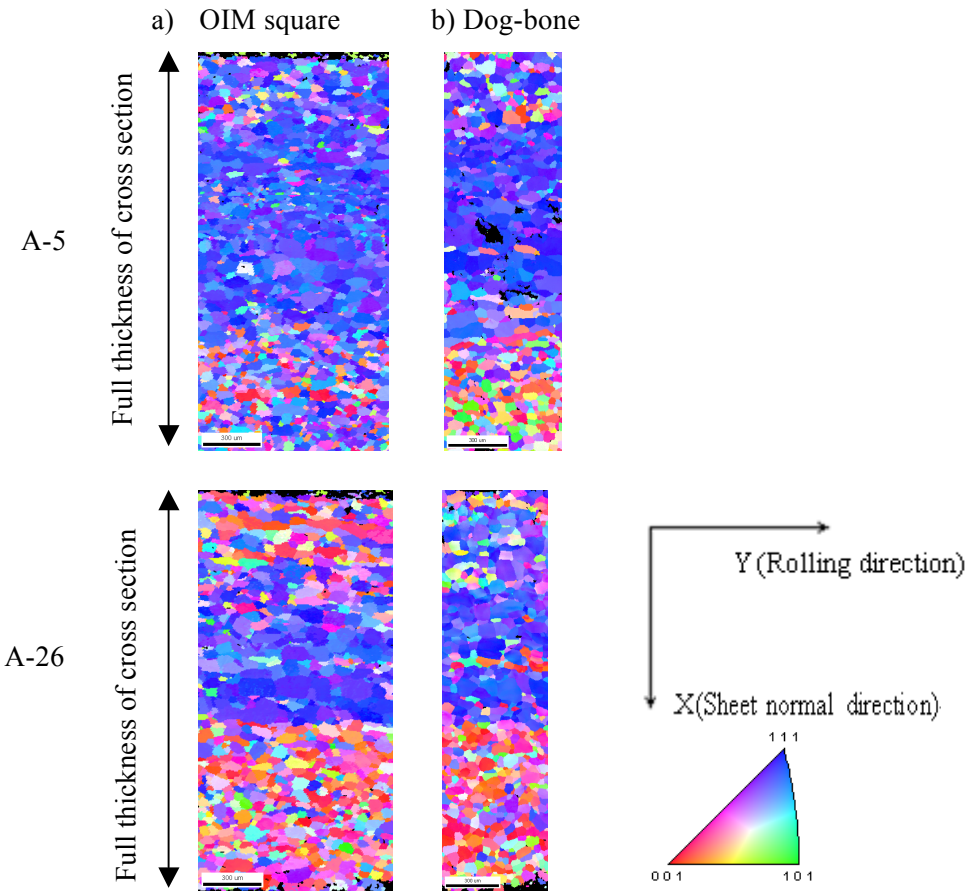

Figure 26: IPF maps of a) OIM square, b) Grip of dog-bone of niobium sheet A-5 and A-26 with thickness 2mm. (Ningxia)

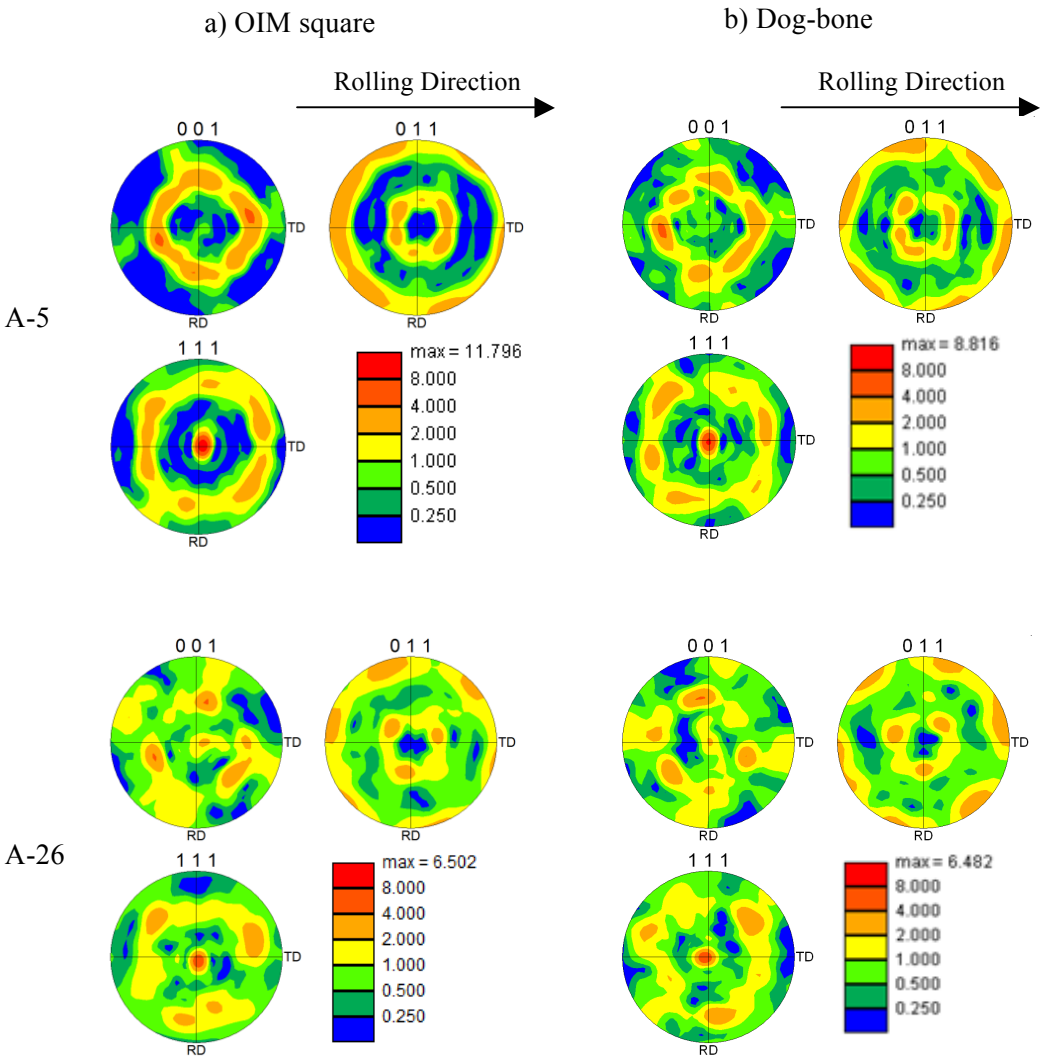

Figure 27: PFs of a) OIM square, b) Grip of dog-bone of niobium sheet A-5 and A-26 with thickness 2mm. (Ningxia)

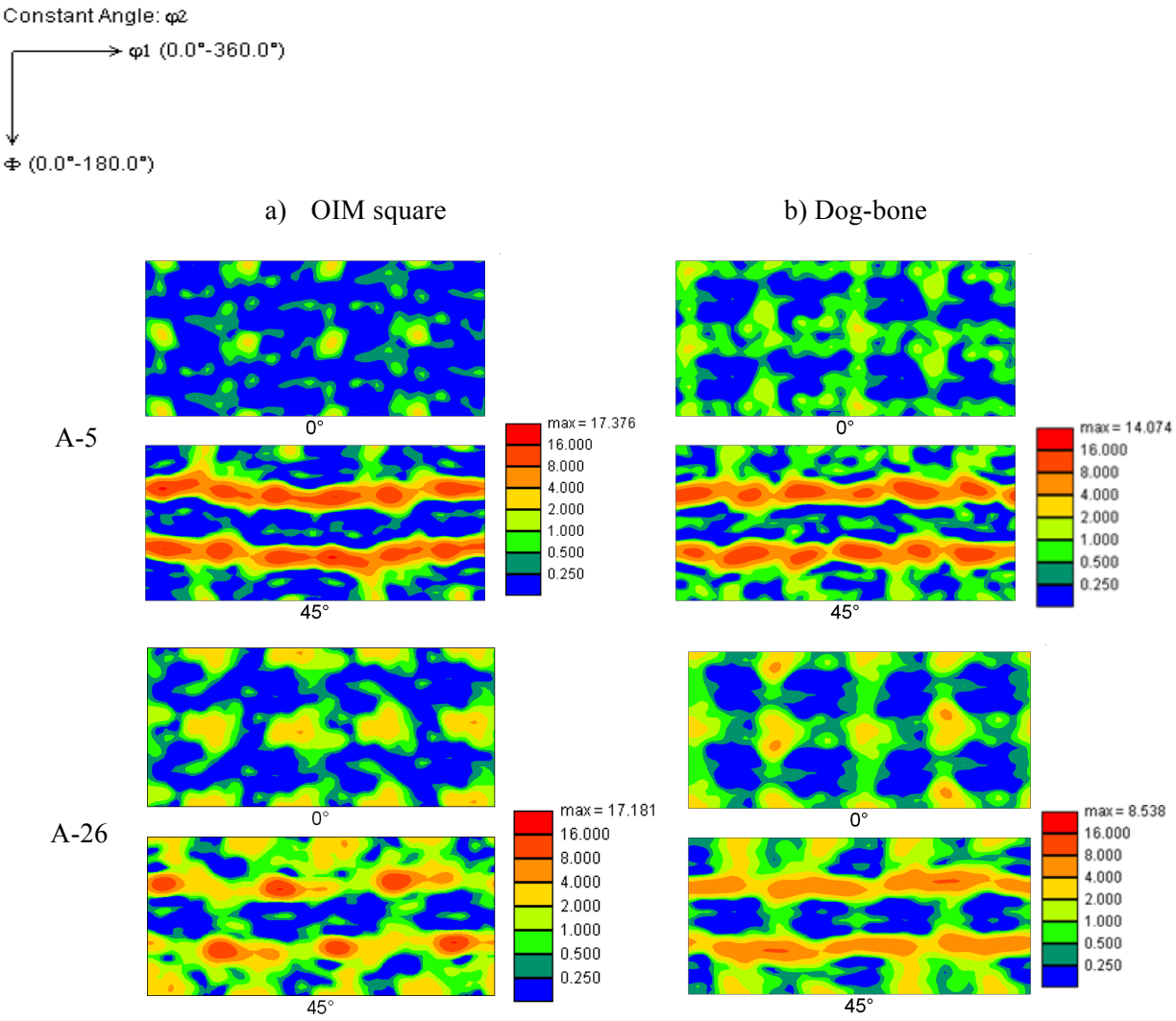

Figure 28: ODF plots of ϕ_2 equals 0° (top) and 45° (bottom) of a) OIM square, b) Grip of dog-bone of niobium sheet A-5 and A-26 with thickness 2mm. (Ningxia)

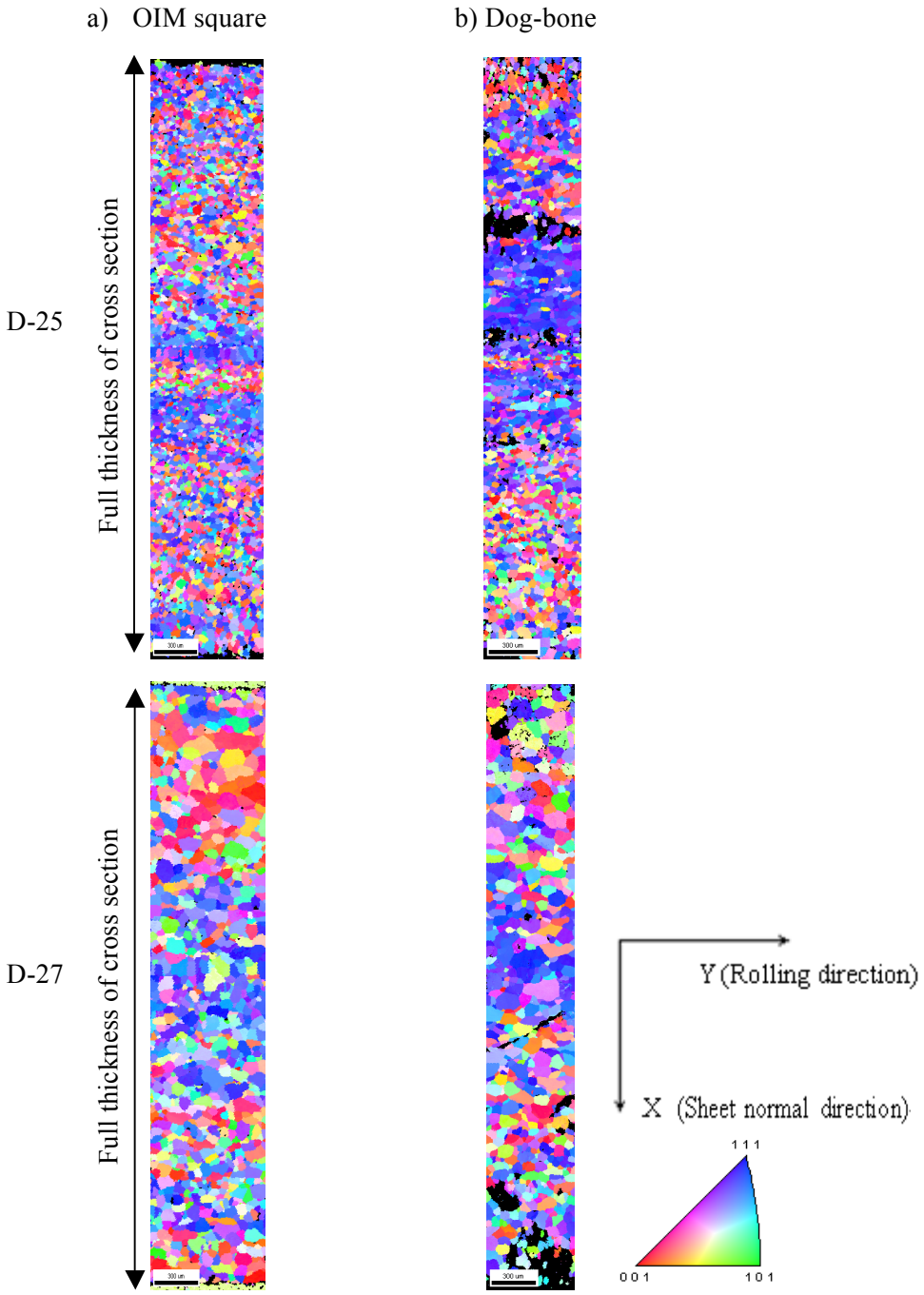

Figure 29: IPF maps of a) OIM square, b) Grip of dog-bone of niobium sheet D-25 and D-27 with thickness 3mm. (Ningxia)

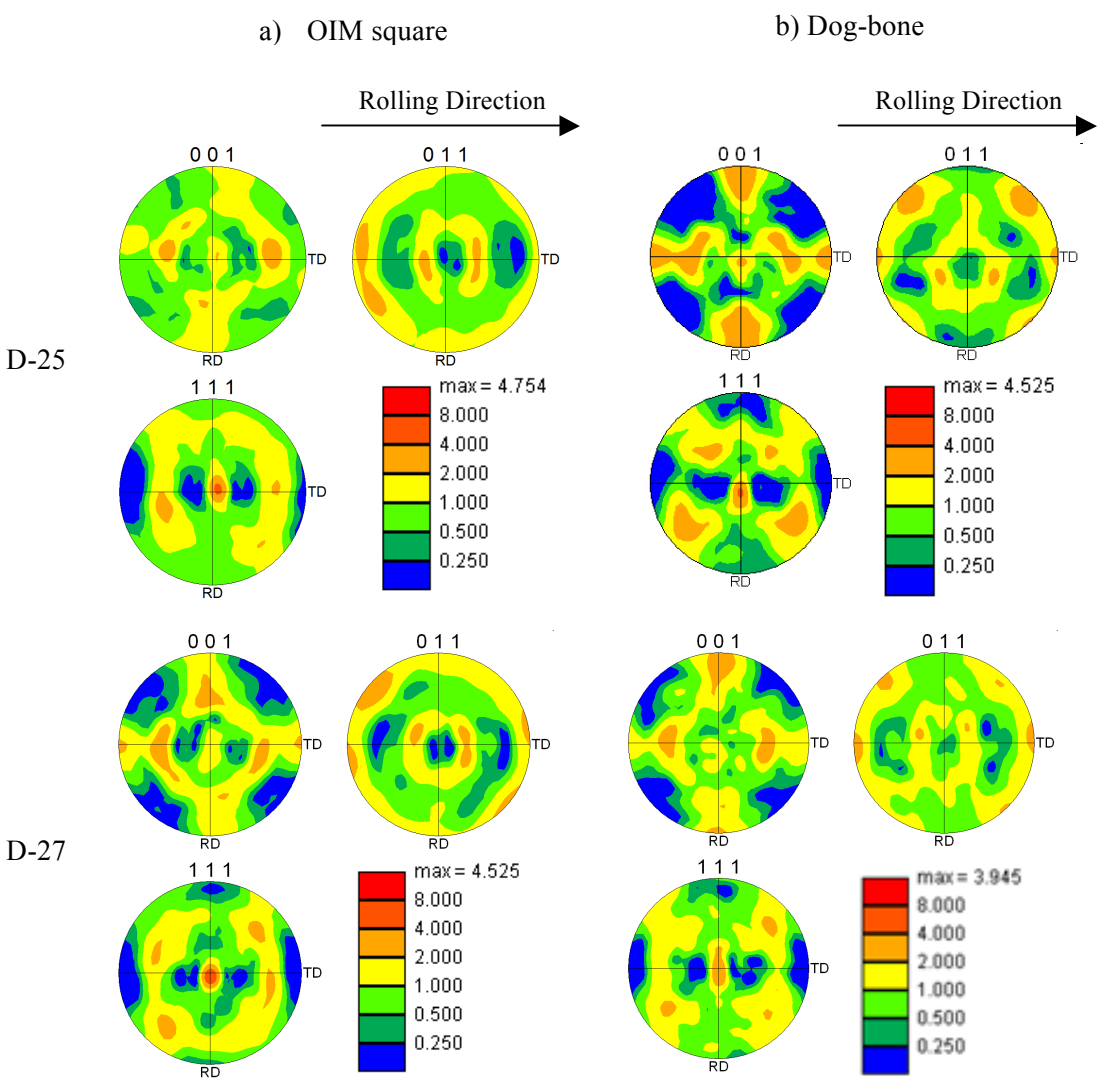

Figure 30: PFs of a) OIM square, b) Grip of dog-bone of niobium sheet D-25 and D-27 with thickness 3mm. (Ningxia)

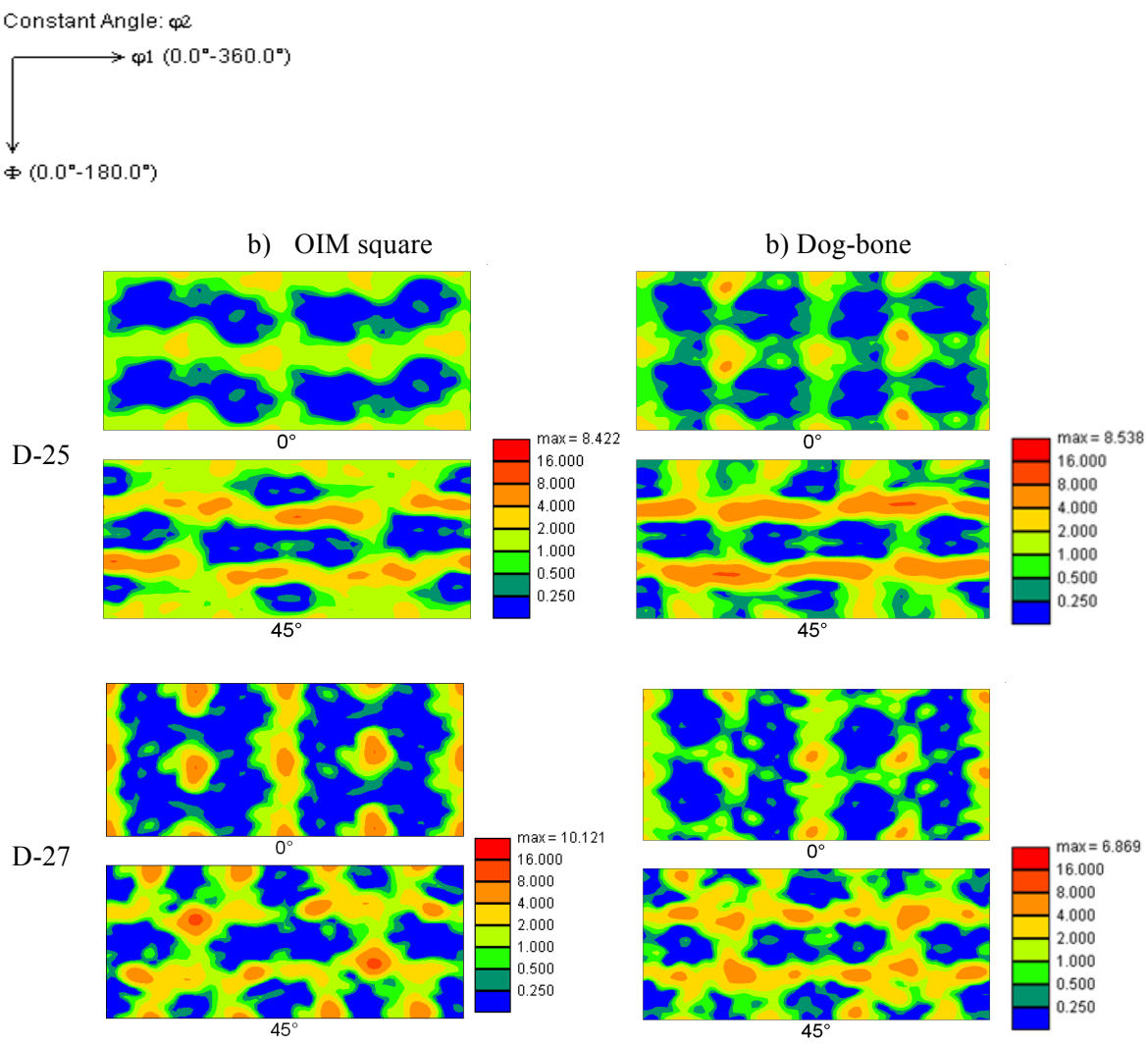

Figure 31: ODF plots of ϕ_2 equals 0° (top) and 45° (bottom) of a) OIM square, b) Grip of dog-bone of niobium sheet D-25 and D-27 with thickness 3mm. (Ningxia)

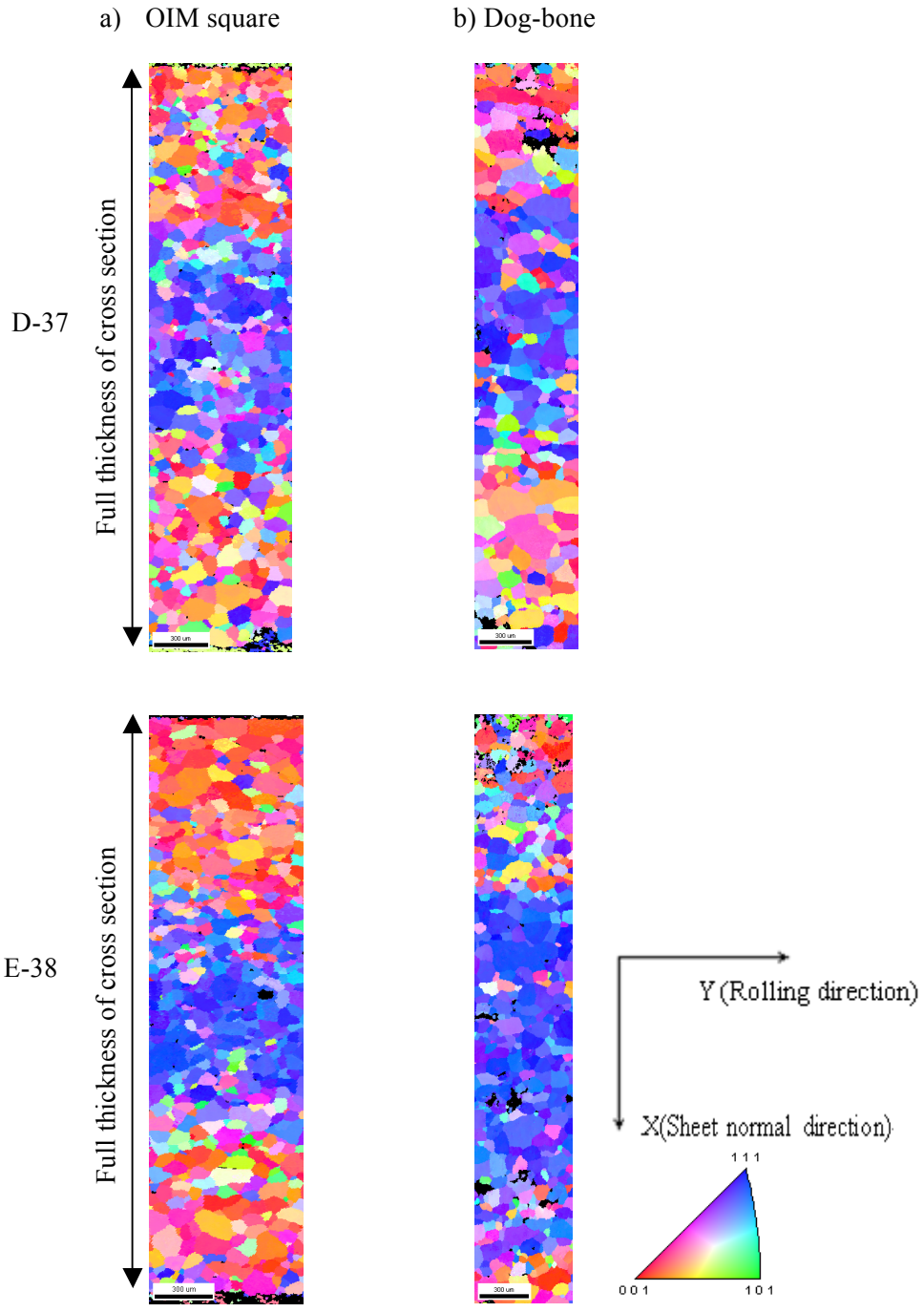

Figure 32: IPF maps of a) OIM square, b) Grip of dog-bone of niobium sheet E-37 and E-38 with thickness 3mm. (Ningxia)

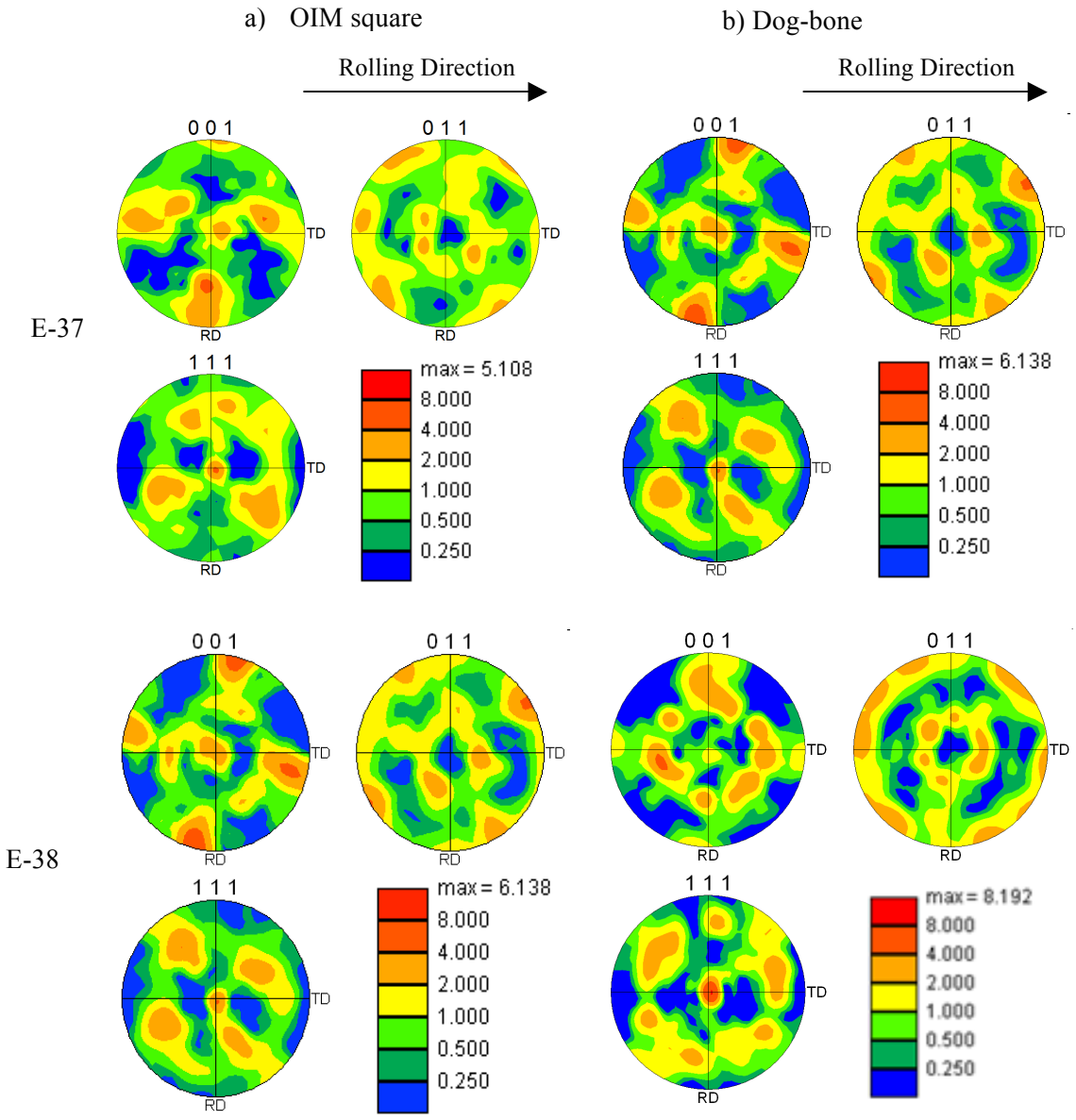

Figure 33: PFs of a) OIM square, b) Grip of dog-bone of niobium sheet E-37 and E-38 with thickness 3mm. (Ningxia)

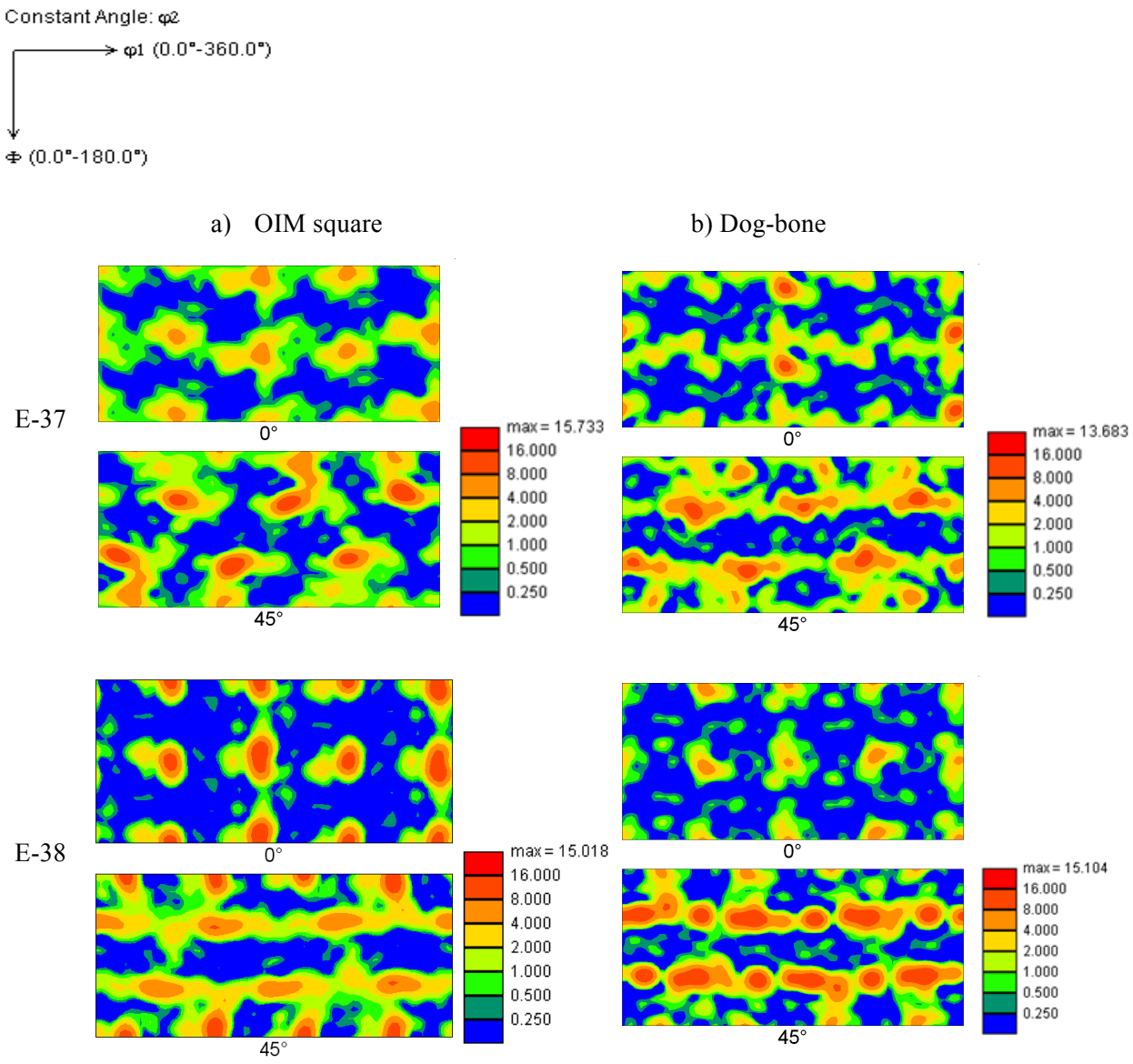

Figure 34: ODF plots of ϕ_2 equals 0° (top) and 45° (bottom) of a) OIM square, b) Grip of dog-bone of niobium sheet E-37 and E-38 with thickness 3mm. (Ningxia)

2. Result of mechanical and microstructural properties

Stress-strain curves of Tokyo Denkai and Ningxia samples are shown in Figure 35 and 36 below. The UTS is in the range of 180 to 205 MPa for Tokyo Denkai, where for Ningxia, UTS is in the range of 168 to 195 MPa. Elongation at fracture is from 50% to 75% for Tokyo Denkai, and 50% to 70% for Ningxia. 0.2% yield strength for Tokyo Denkai is in the range of 45 to 90 MPa and in the range of 50 to 90 MPa for Ningxia. Tables 3 and 4 provide elongation, 0.2% yield stress, and UTS for each of the samples from the two suppliers, and the maximum and minimum values are indicated with bold text. Average values show that Ningxia and Tokyo Denkai samples have similar elongation and yield strength, but the UTS is significantly higher for the Tokyo Denkai material.

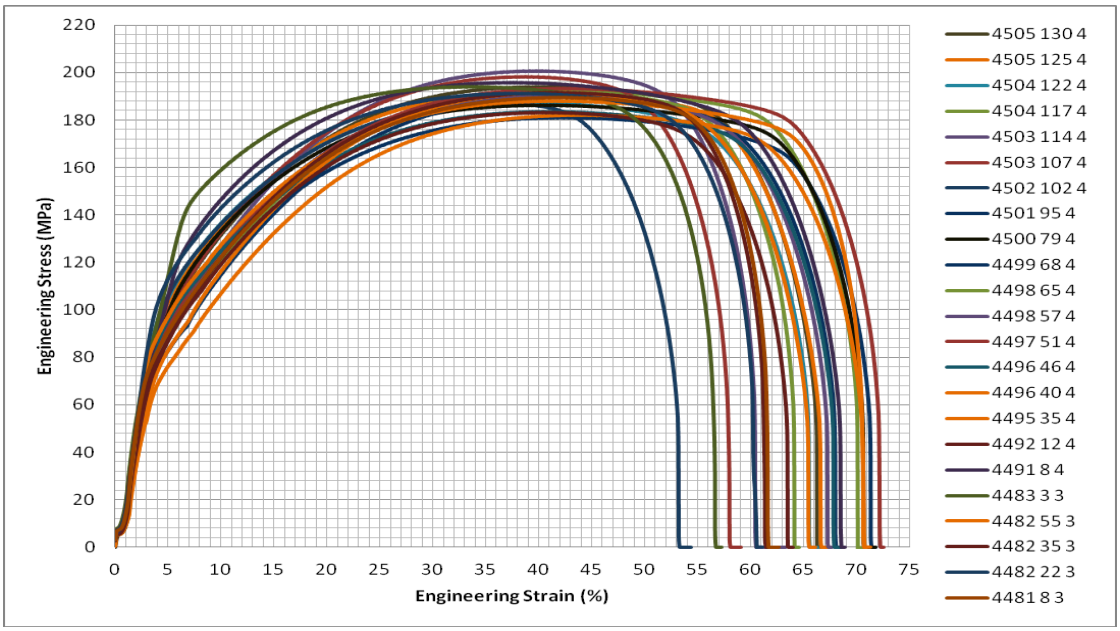

Figure 35: Stress-strain curves of samples from Tokyo Denkai.

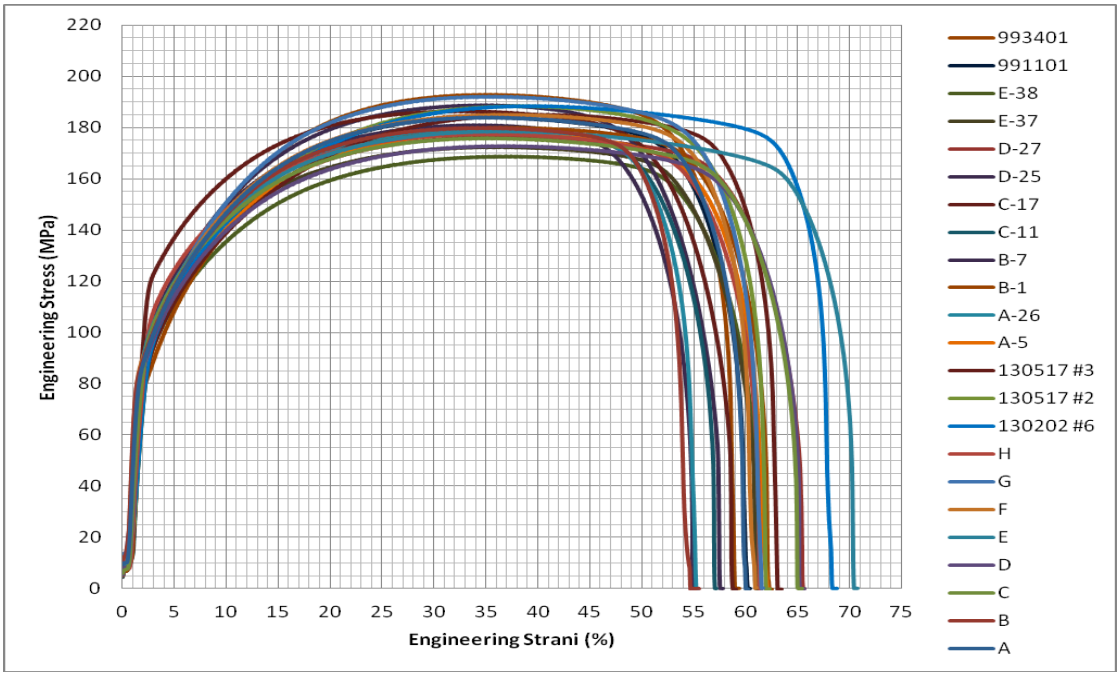

Figure 36: Stress-strain curves of samples from Ningxia.

LAM and KAM map of Tokyo Denkai and Ningxia are shown in Figure 37 and 38 below. Table 3 and 4 provide peak height and angle for each of the samples from the two suppliers, and the maximum and minimum values are indicated with bold text.

The hardening rate (after a 9-point smoothing of the original stress-strain curves) of Tokyo Denkai and Ningxia samples are shown in Figures 39 and 40. The hardening values at 10% strain and 25% strain are tabulated in Table 3 and 4, where maximum and minimum values are in bold font.

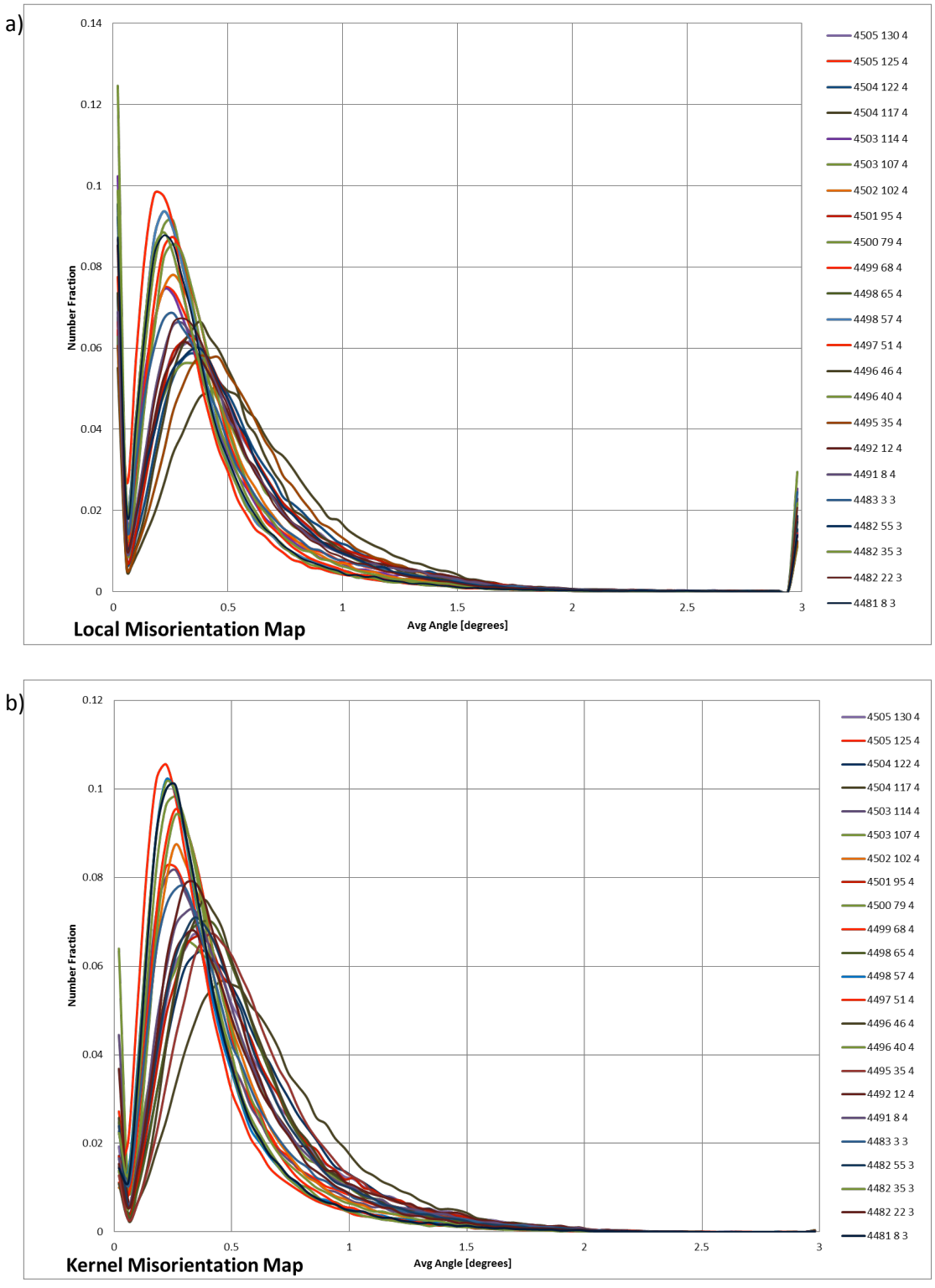

Figure 37: a) Local Average Misorientation and b) Kernel Average Misorientation for samples from Tokyo Denkai.

a)

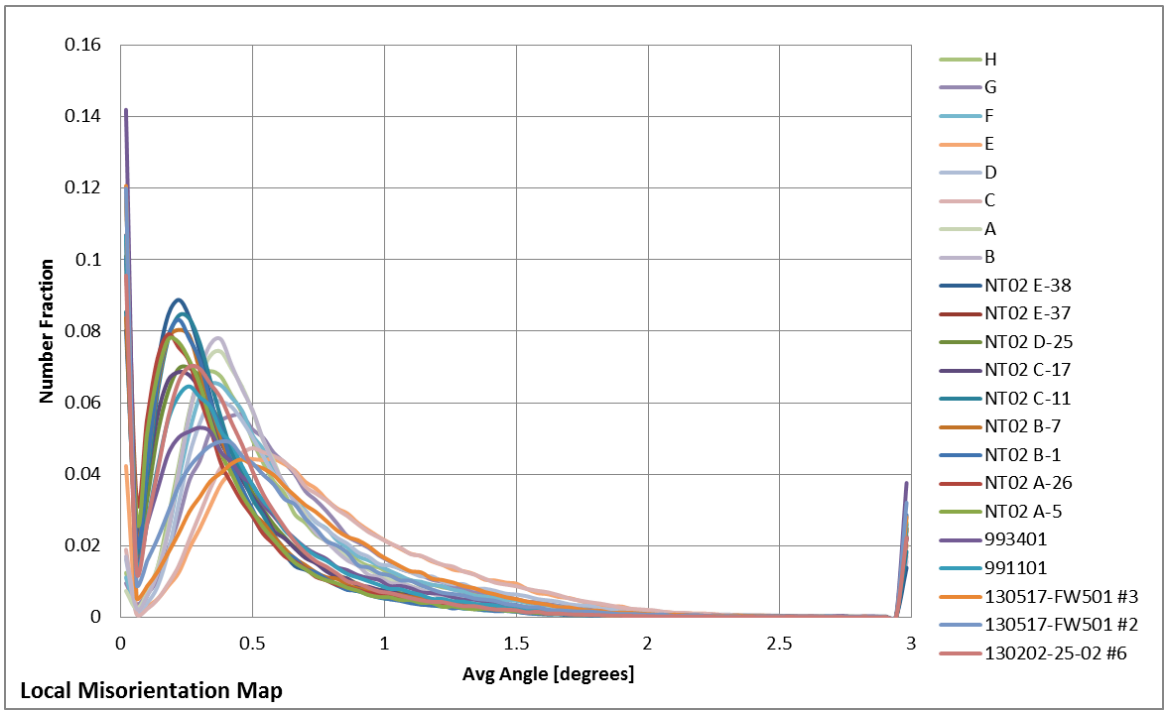

b)

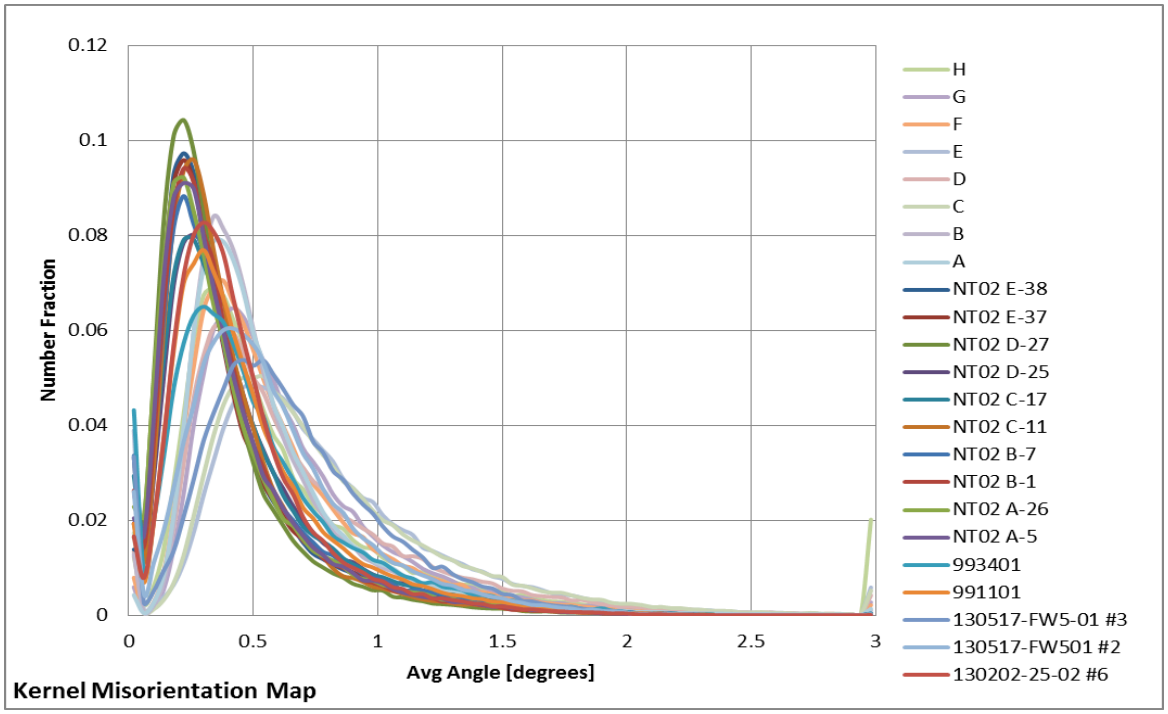

Figure 38: a) Local Average Misorientation and b) Kernel Average Misorientation for samples from Ningxia.

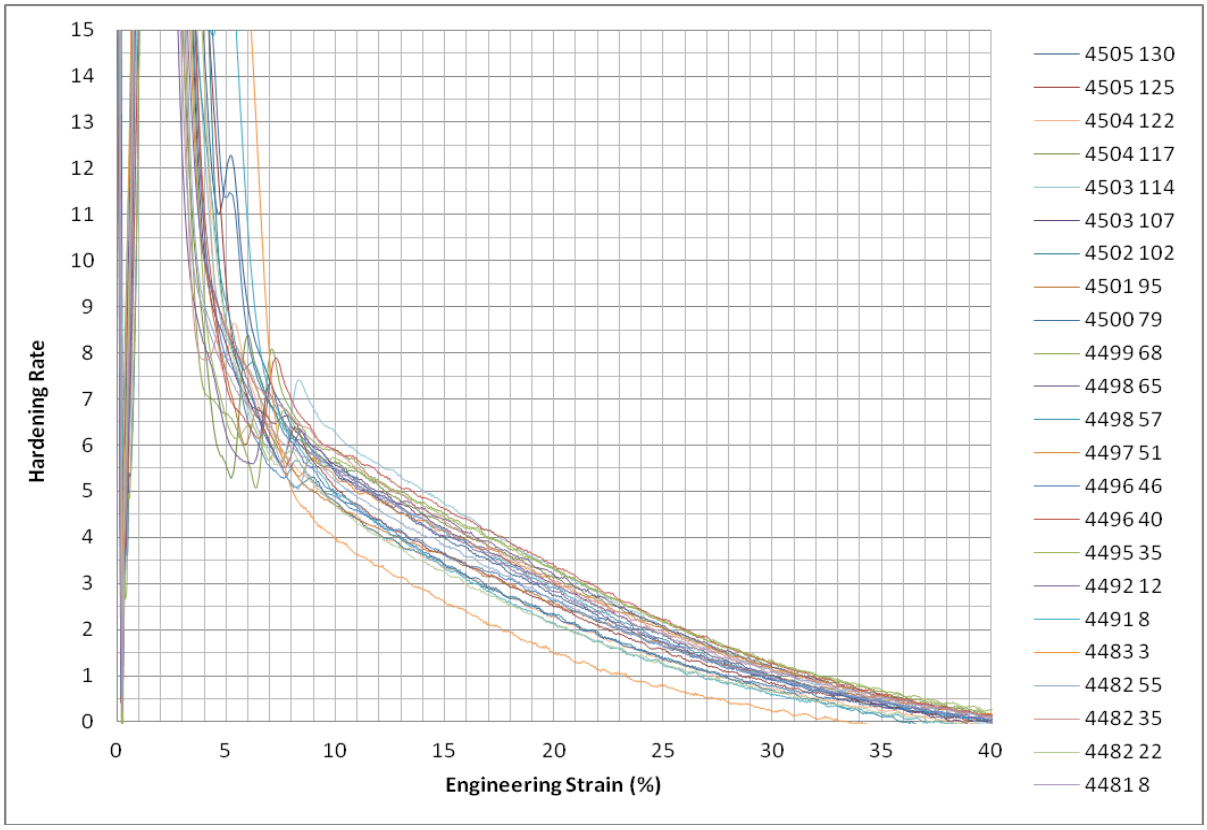

Figure 39: Hardening rate curve after 9-point smoothing of stress-strain curves for samples from Tokyo Denkai.

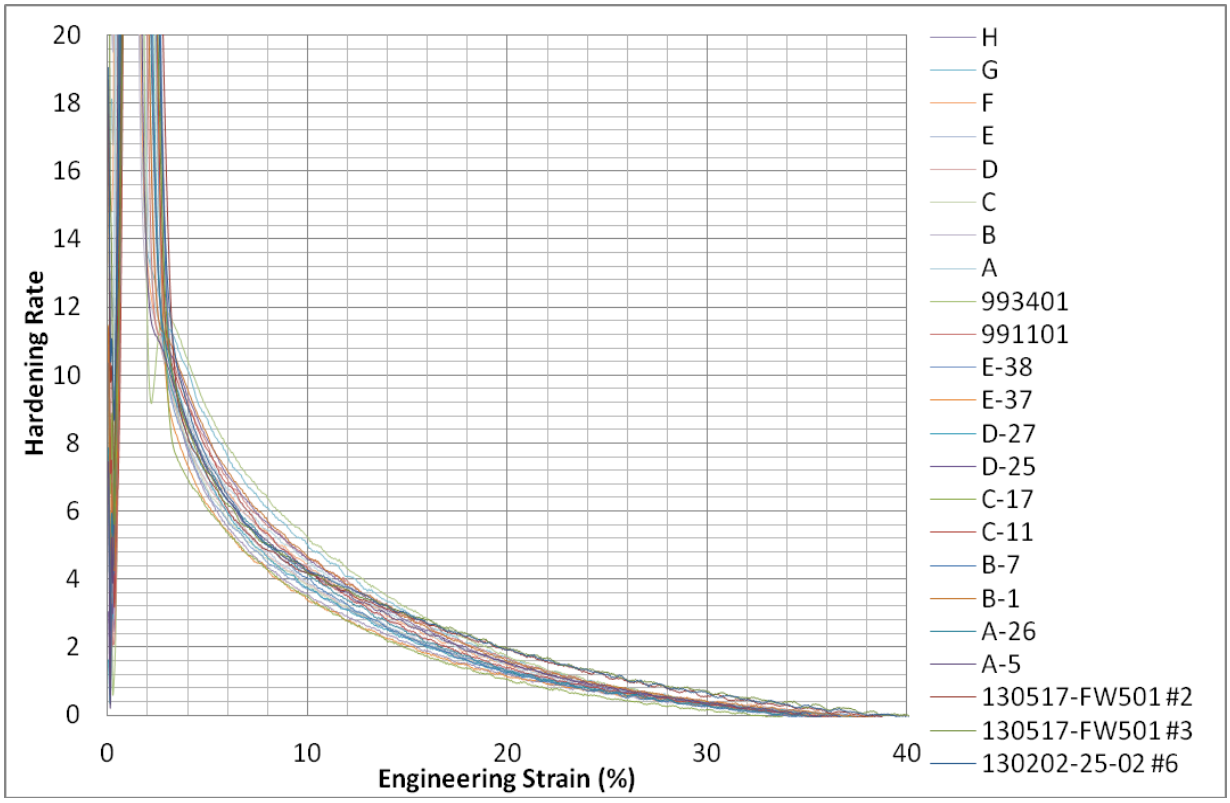

Figure 40: Hardening rate curve after 9-point smoothing of stress-strains curve for samples from Ningxia.

A different version of the Matlab code found in Appendix A can plot any layer of the ODF. As the ODF shows spread of the γ-fiber along Φ direction in the $\phi_2 = 45°$ section, the spread was also assessed in the ϕ_2 direction. Figure 41 plots the average intensity of a rectangular portion of the ODF for Φ(45°-65°) and ϕ_1 (0°-180°) at each value of ϕ_2, for each sample lot of the Tokyo Denkai material. The γ-fiber is at the center of the plot. This shows that the γ-fiber is spread over a range of ±10° in ϕ_2, but there is a smooth Gaussian distribution. The average intensity of the γ-fiber varies from about 2 to 7 for the different lots. Similarly, Figure 41 b) shows the maximum value within the rectangular sections, which indicates that the peaks of the γ-fiber can occur anywhere in the spread of ϕ_2 between 35° and 60°. For the Ningxia material shown in Figure 42, similar features are apparent, but the average intensity of γ-fiber varies from 1 to 8, with a spread over a range of ±15° in ϕ_2. From Figure 42 b), the peaks of γ-fiber can occur anywhere in the spread of ϕ_2 between 35° and 55°.

Table 3 and 4 provide all of the average and maximum ODF value at 45° for samples from the two suppliers, and the maximum and minimum values are indicated in bold text. Unlike the average ODF value, which only has one peak, more peaks can be found for the maximum ODF value at different ϕ_2.

The contrast factors along the Y-axis for both companies are in the range of 0 to 1, with small variation. Average grain size varied from 20 μm to 65μm for both two companies, mostly in between 30 μm to 40μm. Tables 3 and 4 also contain values of the grain boundary weight factor for [100] and [111] with respect to the sample Y axis, rolling direction of samples, the average grain size, represented by diameter in microns, peak height and angle of local misorientation, and total CSL boundaries fraction from $\sum 3$ to $\sum 29b$ for samples from the two suppliers. The maximum and minimum in each column are indicated in bold text.

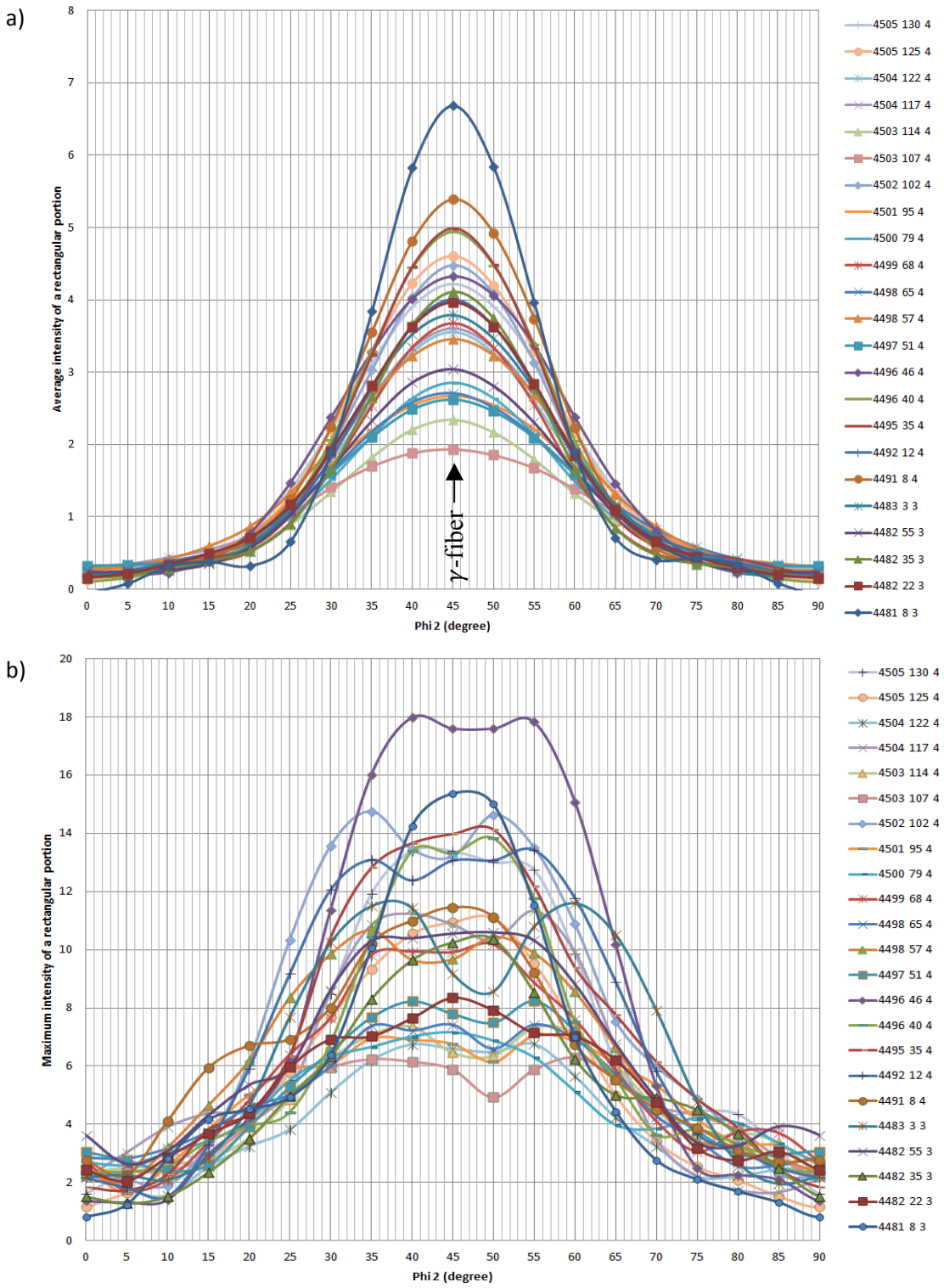

Figure 41: a) Average and b) Maximum intensity of a rectangular portion on the ODF for Φ(45°-65°) and ϕ_1 (0°-180°) vs. ϕ_2 for samples from Tokyo Denkai.

a)

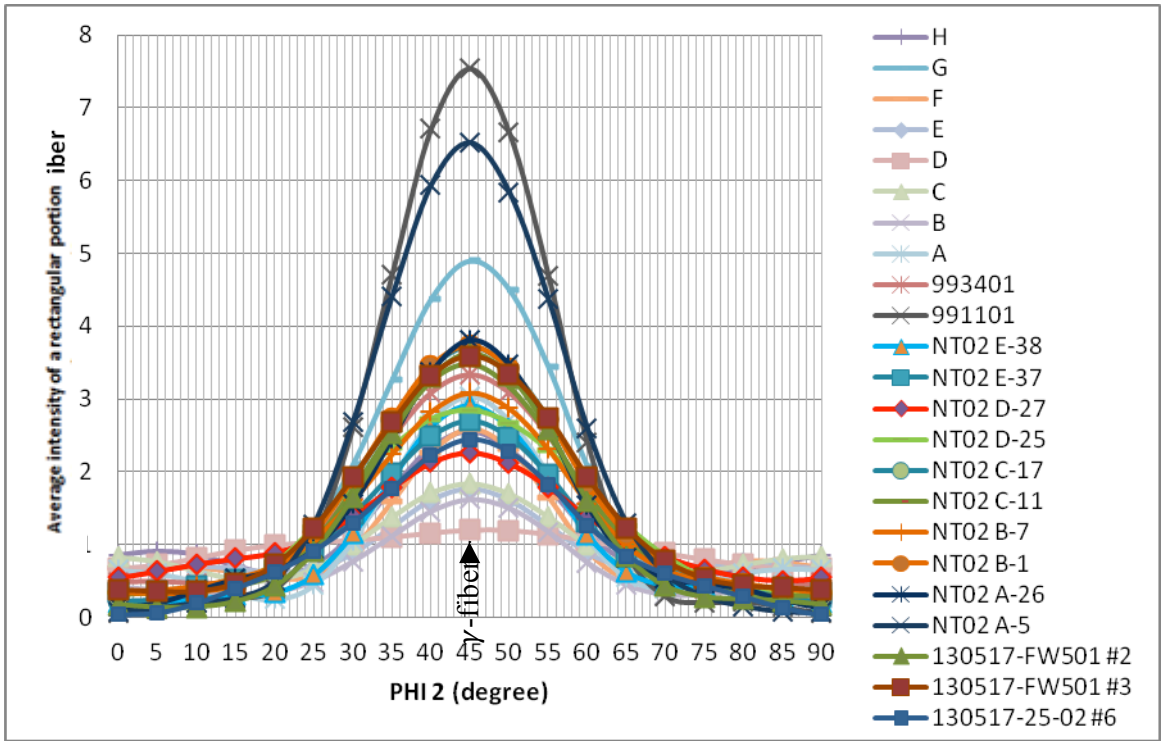

b)

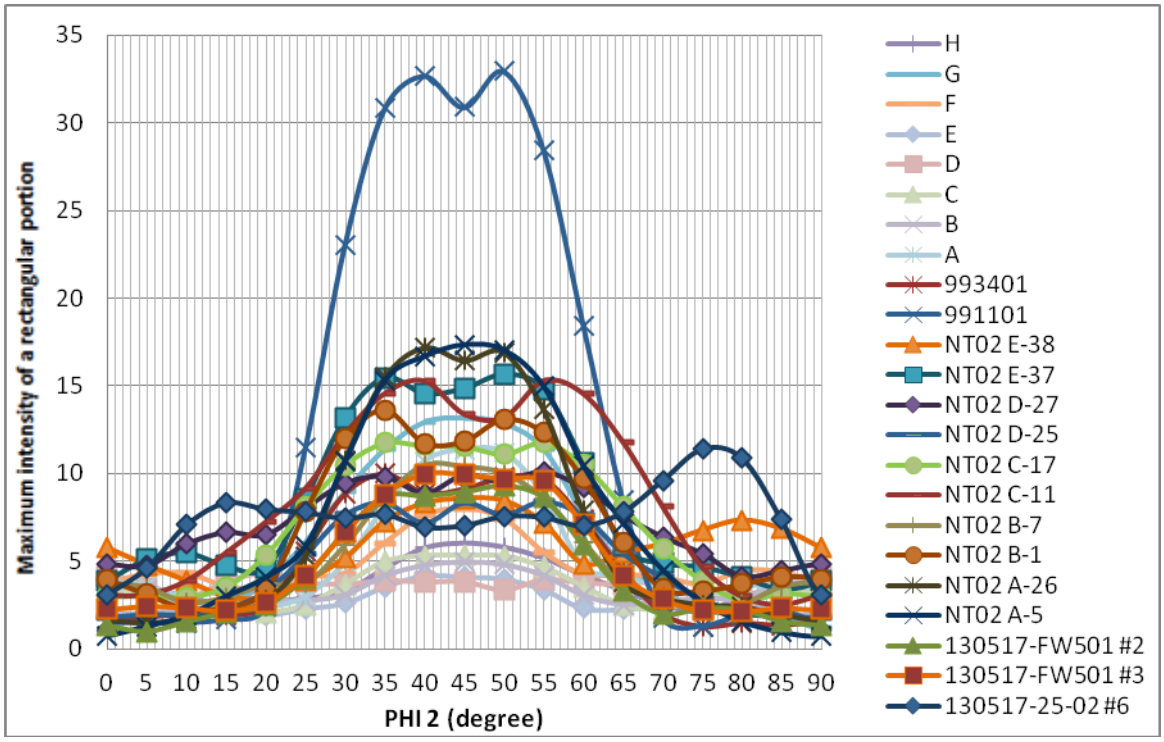

Figure 42: a) Average and b) Maximum intensity of a rectangular portion on the ODF for Φ(45°-65°) and ϕ_1 (0°-180°) vs. ϕ_2 for samples from Ningxia.

Table 3: Measured mechanical property and microstructural parameters for Tokyo Denkai samples.

	45 degree			Grain Size (Diameter) (Microns)		Contrast Factor Wtc Y100111	Rolling direction	Peak of LAM		CSL Boundaries			0.2% yield	Hardening Rate	
	SD_G	AVG_G	MAX_G	Average	SD			Angle	Height	Fraction	UTS	Elongation		10%	25%
4481 8 3	3.9683	**6.6876**	**15.3772**	38.2395	22.9311	0.7557	-45	0.22	0.087727	0.094	189.6209	61.64611	70	5.42	1.92
4482 22 3	1.9316	3.9659	8.3516	35.4115	21.4135	0.7714	45	0.3	0.067331	0.097	191.3980	60.53991	**90**	4.62	1.27
4482 35 3	2.411	4.1137	10.25	30.71644	17.1924	0.7715	-45	0.22	0.088531	0.101	191.7985	61.46859	63	5.80	1.97
4482 55 3	2.5507	3.0414	10.5583	31.4478	17.7768	0.7751	45	0.38	0.059889	0.091	188.1964	70.72645	52	5.15	1.63
4483 3 3	1.98	3.793	9.176	31.5225	16.9158	0.7601	45	0.26	0.068623	0.084	194.2306	56.66765	53	**3.90**	**0.78**
4491 8 4	2.7623	5.3903	11.4517	36.385	22.2671	0.7613	-45	0.3	0.066239	0.092	195.9447	68.57932	49	4.92	1.24
4492 12 4	2.3783	4.0049	13.0652	28.8801	15.6931	0.7674	45	0.3	0.061354	0.082	183.3167	63.53476	54	5.42	1.73
4495 35 4	3.1931	4.9849	13.9853	43.9841	28.9755	0.7708	-45	0.38	0.05807	0.084	182.2653	70.71983	48	5.70	2.20
4496 40 4	3.0909	4.9443	13.3245	40.1259	23.9834	0.7642	-45	0.26	0.085617	0.104	191.6224	65.62399	**46**	5.82	**2.21**
4496 46 4	3.8923	4.3241	17.6124	**47.5242**	31.957	0.7672	-45	0.38	0.066467	**0.079**	183.6209	67.96442	67	4.84	1.66
4497 51 4	1.6818	2.625	7.7948	37.6559	21.7654	0.7625	45	0.26	0.08736	0.106	193.5331	**72.23425**	62	5.22	2.05
4498 57 4	2.0987	3.4541	9.6733	41.9474	25.0736	0.7667	-45	0.22	0.093669	**0.11**	190.2206	67.33408	59	5.47	1.82
4498 65 4	1.5241	2.7095	7.4131	34.4373	19.1244	0.7704	45	0.38	0.063218	0.106	191.5287	64.18020	48	5.34	2.08
4499 68 4	2.4025	3.681	9.9017	37.8979	23.0434	0.7582	45	**0.18**	**0.098053**	0.095	189.8836	68.08945	50	**5.83**	2.19
4500 79 4	1.6778	2.851	7.1579	40.0066	25.1514	**0.7897**	45	0.26	0.091486	0.108	186.2888	70.73087	47	4.83	1.36
4501 95 4	1.7447	2.6694	6.7686	42.4931	26.0915	0.7677	-45	0.34	0.063012	0.089	**181.0271**	71.43163	67	4.64	1.65
4502 102 4	2.6323	4.474	13.2008	41.4541	24.2673	**0.7528**	-45	0.26	0.078049	0.1	187.0230	**53.35079**	82	4.68	1.36
4503 107 4	1.2296	**1.9374**	**5.8912**	**20.5443**	8.9703	0.7605	45	0.34	0.056292	0.083	198.4086	58.11973	69	5.54	2.08
4503 114 4	1.3471	2.345	6.4694	22.9988	10.5561	0.7635	45	0.22	0.074287	0.089	**200.9259**	60.58136	62	5.54	1.91
4504 117 4	2.204	3.6046	10.868	32.7631	18.3048	0.7624	-45	**0.46**	**0.051157**	0.091	192.2246	70.08756	53	5.57	2.02
4504 122 4	1.5946	3.5572	6.5948	33.4224	19.4672	0.7801	45	0.34	0.058712	0.1	187.5833	65.63449	72	4.71	1.35
4505 125 4	3.0199	4.6025	10.9505	33.8436	17.7097	0.7758	45	0.22	0.074616	0.093	191.5340	66.76817	77	4.99	1.59
4505 130 4	2.9461	4.2166	13.3845	39.7828	23.9452	0.7738	45	0.34	0.061624	0.088	194.1035	66.25665	52	5.28	1.73

Table 4: Measured mechanical property and microstructural parameters for Ningxia samples

	45 degree			Grain Size (Diameter) (Microns)		Contrast Factor Wtc Y100111	Rolling direction	Local Average Misorientation		CSL Boundaries			0.2% yield	Hardening Rate	
	SD_G	AVG_G	MAX_G	Average	SD			Angle	Fraction	Fraction	UTS	Elongation		10%	25%
#6	1.6643	2.4428	**7.0509**	39.1276	22.6383	0.7970	90	0.26	0.0701	0.099	188.3728	68.33298	82	4.25	1.25
#2	2.0789	3.6258	8.9571	29.4169	14.5909	**0.7648**	0	0.38	0.049173	0.096	188.6362	61.92162	81	4.2	1.1
#3	2.4262	3.5857	9.9238	32.028	17.4199	0.7918	90	**0.46**	**0.044162**	0.084	185.1464	63.06610	63	4.2	**1.3**
A-5	4.2293	6.5222	17.351	32.9097	18.8692	0.7827	90	0.18	0.077718	0.103	177.9324	62.06783	62	4.2	0.8
A-26	3.6437	3.807	16.4477	36.9757	21.928	0.7856	0	0.18	0.079161	0.097	179.5656	55.26768	62	4.2	0.7
B-1	2.5859	3.738	11.8328	28.0453	15.6602	0.7992	90	0.22	0.083235	0.101	179.8646	62.26847	56	4.65	0.9
B-7	2.3495	3.0891	10.3684	30.9694	18.2426	0.7675	90	0.22	0.080405	0.088	181.0096	**55.01490**	71	4	0.6
C-11	3.1984	3.4881	13.4016	35.2342	19.8824	0.7815	0	0.22	0.084378	0.095	179.5396	57.07664	54	4.3	0.75
C-17	2.4776	3.7187	11.5592	30.7457	16.098	0.7820	0	0.22	0.068596	0.099	186.5553	58.75577	**88**	3.5	**0.5**
D-25	1.7936	2.8449	8.3591	26.1685	12.3543	0.7993	90	0.26	0.069723	0.097	188.9413	57.49422	65	4.6	0.8
D-27	1.7875	**2.2688**	9.9292	43.7255	26.3489	0.7790	0	**0.18**	**0.095012**	**0.107**	176.6338	65.47932	59	3.75	0.75
E-37	3.3292	2.7043	14.8264	50.4752	31.3392	0.7998	90	0.22	0.087471	0.08	172.6605	61.03919	62	**3.4**	0.65
E-38	1.8934	2.9115	8.5802	49.0419	31.4148	0.7861	0	0.22	0.088799	**0.075**	**168.8100**	61.30613	**51**	3.75	0.65
991101	7.2105	**7.5366**	**30.8886**	32.6345	19.1497	0.7960	90	0.26	0.064604	0.107	184.1138	60.20157	70	3.75	0.85
993401	2.1545	3.3334	9.1396	**25.661**	11.4882	0.7891	90	0.3	0.053043	0.1	**193.0245**	59.00088	71	**5.25**	0.9
A	2.7538	3.0378	11.3744	40.6903	22.2383	0.799	0	0.38	0.074289	0.097	184.0176	60.25796	77	4.52	0.71
B	1.3283	1.6231	4.9719	**60.9965**	37.9517	0.785	90	0.38	0.077757	0.084	180.1521	55.56956	81	4.43	0.70
C	1.1436	1.8442	5.3184	51.3847	29.9836		90	0.5	0.047311	0.069	175.9854	65.43047	76	3.80	0.69
D	0.6778	1.2035	3.8497	44.7146	25.6731	0.8019	0	0.34	0.060348	0.087	173.0056	65.68459	80	3.84	0.72
E	0.9102	1.7609	4.104	40.5865	21.8615		0	0.5	0.044272	0.071	178.8183	**70.72081**	83	3.92	0.69
F	1.753	2.5877	7.9945	38.3798	20.7938	**0.8042**	0	0.34	0.065253	0.095	185.1786	61.05731	82	4.36	0.82
G	2.9935	4.898	13.186	33.7379	18.3644	0.79	90	0.46	0.056503	0.095	192.3179	61.68762	77	5.03	0.86
H	1.3274	2.5542	6.0365	47.0651	26.237	0.7968	0	0.34	0.068847	0.096	177.5971	61.54861	76	3.53	0.65

*Error in Matlab code calculating contrast factor of C and E.

3. Result of texture of extremes value in tensile test

Among samples from Tokyo Denkai, Lot 4497 #51 has the highest elongation and Lot 4502 #102 has the lowest elongation. Lot 4503 # 114 has the maximum UTS and Lot 4501 #95 has the minimum UTS. Lot 4482 #22 has maximum 0.2% yield strength and Lot 4496 #40 has the minimum 0.2% yield strength.

The IPF map, PF and ODF plot for $\phi_2 = 45°$ for representative Tokyo Denkai samples are shown in Figures 43-48. The γ fiber is evident at $\Phi \sim 55°$ and $\Phi \sim 125°$ in the ODF plots, where some samples show a consistent intensity for all ϕ_2 values, and other show significant peaks. Similarly representative samples from the Ningxia samples are presented in Figures 49-53. Among samples from Ningxia, E has the highest elongation and NT02 B-7 has the lowest elongation. 993401 has the maximum UTS and NT02 E-38 has the minimum UTS and minimum 0.2% yield strength. NT02 C-17 has maximum 0.2% yield strength. All IPF map, PF and ODF slice for other samples from Tokyo Denkai and Ningxia can be found in Appendices C and D respectively.

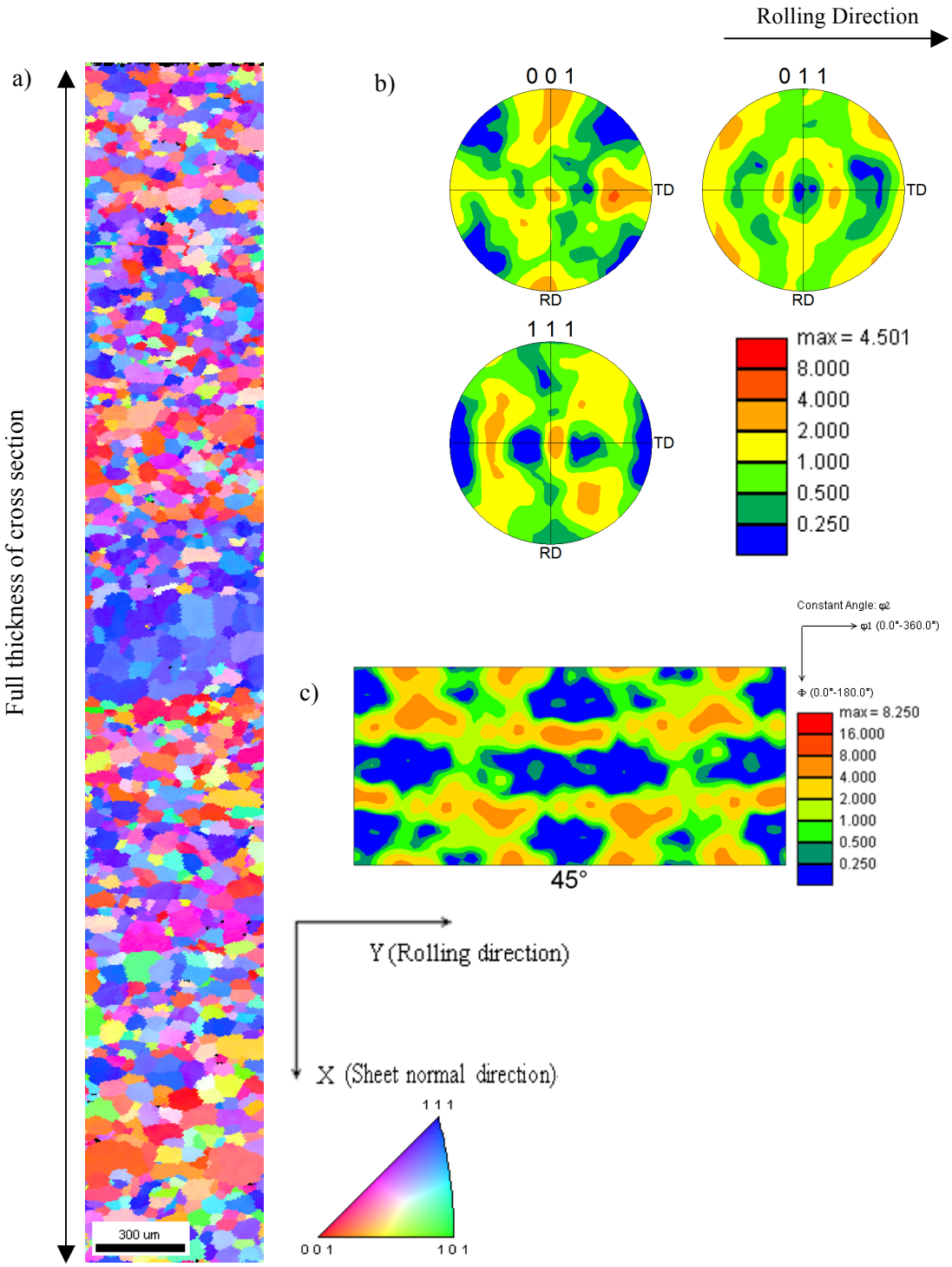

Figure 43: a) IPF map, b) PF and c) ODF plot when ϕ_2 equals 45° of niobium sheet Lot 4497 #51 with thickness 4mm. (Tokyo Denkai)

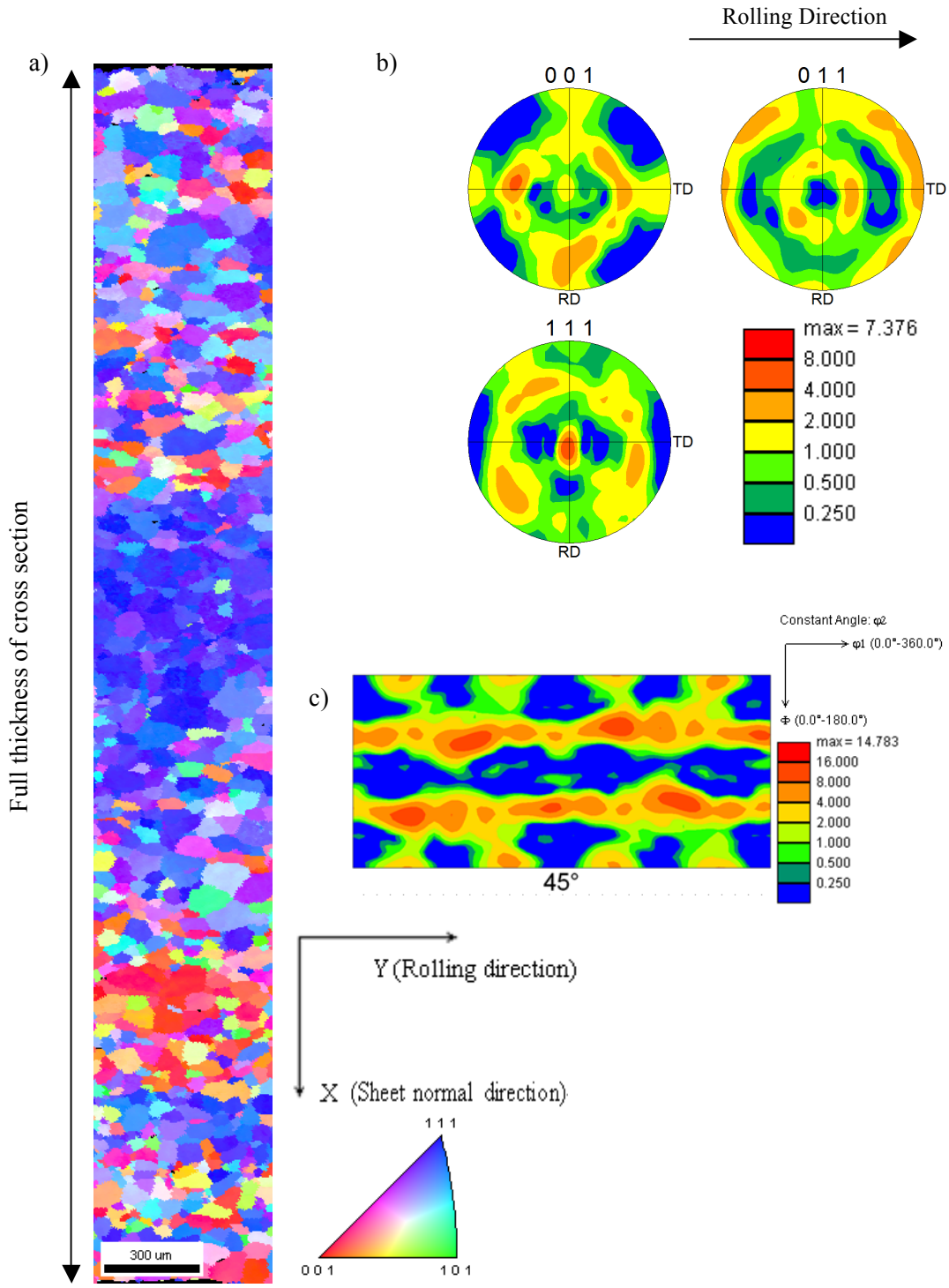

Figure 44: a) IPF map, b) PF and c) ODF plot when ϕ_2 equals 45° of niobium sheet Lot 4502 #102 with thickness 4mm. (Tokyo Denkai)

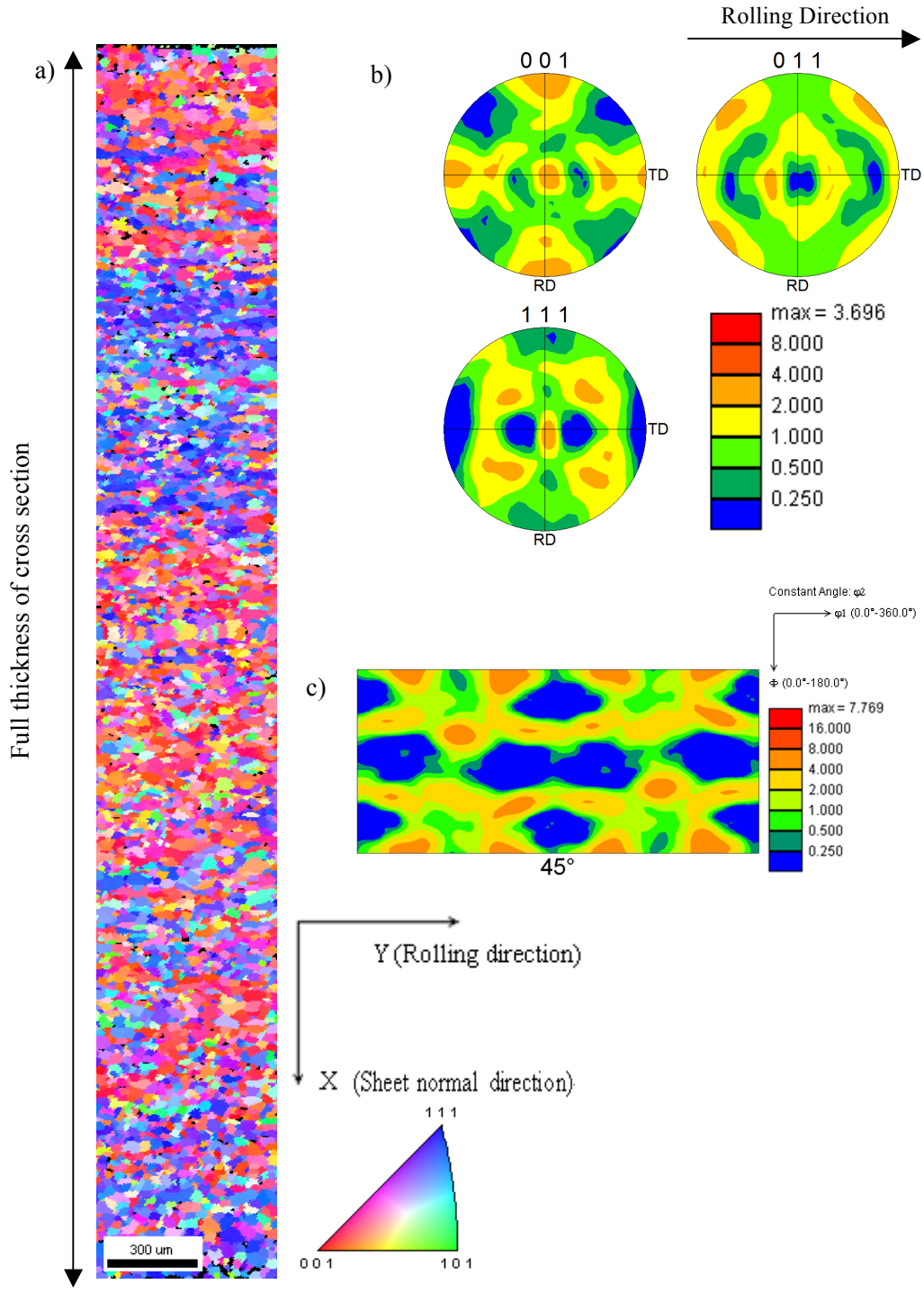

Figure 45: a) IPF map, b) PF and c) ODF plot when ϕ_2 equals 45° of niobium sheet Lot 4503 #114 with thickness 4mm. (Tokyo Denkai)

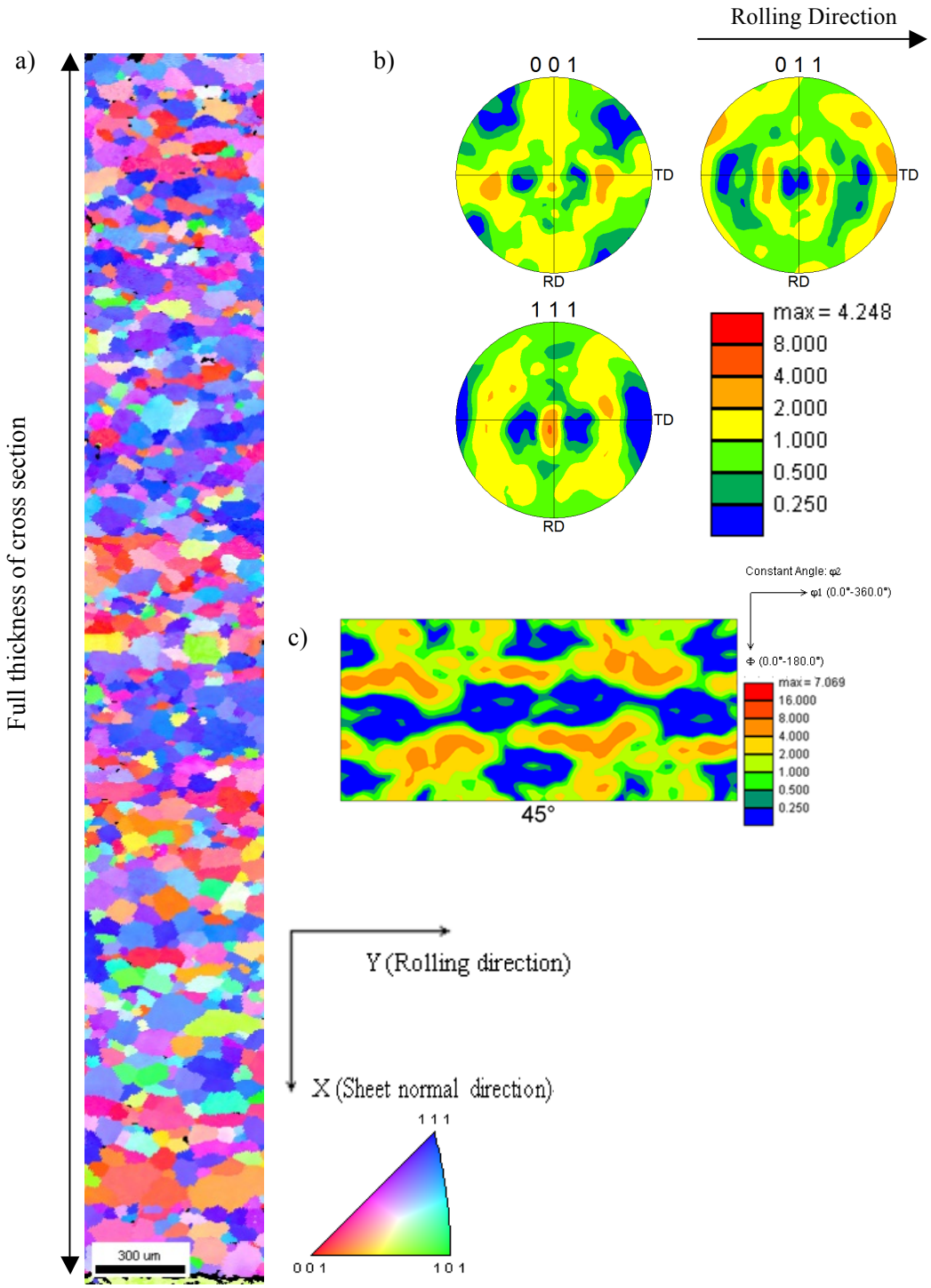

Figure 46: a) IPF map, b) PF and c) ODF plot when ϕ_2 equals 45° of niobium sheet Lot 4501 #95 with thickness 4mm. (Tokyo Denkai)

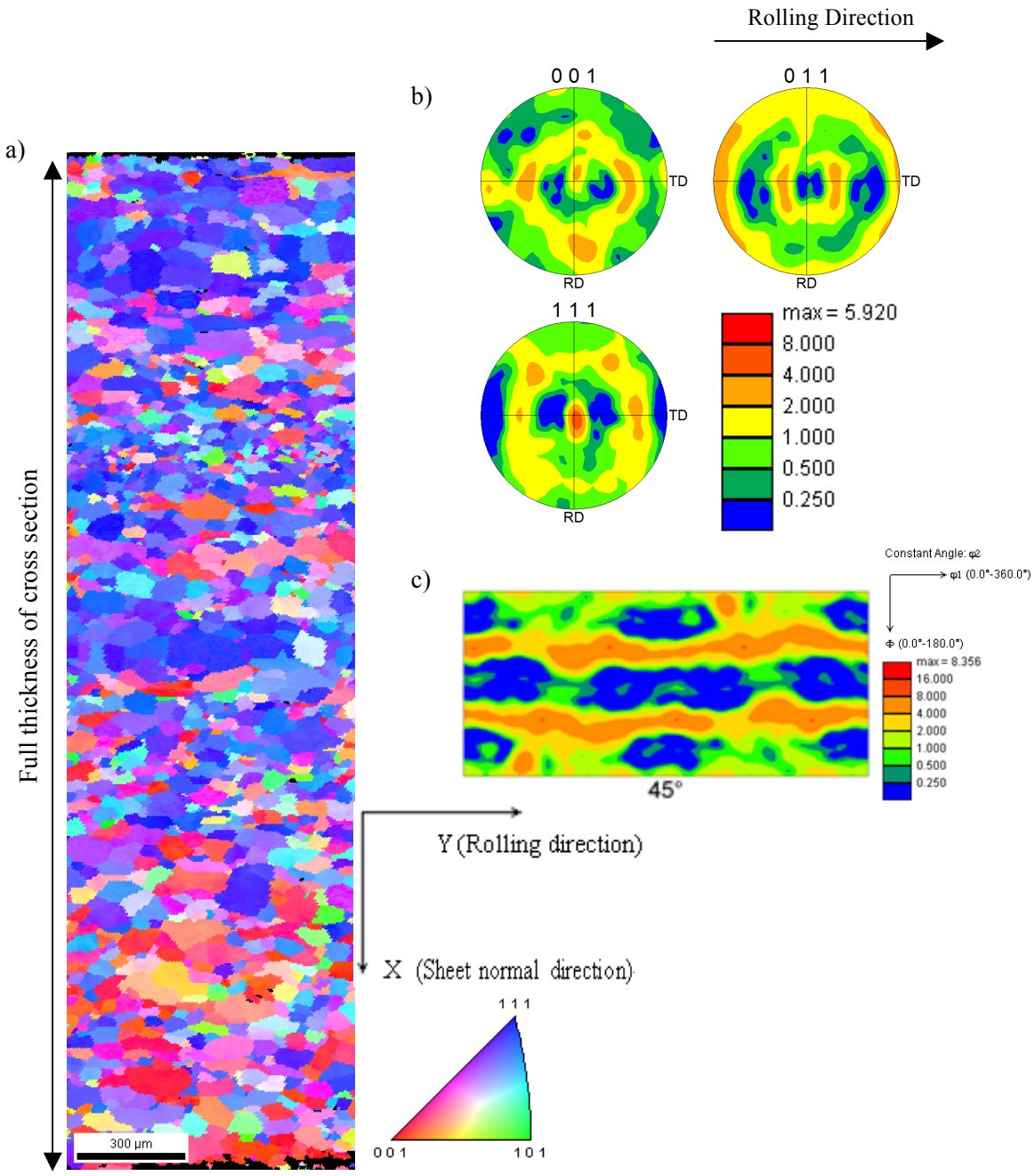

Figure 47: a) IPF map, b) PF and c) ODF plot when ϕ_2 equals 45° of niobium sheet Lot 4482 #22 with thickness 3mm. (Tokyo Denkai)

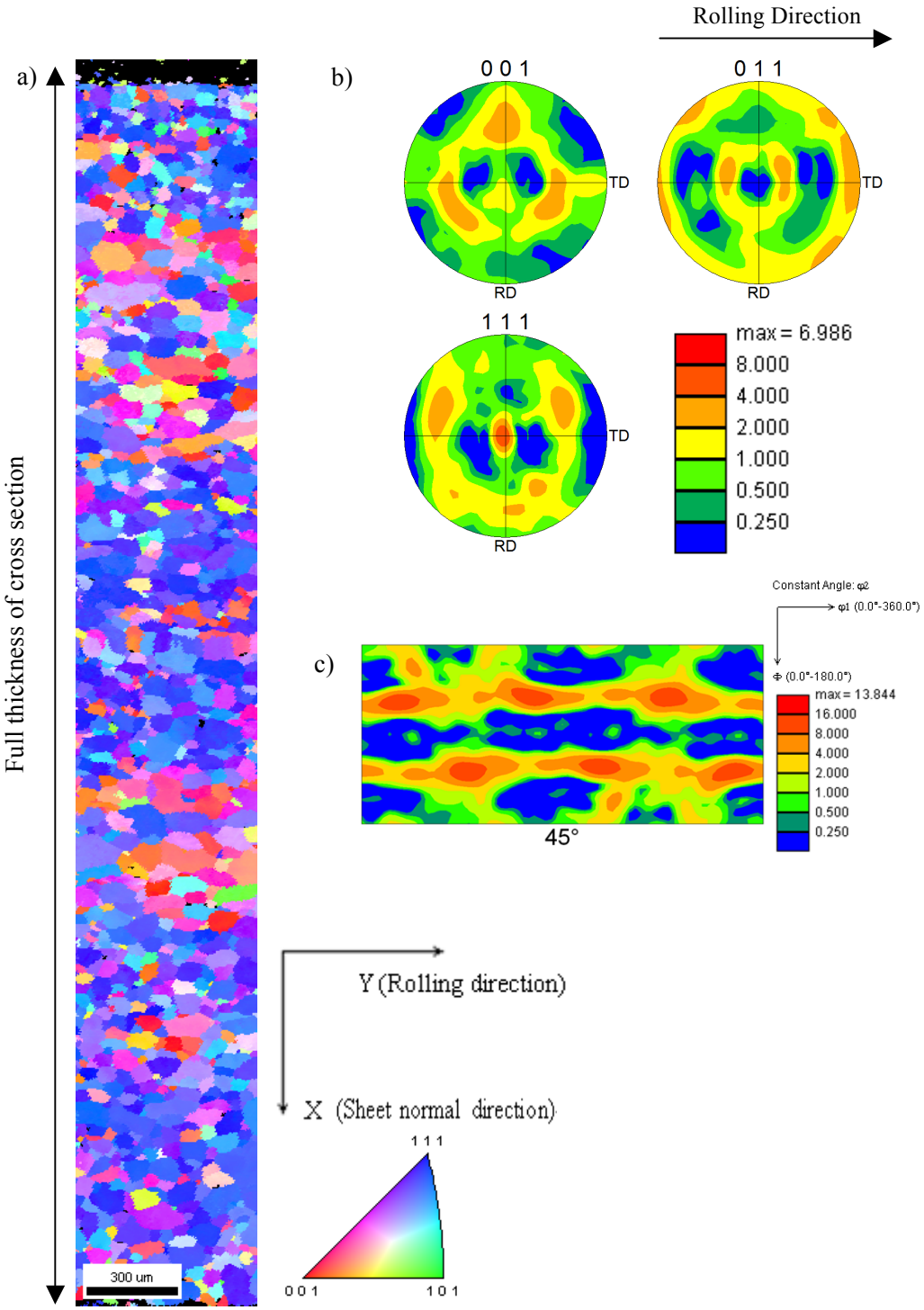

Figure 48: a) IPF map, b) PF and c) ODF plot when ϕ_2 equals 45° of niobium sheet Lot 4496 #40 with thickness 4mm. (Tokyo Denkai)

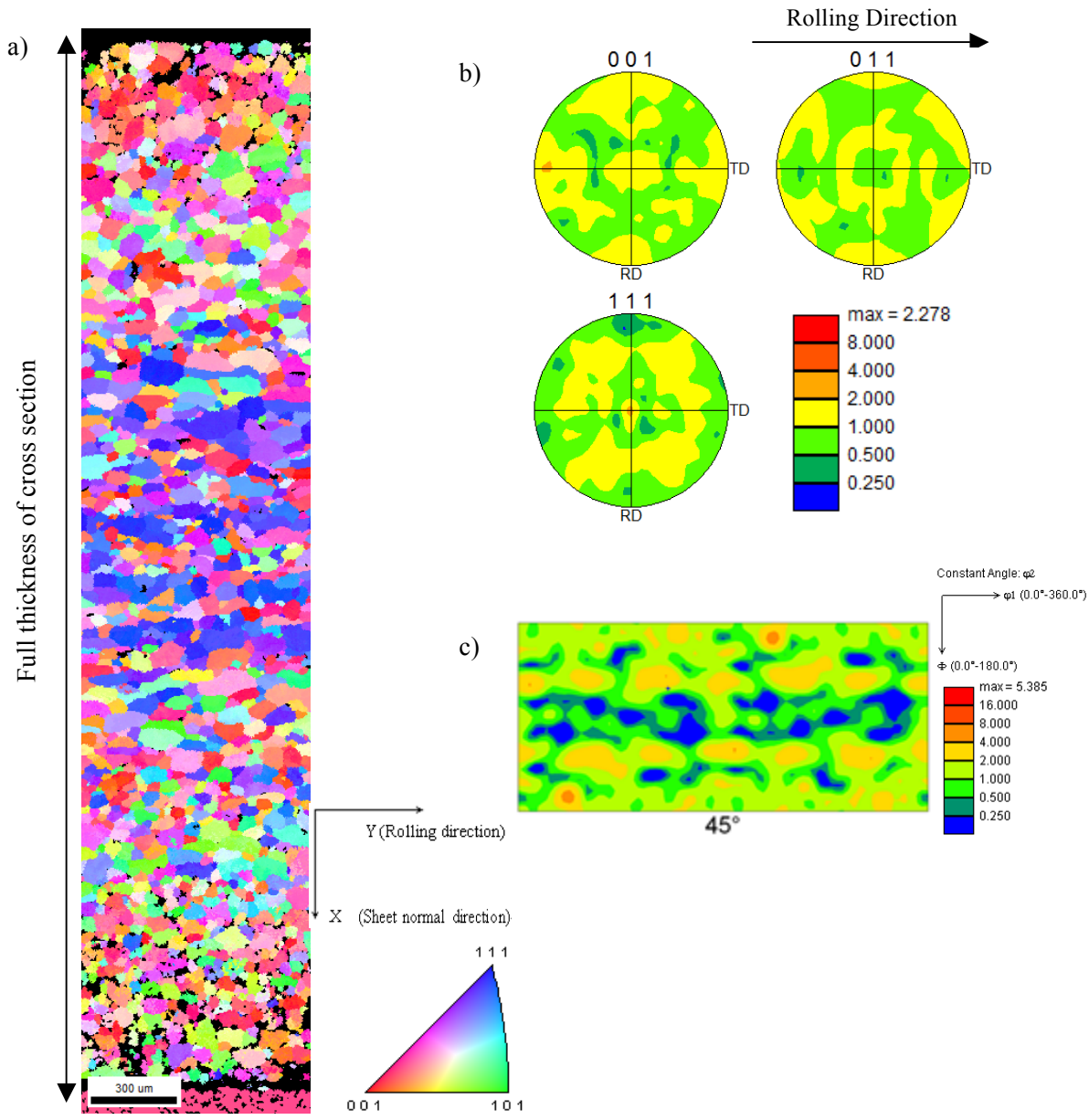

Figure 49: a) IPF map, b) PF and c) ODF plot when ϕ_2 equals 45° of niobium sheet E with thickness 3mm. (Ningxia)

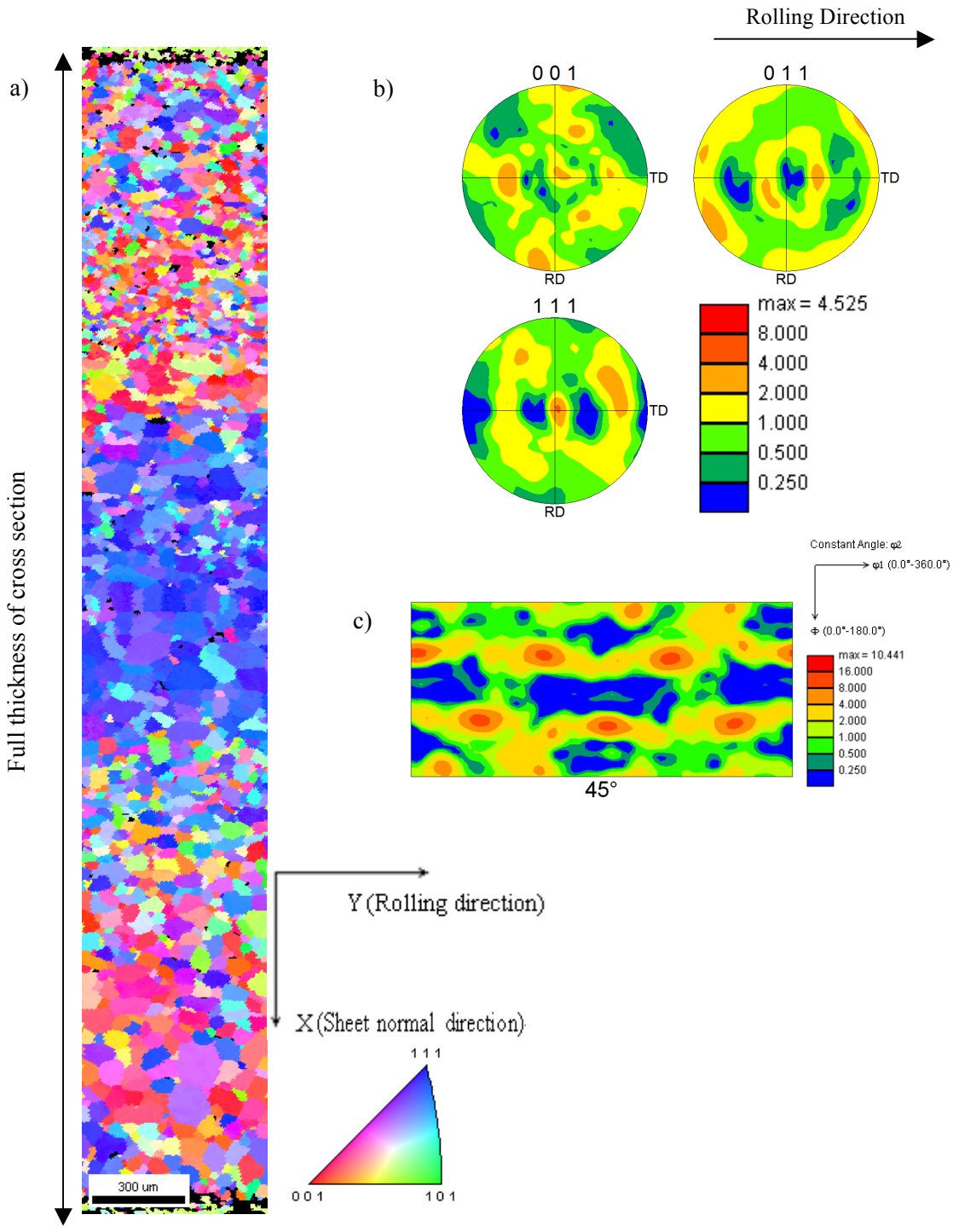

Figure 50: a) IPF map, b) PF and c) ODF plot when ϕ_2 equals 45° of niobium sheet NT02 B-7 with thickness 3mm. (Ningxia)

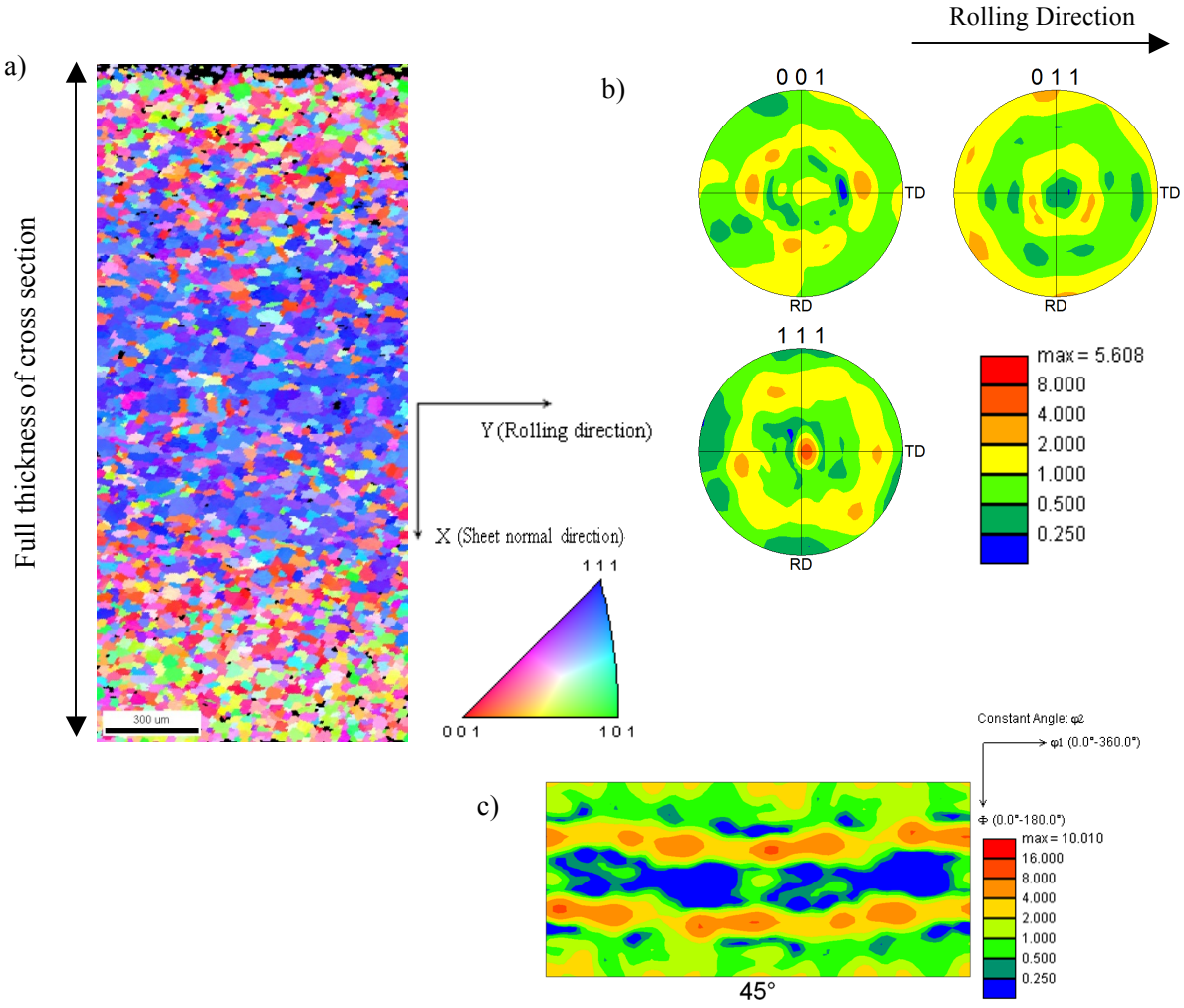

Figure 51: a) IPF map, b) PF and c) ODF plot when ϕ_2 equals 45° of niobium sheet 993401 with thickness 2mm. (Ningxia)

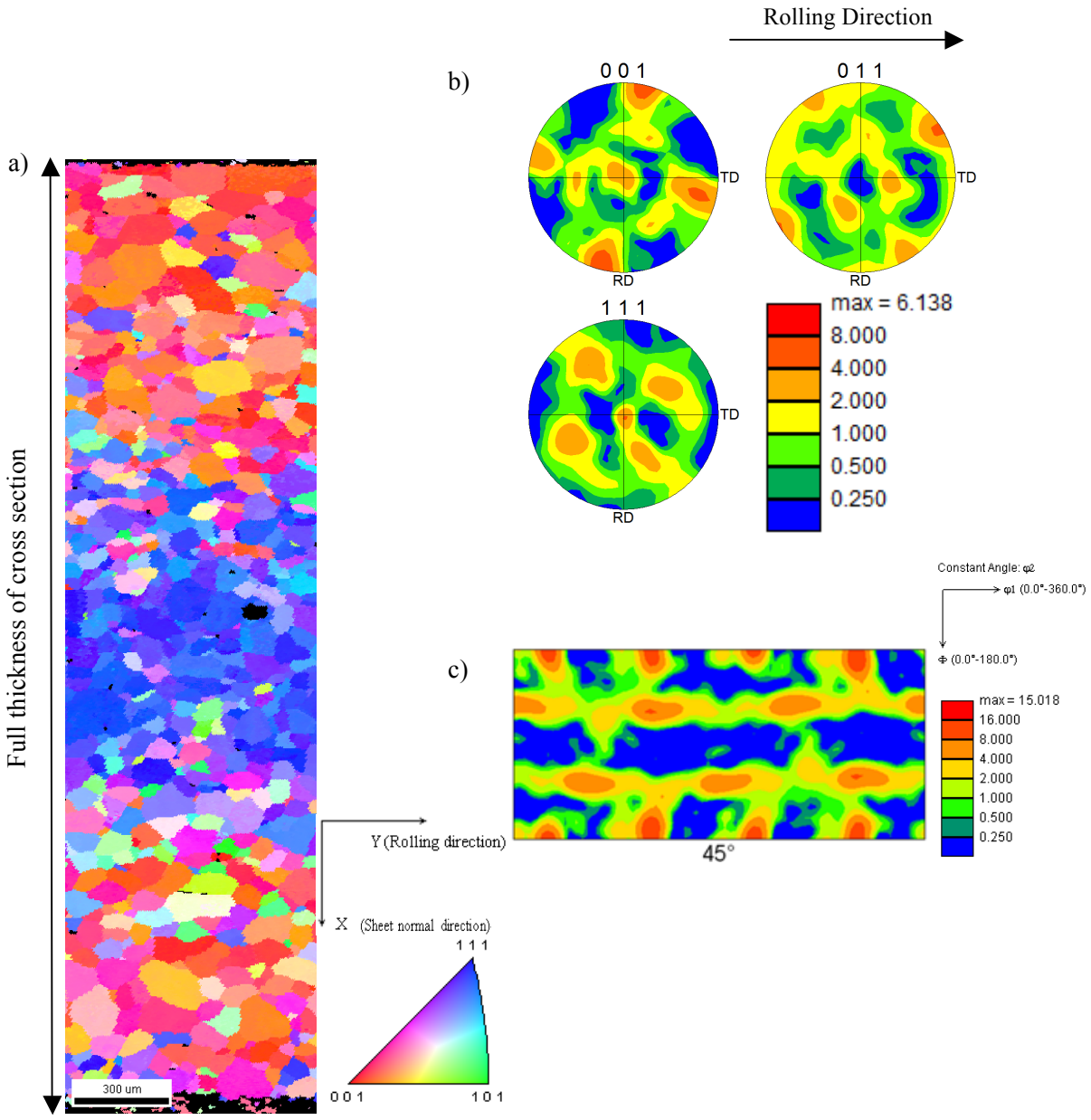

Figure 52: a) IPF map, b) PF and c) ODF plot when ϕ_2 equals 45° of niobium sheet NT02 E-38 with thickness 3mm. (Ningxia)

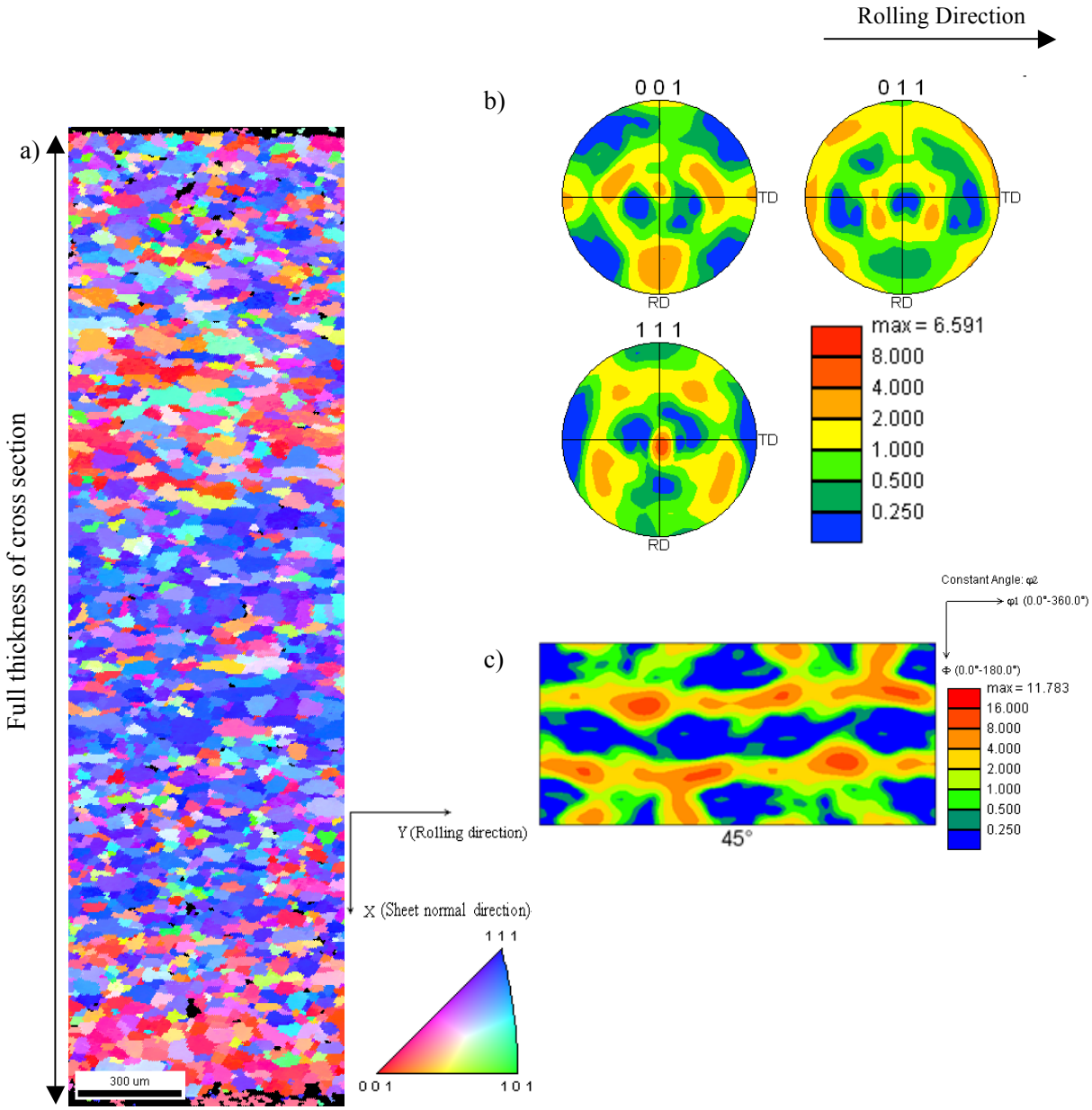

Figure 53: a) IPF map, b) PF and c) ODF plot when ϕ_2 equals 45° of niobium sheet NT02 C-17 with thickness 3mm. (Ningxia)

4. Result of correlation between mechanical and microstructural properties

Relationships between the metrics presented in Table 3 and 4 are plotted in Figures 54 to 62, for the Tokyo Denkai samples, and in Figures 63 to 70 for the Ningxia samples. (Since Ningxia has two cutting direction, figures are plotted as different direction.) Except Figure 59 shows a relationship between peck position and corresponding angle for LAM for a) Tokyo Denkai and b) Ningxia. A Negative correlation can be observed in these relationships. The relationships between mechanical and microstructural properties show a shotgun scatter with low correlation for all Tokyo Denkai samples. There is a trend in Figure 63 b) that shows a negative correlation between elongation and average value of ODF intensity on γ-fiber at ϕ_2 equals to 45° for Ningxia samples cut parallel to rolling direction. And Figure 69 a) shows a negative correlation between UTS and average grain size for Ningxia samples cut parallel to rolling direction. Others for Ningxia show a relative scatter plat that have low correlation.

a)

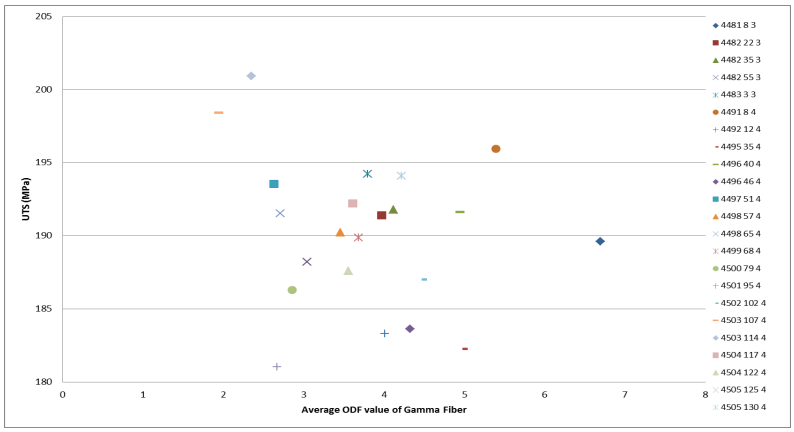

b)

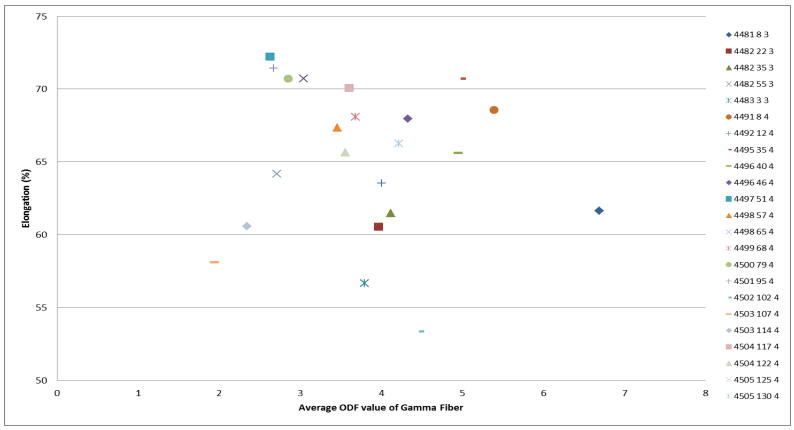

c)

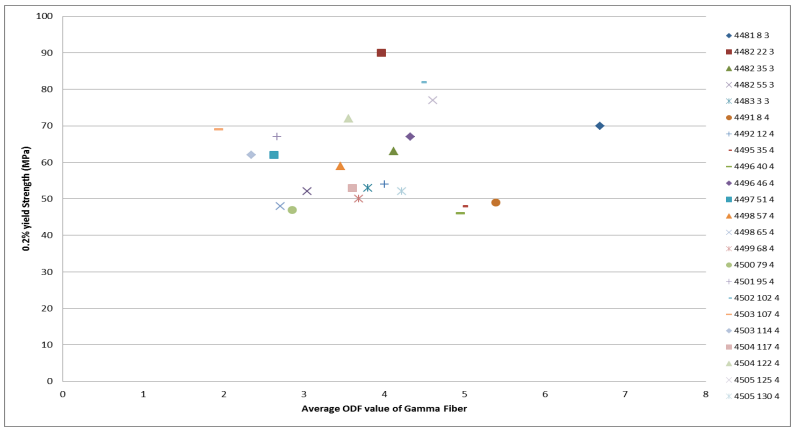

Figure 54: a) UTS, b) elongation and c) 0.2% yield strength vs. average ODF value of γ-fiber at ϕ_2 = 45° (Tokyo Denkai)

a)

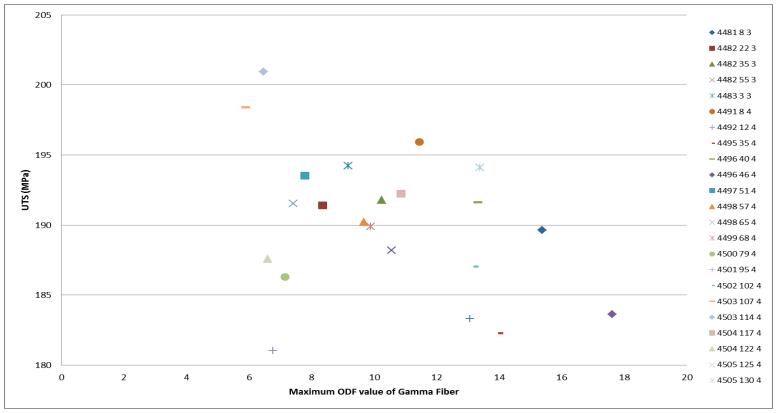

b)

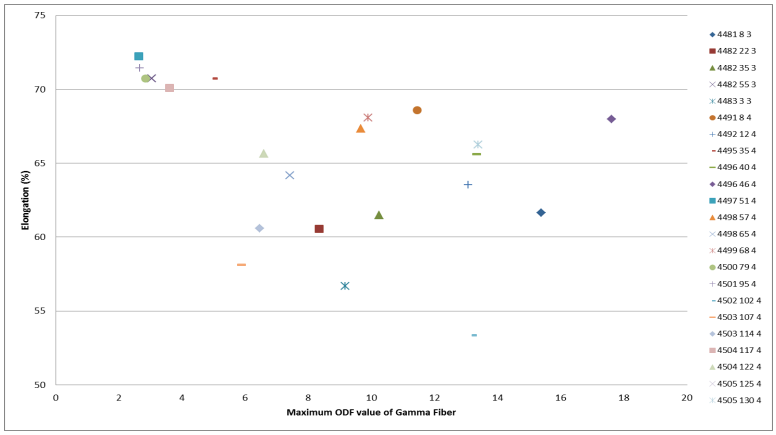

c)

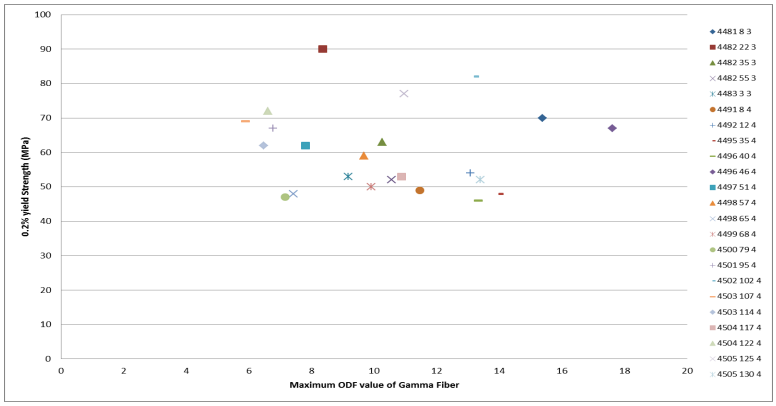

Figure 55: a) UTS, b) elongation and c) 0.2% yield strength vs. maximum ODF value of γ-fiber at $\phi_2 = 45°$ (Tokyo Denkai)

a)

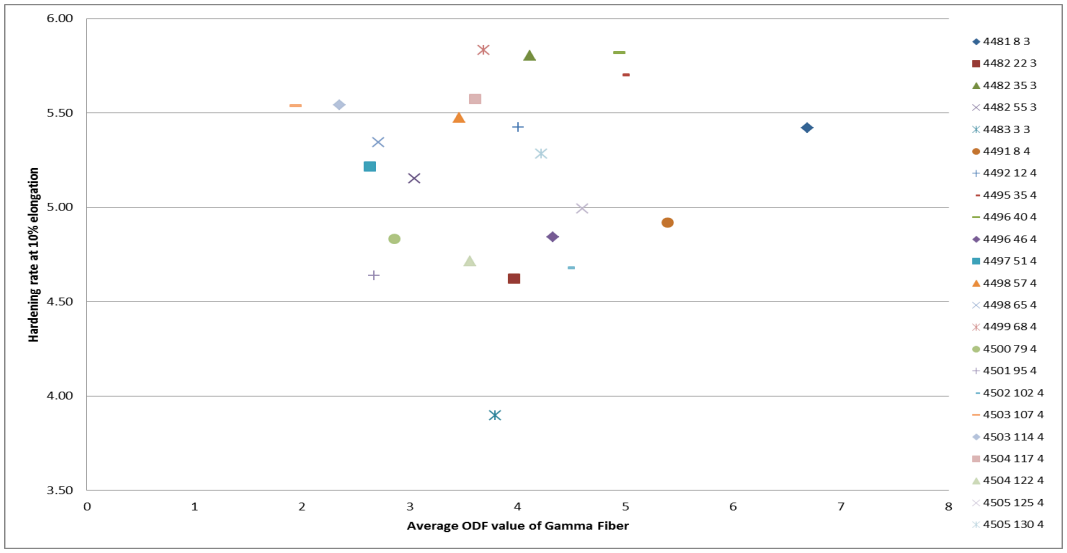

b)

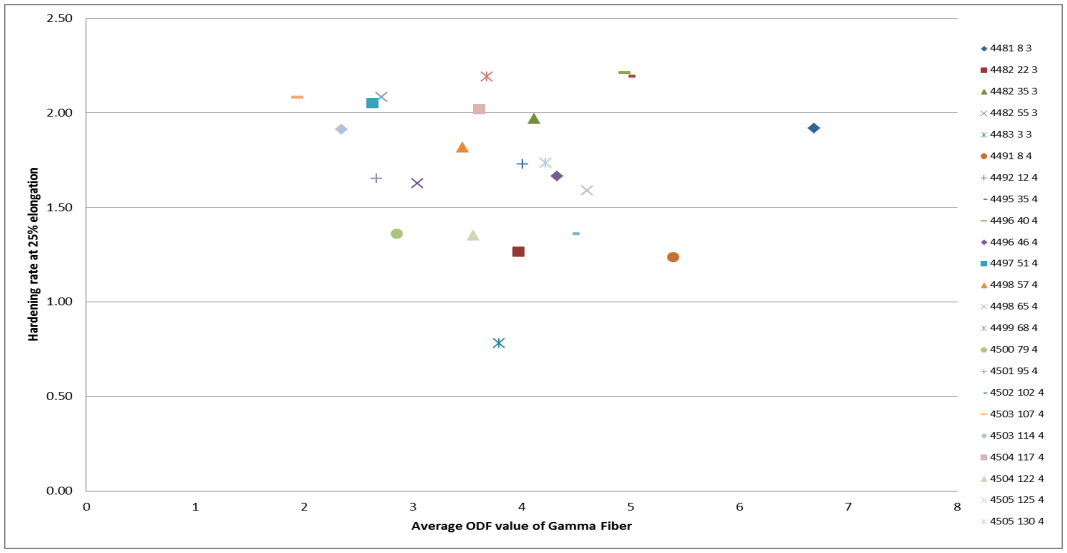

Figure 56: Hardening rate at a) 10% and b) 25% elongation vs. average ODF value of γ-fiber at ϕ_2 = 45° (Tokyo Denkai)

a)

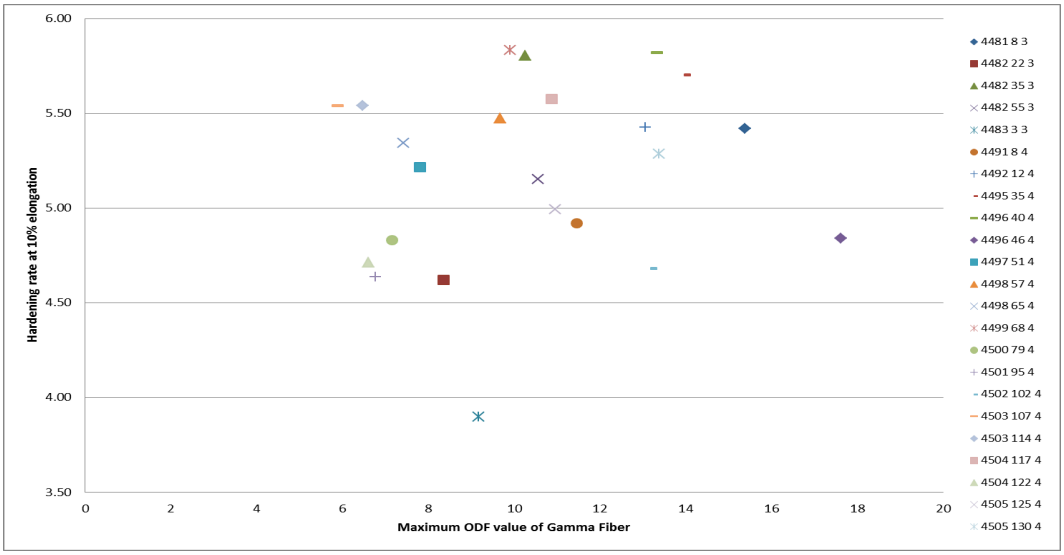

b)

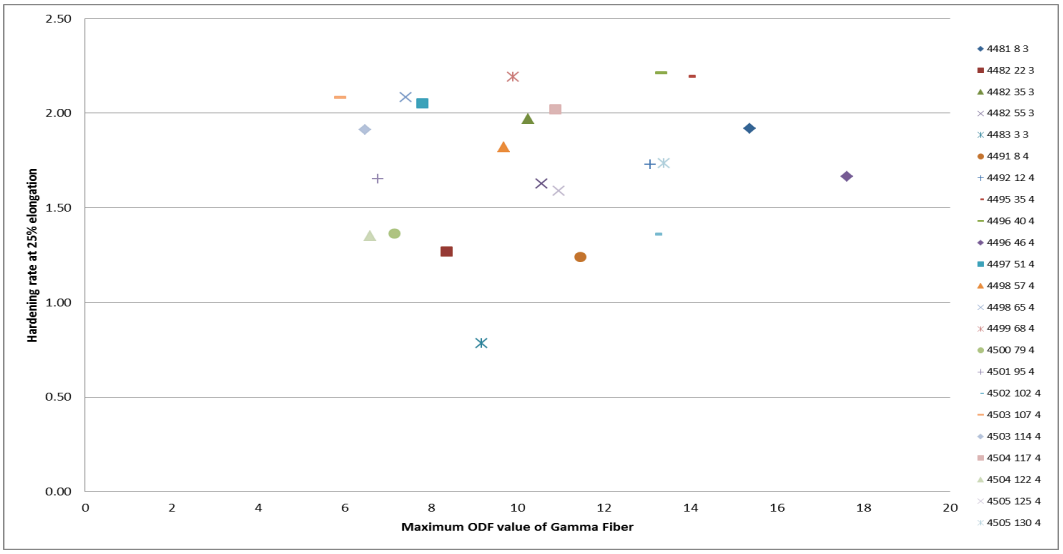

Figure 57: Hardening rate at a) 10% and b) 25% elongation vs. maximum ODF value of γ-fiber at ϕ_2 = 45° (Tokyo Denkai)

a)

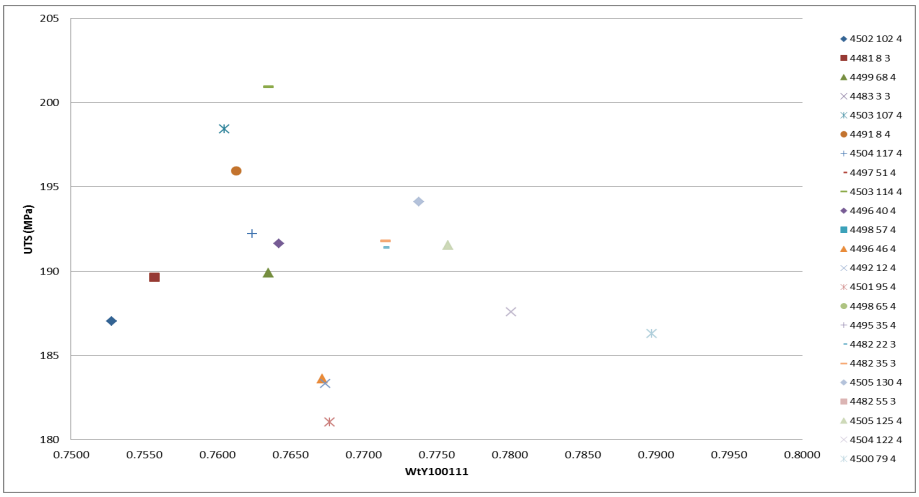

b)

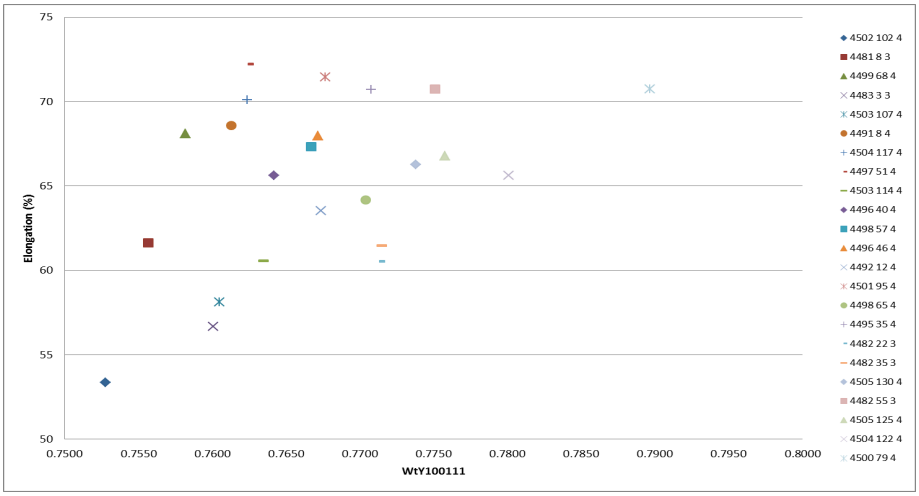

c)

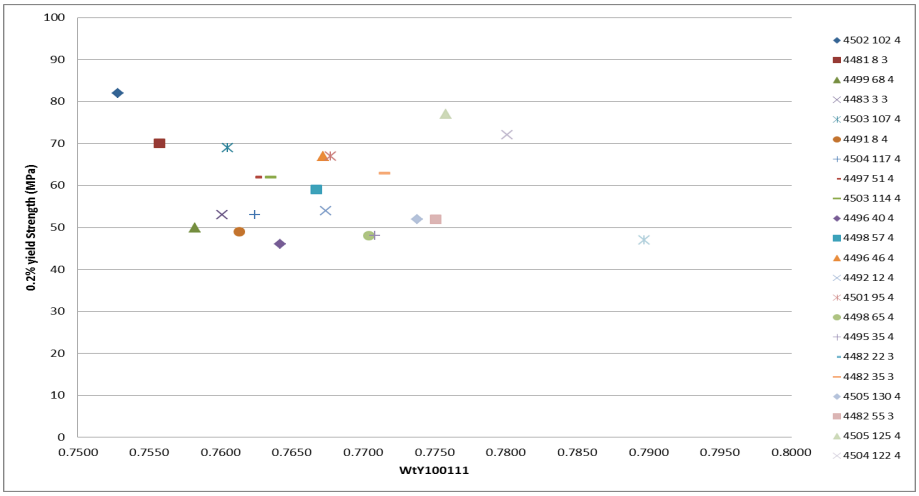

Figure 58: a) UTS, b) elongation and c) 0.2% yield strength vs. contrast factor Y100111. (Tokyo Denkai)

a)

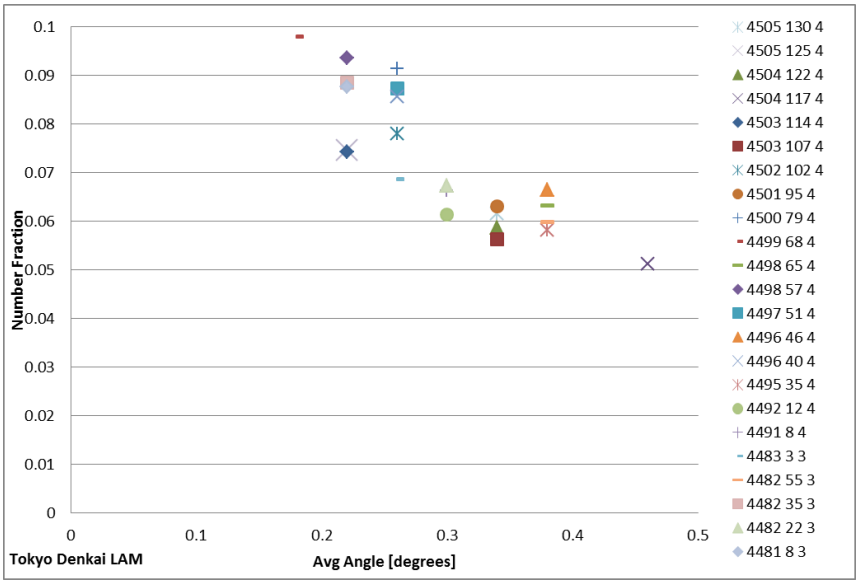

b)

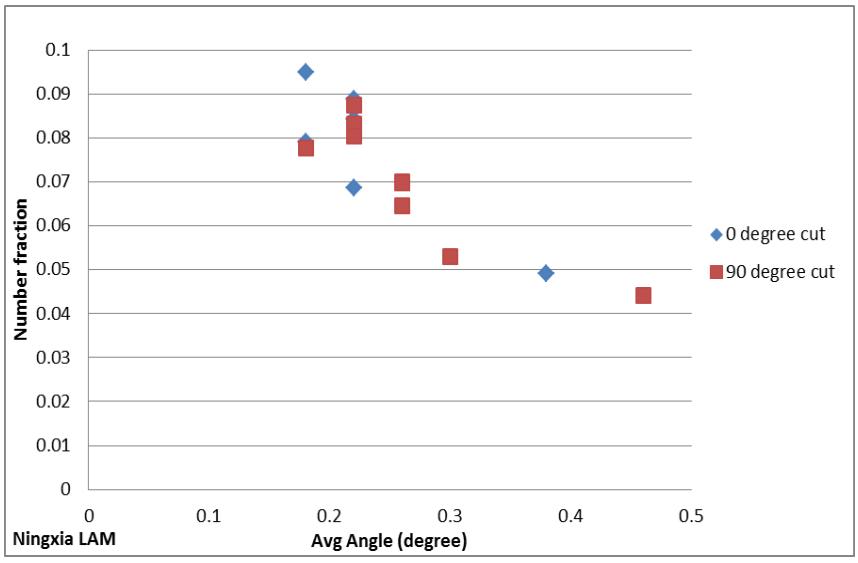

Figure 59: Number fraction vs. Average angel in degree of LAM for a) Tokyo Denkai and b) Ningxia.

a)

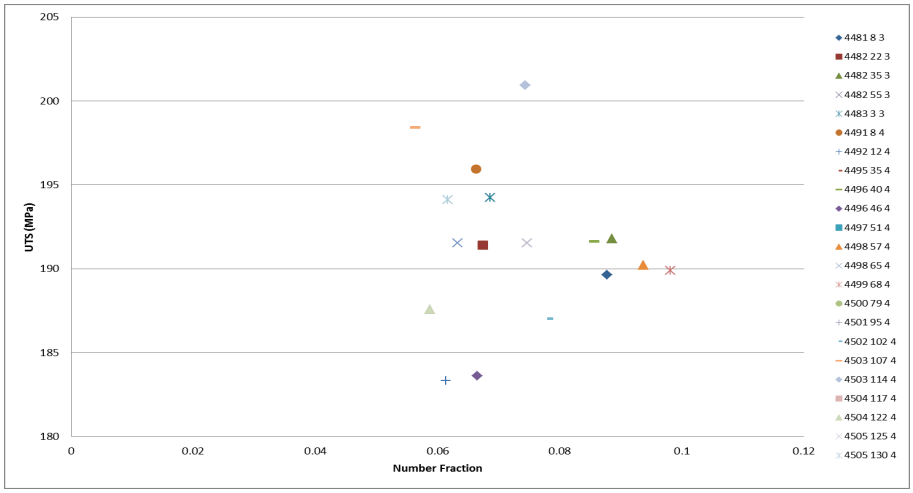

b)

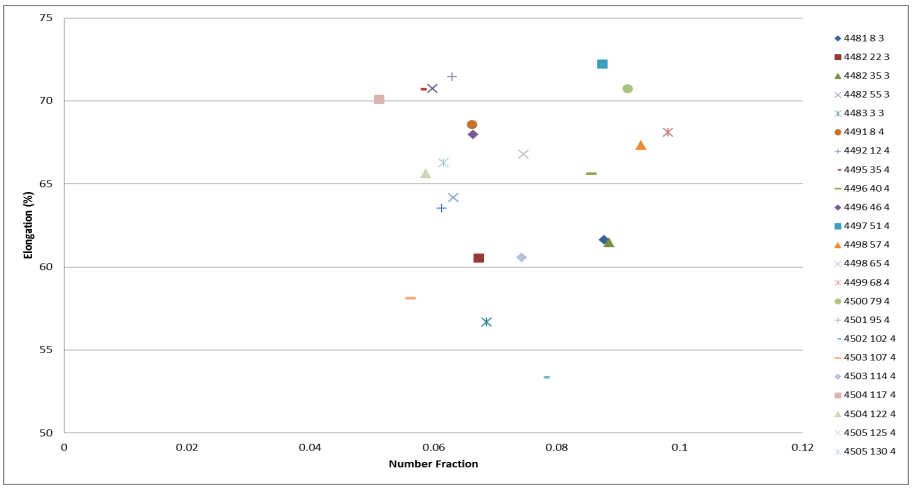

c)

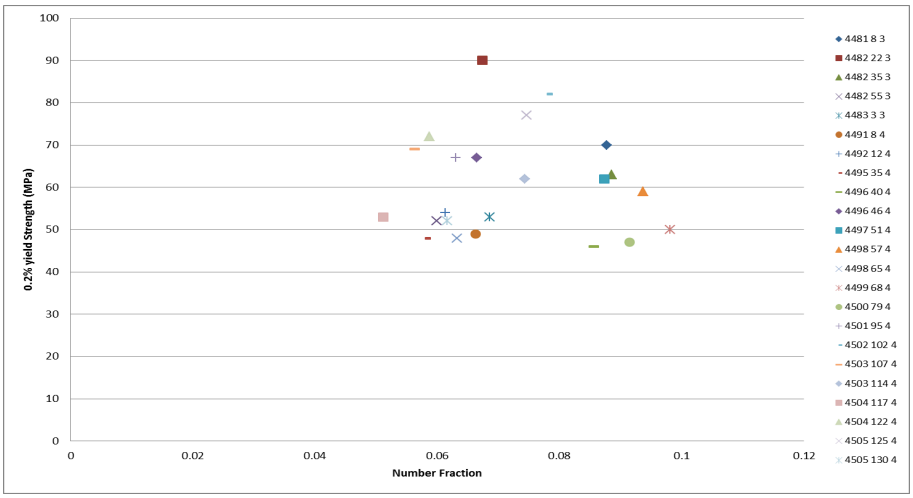

Figure 60: a) UTS, b) elongation and c) 0.2% yield strength vs. number fraction at peak of LAM.

(Tokyo Denkai)

a)

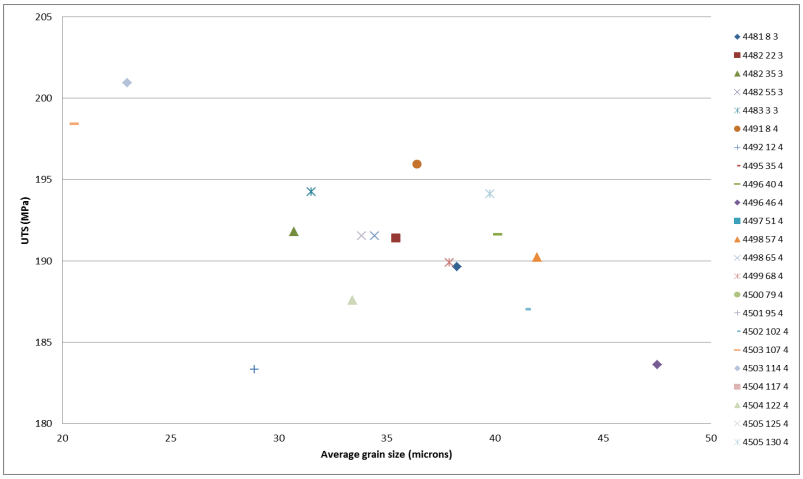

b)

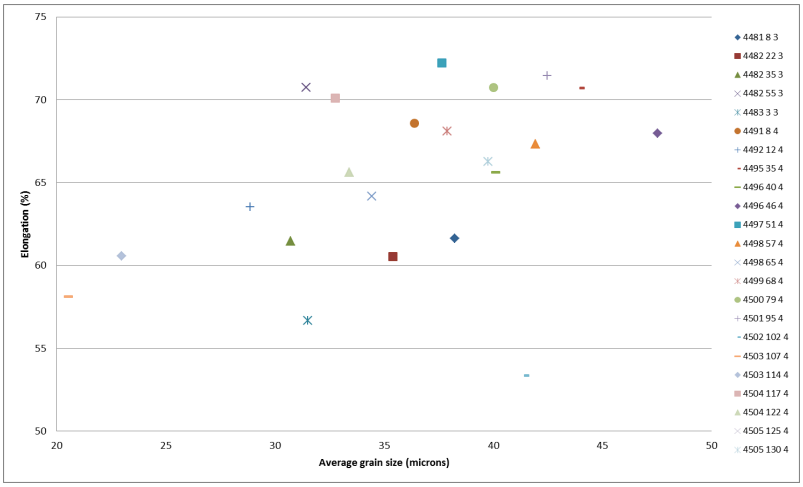

c)

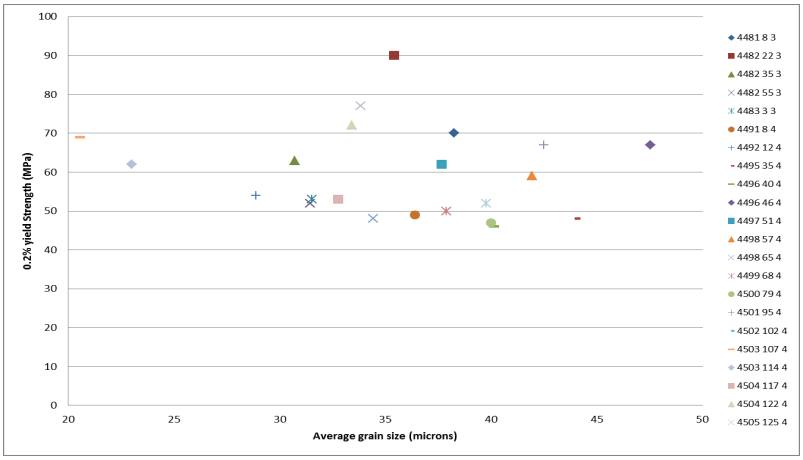

Figure 61: a) UTS, b) elongation and c) 0.2% yield strength vs. average grain size as diameter in microns. (Tokyo Denkai)

a)

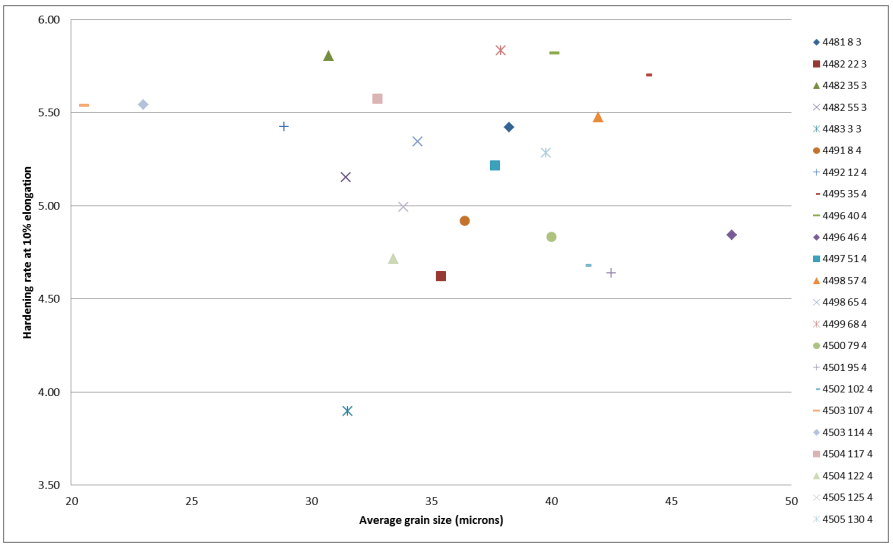

b)

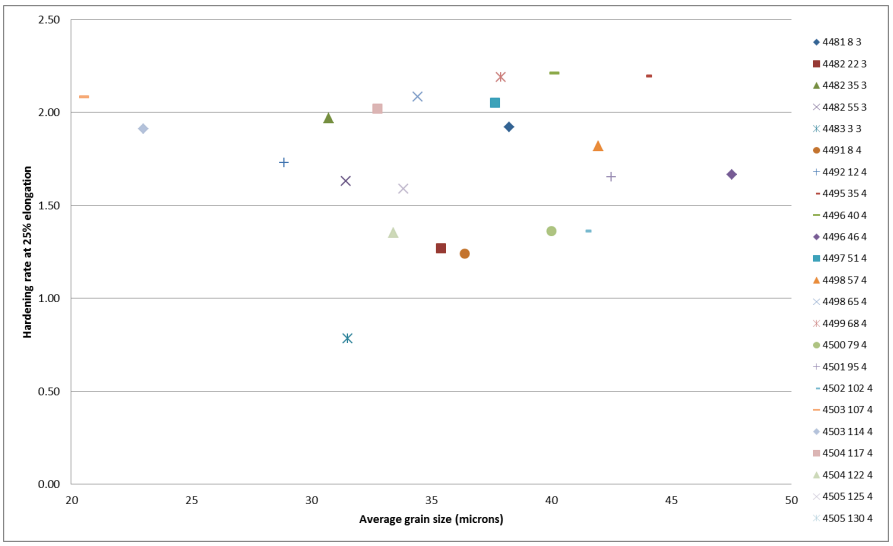

Figure 62: Hardening rate at a) 10% and b) 25% elongation vs. average grain size (diameter) in microns. (Tokyo Denkai)

a)

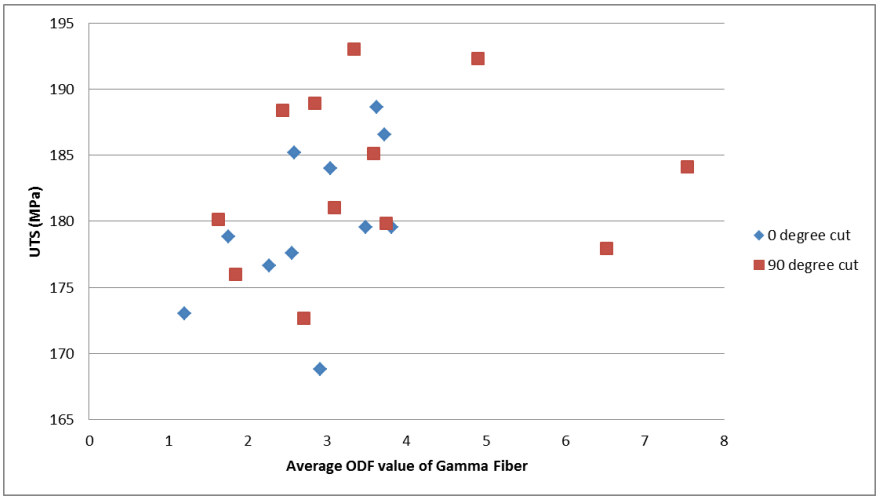

b)

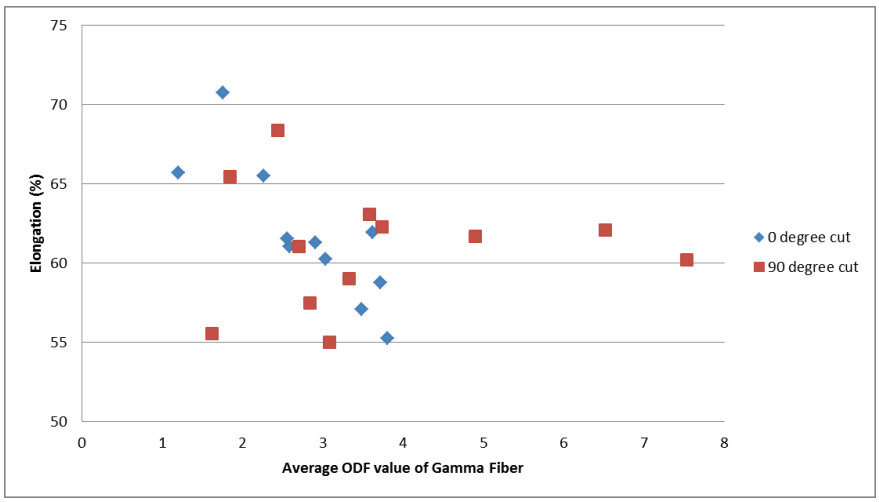

c)

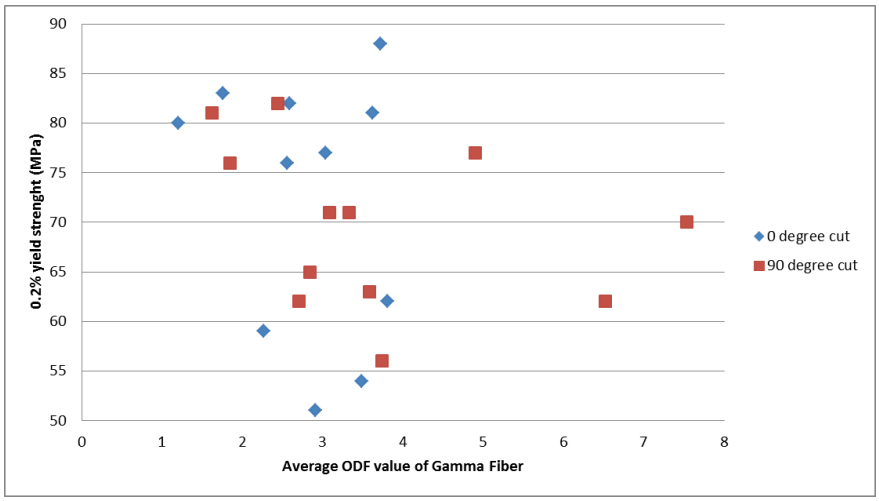

Figure 63: a) UTS, b) elongation and c) 0.2% yield strength vs. average ODF value of γ-fiber at $\phi_2 = 45°$. (Ningxia)

a)

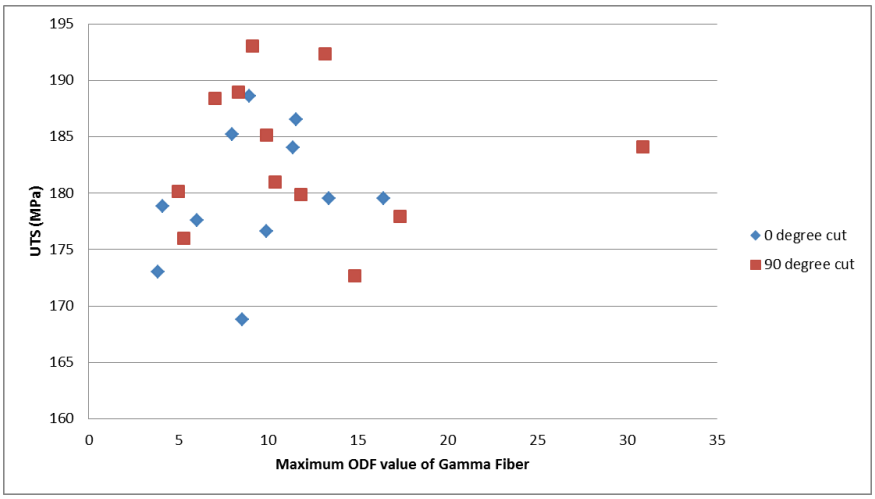

b)

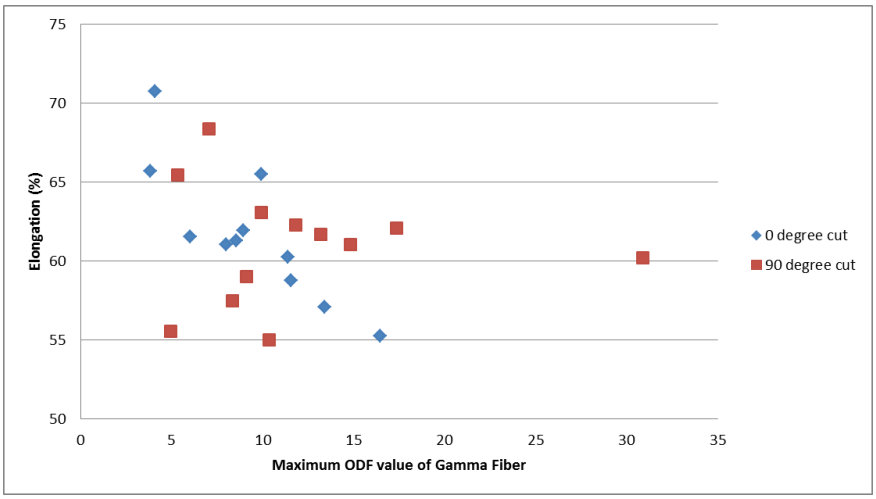

c)

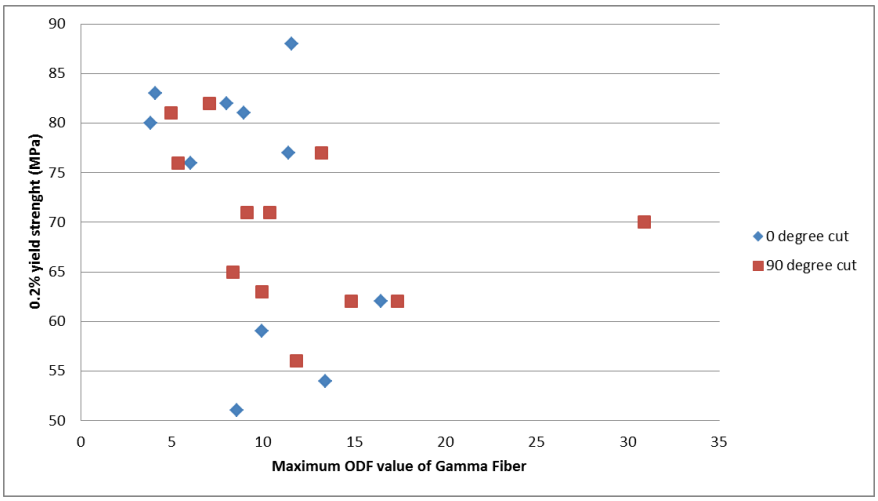

Figure 64: a) UTS, b) elongation and c) 0.2% yield strength vs. maximum ODF value of γ-fiber at $\phi_2 = 45^\circ$. (Ningxia)

a)

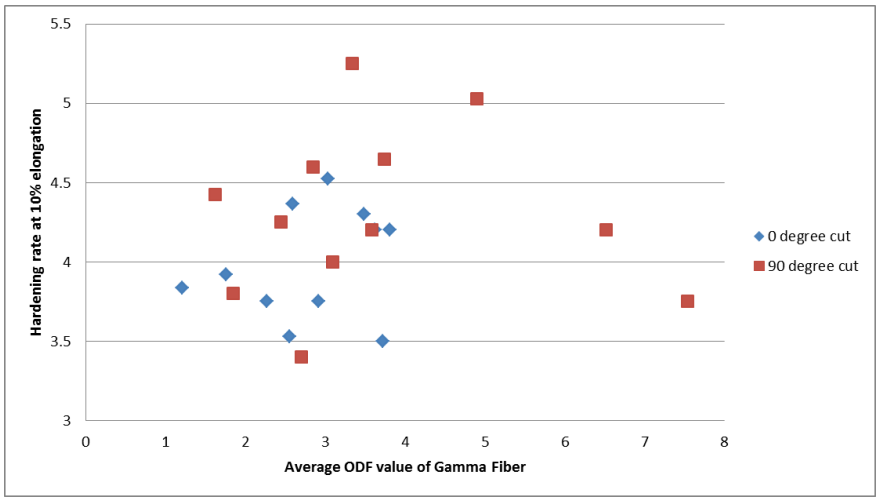

b)

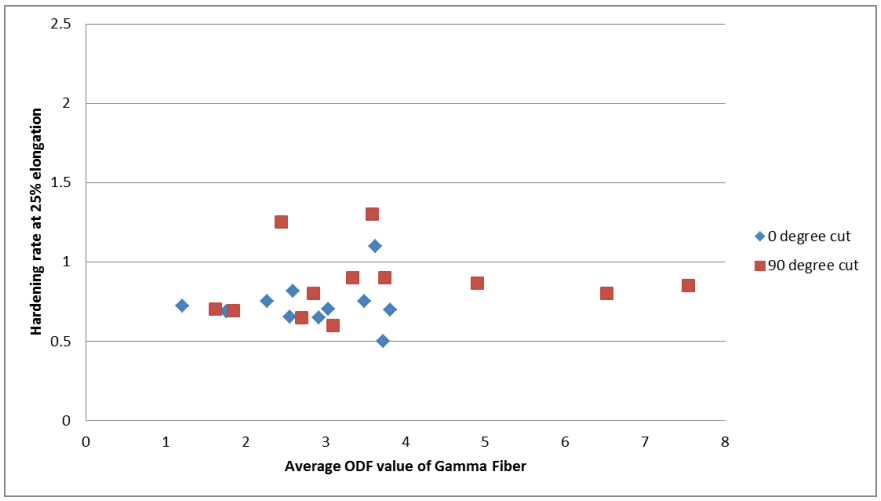

Figure 65: Hardening rate at a) 10% and b) 25% elongation vs. average ODF value of γ-fiber at $\phi_2 = 45°$. (Ningxia)

a)

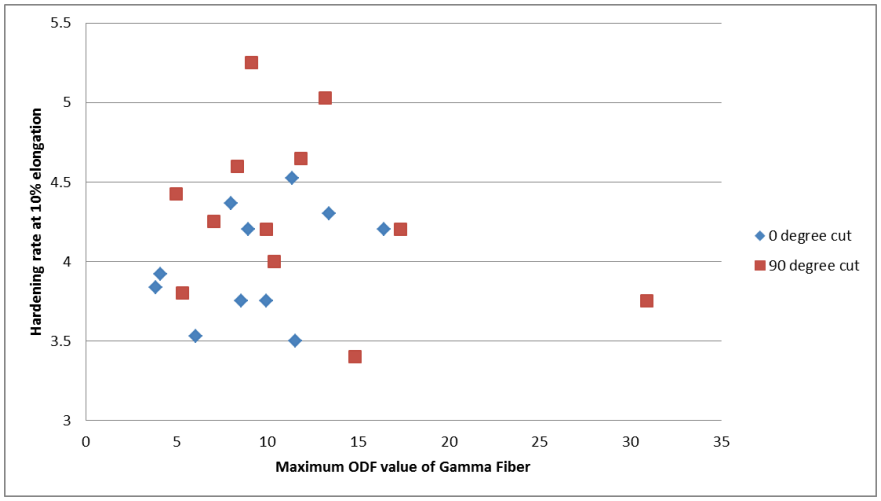

b)

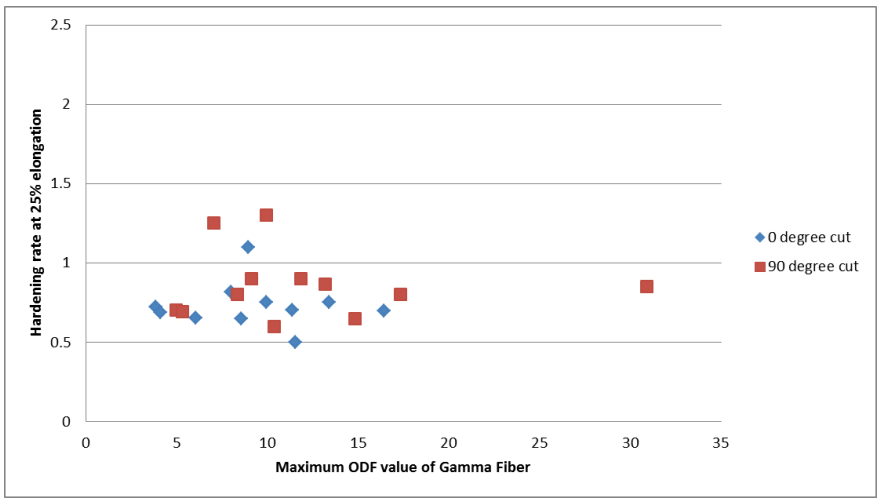

Figure 66: Hardening rate at a) 10% and b) 25% elongation vs. maximum ODF value of γ-fiber at $\phi_2 = 45°$. (Ningxia)

a)

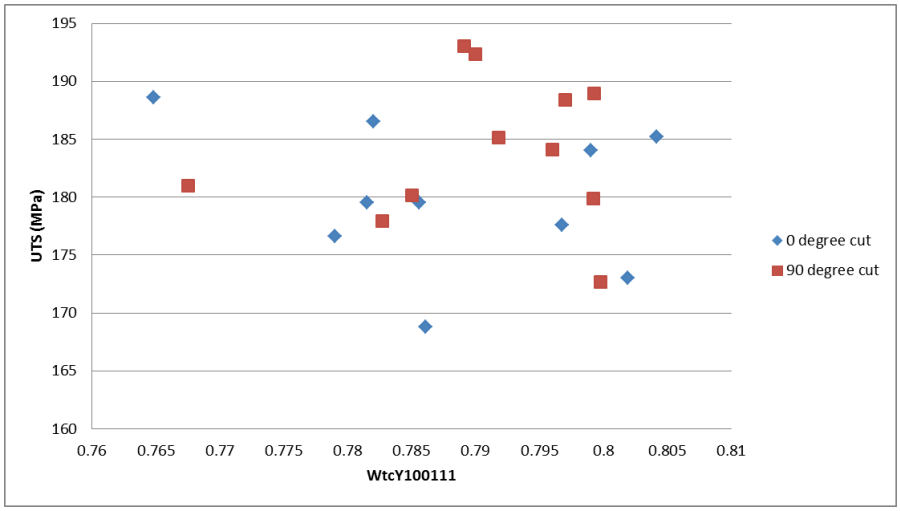

b)

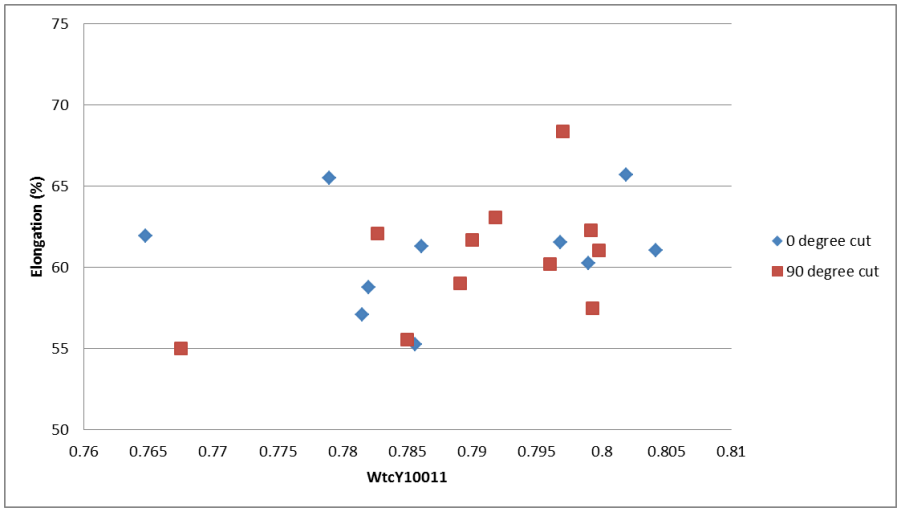

c)

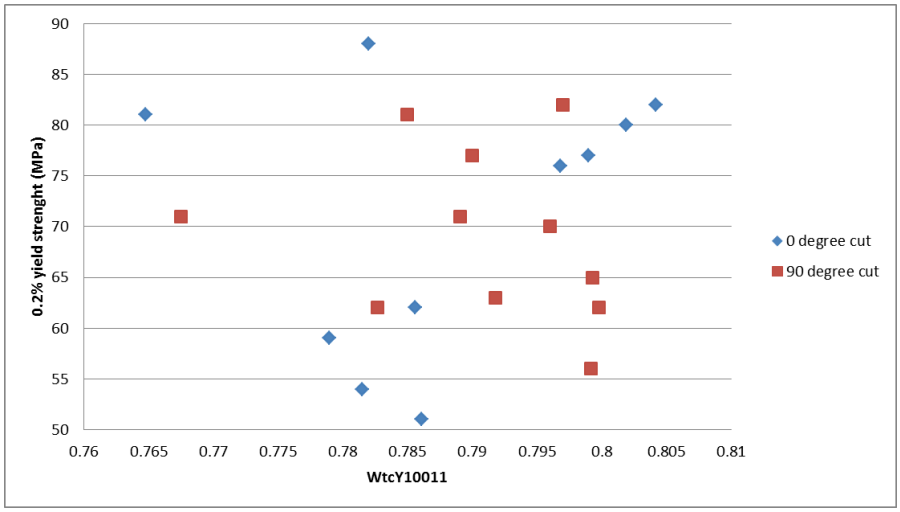

Figure 67: a) UTS, b) elongation and c) 0.2% yield strength vs. contrast factor Y100111. (Ningxia)

a)

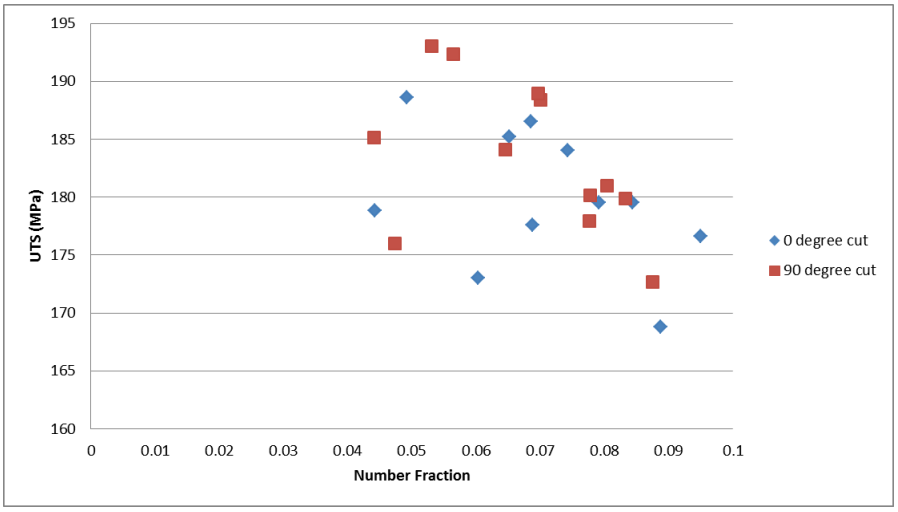

b)

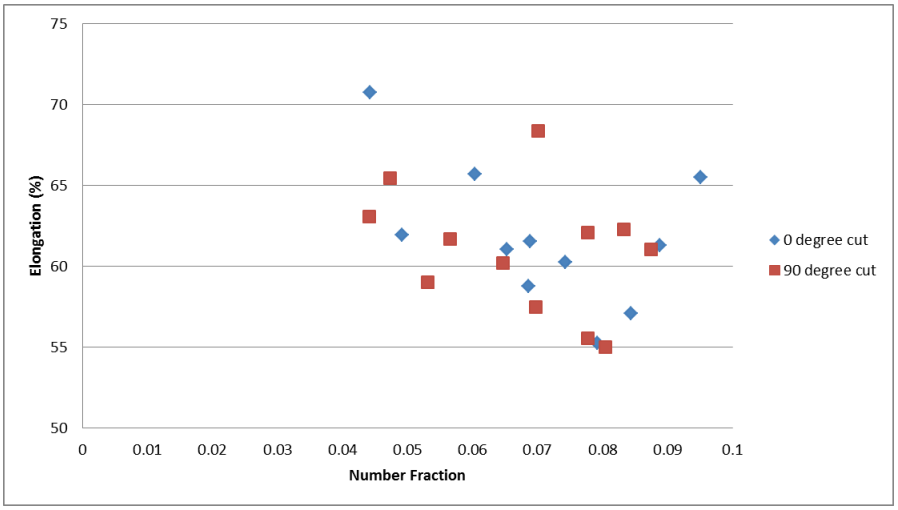

c)

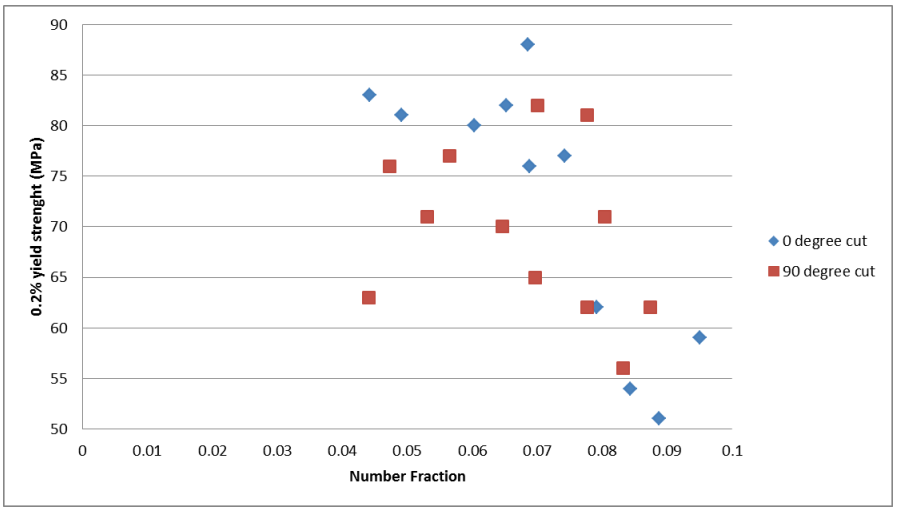

Figure 68: a) UTS, b) elongation and c) 0.2% yield strength vs. number fraction at peak of LAM.

(Ningxia)

a)

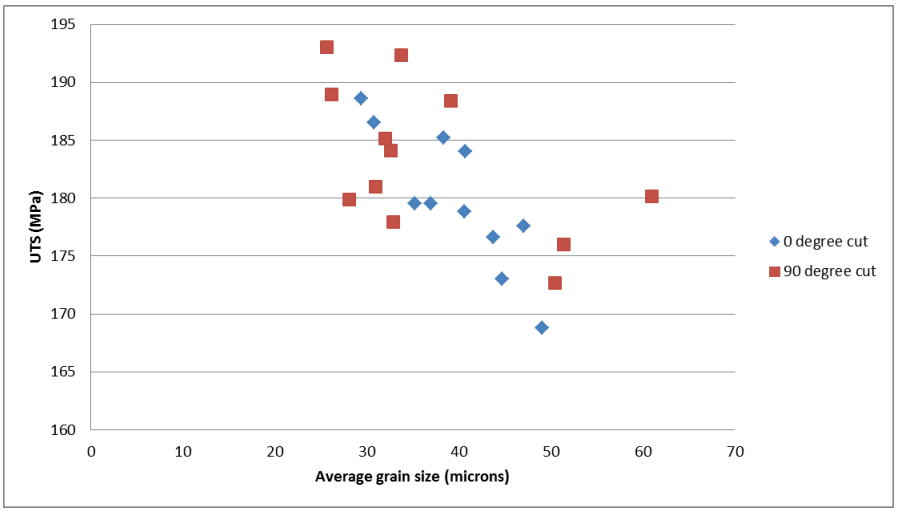

b)

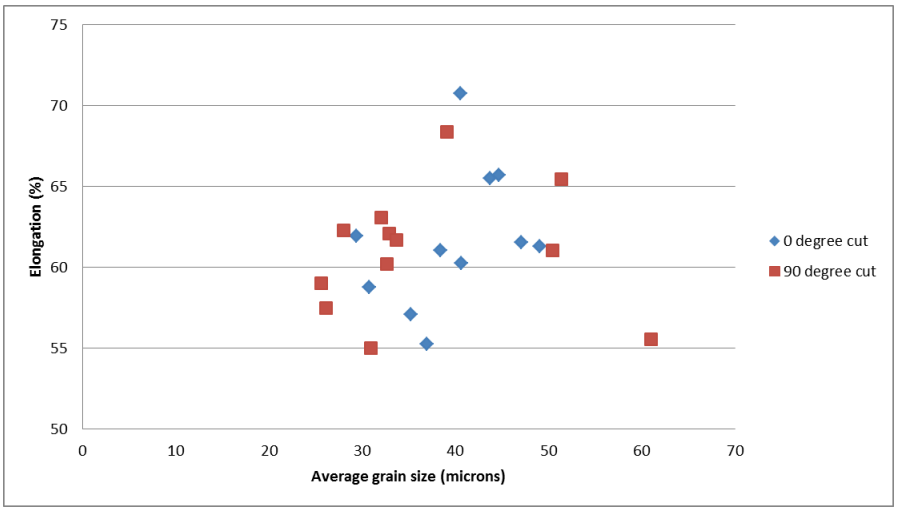

c)

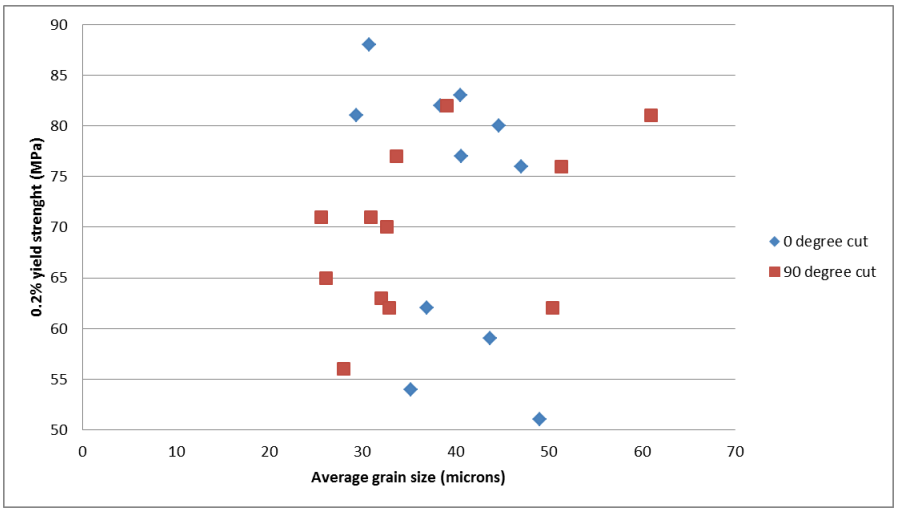

Figure 69: a) UTS, b) elongation and c) 0.2% yield strength vs. average grain size (diameter) in microns. (Ningxia)

a)

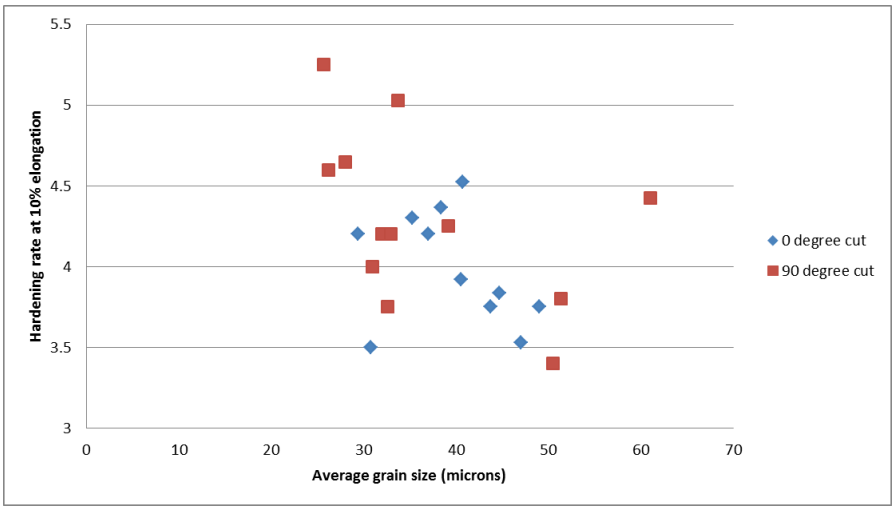

b)

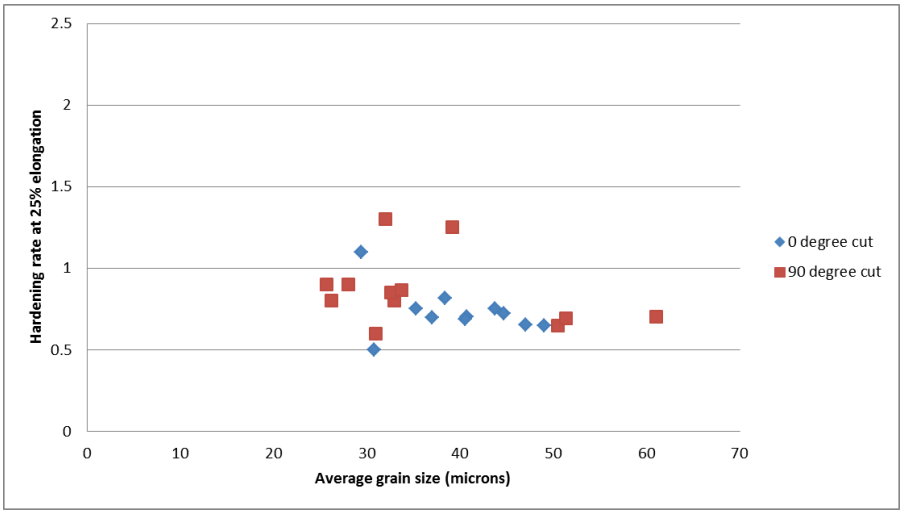

Figure 70: Hardening rate at a) 10% and b) 25% elongation vs. average grain size (diameter) in microns. (Ningxia)

V. DISCUSSION

The IPF maps of left and right grip of dog-bone samples and OIM square share similarity and have some differences to each other, but they are subtle. From Figures 16-34, the data acquired from OIM squares are representative for where the samples were cut and area around it. Even though one of Ningxia's sample, E-38, shows a different pattern between OIM square and dog-bone sample, it may due to the height of cut sample is decreasing though out the sample, which means the sample was not cut perpendicular to the longitude direction of the sample. As a result, the microstructural properties of the OIM square can be used to correlate with mechanical properties.

From the IPF maps, the texture of niobium contains mostly preferred [111] || ND orientations, which is blue in the color scale and [001] || ND, which is red on color scale. Figure 52 shows a red-blue-red orientation as expected, but others are more or less mixed up or appear to be more banded. For example, Figure 44 has a blue-red-blue-red-blue and no particular band can be seen from Figure 46. But for samples having the same number of bands, the mechanical properties show no similarity. The grain size is varied, for example Figures 45 and 46 for Tokyo Denkai, and 51 and 52 for Ningxia. The samples with smaller grain sizes tend to have higher UTS. However, the trend only occurs in extreme samples.

From Table 3 and Figure C. 21 in Appendix C, niobium sheets that came from the same ingot 4505 have similar texture and elongation for both the samples. However other samples that come from the same ingot do not have a similar elongation. For example, Ningxia samples D-25 and D-27, which is Figure D. 10 in Appendix D, have textures with even different grain size and large difference in elongation and UTS. The differences in mechanical properties between these two companies may result from the different manufacturing process, or the fact that samples were tested in two different directions. However, the specific manufacturing process is confidential to the

companies and hard to determine from measurements, as the initial microstructural properties are unknown.

Since the y-axis in computing contrast factor is the tensile axis of the sample, it is useful to relate it to the mechanical properties. It is expected that a uniform grain color, either red or blue, will have a low contrast factor and contributes to more uniform deformation (higher elongation). However, except for the extreme value when having smallest elongation for Tokyo Denkai's sample, the result shows a shotgun scatter plot. If LAM is higher, this implies more lattice curvature and probably more low angle grain boundaries that could inhibit dislocation motion, and hence a higher work hardening rate and perhaps, UTS, but it also shows a shotgun scatter plot. The fraction of CSL boundaries is too small, around 0.09, which cannot imply any useful results.

Despite obvious differences in microstructures, texture, and mechanical properties, there appears to be little evidence of correlations; shotgun scatter is consistently observed. Figure 61 c) and Figure 69 c), similar to the Hall-Petch relation, also implies either there is no correlation or the 0.2% yield strength is not accurate enough and cannot use as to correlate with microstructural properties. Even though there is negative correlation between elongation and average ODF value on γ-fiber at ϕ_2 equals 45°, and between UTS and average grain size for samples cut parallel to the rolling direction in Ningxia. However, they are too particular that may results from unknown reason or by chance. All the results may suggest that niobium could have unique properties compare with other metal and more consistency in cutting test samples are desired, as to cut all parallel to the rolling direction.

Even though no clear trend can be drawn on the correlation plots, all the samples are qualified by the requirements FRIB set, and can be used in manufacturing SRF cavities. It is expected that, except for implications of cost, SRF cavities should be made from samples that having similar properties. This assessment will provide a database to provide a foundation for comparing the quality

of cavities that are manufactured for the FRIB, and may provide a basis for making improvements in specifications for niobium sheet metal for SRF cavities.

VI. CONCLUSIONS

Microstructural and mechanical properties of high purity niobium, which is being used for SRF cavities for the FRIB, varied in all samples that were received from two different companies. The correlation between microstructural and mechanical properties was examined. Instead of a clear trend, scatter plot that has low correlation is found, and the suggestion of a trend can be seen only from the extreme cases and samples cut parallel to rolling direction, for which the reasons are not clear. To achieve the goal of making uniform grains and texture, further analysis on different ways to quantify texture are needed and more sampling for consistency in measurements for each lot should be explored. Moreover, samples having significantly different properties should be used to make different single cell cavities to examine whether there is a difference in the performance, to further improve understanding of the relationship between performance, microstructural properties, and ultimately, cost.

APPENDICES

Appendix A: The Matlab code used to calculate standard deviation, average, maximum value for all ODF slice.

```
ODFHeaderLines = 5;
fnameODF = 'E:\Master\ODF\Ningxia\993401 center odf.txt';
filename = 993401;
fileODF = fopen(fnameODF)
dataODF = importdata(fnameODF, ' ', ODFHeaderLines)
ODF = dataODF.data;
PF = xlsread('PF_ningxia.xlsx');

fclose('all')

%%
sizeODF = size(ODF);

for i=0:5:360
   ai= (ODF(:,3) ==i);
   ph2i = ODF(ai,:);
   ph2i(:,3)=[];
   %plot the 3D ODF
   x = ph2i(:,1);
   y = ph2i(:,2);
   z = ph2i(:,3);
   %Convert Alpha and Sigma to new axis due to the different rolling direction
   n = find(PF(:,1) == filename);
   cn = PF(n,:);
   cx = ph2i(:,1) + cn (:,2);

%%
   bi = find(ph2i(:,2) >=45 & ph2i(:,2) <=65);
   ph2i = ph2i(bi,:);
   SD_G = std(ph2i(:,3));
   AVG_G = mean(ph2i(:,3));
   MAX_G = max(ph2i(:,3));
   AA = [SD_G, AVG_G, MAX_G]

end
```

Appendix B: Excerpt from Dr. Bieler's Matlab code used to calculate contrast factor, relevant parts in red.

```
% T.R. Bieler - m' Schmid and fip calculator, 4 June-14 with input from Adam L Pilchak
modified 1 July 2015
% contains pieces from prior codes that are probably right, but no guarantees, use at
your own risk.
% sources for these ideas are discussed in                written and used in Matlab
release R2009b
% Bieler et al. Int. J. Plasticity 25(9), 1655-1683, 2009, and
% Kumar et al. J. Engineering and Materials Technology 130, 021012, 2008
% and related prior work.
…
% Stress tensor is defined using TSL convensions with x down !!!  put the one you want
last
sigma = [1,0,0; 0,0,0; 0,0,0];
sigma = [0,1,0; 1,0,0; 0,0,0];  sigma = [0,0,0; 0,0,0; 0,0,1]; sigma = [0,0,0; 0,1,0;
0,0,0];
sigman = sigma/norm(sigma,'fro');   % Frobenius norm - unitize stress tensor to get
generalized Schmid factor
sigmav = [sigma(1,1) sigma(2,2) sigma(3,3)]';  % vectorized version of trace
nsten = 0;  %<---*** 0 if using a uniform stress, otherwise, enter number of stresses
loaded below:.

…

%   BCC            plane   direction   ---------------------------------------
ssbcc(:,:,1) =  [ 1 -1  0 ;  1  1  1 ; 0 0 0 ; 1 1 0 ; 1 1 1 ; 0 0 1 ; 0 0 1 ; 0 0 1];
ssbcc(:,:,2) =  [-1  0  1 ;  1  1  1 ; 0 0 0 ; 1 0 1 ; 1 1 1 ; 0 1 0 ; 0 1 0 ; 0 1 0];
ssbcc(:,:,3) =  [ 0 -1  1 ;  1  1  1 ; 0 0 0 ; 1 0 0 ; 1 1 1 ; 0 1 1 ; 0 1 1 ; 0 1 1];

ssbcc(:,:,4) =  [ 1  1  0 ; -1  1  1 ; 1 0 0 ; 0 1 0 ; 0 1 1 ; 1 0 1 ; 1 0 1 ; 1 0 1];
ssbcc(:,:,5) =  [ 1  0  1 ; -1  1  1 ; 1 0 0 ; 1 1 0 ; 0 1 1 ; 0 0 1 ; 0 0 1 ; 0 0 1];
ssbcc(:,:,6) =  [ 0 -1  1 ; -1  1  1 ; 1 0 0 ; 1 1 1 ; 0 1 1 ; 0 0 0 ; 0 0 0 ; 0 0 0];

ssbcc(:,:,7) =  [ 1 -1  0 ; -1 -1  1 ; 1 1 0 ; 0 0 0 ; 0 0 1 ; 1 1 1 ; 1 1 1 ; 1 1 1];
ssbcc(:,:,8) =  [ 1  0  1 ; -1 -1  1 ; 0 0 1 ; 1 0 0 ; 1 1 0 ; 0 1 1 ; 0 1 1 ; 0 1 1];
ssbcc(:,:,9) =  [ 0  1  1 ; -1 -1  1 ; 1 1 0 ; 0 1 0 ; 0 0 1 ; 1 0 1 ; 1 0 1 ; 1 0 1];

ssbcc(:,:,10) = [ 1  1  0 ;  1 -1  1 ; 0 1 0 ; 0 1 1 ; 1 0 1 ; 1 0 0 ; 1 0 0 ; 1 0 0];
ssbcc(:,:,11) = [-1  0  1 ;  1 -1  1 ; 0 1 0 ; 0 0 0 ; 1 0 1 ; 1 1 1 ; 1 1 1 ; 1 1 1];
ssbcc(:,:,12) = [ 0  1  1 ;  1 -1  1 ; 0 1 0 ; 0 0 1 ; 1 0 1 ; 1 1 0 ; 1 1 0 ; 1 1 0];
i110 = 1;
f110 = 12;

% Mode 2,   plane direction, Define four points in the plane
ssbcc(:,:,13) = [-1 -1  2 ;  1  1  1 ; 0 0 0 ; 1 0 0.5 ; 1 1 1 ; 0 1 0.5 ; 0 1 0.5 ; 0
1 0.5]; %ok
ssbcc(:,:,14) = [ 1 -2  1 ;  1  1  1 ; 0 0 0 ; 1 0.5 0 ; 1 1 1 ; 0 0.5 1 ; 0 0.5 1 ; 0
0.5 1]; %ok
ssbcc(:,:,15) = [-2  1  1 ;  1  1  1 ; 0 0 0 ; 0.5 0 1 ; 1 1 1 ; 0.5 1 0 ; 0.5 1 0 ;
0.5 1 0]; %ok

ssbcc(:,:,16) = [ 1 -1  2 ; -1  1  1 ; 1 0 0 ; 1 1 0.5 ; 0 1 1 ; 0 0 0.5 ; 0 0 0.5 ; 0
0 0.5]; %ok
ssbcc(:,:,17) = [-1 -2  1 ; -1  1  1 ; 1 0 0 ; 1 0.5 1 ; 0 1 1 ; 0 0.5 0 ; 0 0.5 0 ; 0
0.5 0]; %ok
ssbcc(:,:,18) = [ 2  1  1 ; -1  1  1 ; 1 0 0 ; 0.5 1 0 ; 0 1 1 ; 0.5 0 1 ; 0.5 0 1 ;
0.5 0 1]; %ok

ssbcc(:,:,19) = [ 1  1  2 ; -1 -1  1 ; 1 1 0 ; 0 1 0.5 ; 0 0 1 ; 1 0 0.5 ; 1 0 0.5 ; 1
0 0.5]; %ok
```

```
ssbcc(:,:,20) = [-1  2  1 ; -1 -1  1 ; 1 1 0 ; 0 0.5 0 ; 0 0 1 ; 1 0.5 1 ; 1 0.5 1 ; 1
0.5 1]; %ok
ssbcc(:,:,21) = [ 2 -1  1 ; -1 -1  1 ; 1 1 0 ; 0.5 1 1 ; 0 0 1 ; 0.5 0 0 ; 0.5 0 0 ;
0.5 0 0]; %ok

ssbcc(:,:,22) = [-1  1  2 ;  1 -1  1 ; 0 1 0 ; 0 0 0.5 ; 1 0 1 ; 1 1 0.5 ; 1 1 0.5 ; 1
1 0.5];
ssbcc(:,:,23) = [ 1  2  1 ;  1 -1  1 ; 0 1 0 ; 0 0.5 1 ; 1 0 1 ; 1 0.5 0 ; 1 0.5 0 ; 1
0.5 0]; %ok
ssbcc(:,:,24) = [-2 -1  1 ;  1 -1  1 ; 0 1 0 ; 0.5 0 0 ; 1 0 1 ; 0.5 1 1 ; 0.5 1 1 ;
0.5 1 1]; %ok
i112 = 13;
f112 = 24;

…

mnslp = max(nslp);
ss = zeros(8,3,mnslp,4);

for i=1:1:mnslp   % Change n & m to unit vector,
…
    if i <= nslpbcc
        n = [ssbcc(1,1,i),ssbcc(1,2,i),ssbcc(1,3,i)/c_a_bcc];   % slightly tetragonal
has c/a <> 1.0
        m = [ssbcc(2,1,i),ssbcc(2,2,i),ssbcc(2,3,i)*c_a_bcc];
        ss(1,:,i,2) = n/norm(n);  % bcc plane
PHASE 2 is BCC
        ss(2,:,i,2) = m/norm(m);  % bcc direction
        ss(3,:,i,2) = [ssbcc(3,1,i),ssbcc(3,2,i),ssbcc(3,3,i)*c_a_bcc]; % point 1
        ss(4,:,i,2) = [ssbcc(4,1,i),ssbcc(4,2,i),ssbcc(4,3,i)*c_a_bcc]; % point 2
        ss(5,:,i,2) = [ssbcc(5,1,i),ssbcc(5,2,i),ssbcc(5,3,i)*c_a_bcc]; % point 3
        ss(6,:,i,2) = [ssbcc(6,1,i),ssbcc(6,2,i),ssbcc(6,3,i)*c_a_bcc]; % point 4
        ss(7,:,i,2) = [ssbcc(7,1,i),ssbcc(7,2,i),ssbcc(7,3,i)*c_a_bcc]; % point 5
        ss(8,:,i,2) = [ssbcc(8,1,i),ssbcc(8,2,i),ssbcc(8,3,i)*c_a_bcc]; % point 6
    end

…

end

%%  Loop for grains to establish slip conditions for each grain
grcen = zeros(int16(dIDgr(1,1)*1.1),18);  % this sets up an array for grain
information
EY = zeros(int16(dIDgr(1,1)*1.1),3);
Sfplbv = zeros(mnslp+1,30);
sortmv = zeros(mnslp+1,30,int16(dIDgr(1,1)*1.1));
grcen(:,1) = -1;    % that is a little bigger that needed because some grain numbers
are skipped,
                    % and are thus marked with -1.  Grains are processed by grain
number, not array location
grmax = 0;    ngcount = 0;   r3 = 3^.5;   fprintf('Numbers and vectors computed for
Grain # ');
for ng=1:1:dIDgr; %    generalized Schmid factor calculation loop for each grain ng

…

    if ig > 0
        grcen(ig,1:6) = [IDgr(ng,10) IDgr(ng,5:6) IDgr(ng,2:4)];
        phid = grcen(ig,4:6);   % phid is Euler phi angles in degrees

        ph = grcen(ig,1);   % phase ID set

        if hkl == 1
```

```
            phid(1) = phid(1) + 0 ; % or +90 to convert hkl to TSL software default
            if phid(1)>360          % or +180 to modify TSL Euler angle coordinate
system to have X down and Y right;
                phid(1) = phid(1) - 360;
            elseif phid(1) < 0
                phid(1) = phid(1) + 360;
            end
        end

        g1=[cosd(phid(1)),sind(phid(1)),0; -sind(phid(1)),cosd(phid(1)),0; 0,0,1];
        g2=[1,0,0; 0,cosd(phid(2)),sind(phid(2)); 0,-sind(phid(2)),cosd(phid(2))];
        g3=[cosd(phid(3)),sind(phid(3)),0; -sind(phid(3)),cosd(phid(3)),0; 0,0,1];
        g=g3*g2*g1;   % calculate orientation matrix
        if nsten == 0
            sigma_n(:,:,ig) = sigman;
            sigma_v(:,ig) = sigmav';
        end
        gsgT = g*sigma_n(:,:,ig)*g'; %rotated stress tensor
% compute directions of 100 and 111 vectors using X = g'x
        X100 = [max(abs(g(:,1)))  max(abs(g(:,2))) max(abs(g(:,3)))]; % largest <100>
component in X,Y,Z directions
        a111 = [g'*[1 1 1]'./r3  g'*[-1 1 1]'./r3  g'*[-1 -1 1]'./r3  g'*[1 -1
1]'./r3]';  % four <111> unit vectors in X,Y,Z ; r3 is 3^.5
        X111 = [max(abs(a111(:,1))) max(abs(a111(:,2))) max(abs(a111(:,3)))];  %
largest <111> component in X,Y,Z
        grcen(ig,7:21) = [g(1,:) g(2,:) g(3,:) X100 X111];
        % Orientation matrix is stored, with largest direction of x, y, z, and 111
vectors in global coordinate system

…

        for j=1:1:nslp(ph)  %  direction          plane    Sfplbv means Schmid factor,
plane and Burgers vector (and points on plane)
            Sfplbv(j,1) = j;    %  n * sigma * m
            Sfplbv(j,2) = ss(2,:,j,ph)*gsgT*ss(1,:,j,ph)';  %  generalized Schmid
factor
            if ph == 1 && j>24 && Sfplbv(j,2)<0
                Sfplbv(j,2) = 0.001*Sfplbv(j,2) ;    % this is to prevent anti-twin
shears from being seriously considered later
            end
            Sfplbv(j,3) = abs(Sfplbv(j,2));   % abs(generalized schmid factor)
            Sfplbv(j,4:6) = g'*ss(1,:,j,ph)'; % plane normal in lab coords
            Sfplbv(j,7:9) = g'*ss(2,:,j,ph)'; % bv direction in lab coords
            Sfplbv(j,10:12) = cross(Sfplbv(j,4:6),[0,0,1]); % plane trace
            for k = 1:1:6
                is = 3*k+10;
                ie = is+2;
                Sfplbv(j,is:ie) = g'*ss(k+2,:,j,ph)'; % plane plotting vectors from
origin to points in cell, in lab coords
            end
        end                         %useful plotting for hexahedral tetragonal unit
cell vectors that sort to bottom row
        Sfplbv(mnslp+1,:) = [ph 1 -1 [1 0 0]*g [0 1 0]*g [0 0 1*c_a(ph)]*g 0 0 0  0 0
0  0 0 0  0 0 0  0 0 0  0 0 0]; % don't change g to g' here! otherwise it may make
incorrect cubic prisms
        sortmv(:,:,ig)  = sortrows(Sfplbv,-3);  % Sort slip systems by Schimd factor
    end  %  ig > 0 check
end  % ng loop
fprintf(' %d\n ', ng);


%%  Now start processing by grain boundary...
gbnorm = zeros(dRBdy(1,1),3);
```

```
gbtrac = zeros(dRBdy(1,1),3);
RBout  = zeros(dRBdy(1,1),35);
LAM    = zeros(dRBdy(1,1),3);
mpr    = zeros(mnslp+1,mnslp+1,dRBdy(1,1));
himp4  = zeros(mnslp,4,dRBdy(1,1));
nbcount = 0;  fprintf('Computing grain boundary parameters for GB # ');
jk4max = 1; top3d3 = 0; top3d2 = 0; top3d1 = 0; top3d0 = 0;
GBlensum = 0; cX100111 = zeros(dRBdy(1,1)); cY100111 = zeros(dRBdy(1,1)); cZ100111 =
zeros(dRBdy(1,1));
for gbnum = 1:1:dRBdy;  %gbnum is grain boundary number, will calculate m' and other
damage parameters
    if gbnum>nbcount+dRBdy/10;
        nbcount=nbcount+dRBdy/10;
        fprintf(' %d ',gbnum);     %, jk4max
    end

    grA = RBdy(gbnum,13);    grB = RBdy(gbnum,14);
    jk = 1;   % counter for the number of m' calculations made where Schmid factors
are > low tolerance
    jk4 = 1;  % counter for the number of m' calculations made where Schmid factors
are > high tolerance
    mpmax = 0;    mploc = 0;
    dpsum = 0;    dpsum4 = 0;
    mpsum = 0;    mpsum4 = 0;
    damage = 0;   damage4 = 0;
    mpm0 = 0;   mpm2 = 0;   mpm4 = 0;
    mpm0n = 0;   mpm2n = 0;   mpm4n = 0;
    mpr(1,1,gbnum) = grA+grB/1000; % m-prime table label for grain numbers in mpr()

    if strcmp(num2str(sigma_v(:,ig)),num2str([1 0 0]')) % stress axis || [100] (X)
        EgrA = EY(grA,1); EgrB = EY(grB,1);
    elseif strcmp(num2str(sigma_v(:,ig)),num2str([0 1 0]')) % stress axis || [010] (Y)
        EgrA = EY(grA,2); EgrB = EY(grB,2);
    elseif strcmp(num2str(sigma_v(:,ig)),num2str([0 0 1]')) % stress axis || [001] (Z)
        EgrA = EY(grA,3); EgrB = EY(grB,3);
    elseif trace(sigma_n(:,:,ig)) == 0    % Crude estimate of shear effects follows,
may not be meaningful
            EgrA = EY(grA,3)*abs(sigma_n(1,2,ig)) + EY(grA,2)*abs(sigma_n(1,3,ig)) +
EY(grA,1)*abs(sigma_n(2,3,ig));
            EgrB = EY(grB,3)*abs(sigma_n(1,2,ig)) + EY(grB,2)*abs(sigma_n(1,3,ig)) +
EY(grB,1)*abs(sigma_n(2,3,ig));
    else
        fprintf('Can''t calculate modulus for this stress state\r');
        EgrA = 1; EgrB = 1  %pause
    end
        Eratio = min(EgrA,EgrB)/max(EgrA,EgrB);        % always use Emin/Emax!

    F1A = zeros(1,mnslp); % F1 FIP, Simkin et al. 2003 for grain A
%     F14A = 0; % F1 FIP w/ restriction on Schmid factor value for grain A
    F1B = zeros(1,mnslp); % F1 FIP for grain B
%     F14B = 0; % F1 FIP w/ restriction on Schmid factor value for grain B
    F1 = 0; % F1 for grainA/grainB
    F14A = zeros(1,mnslp); % F14 for grainA (with restriction on Schmid factor value)
    F14B = zeros(1,mnslp);

    normdp4 = .75;  % These values indicate instances where values
    normp4 = .55;   % of dm' or m' are too low to take seriously
%    RBdy(gbnum,1:6) = (180/pi).*RBdy(gbnum,1:6);
    gbnorm(gbnum,:) = [cosd(RBdy(gbnum,8)) sind(RBdy(gbnum,8)) 0];
    gbtrac(gbnum,:) = sigma_n(:,:,grA)*gbnorm(gbnum,:)';


…
```

```
%     Variables evaluated above in the loops:     dpsum     mpsum     jk4     dpsum4
mpsum4     F1     F14
    gbodam = damage*abs(norm(gbtrac(gbnum,:))) ;  % damage parameter modified by
apparent GB inclination
    gbodam4 = damage4*abs(norm(gbtrac(gbnum,:))) ; % damage parameter for high schmid
modified by GB inclination
    caxmis = (1-(grcen(grA,12:15)*grcen(grB,12:15)')^2)^.5;  % misorientation of c-
axes (not meaningful for cubic)
    normdp = dpsum/(jk-1);  % average value of dm'
    normp = mpsum/(jk-1);  % average value of m'
    normpm4 = mpm4/mpm4n;  % average value of m'*Schmid factor for m>0.4
    normpm2 = mpm2/mpm2n;  % average value of m'*Schmid factor for m>0.2
    normpm0 = mpm0/mpm0n;  % average value of m'*Schmid factor for all
    F1Asort = sort(F1A,'descend'); F1Bsort = sort(F1B,'descend');
    F14Asort = sort(F14A,'descend'); F14Bsort = sort(F14B,'descend');
    maxF1 = max(F1Asort(1),F1Bsort(1));
    maxF14 = max(F14Asort(1),F14Bsort(1));
    cX100111(gbnum) = max(grcen(grA,16)*grcen(grB,19), grcen(grB,16)*grcen(grA,19)); %
max of two possible 100-111 direction cosine products in X direction
    cY100111(gbnum) = max(grcen(grA,17)*grcen(grB,20),
grcen(grB,17)*grcen(grA,20)); % ... Y  contrast factor, the product is 100 * 111
components
    cZ100111(gbnum) = max(grcen(grA,18)*grcen(grB,21),
grcen(grB,18)*grcen(grA,21)); % ... Z  contrast factor, RBdy(gbnum,7 is boundary
segment length)
    GBlensum = GBlensum + RBdy(gbnum,7);  % will later compute weighted sum using
total grain boundary length
    if jk4> 1
        normdp4 = dpsum4/(jk4-1);  %average value of damage for slip systems with m >
0.4
        normp4 = mpsum4/(jk4-1);  %average value of m' for slip systems with m > 0.4
    end

    jk6 = 0; jktop36 = 0;  % counters for number of m' values to average later.
    top6mpn = 0; top3mp6 = 0;

    Spair = zeros(5:5); maxij = [.799 1 1];% Spairmp = zeros(5:5);
    for k = 1:1:5        % Rather than finding all m' values for m > tolH, look only
for top 3 or top 6
        for j = 1:1:5    % find sum of schmid factors for each element of mpr array
and put in Spair()
            Spair(k,j) = mpr(k+1,1,gbnum)-fix(mpr(k+1,1,gbnum)) + mpr(1,j+1,gbnum)-
fix(mpr(1,j+1,gbnum));
%            Spairmp(k,j) = Spair(k,j);
        end
    end
    while (jk6 < 6 || jktop36 < 3) && maxij(1) > 0.79
        maxij = [0 0 0];
        for k = 1:1:5
            for j = 1:1:5
                if Spair(k,j)>maxij(1)  %finds largest Spair value in 5x5 Spair()
                    maxij = [Spair(k,j) k j]; %identifies location k j of sum of
Schmid factors
                end
            end
        end
        mpchk = abs(mpr(maxij(2)+1,maxij(3)+1,gbnum));  % puts (next) highest m' into
mpchk
        if jk6 < 6 && maxij(1) > 0
            top6mpn = top6mpn + mpchk;
            Spair(maxij(2),maxij(3)) = -1;  % Now that highest Spair value is found
and recorded, wipe it out
```

```
            jk6 = jk6 + 1;
            if jk6 == 3;
                top3mpn = top6mpn;  %  capture top 3 values in this variable
            end
        end
        if jktop36 < 3 && maxij(1) > 0
            Spair(maxij(2),maxij(3)) = Spair(maxij(2),maxij(3)) -1; % mark position
with -2 if inside this query
            if mpchk > 0.6
                top3mp6 = top3mp6 + mpchk;  % more stringent criterion for m' only >
0.6 used.
                jktop36 = jktop36 + 1;
            end
        end
    end
    top6mpn = top6mpn/jk6;   % These average values of m' are without regard to size
of m'
    if top3mpn > 0
       top3mpn = top3mpn/3;
    else
        top3mpn = top6mpn;
    end
    if jktop36 == 3
        top3mp6 = top3mp6/jktop36;
        top3d3 = top3d3 + 1;
    elseif jktop36 == 2
        top3mp6 = top3mp6/jktop36;
        top3d2 = top3d2 + 1;
    elseif jktop36 == 1
        top3mp6 = top3mp6/jktop36;
        top3d1 = top3d1 + 1;
    elseif jktop36 == 0
        top3mp6 = 0;
        top3d0 = top3d0 + 1;
    end
            % this is a summary matrix used for plotting
    RBout(gbnum,1:34) = [mploc mpmax 0 dpsum damage gbodam caxmis dpsum4 damage4
gbodam4 normdp normdp4 normp normp4 ...
        maxF1 maxF14 maxF1*Eratio maxF14*Eratio Eratio top3mpn top6mpn top3mp6 mpm4
mpm2 mpm0 normpm4 normpm2 normpm0 ...
        mpm4n mpm2n mpm0n cX100111(gbnum) cY100111(gbnum) cZ100111(gbnum)];
end  % of gbnum loop
cX100111norm = cX100111*RBdy(:,7) / GBlensum;  % normalize distribution by total GB
length
cY100111norm = cY100111*RBdy(:,7) / GBlensum;
cZ100111norm = cX100111*RBdy(:,7) / GBlensum;
wtcX100111 = sum(cX100111norm); % Weighted average of contract factor in X, Y, Z
directions
wtcY100111 = sum(cY100111norm);
wtcZ100111 = sum(cZ100111norm);

plotname = {'      ','      ','      ','  dm''sum  ','  m*dm''sum  ','  gbo*m*dm''sum
','  cax-mis  ','  dm''sum4  ',...
            '  m*dm''4 ','  gbo*dam4  ','  norm dm''  ','  norm dm''4  ','  norm m''
','  norm m''4  ',...
            '  max(F1A,F1B)  ','  max(F14A,F14B)  ','  Emax(F1A,F1B)  ','
Emax(F14A,F14B)  ','  Eratio  ',...
            ' top3mpn ',' top6mpn ',' top3mp6 ', ' mpm4 ', ' mpm2 ', ' mpm0 ', '
normpm4 ', ' normpm2 ', ' normpm0 ', ...
            ' mpm4n' , ' mpm2n ', ' mpm0n ', ' cX100111 ', ' cY100111 ', ' cZ100111 '};
%
% Definitions of parameters computed:
```

```
%  dampar = dm' = adjustment of m' such that m' = 0.8 is worst case damage condition
(i.e. dm' = 1 when m' = 0.8; When m' = 0.6 or 1, dm' = 0.8)
%       This assumes that damage dm' would less if m' is higher because more slip
transfer occurs with less debris left in the GB,
%       and that damage would be lower for smaller m' values because less slip
transfer would happen
% 2 mpmax maximum value of m'
% 4 dpsum or dm'sum = sum of damage parameter dm' for all m' values computed, e.g. for
m' values > 0.6 and slip systems having
%       Schmid factors > tolL (lowest tolerance of Schmid factors, e.g. 0.2)
% 5 damage or m*dm'sum = Schmid factor times sum of dm' values computed, assuming that
Schmid factor will scale the magnitude of slip transfer that occurs.
% 6 gbodam or gbo*m*dm''sum = damage parameter modified by apparent GB inclination
(boundary normals || tensile axis see more damage).
% 7 caxmis or c-axis-misorientation is the angle between c-axes of the two grain
orientations
% 8 dpsum4 or dm''sum4  Same as dpsum, but only for slip systems with m > tolH (e.g.
0.4)
% 9 damage4 or m*dm''sum4  Same as damage, but only for slip systems with m > tolH
(e.g. 0.4)
% 10 gbodam4 or gbo*dam4  Same as gbodam, but only for slip systems with m > tolH (e.g.
0.4)
% 11 normdp   norm dm''   dpsum averaged (normalized by number of instances)
% 12 normdp4  norm dm''4  dpsum4 averaged (normalized by number of instances)
% 13 normp    norm m''    mpsum averaged (normalized by number of instances)
% 14 normp4   norm m''4   mpsum4 averaged (normalized by number of instances)
% 15 maxF1  the fip F1 is computed for all combinations for which m > tolL, and the
largest value for grain A or B is chosen
% 16 maxF14 the fip F14 is computed for all combinations for which m > tolH, and the
largest value for grain A or B is chosen
% 17 maxF1*Eratio  F1 times Eratio
% 18 maxF14*Eratio F14 times Eratio
% 19 Eratio  Ratio of Moduli such that it is < 1
% 20 top3mpn  Average of the m' values for the top 3 (or fewer) Schmid factor pairs in
5x5 upper left corner of the m' array
% 21 top6mpn  Average of the m' values for the top 6 (or fewer) Schmid factor pairs in
5x5 upper left corner of the m' array
% 22 top3mp6  Average of top 3 or fewer m' values > 0.6 in 5x5 upper left corner of
the m' array
% 23 mpm4 = sum of m' times Schmid factor for m > 0.4
% 24 mpm4 = sum of m' times Schmid factor for m > 0.2
% 25 mpm0 = sum of m' times Schmid factor for all m
% 26 normpm4 = normalized sum of m' times Schmid factor for m > 0.4
% 27 normpm2 = normalized sum of m' times Schmid factor for m > 0.2
% 28 normpm0 = normalized sum of m' times Schmid factor for all m
% 29 mpm4n = m' modified by Schmid factor for m > 0.4
% 30 mpm2n = m' modified by Schmid factor for m > 0.2
% 31 mpm0n = m' modified by Schmid factor for all m
% 32 cX100111 = contrast factor between 100 and 111 orientations across GB when
looking in X direction
% 33 cY100111 = contrast factor between 100 and 111 orientations across GB when
looking in Y direction
% 34 cZ100111 = contrast factor between 100 and 111 orientations across GB when
looking in Z direction


%% Choose which 8 histograms to plot and number of bins for each

bins = [25 25 25 25];
pl = [4 5 6 7 8 9 10 19];        % Group A  or
pl = [13 14 11 12 20 22 33 34];  % Group B
figure, hold on
for i = 1:1:4
```

```
    subplot(4,1,i), hist(RBout(:,pl(i)), bins(i)), ...
    title([num2str(min(RBout(:,pl(i)))), plotname{pl(i)}, num2str(bins(i)), ' bins,
max = ', num2str(max(RBout(:,pl(i))))]);
end
figure, hold on
for i = 1:1:4
    subplot(4,1,i), hist(RBout(:,pl(i+4)), bins(i)), ...
    title([num2str(min(RBout(:,pl(i+4)))), plotname{pl(i+4)}, num2str(bins(i)), ' bins,
max = ', num2str(max(RBout(:,pl(i+4))))]);
end
```

Appendix C: IPF map, PF and ODF plots of ϕ_2 equals 0° and 45° for samples from Tokyo Denkai. (EBSD done by Di Kang)

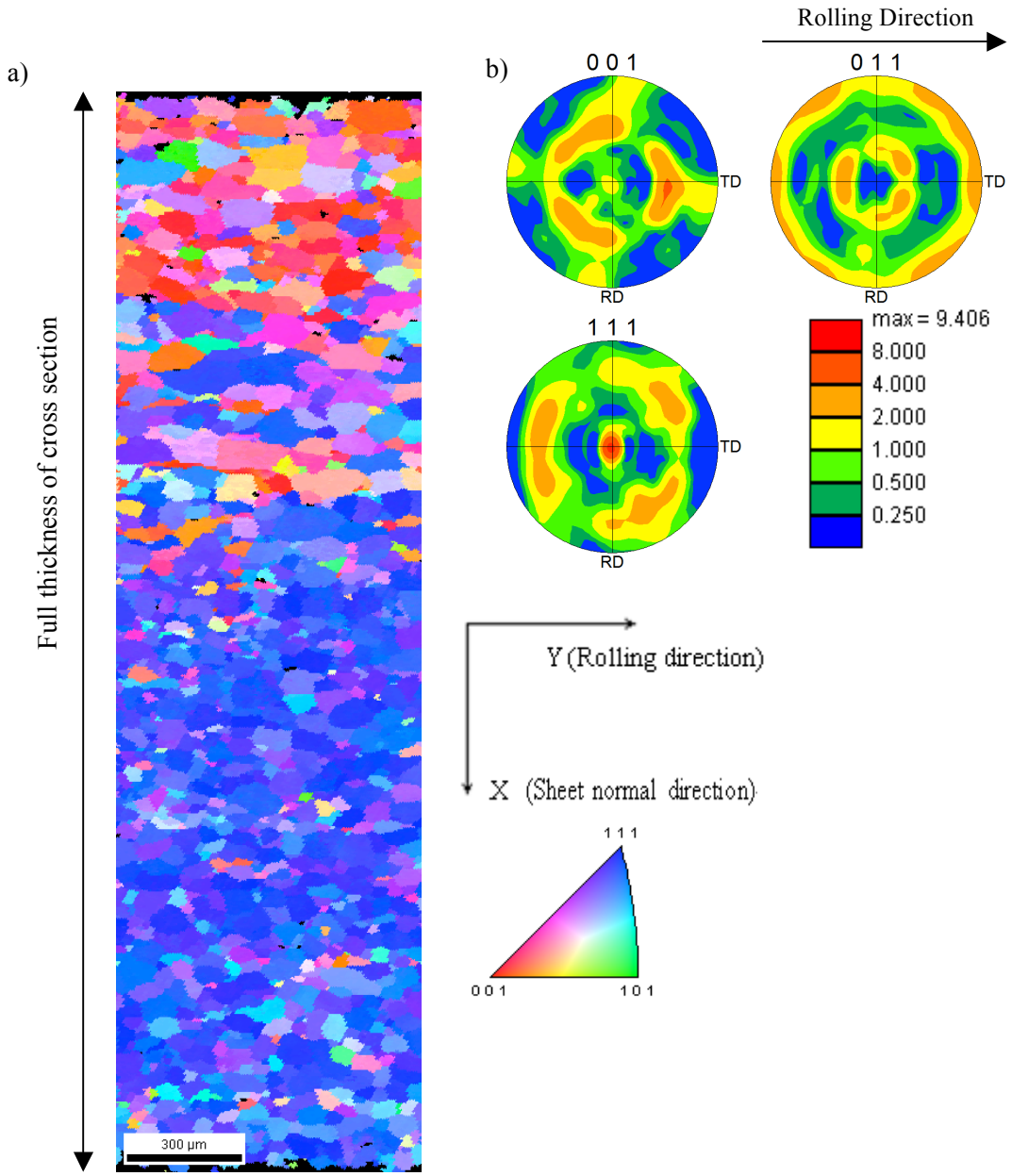

Figure C. 1: a) IPF map and b) PF of niobium sheet Lot 4481 #8 with thickness 3mm.

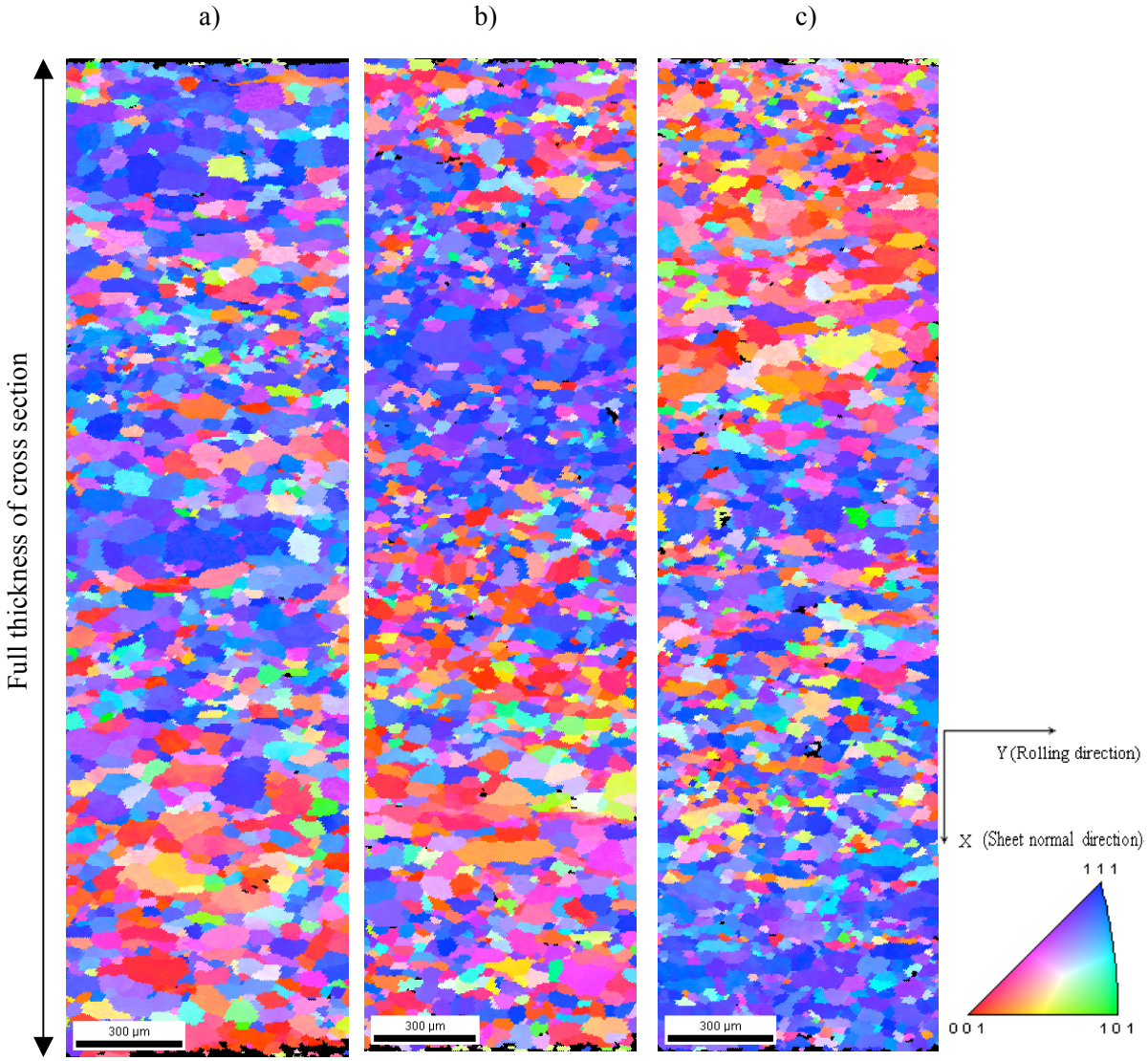

Figure C. 2: IPF maps of niobium sheet Lot 4482 a) #22, b) #35, c) #55 from left to right respectively with thickness 3mm.

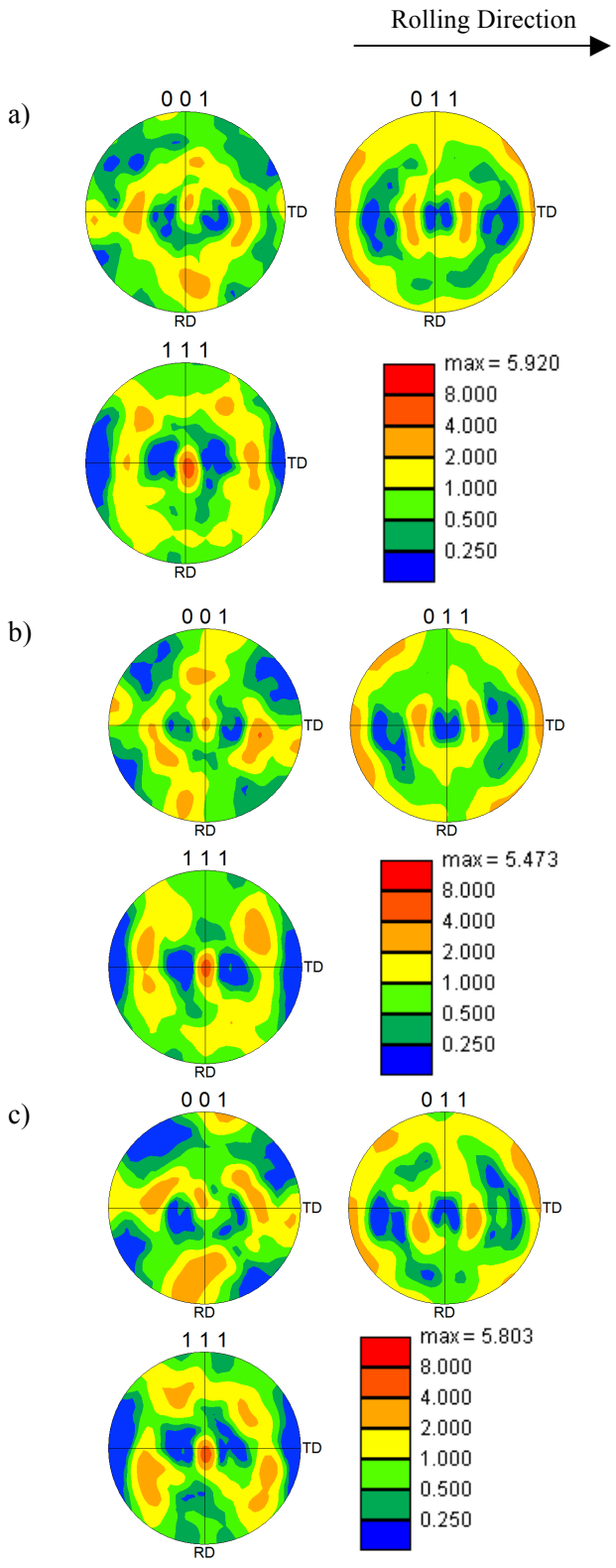

Figure C. 3: PFs of niobium sheet Lot 4482 a) #22, b) #35, c) #55 from top to bottom respectively.

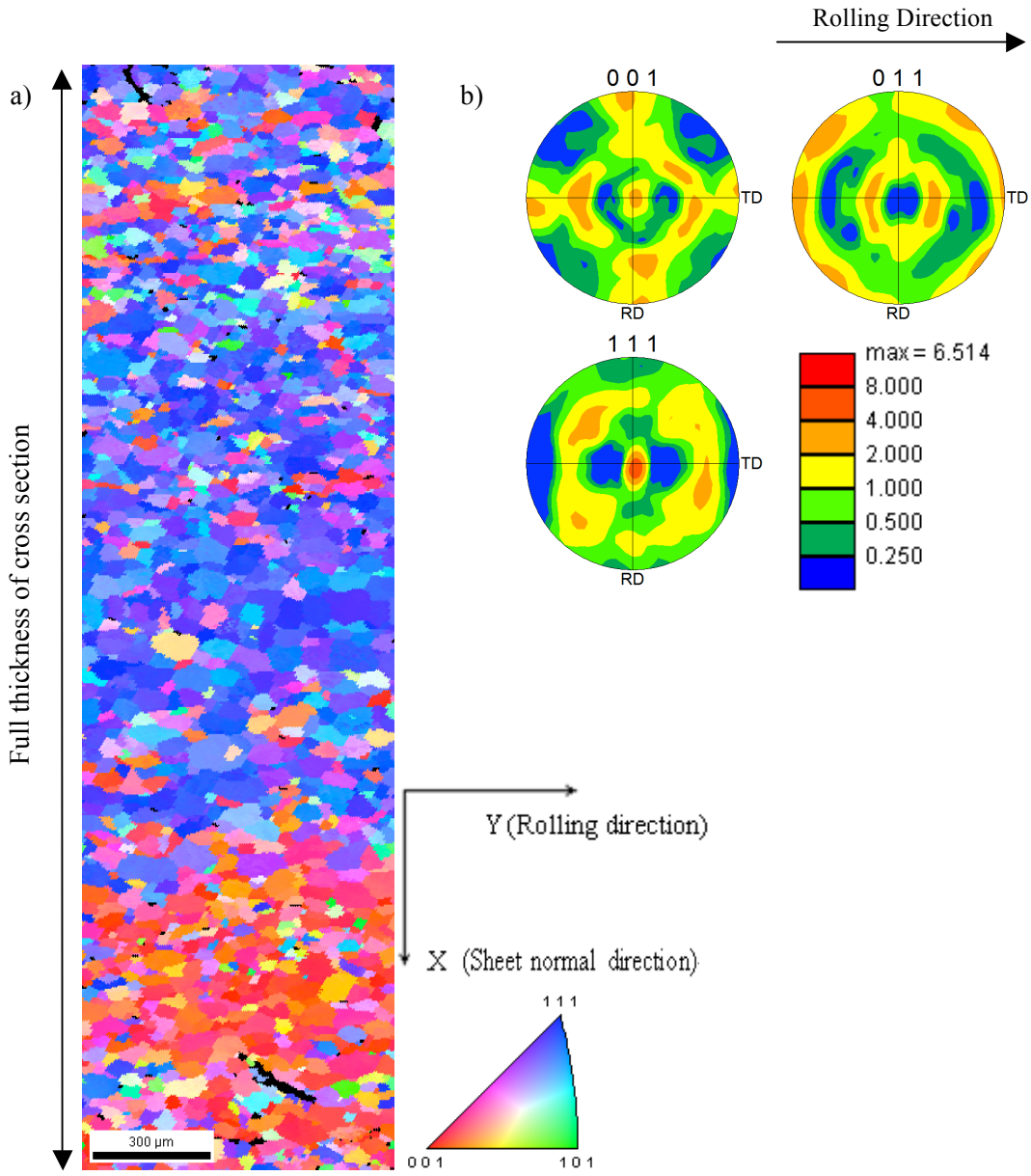

Figure C. 4: a) IPF map and b) PF of niobium sheet Lot 4483 #3 with thickness 3mm.

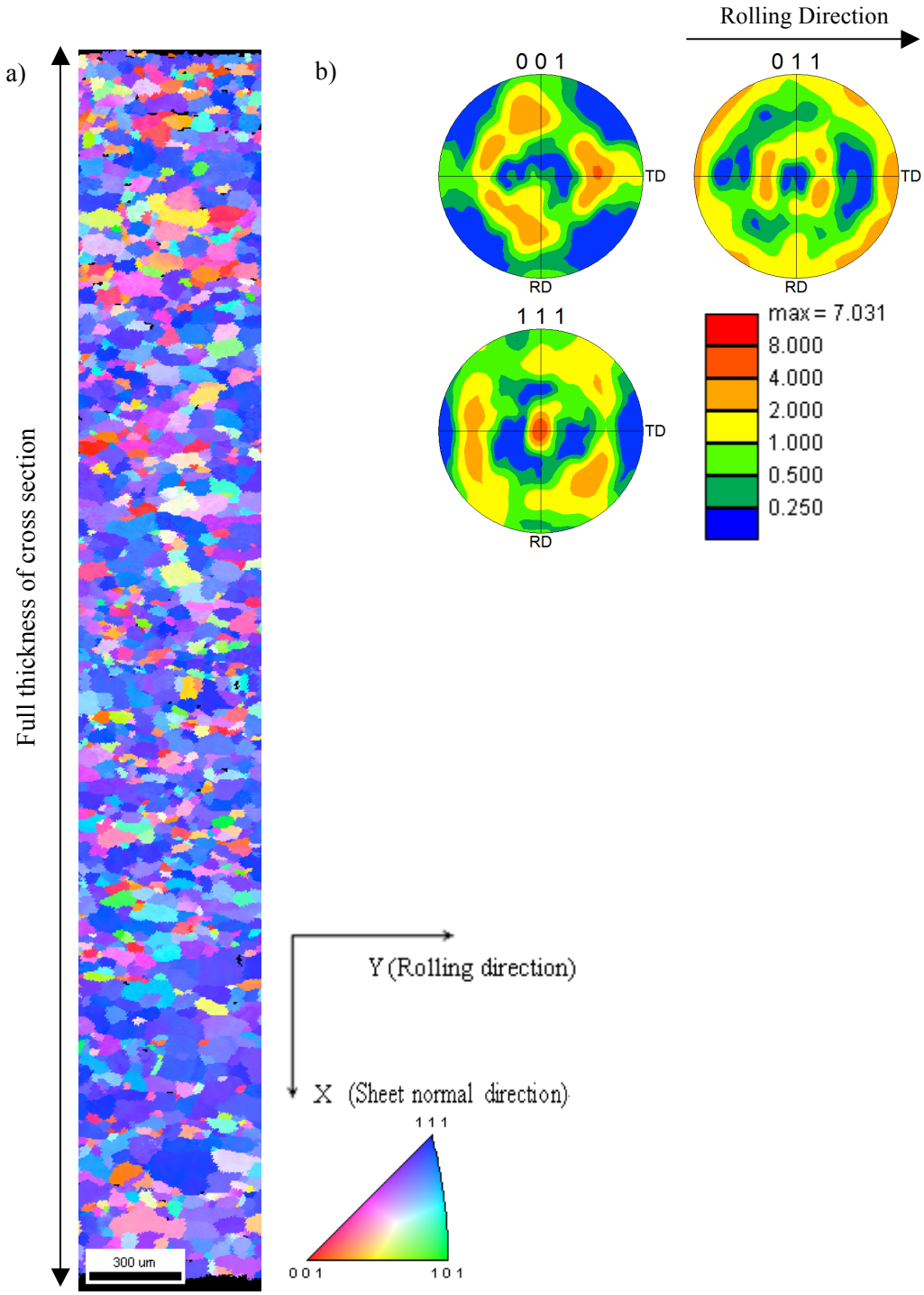

Figure C. 5: a) IPF map and b) PF of niobium sheet Lot 4491 #8 with thickness 4mm.

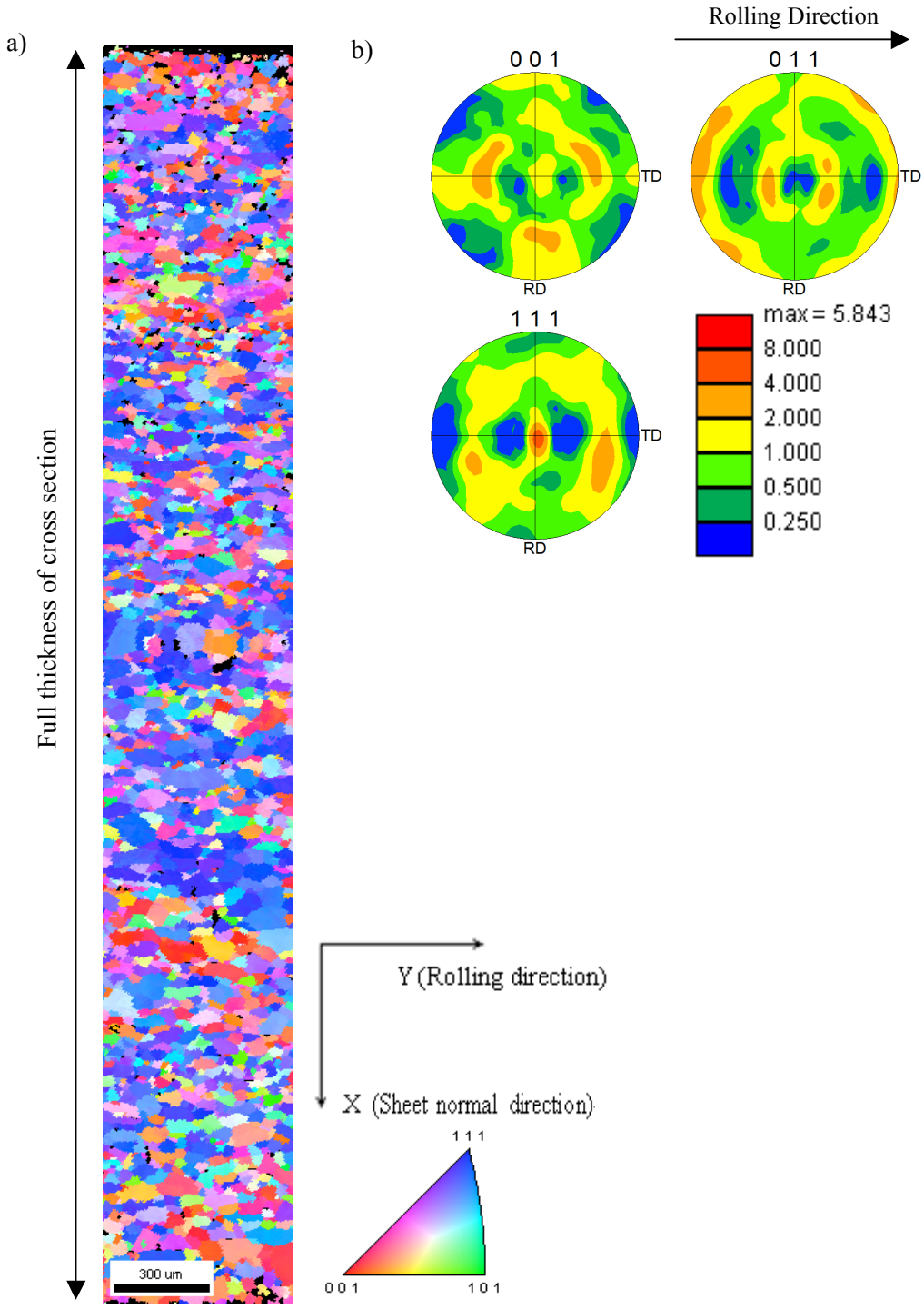

Figure C. 6: a) IPF map and b) PF of niobium sheet Lot 4492 #12 with thickness 4mm.

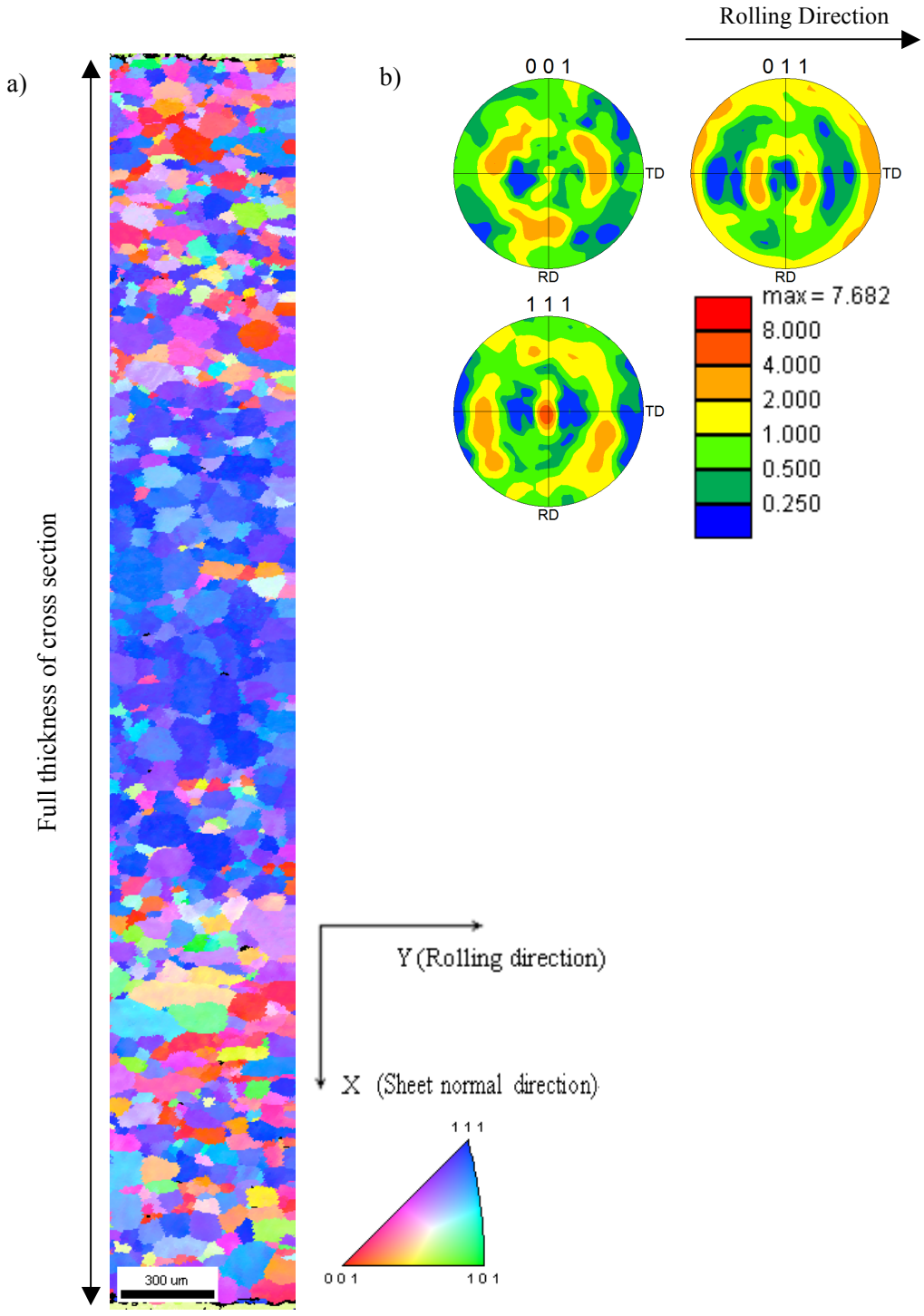

Figure C. 7: a) IPF map and b) PF of niobium sheet Lot 4495 #35 with thickness 4mm.

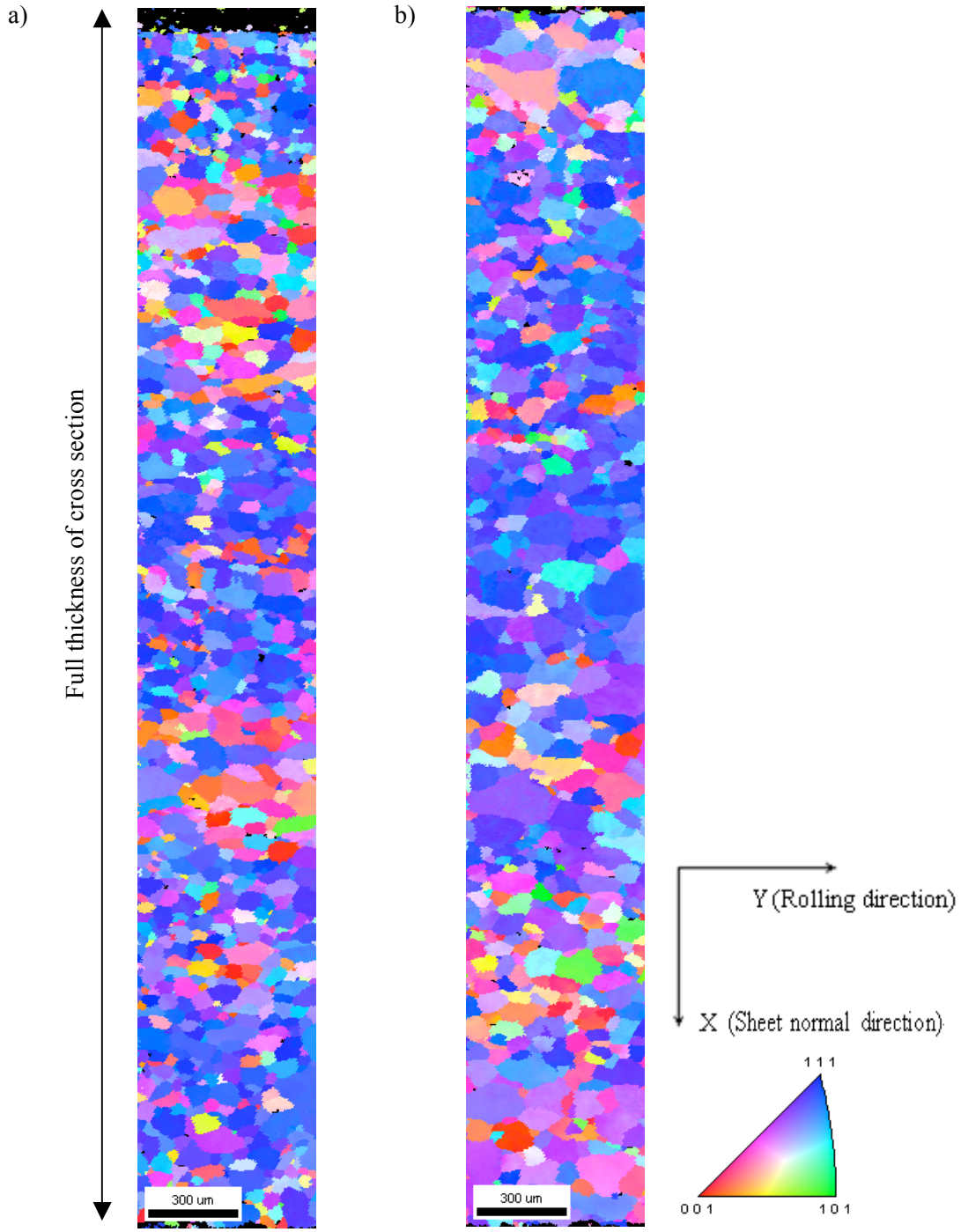

Figure C. 8: IPF maps of niobium sheet Lot 4496 a) #40, b) #46 from left to right respectively with thickness 4mm.

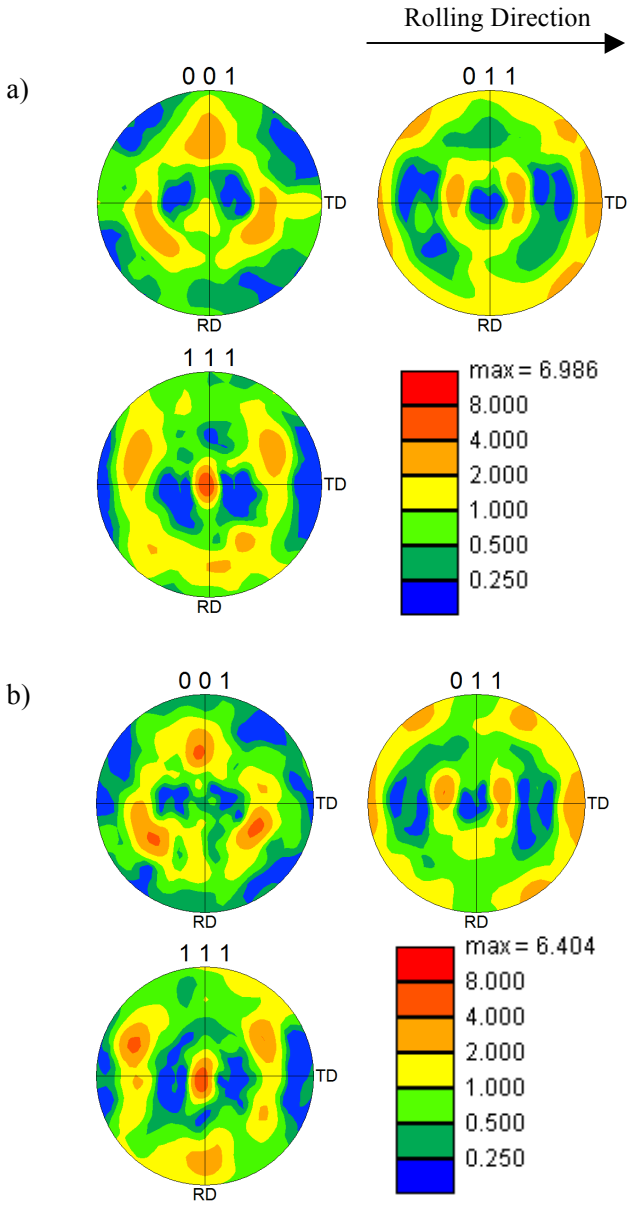

Figure C. 9: PFs of niobium sheet Lot 4496 a) #40, b) #46 from top to bottom respectively.

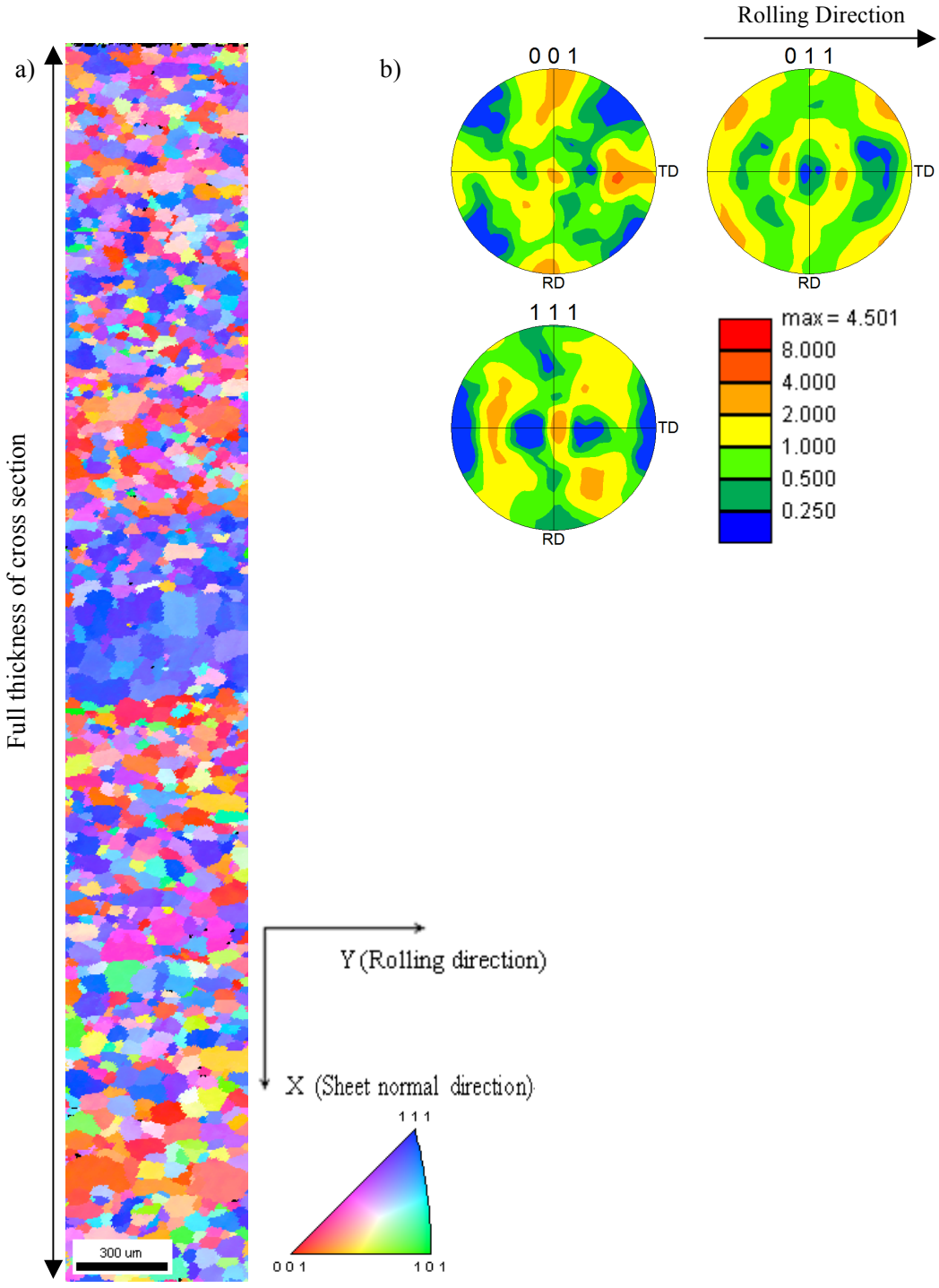

Figure C. 10: a) IPF map and b) PF of niobium sheet Lot 4497 #51 with thickness 4mm.

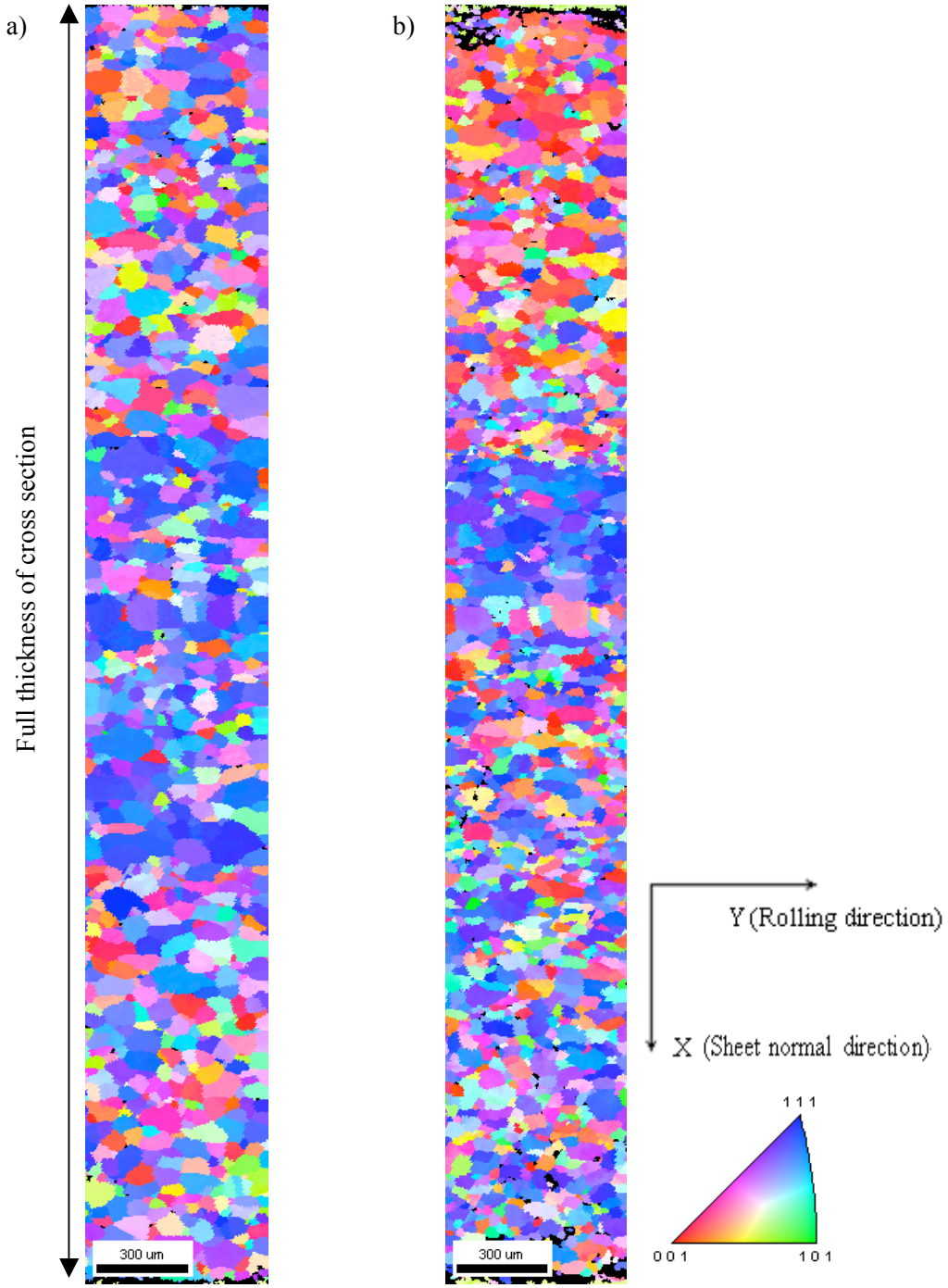

Figure C. 11: IPF maps of niobium sheet Lot 4498 a) #57, b) #65 from left to right respectively with thickness 4mm.

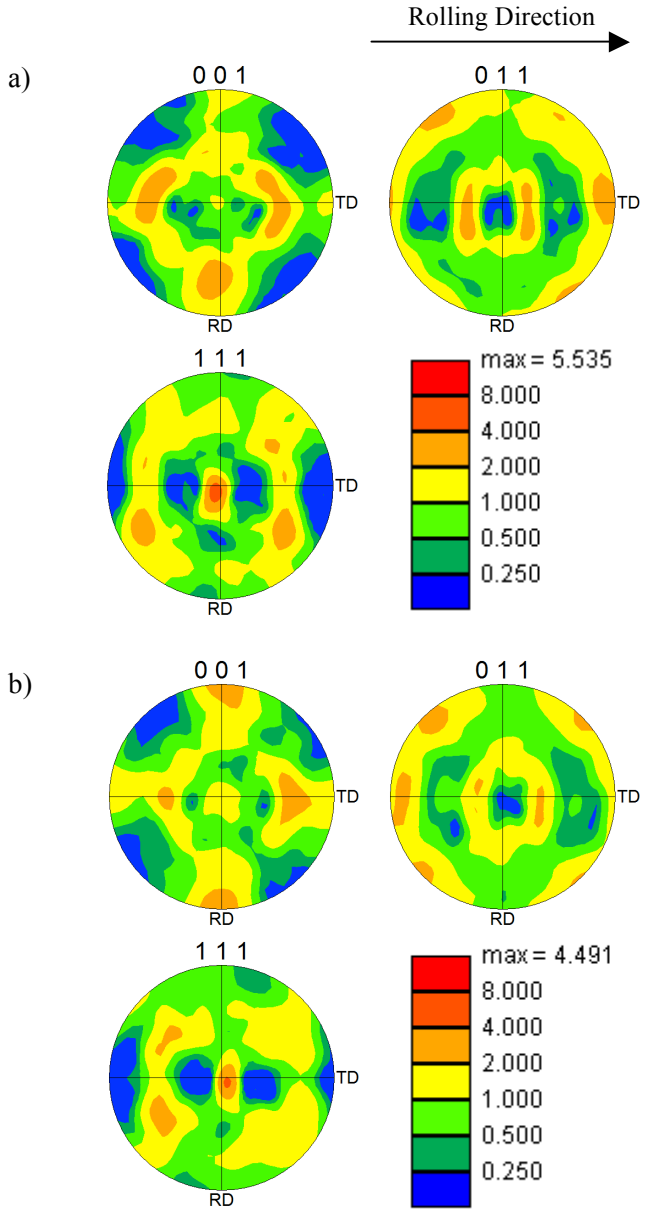

Figure C. 12: PFs of niobium sheet Lot 4498 a) #57, b) #65 from top to bottom respectively.

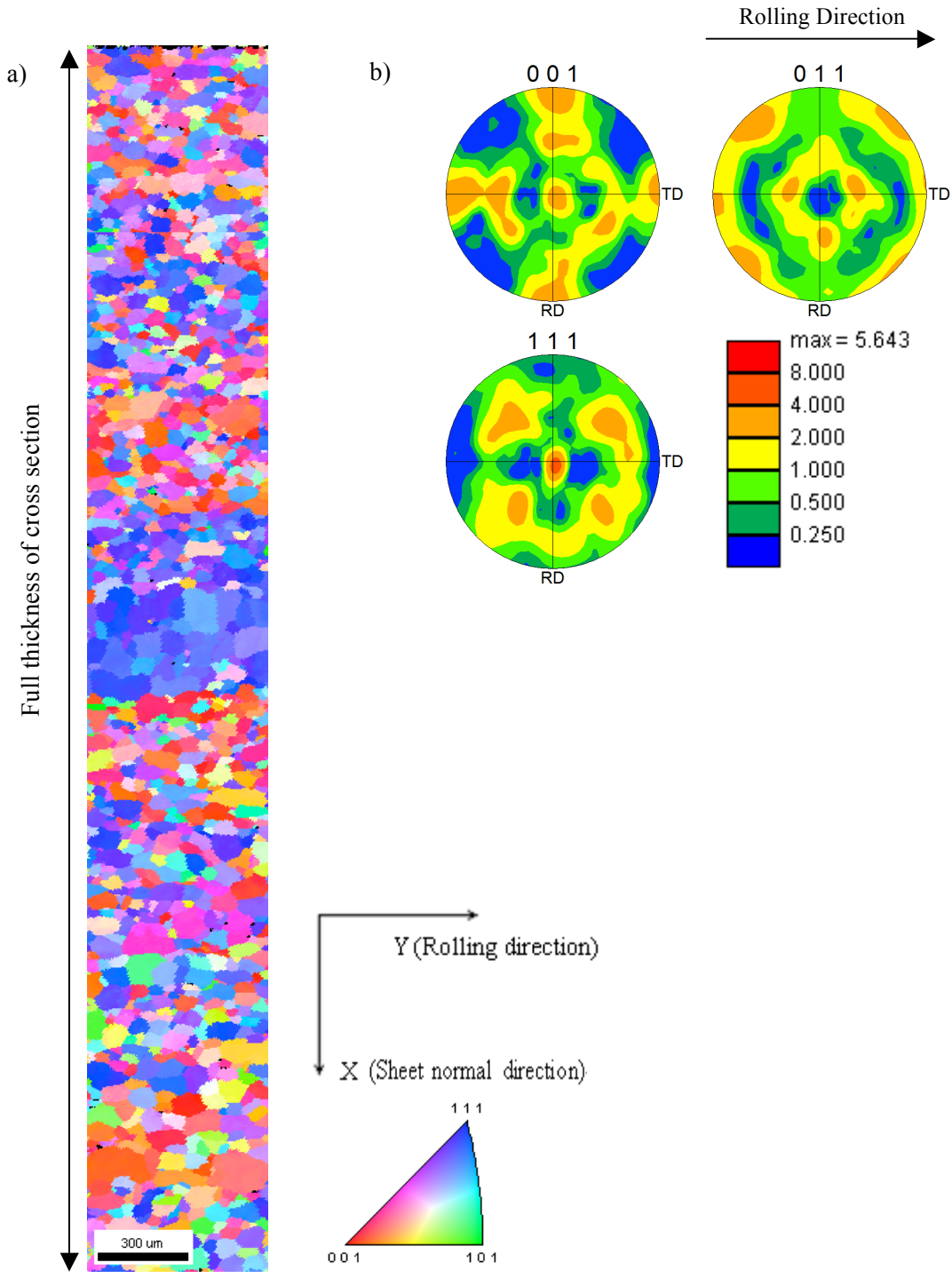

Figure C. 13: a) IPF map and b) PF of niobium sheet Lot 4499 #68 with thickness 4mm.

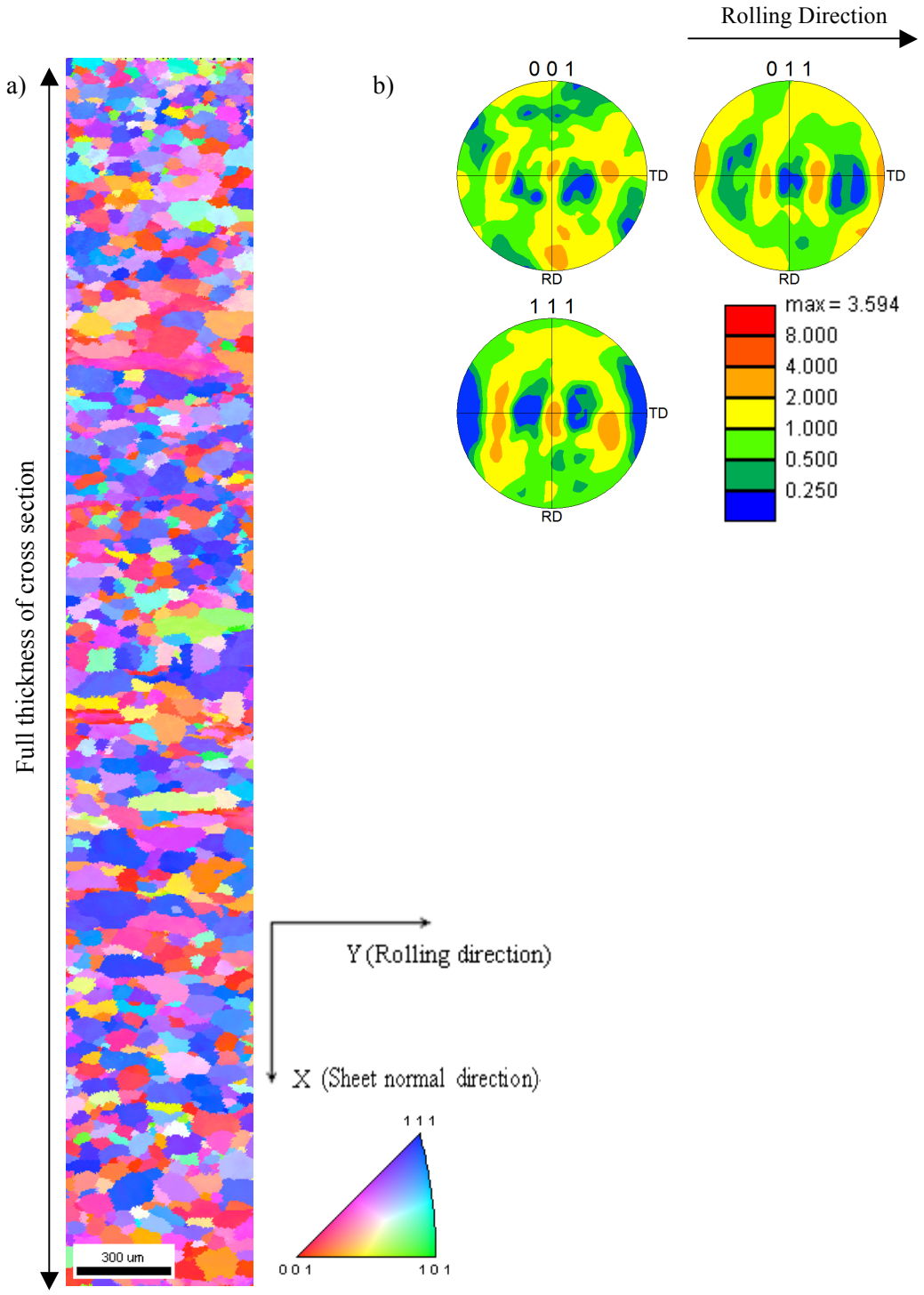

Figure C. 14: a) IPF map and b) PF of niobium sheet Lot 4500 #79 with thickness 4mm.

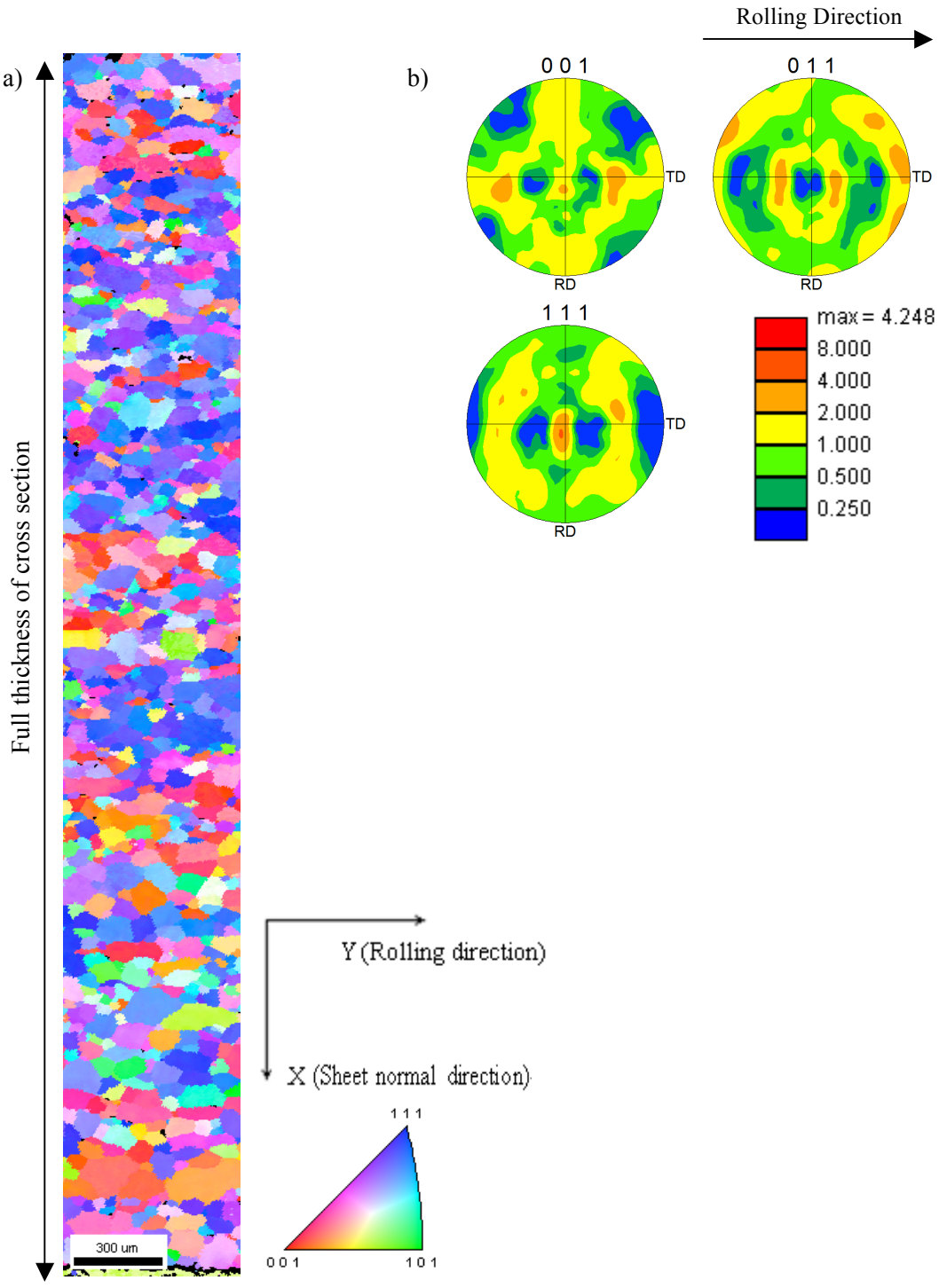

Figure C. 15: a) IPF map and b) PF of niobium sheet Lot 4501 #95 with thickness 4mm.

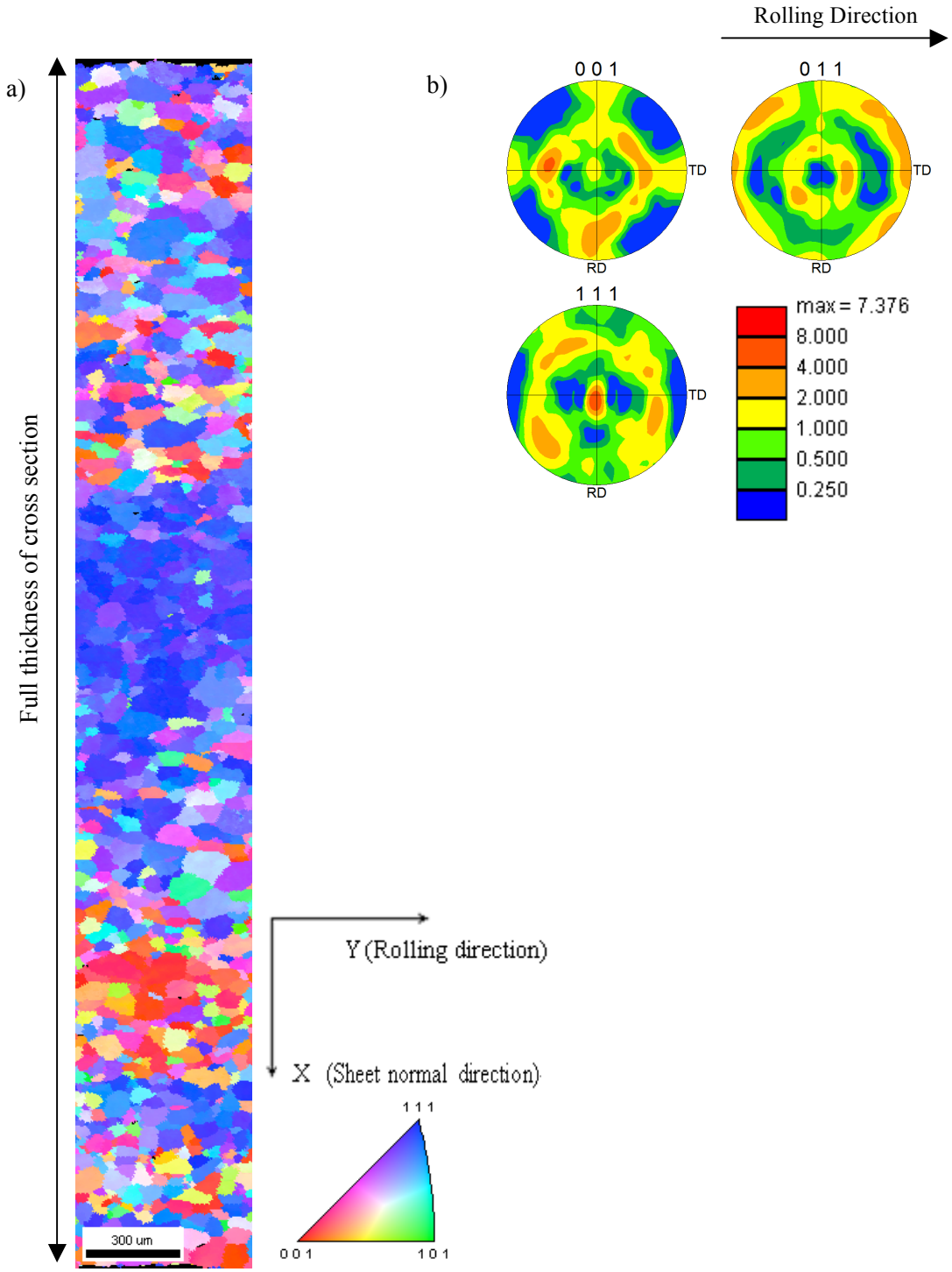

Figure C. 16: a) IPF map and b) PF of Niobium sheet Lot 4502 #102 with thickness 4mm.

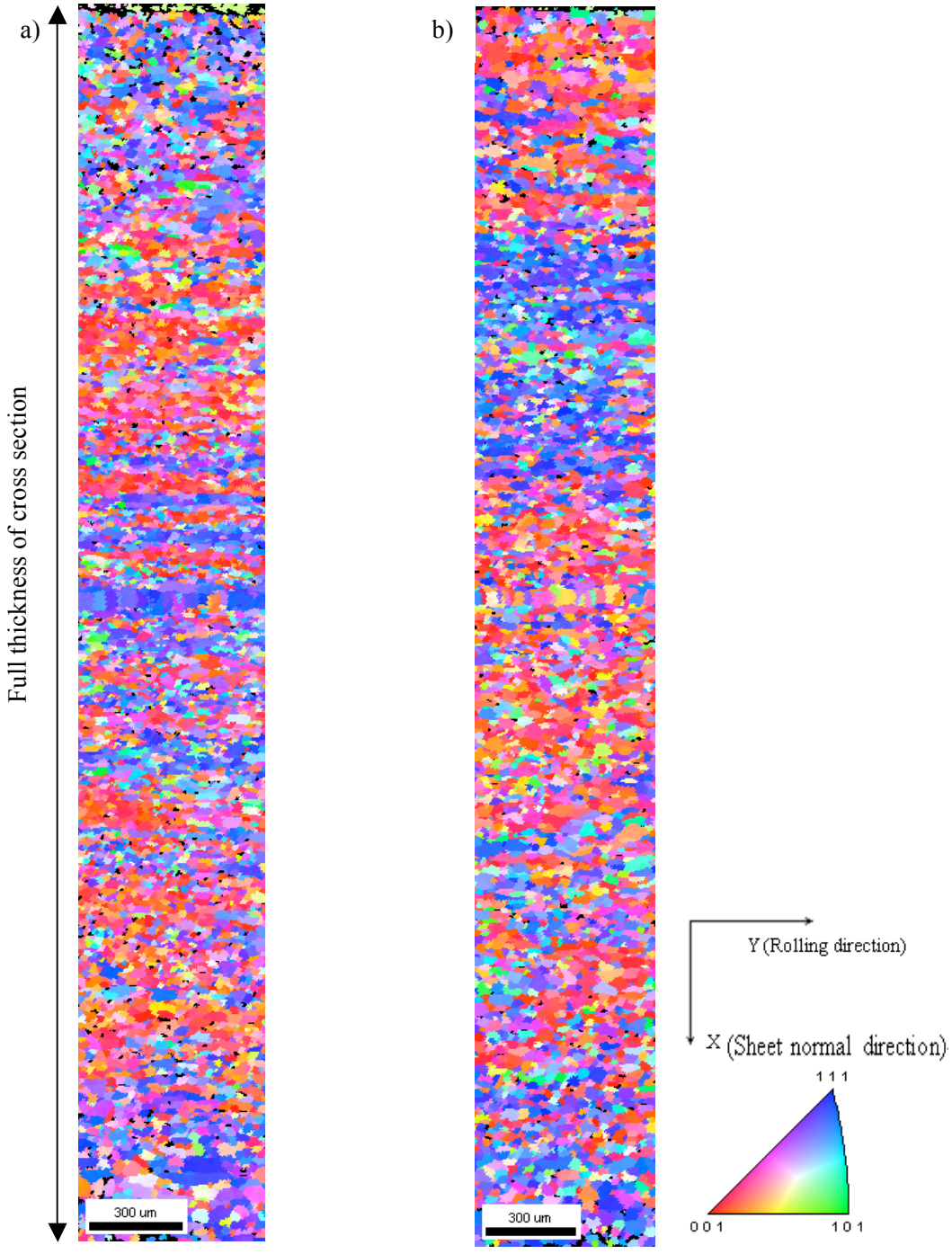

Figure C. 17: IPF maps of niobium sheet Lot 4503 a) #107, b) #114 from left to right respectively with thickness 4mm.

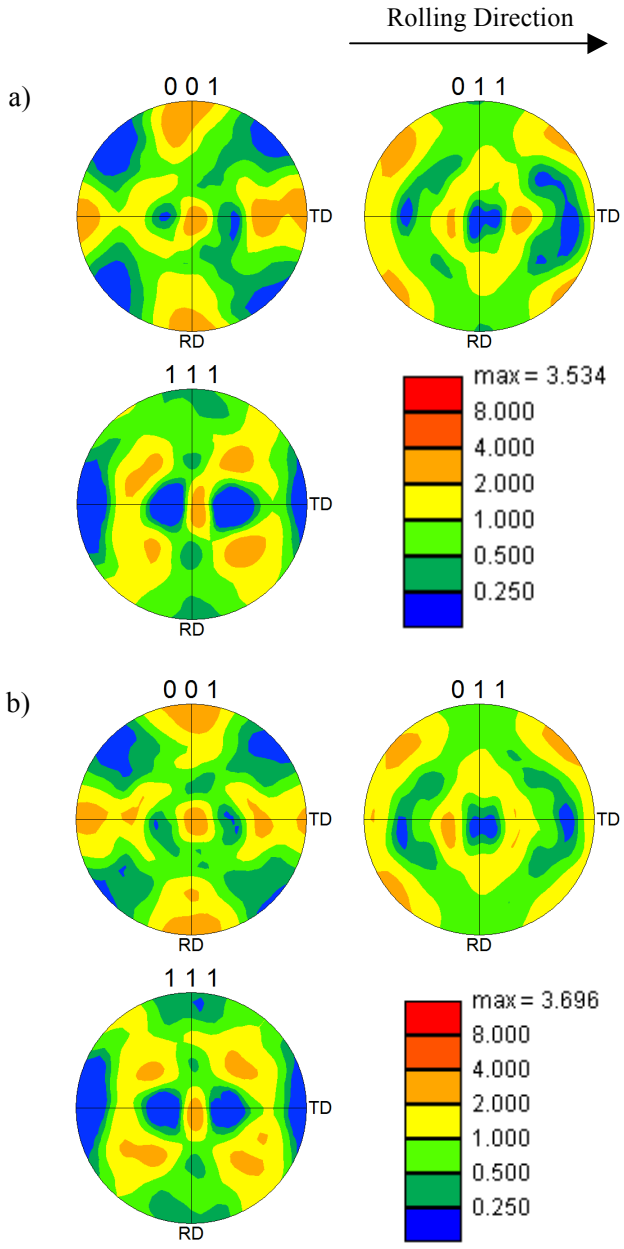

Figure C. 18: PFs of niobium sheet Lot 4503 a) #107, b) #114 from top to bottom respectively.

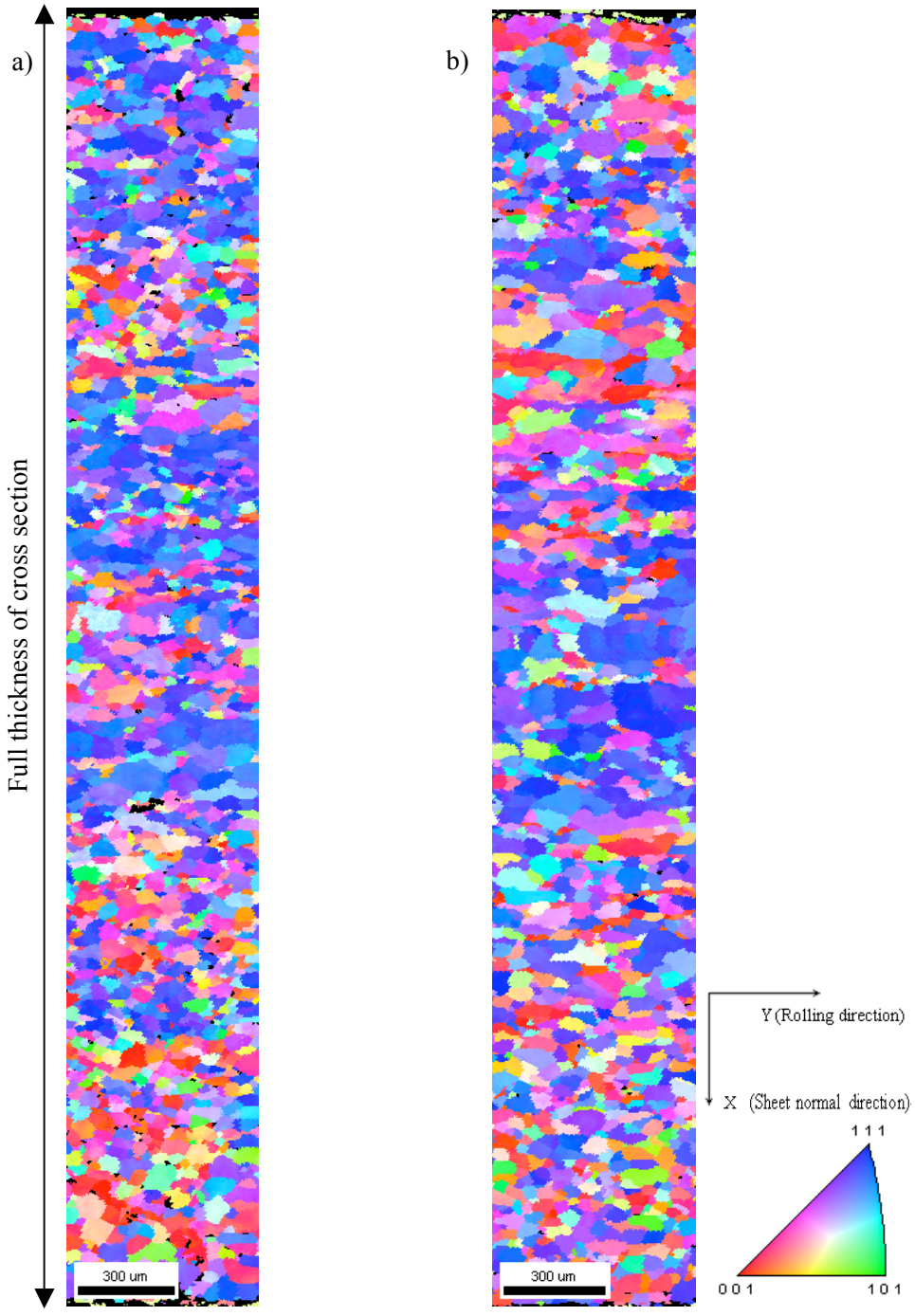

Figure C. 19: IPF maps of niobium sheet Lot 4504 a) #117, b) #122 from left to right respectively with thickness 4mm.

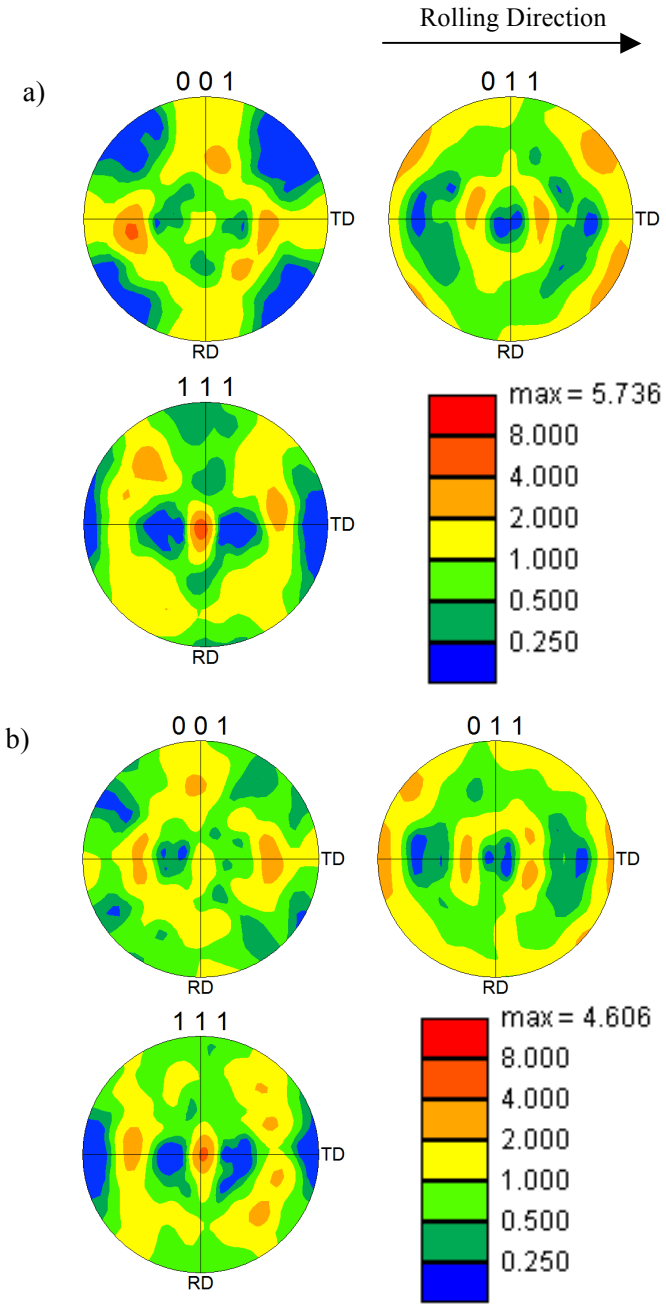

Figure C. 20: PFs of niobium sheet Lot 4504 a) #117, b) #122 from top to bottom respectively.

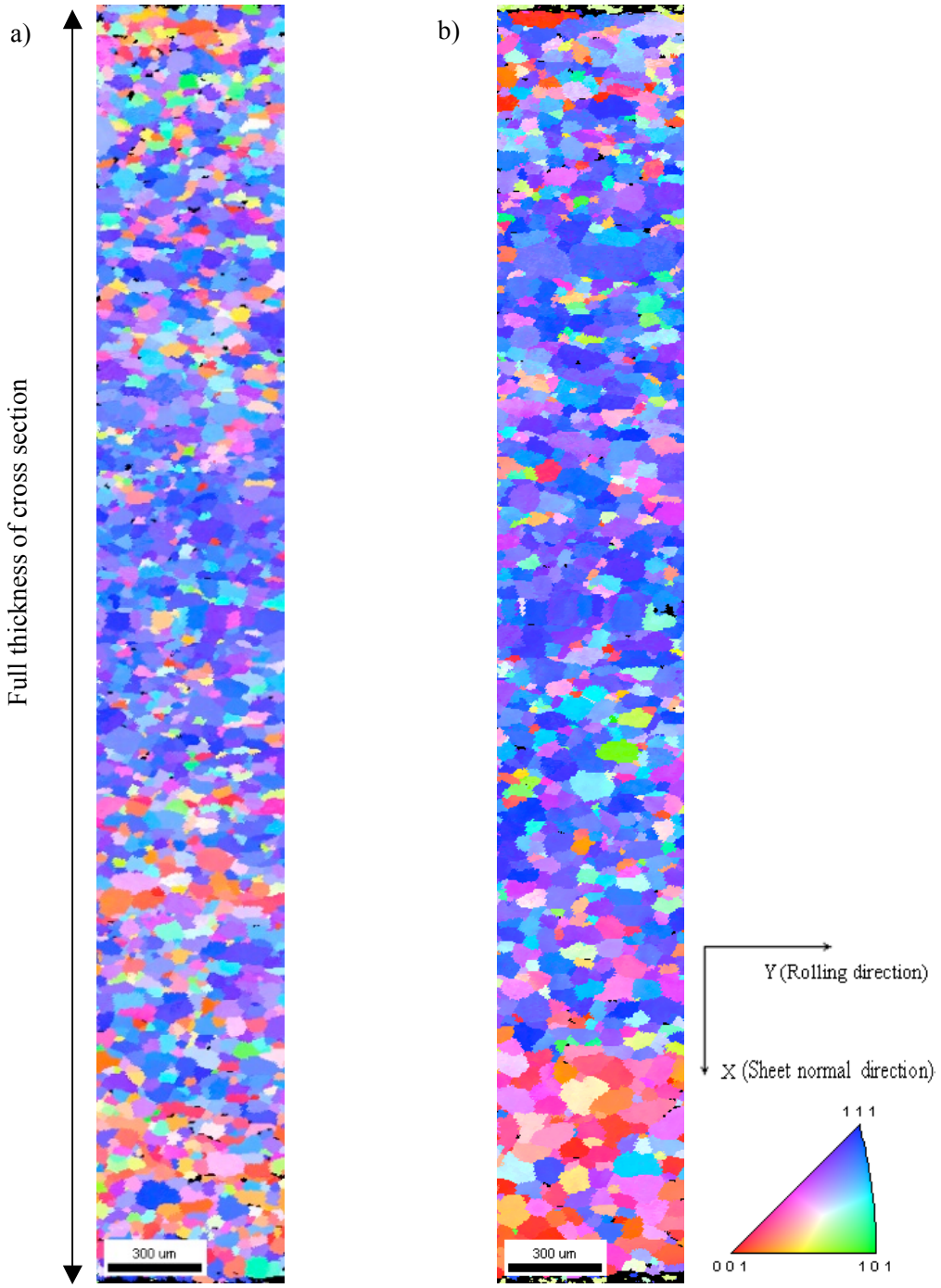

Figure C. 21: IPF maps of niobium sheet Lot 4505 a) #125, b) #130 from left to right respectively with thickness 4mm.

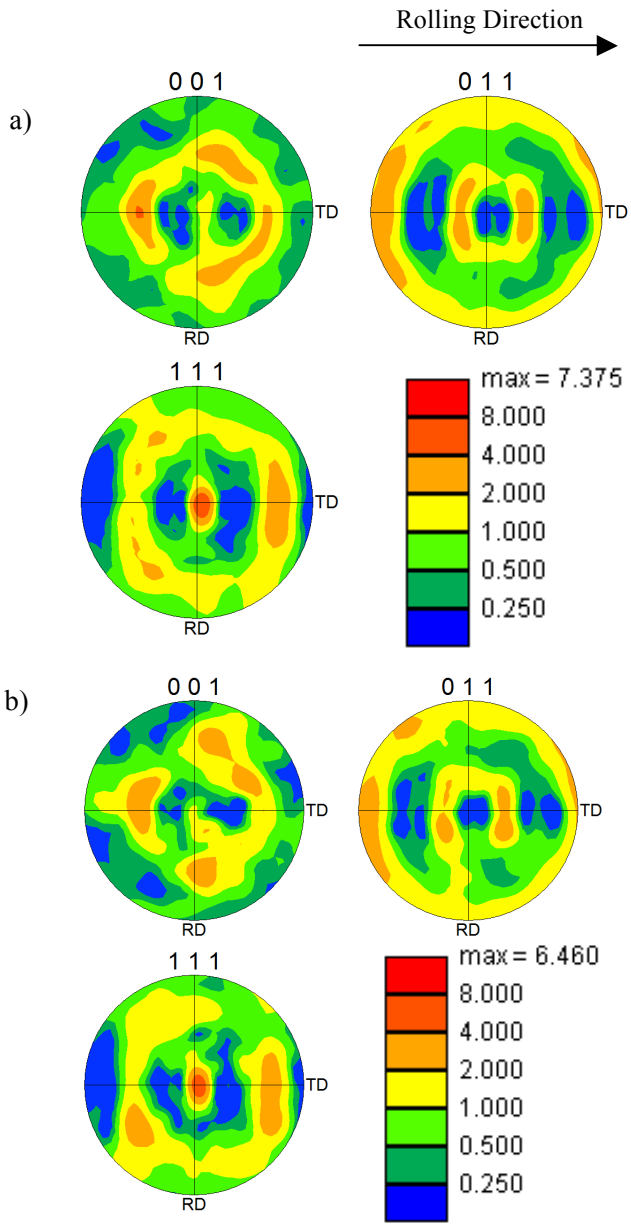

Figure C. 22: PFs of niobium sheet Lot 4505 a) #125, b) #130 from top to bottom respectively.

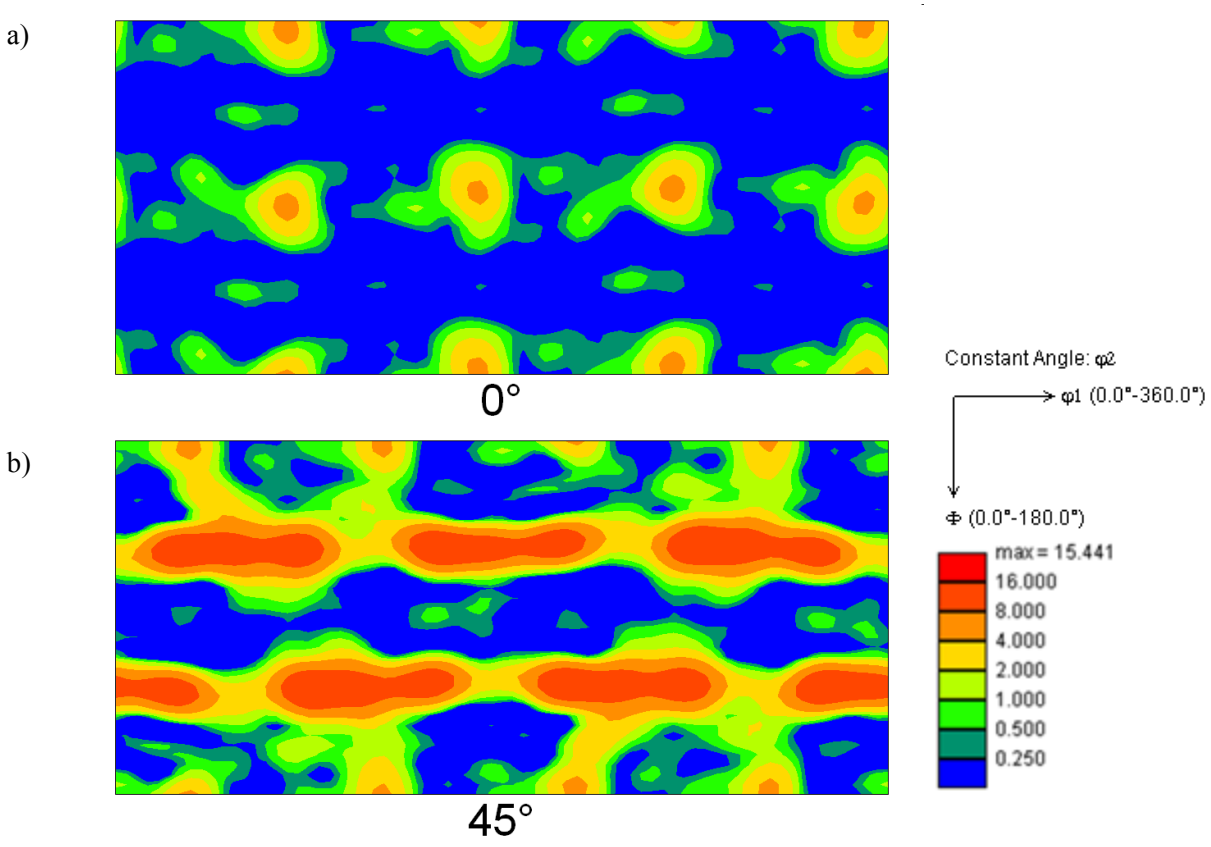

Figure C. 23: ODF plots ϕ_2 equals a) 0° and b) 45° for Lot 4481 #8 with thickness 3mm.

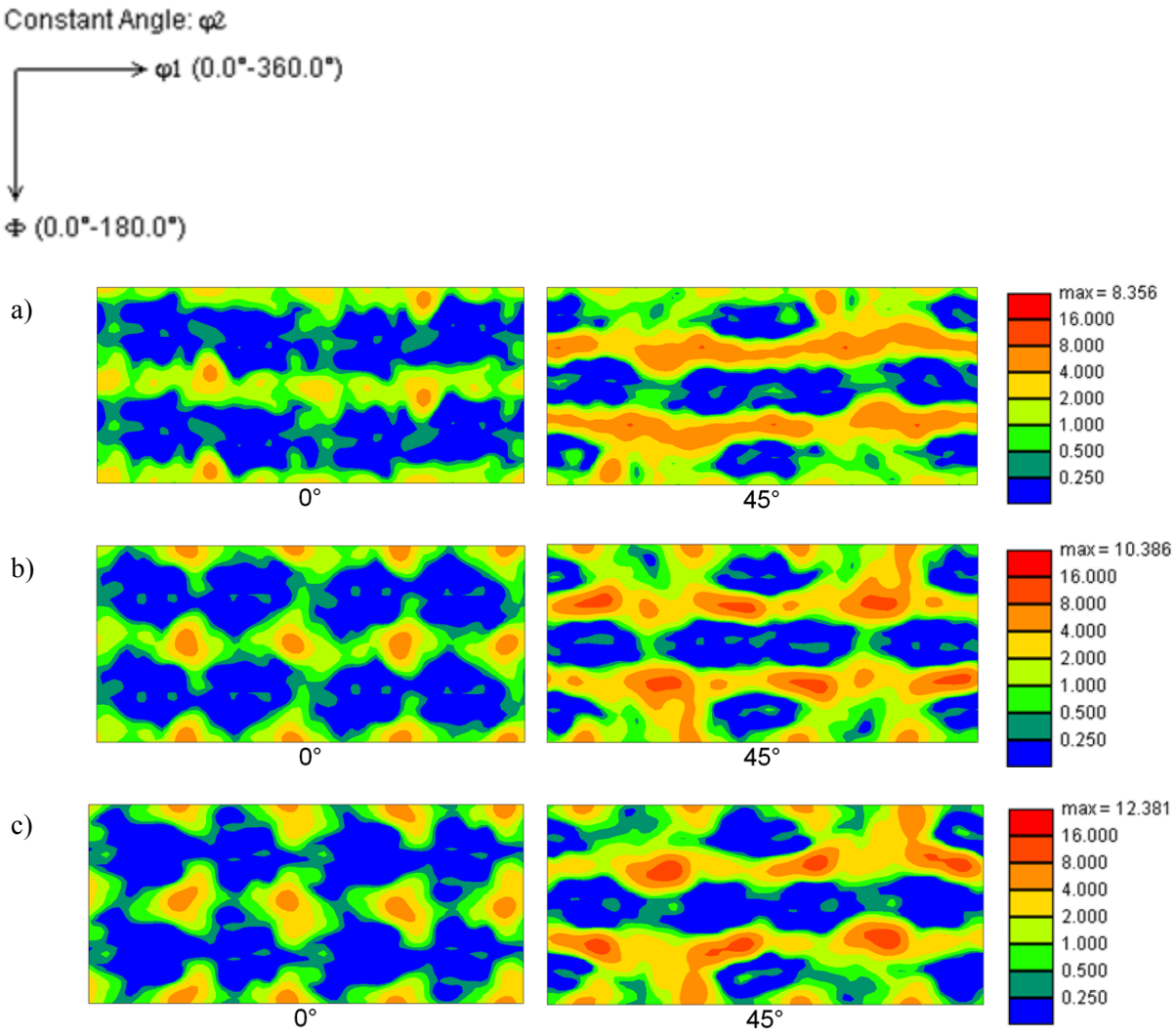

Figure C. 24: ODF plots when ϕ_2 equals 0° and 45° for Lot 4482 a) #22, b) #35, c) #55 with thickness of 3 mm from top to bottom respectively.

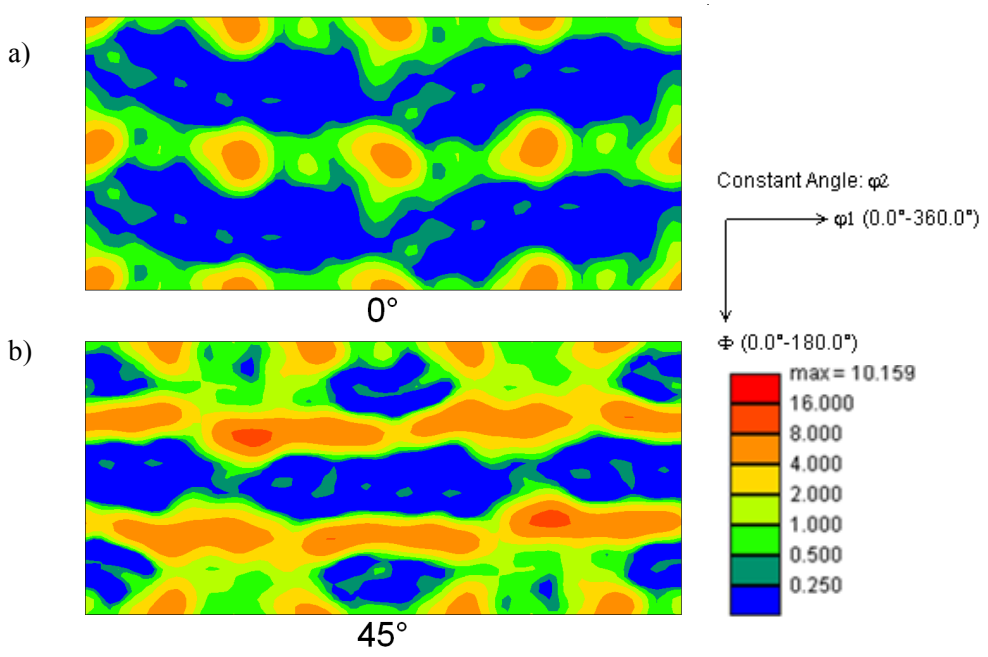

Figure C. 25: ODF plots when ϕ_2 equals a) 0° and b) 45° for Lot 4483 #3 with thickness 3mm.

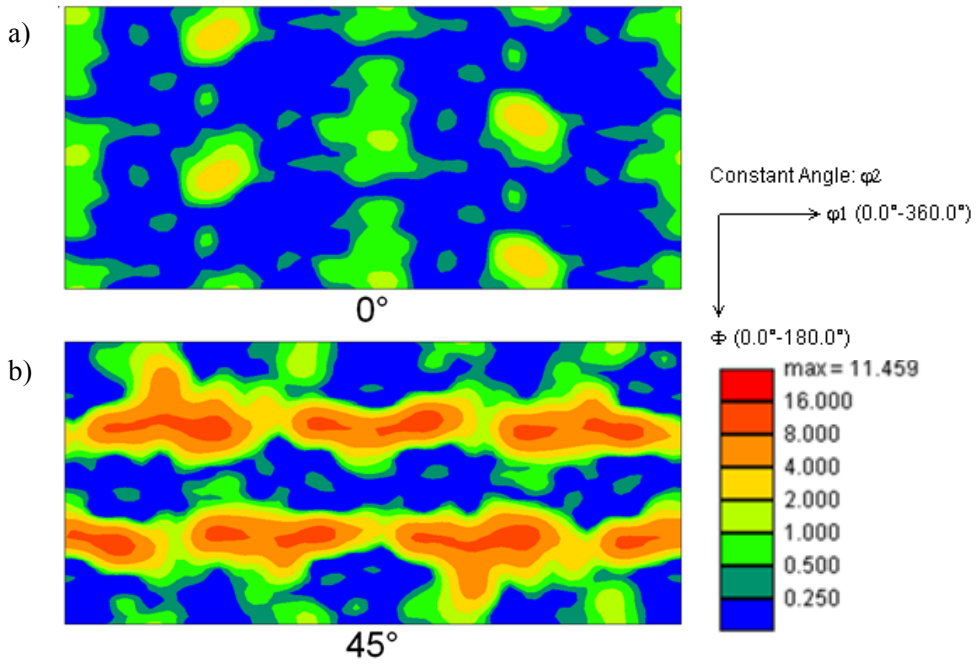

Figure C. 26: ODF plots when ϕ_2 equals a) 0° and b) 45° for Lot 4491 #8 with thickness 4mm.

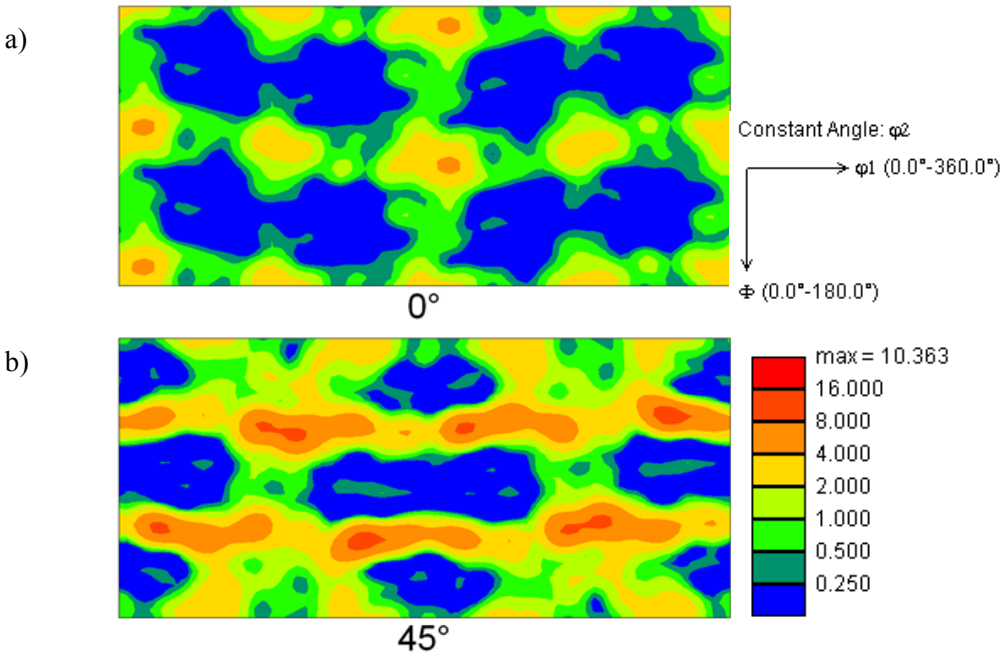

Figure C. 27: ODF plots when ϕ_2 equals a) 0° and b) 45° for Lot 4492 #12 with thickness 4mm.

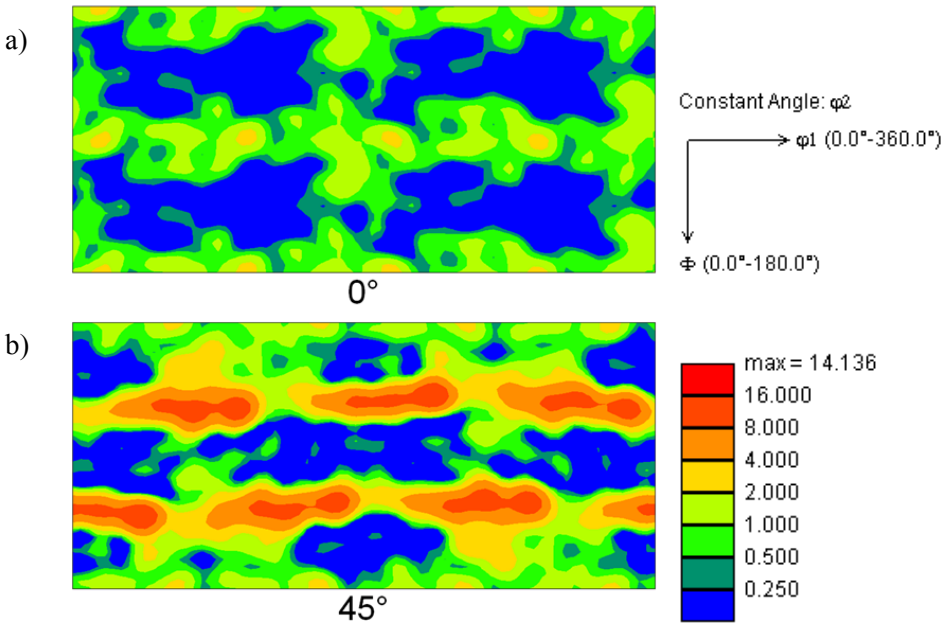

Figure C. 28: ODF plots when ϕ_2 equals a) 0° and b) 45° for Lot 4495 #35 with thickness 4mm.

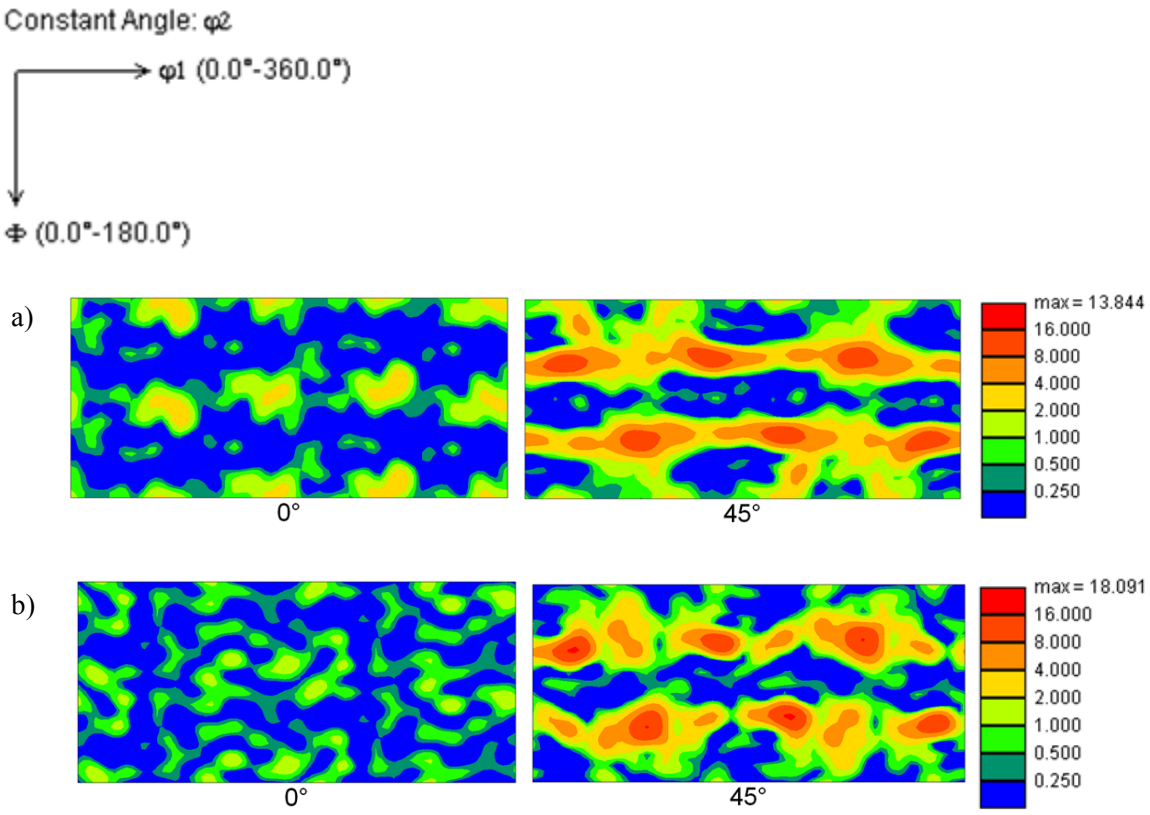

Figure C. 29: ODF plots when ϕ_2 equals 0° and 45° for Lot 4496 a) #40, b) #46 with thickness 4 mm from top to bottom respectively.

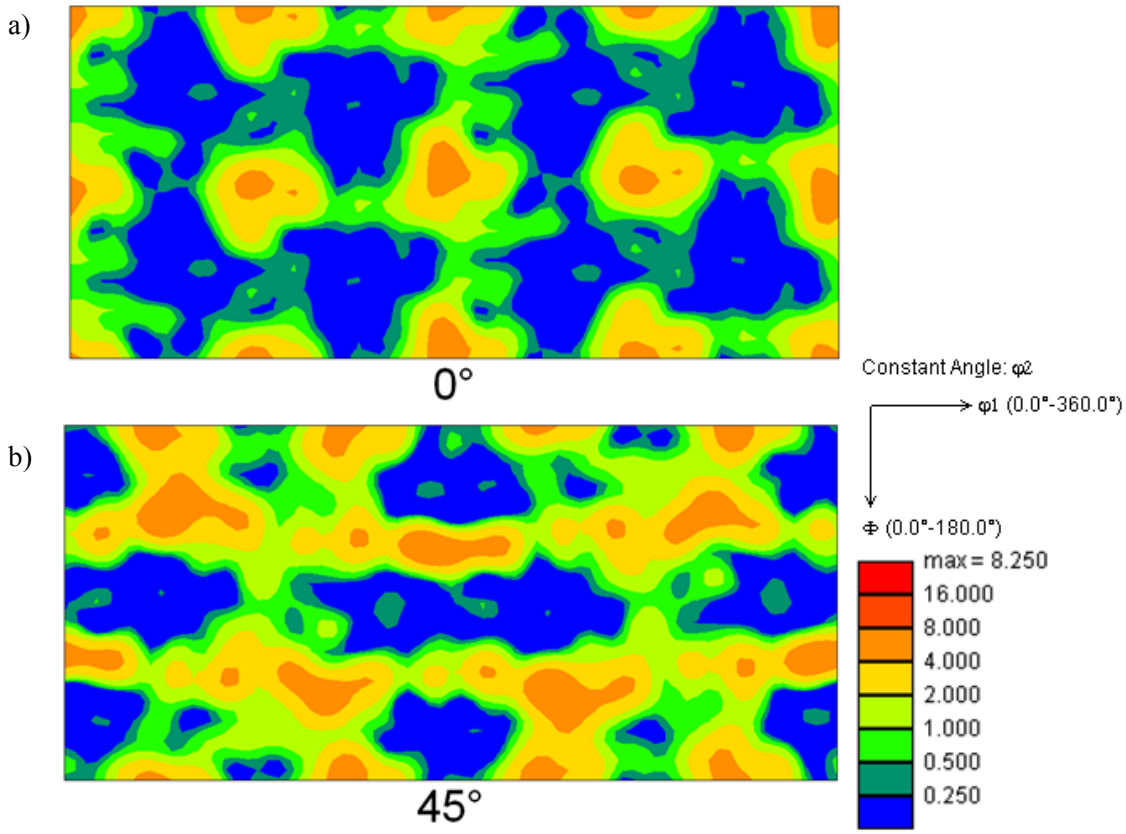

Figure C. 30: ODF plots when ϕ_2 equals a) 0° and b) 45° for Lot 4497 #51 with thickness 4mm.

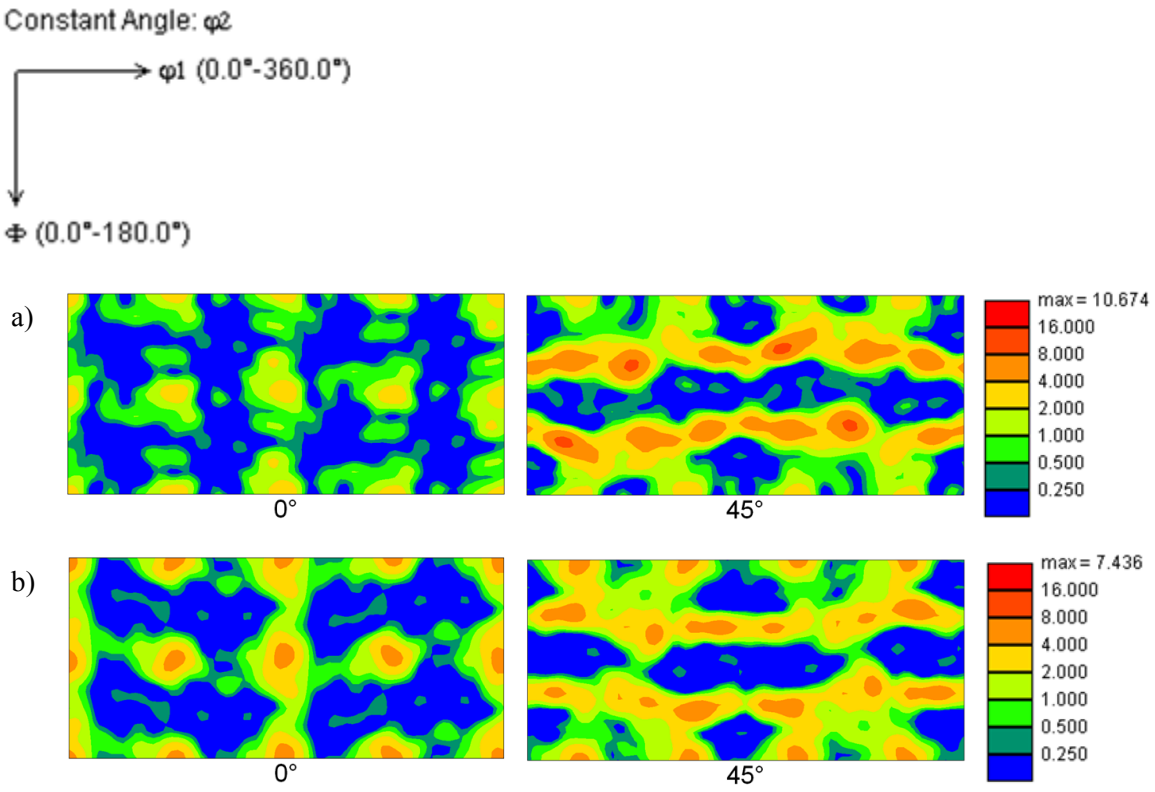

Figure C. 31: ODF plots when ϕ_2 equals 0° and 45° for Lot 4498 a) #57, b) #65 with thickness 4 mm from top to bottom respectively.

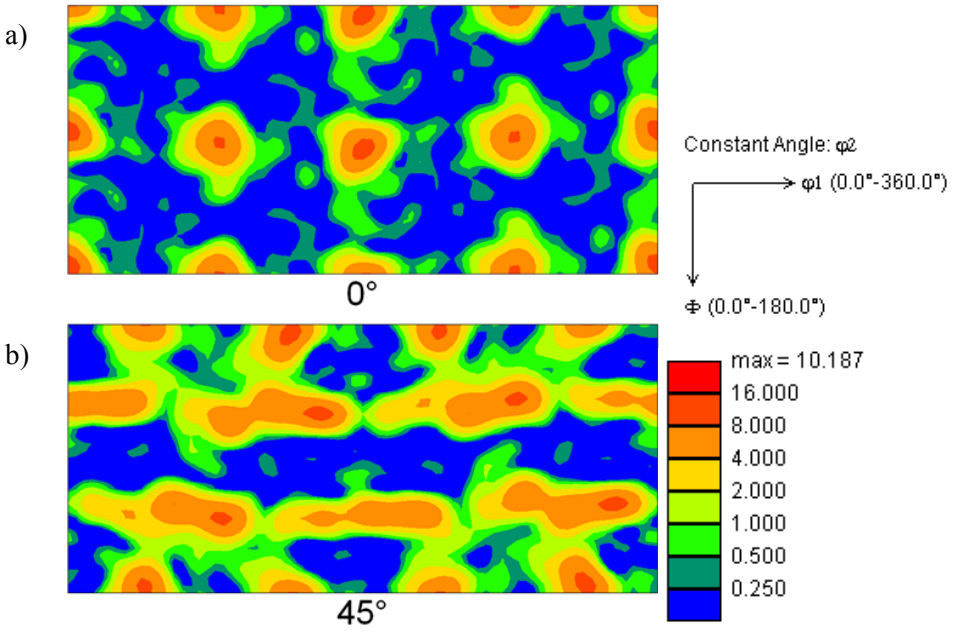

Figure C. 32: ODF plots when ϕ_2 equals a) 0° and b) 45° for Lot 4499 #68 with thickness 4mm.

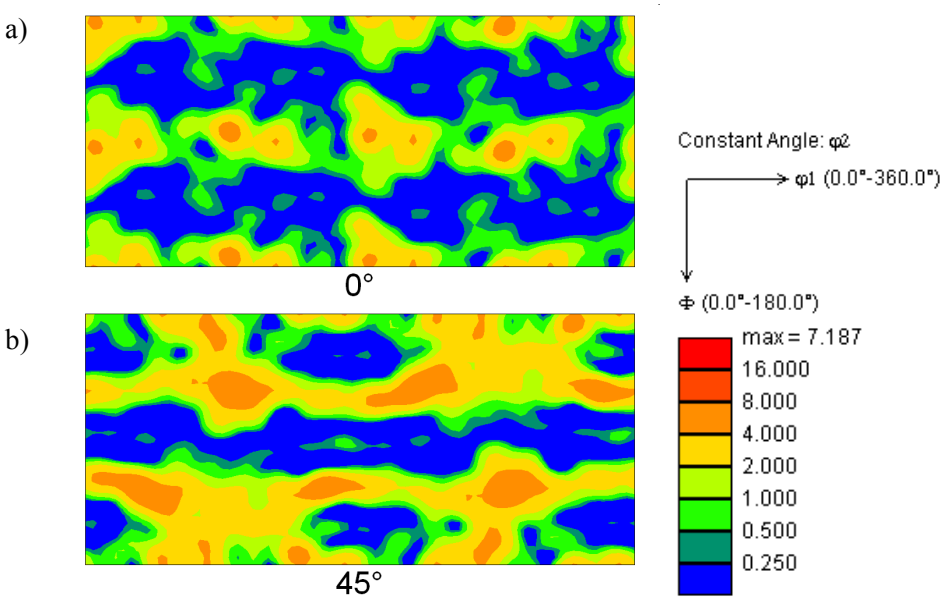

Figure C. 33: ODF plots when ϕ_2 equals a) 0° and b) 45° for Lot 4500 #79 with thickness 4mm.

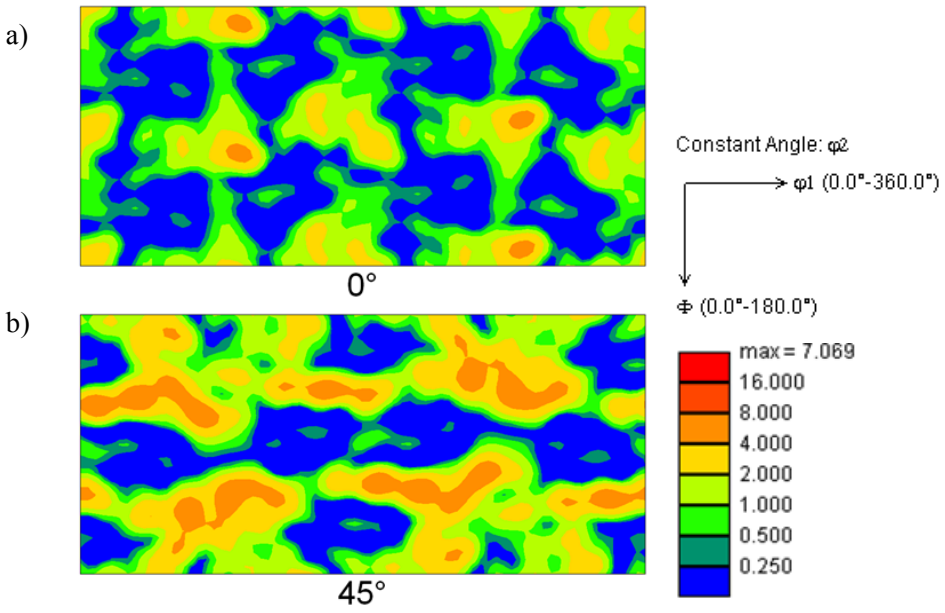

Figure C. 34: ODF plots when ϕ_2 equals a) 0° and b) 45° for Lot 4501 #95 with thickness 4mm.

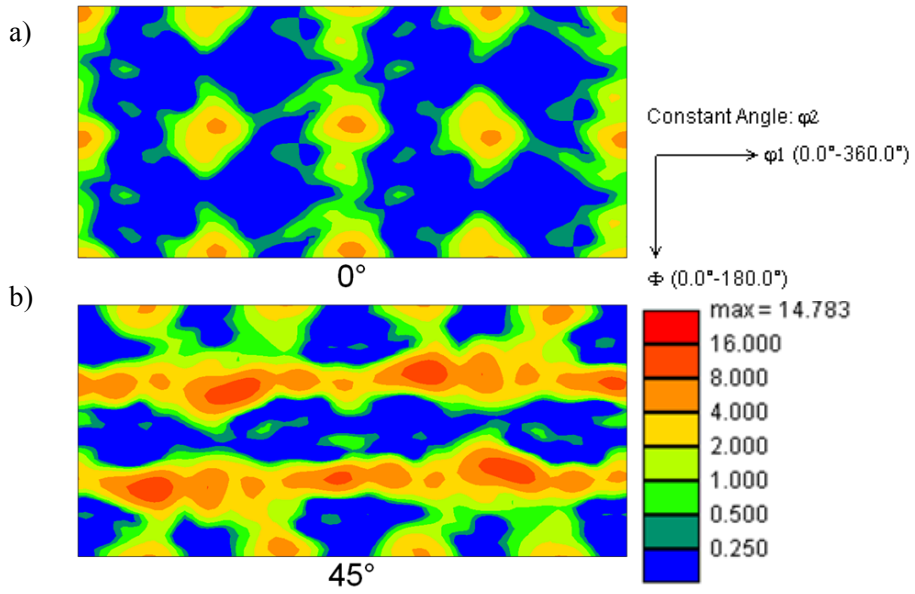

Figure C. 35: ODF plots when ϕ_2 equals a) 0° and b) 45° for Lot 4502 #102 with thickness 4mm.

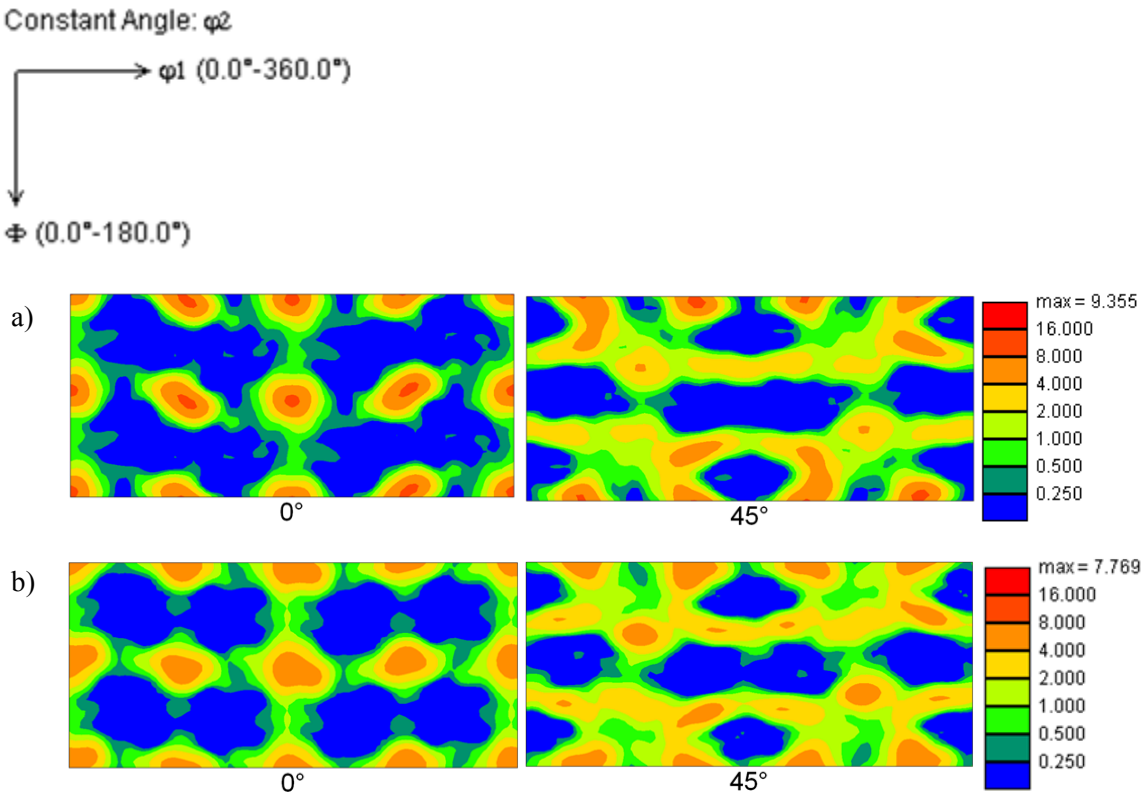

Figure C. 36: ODF plots when ϕ_2 equals 0° and 45° for Lot 4503 a) #107, b) #114 with thickness 4 mm from top to bottom respectively.

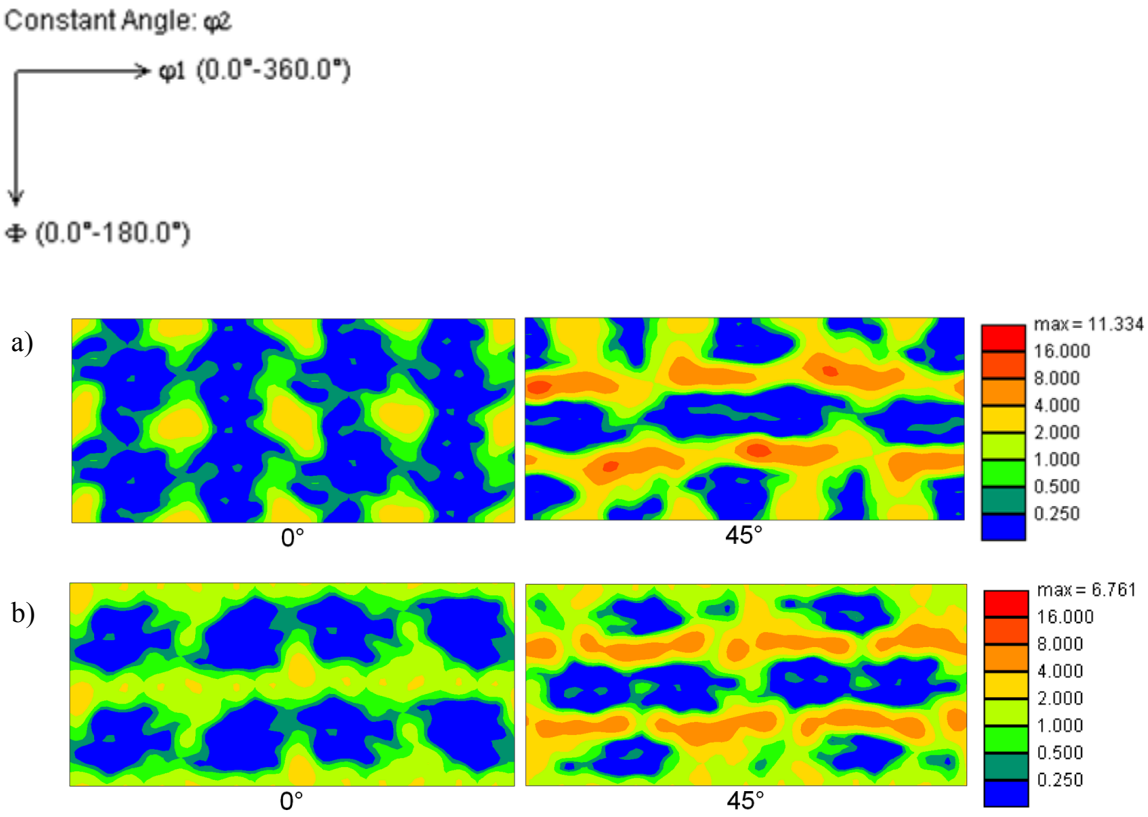

Figure C. 37: ODF plots when ϕ_2 equals 0° and 45° for Lot 4504 a) #117, b) #122 with thickness 4 mm from top to bottom respectively.

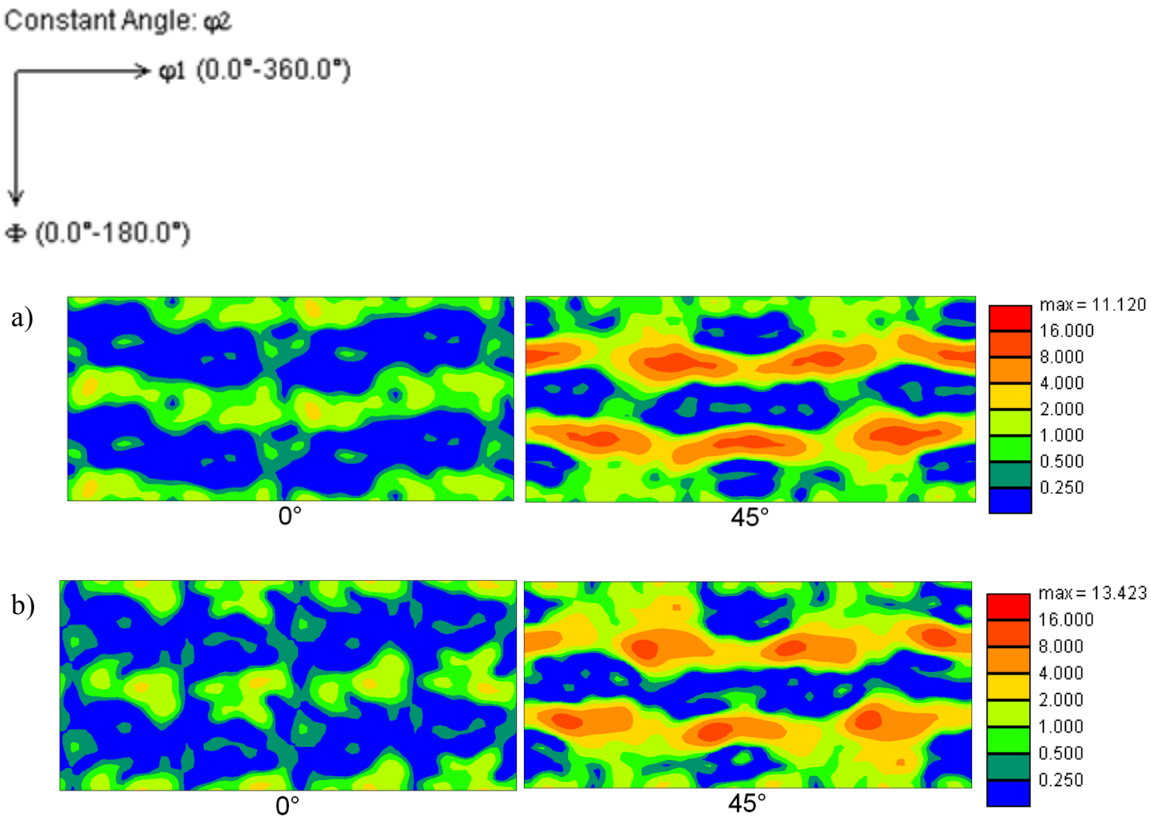

Figure C. 38: ODF plots when ϕ_2 equals 0° and 45° for Lot 4505 a) #125, b) #130 with thickness 4 mm from top to bottom respectively.

Appendix D: IPF map, PF and ODF plots of ϕ_2 equals 0° and 45° for samples from Ningxia. (EBSD scans done by Di Kang)

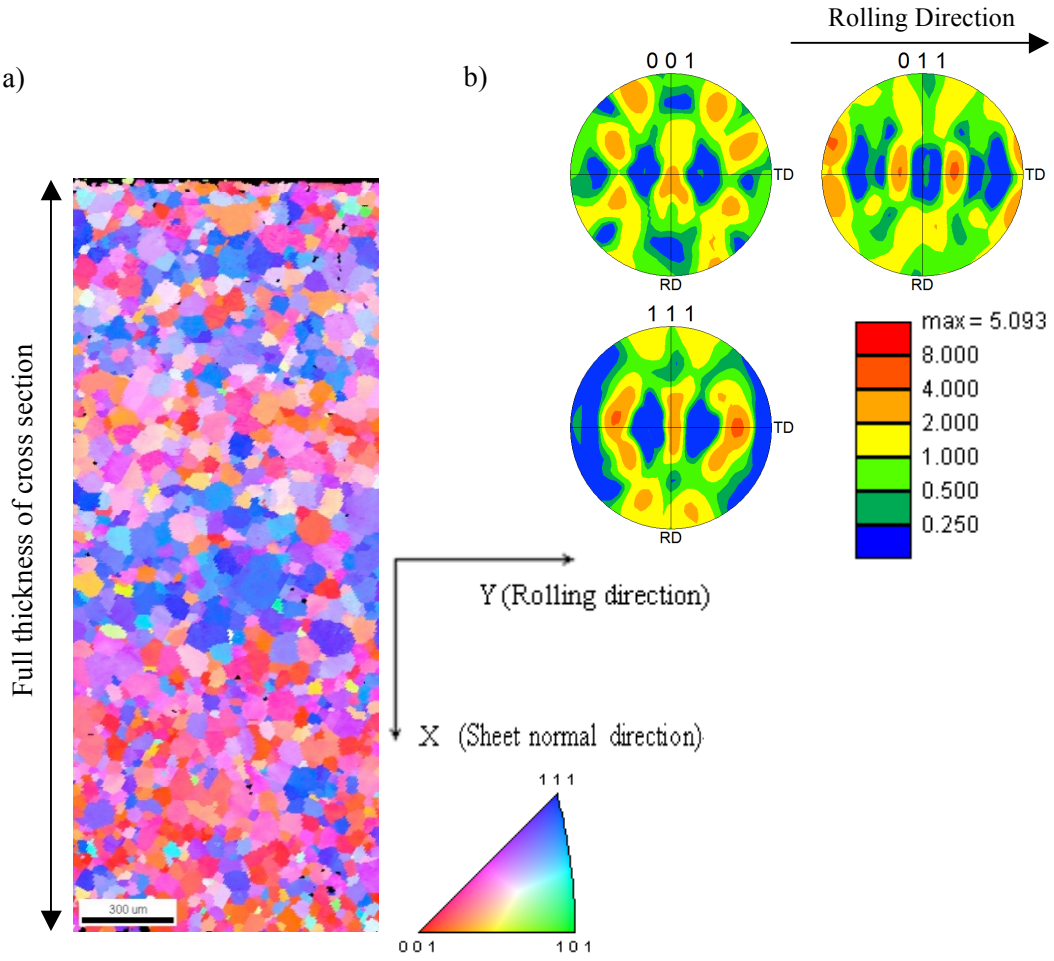

Figure D. 1: a) IPF map and b) PF of niobium sheet 130202-25-02 #6 with thickness 2mm.

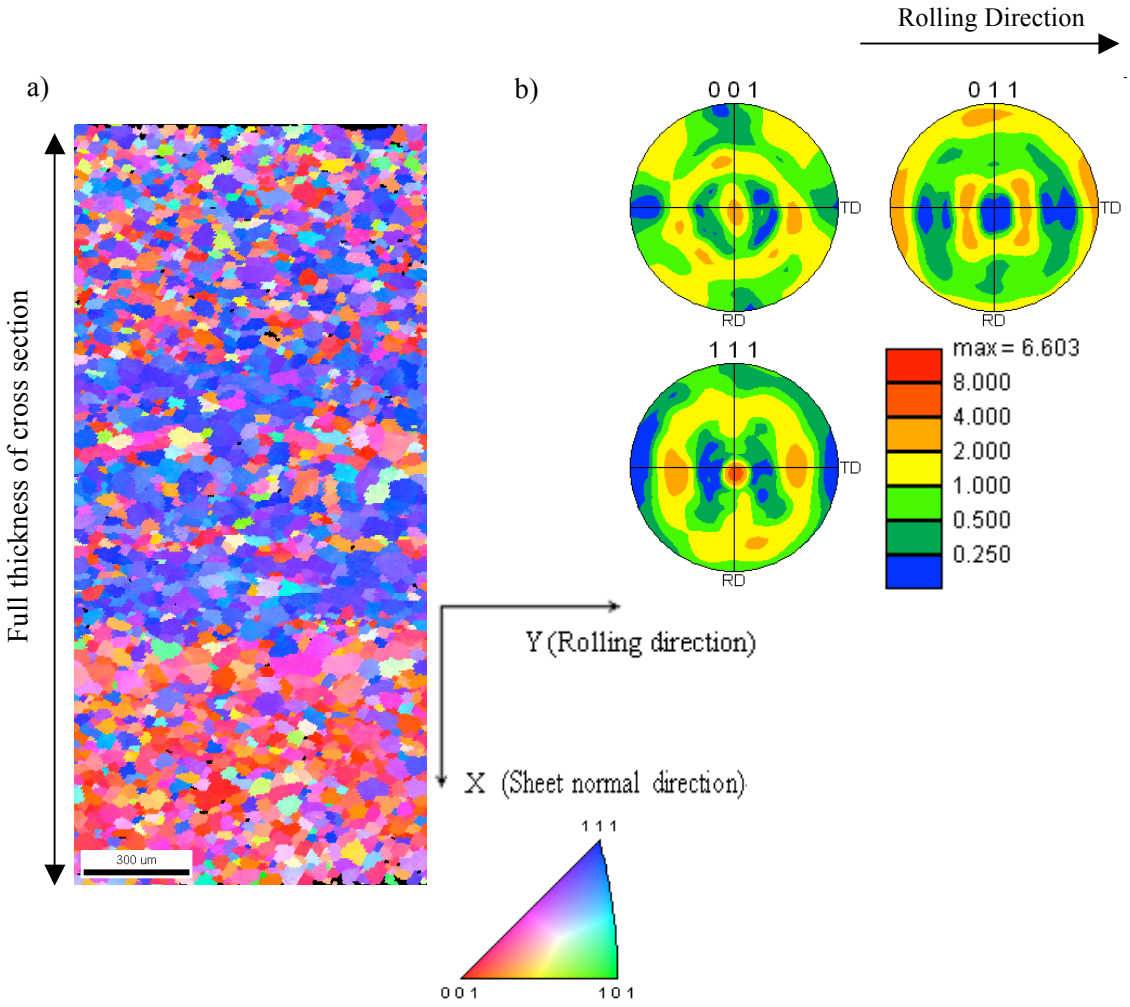

Figure D. 2: a) IPF map and b) PF of niobium sheet 130517-FW501-02 #2 with thickness 2mm.

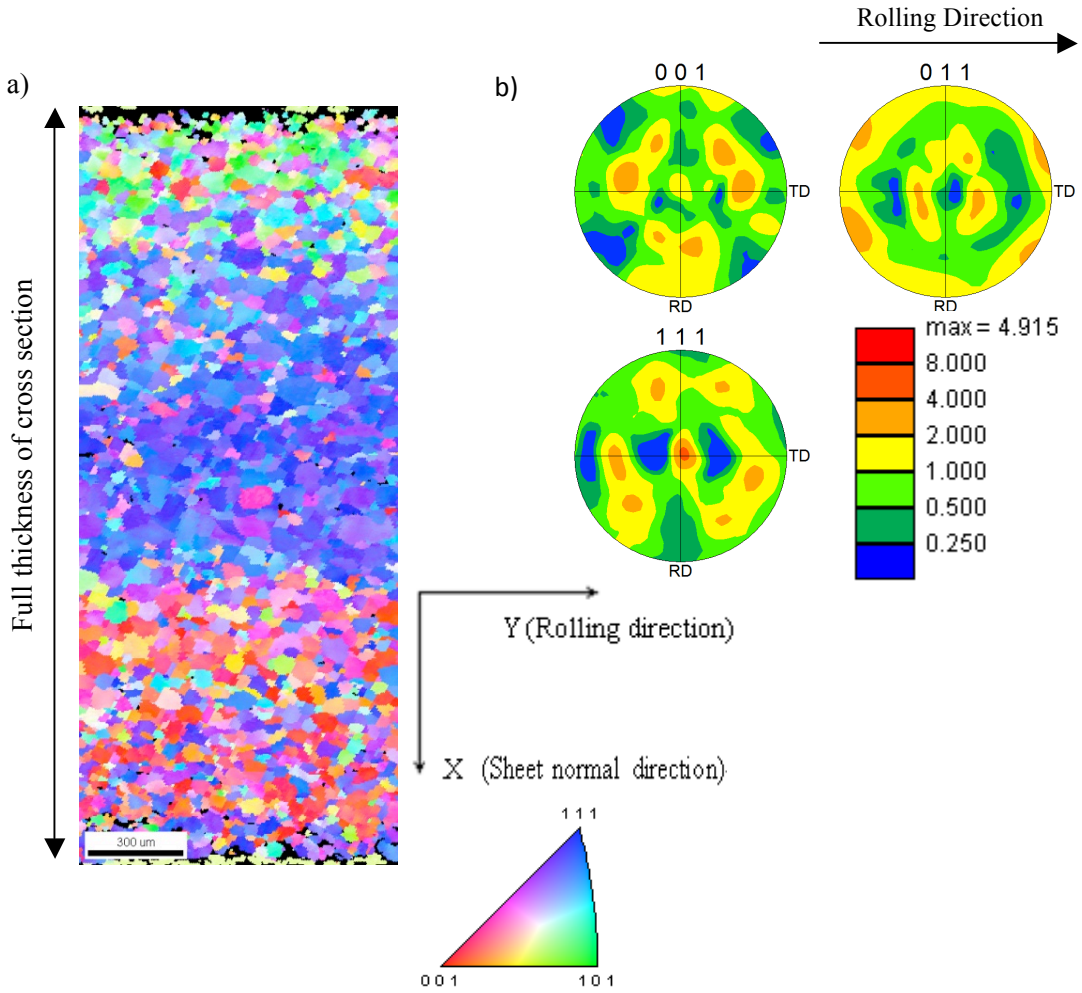

Figure D. 3: a) IPF map and b) PF of niobium sheet 130517-FW501-02 #3 with thickness 2mm.

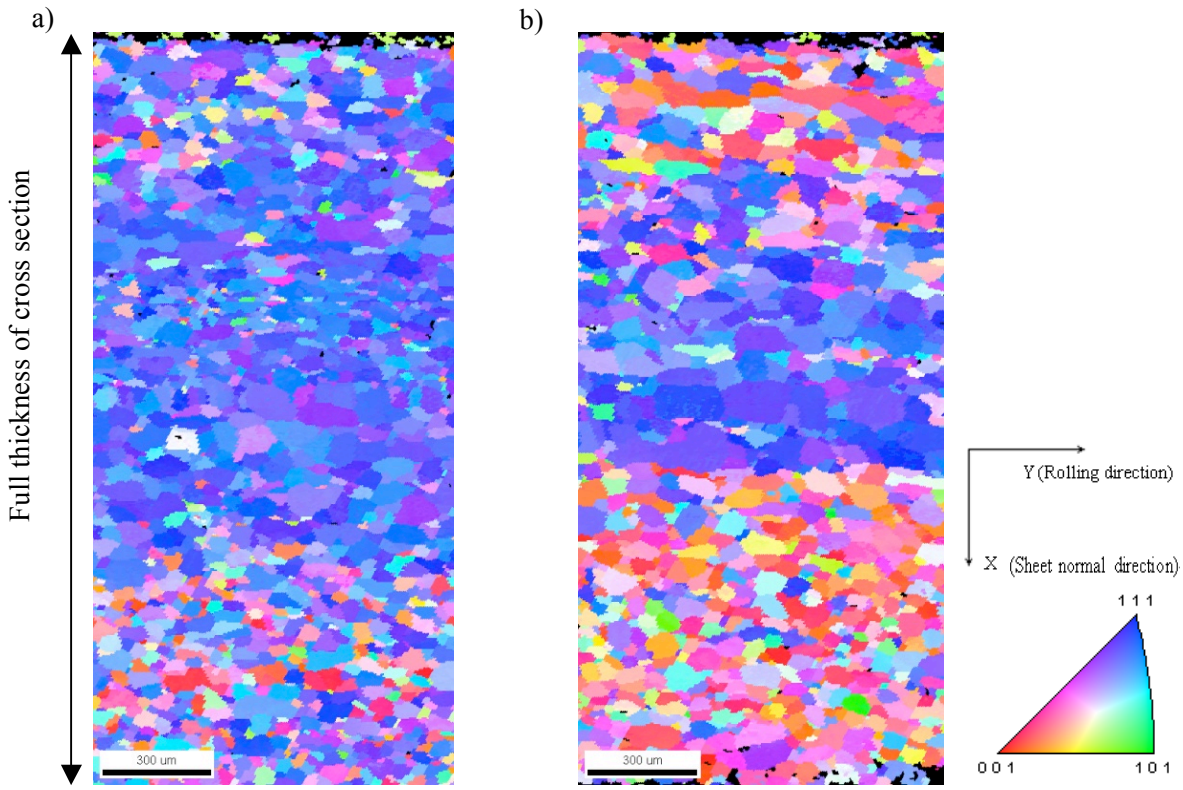

Figure D. 4: IPF maps of niobium sheet NT02 a) A-5 and b) A-26 from left to right respectively with thickness 2mm.

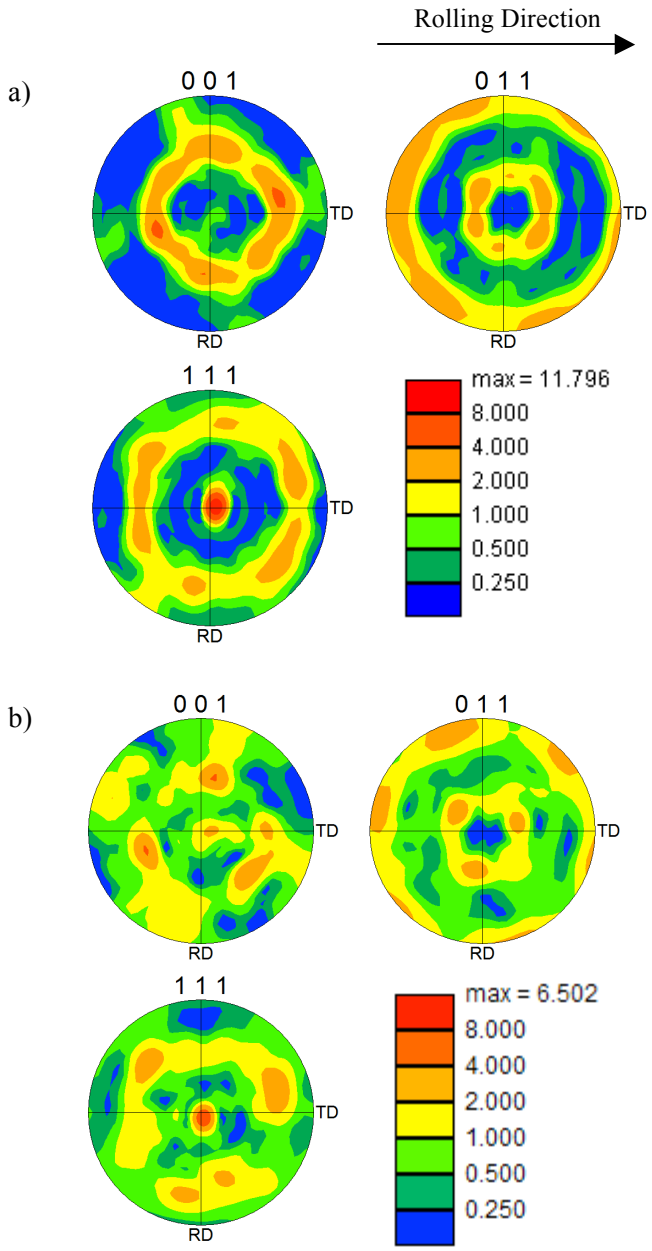

Figure D. 5: PFs of niobium sheet NT02 a) A-5 and b) A-26 from top to bottom respectively with thickness 2mm.

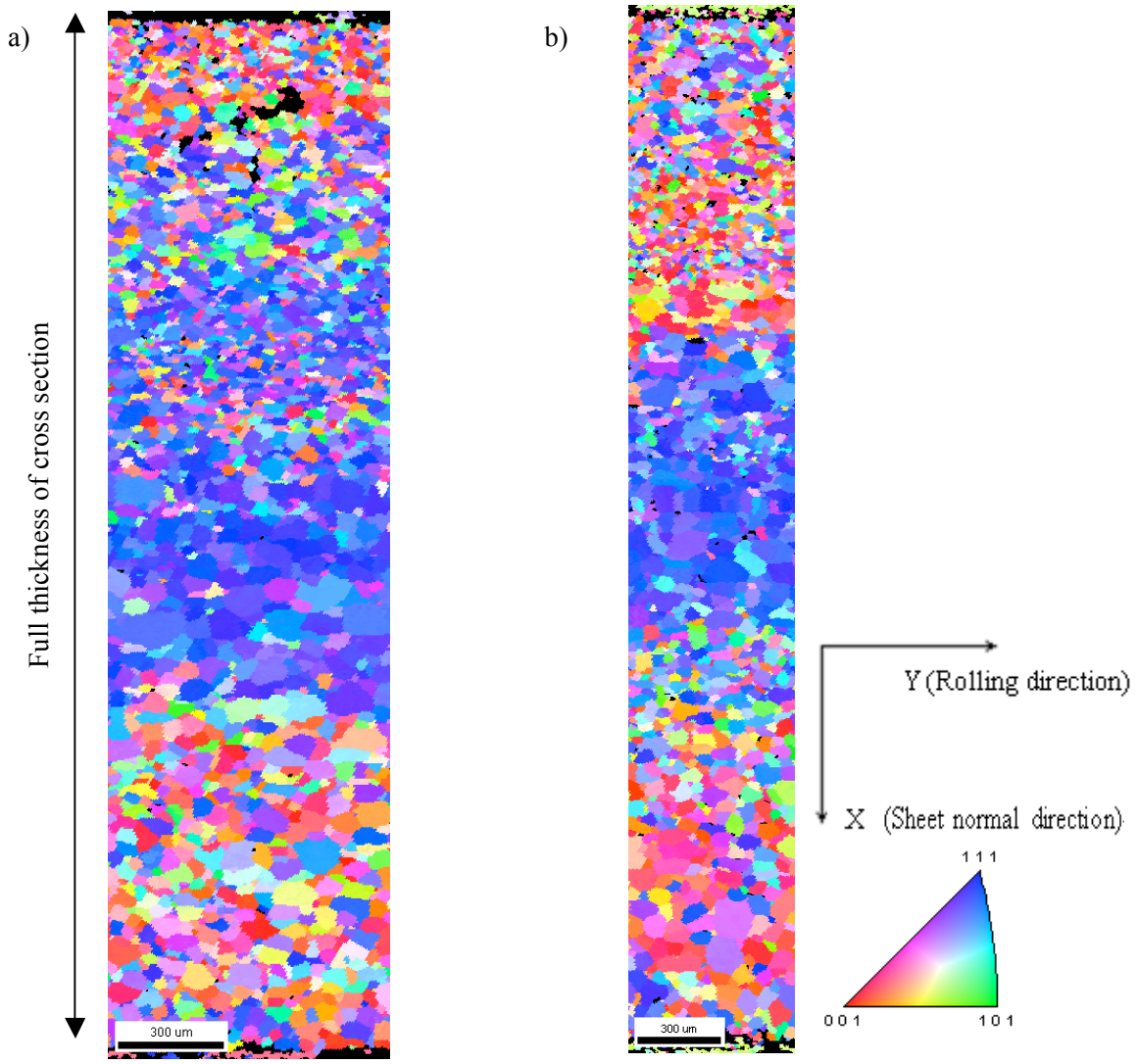

Figure D. 6: IPF maps of niobium sheet NT02 a) B-1 and b) B-7 from left to right respectively with thickness 3mm.

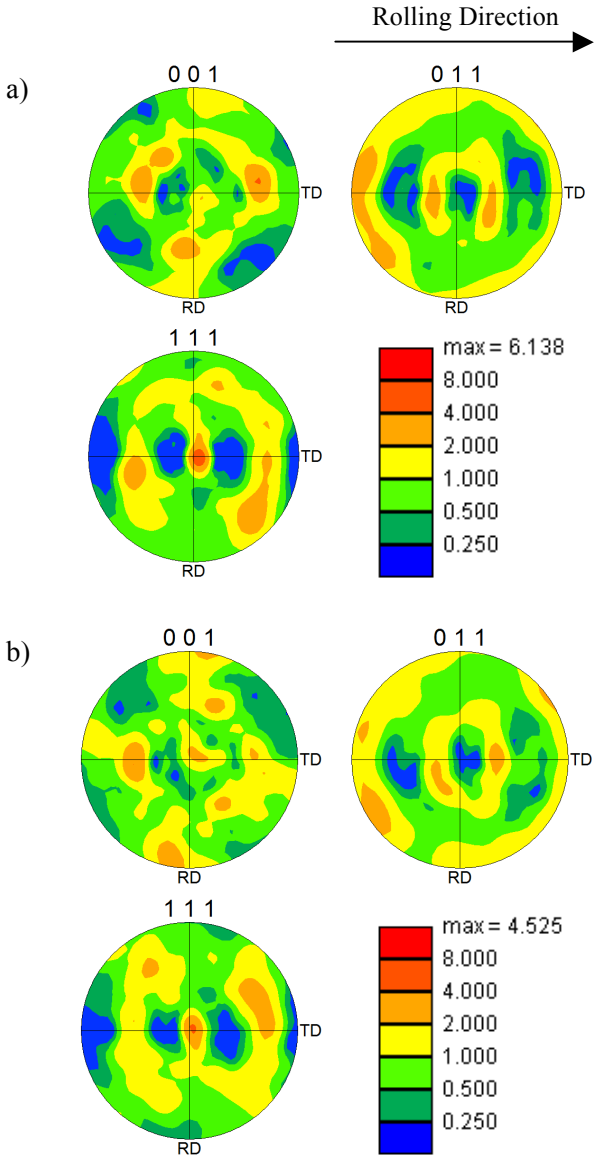

Figure D. 7: PFs of niobium sheet NT02 a) B-1 and b) B-7 from top to bottom respectively with thickness 3mm.

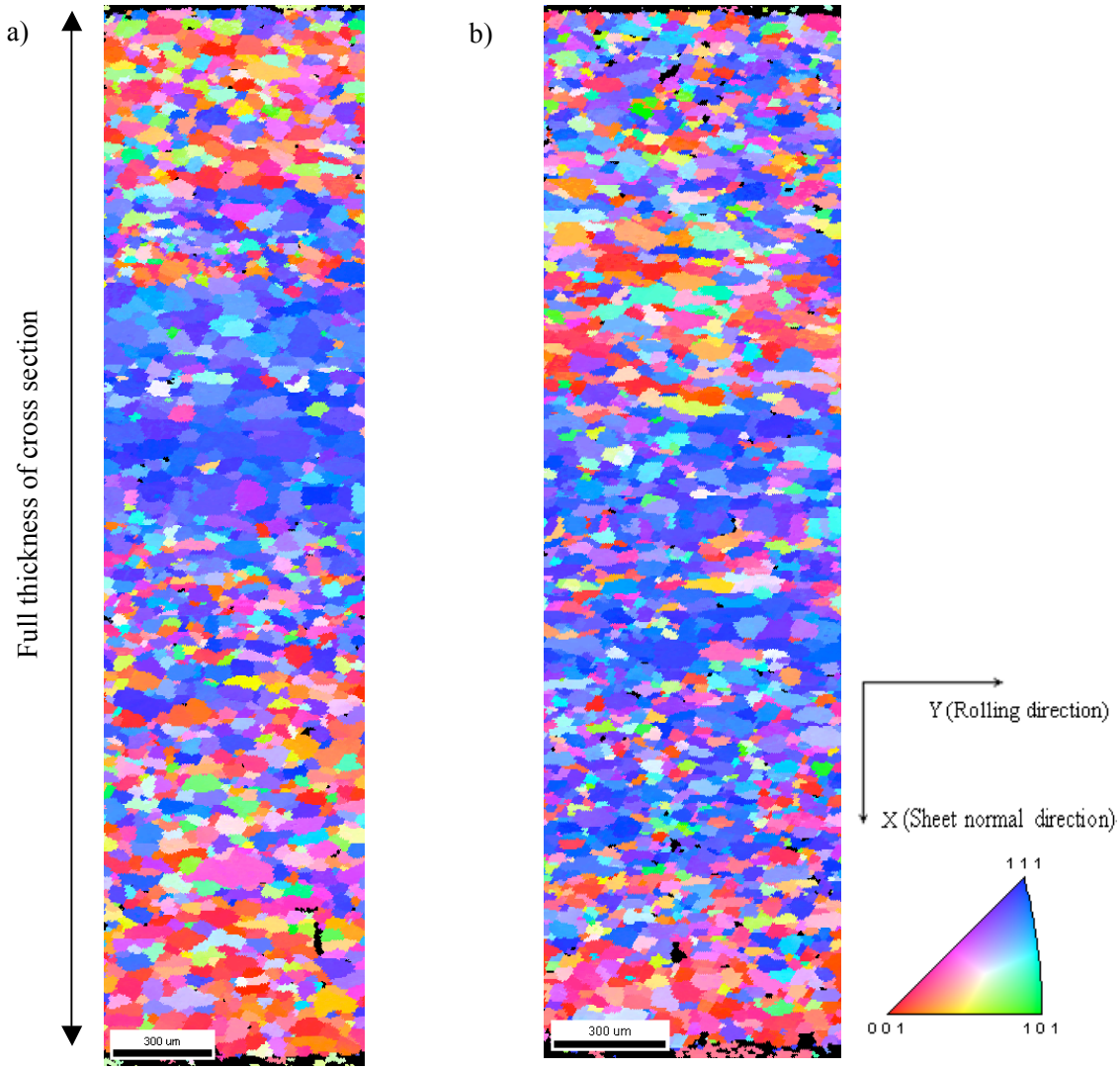

Figure D. 8: IPF maps of niobium sheet NT02 a) C-11 and b) C-17 from left to right respectively with thickness 3mm.

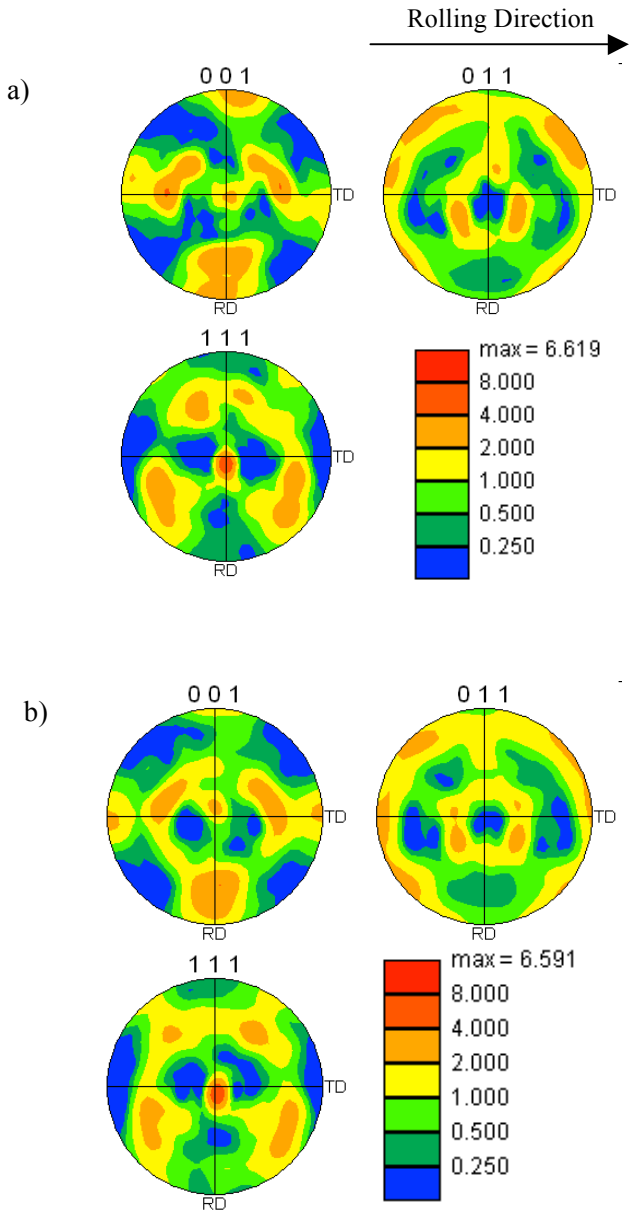

Figure D. 9: PFs of niobium sheet NT02 a) C-11 and b) C-17 from top to bottom respectively with thickness 3mm.

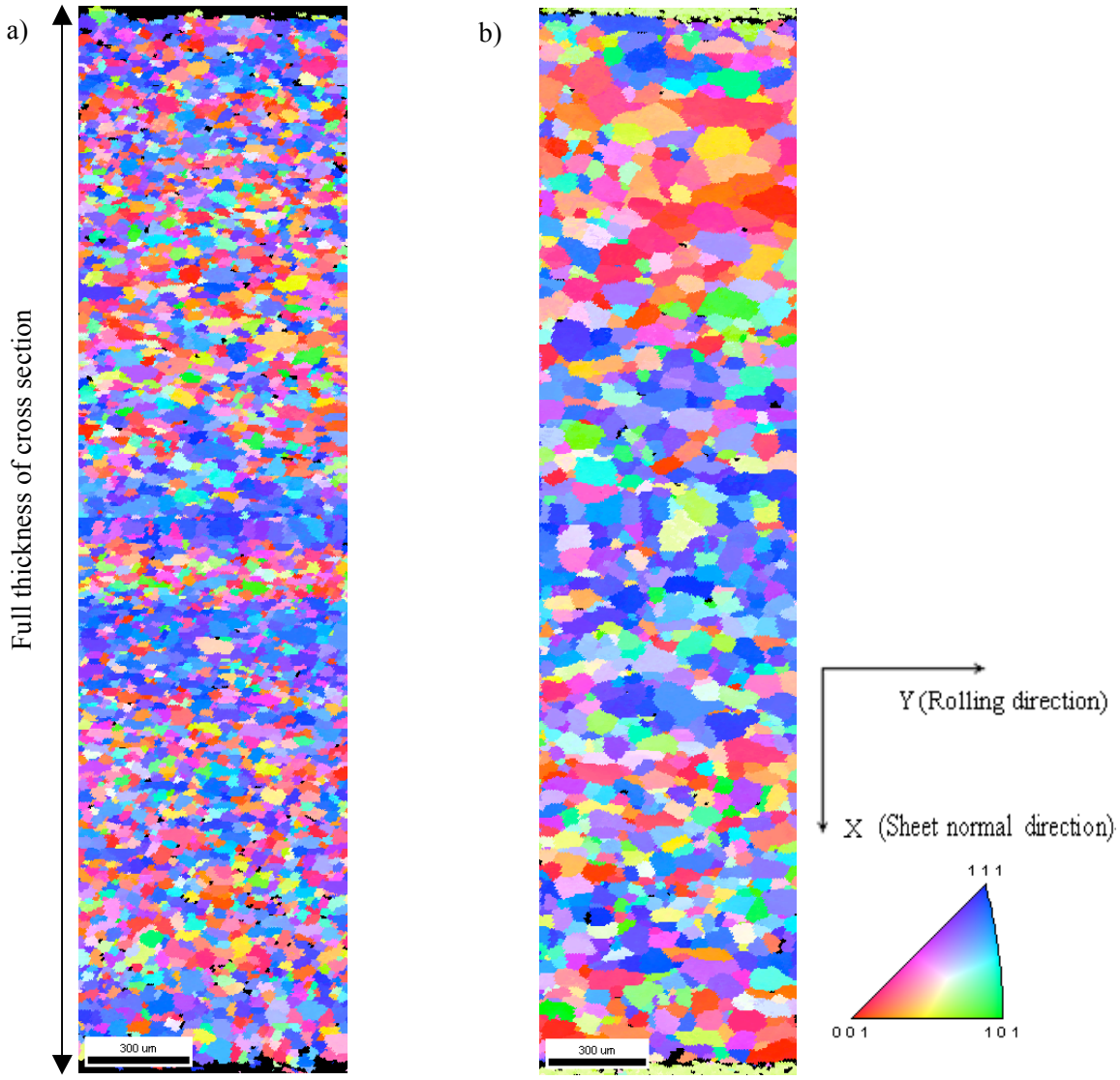

Figure D. 10: IPF maps of niobium sheet NT02 a) D-25 and b) D-27 from left to right respectively with thickness 3mm.

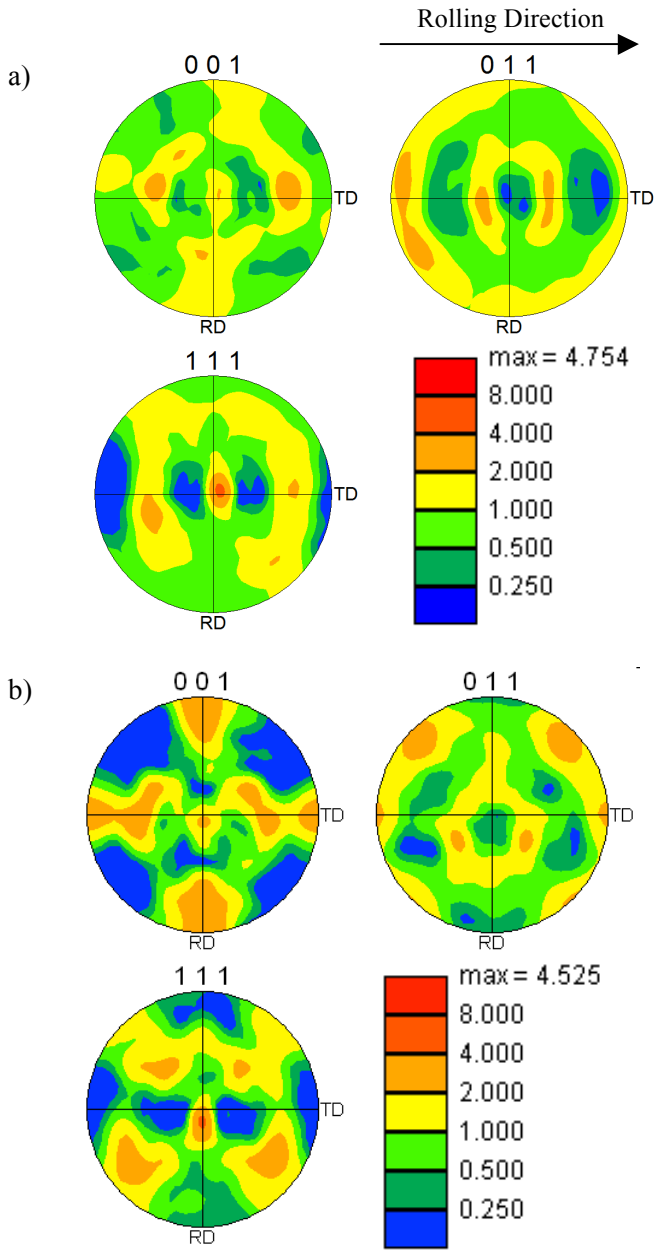

Figure D. 11: PFs of niobium sheet NT02 a) D-25 and b) D-27 from top to bottom respectively with thickness 3mm.

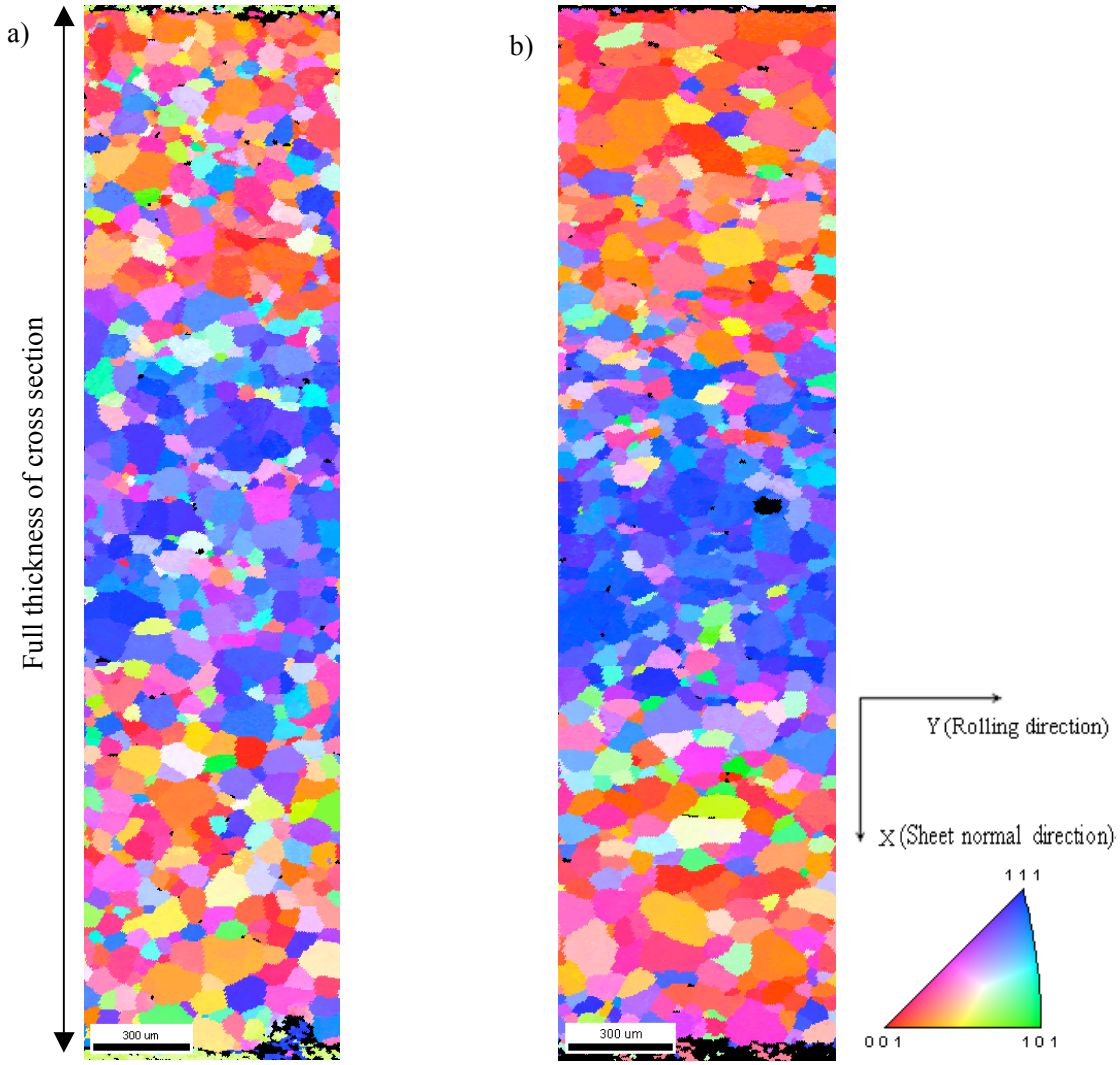

Figure D. 12: IPF maps of niobium sheet NT02 a) E-37 and b) E-38 from left to right respectively with thickness 3mm.

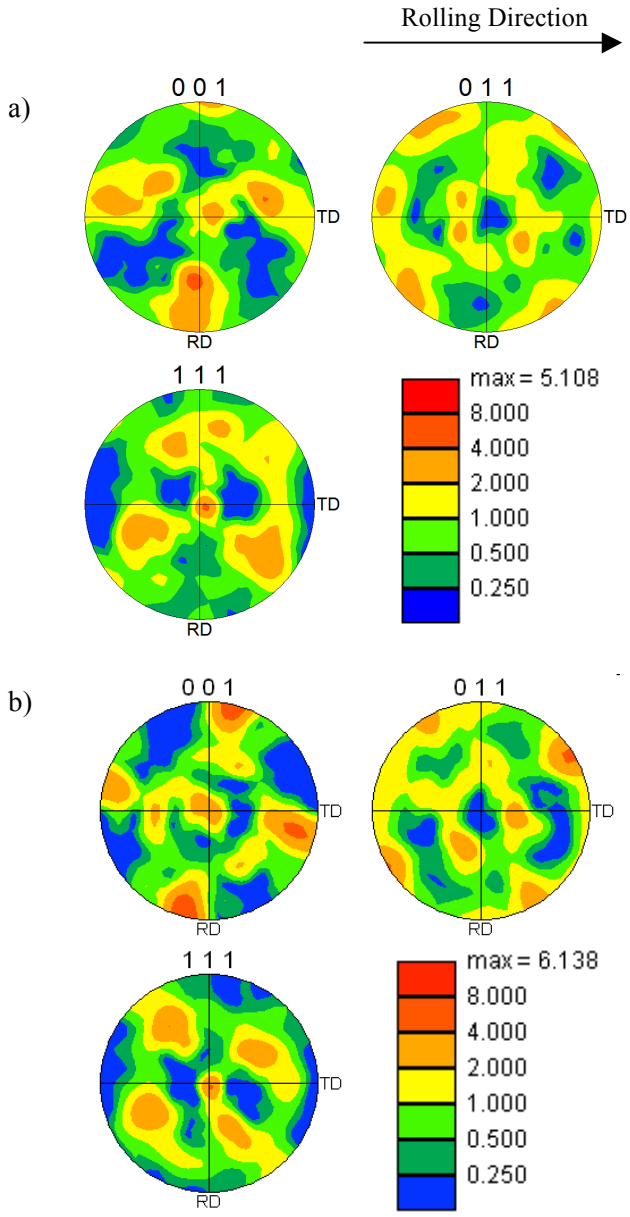

Figure D. 13: PFs of niobium sheet NT02 a) E-37 and b) E-38 from top to bottom respectively with thickness 3mm.

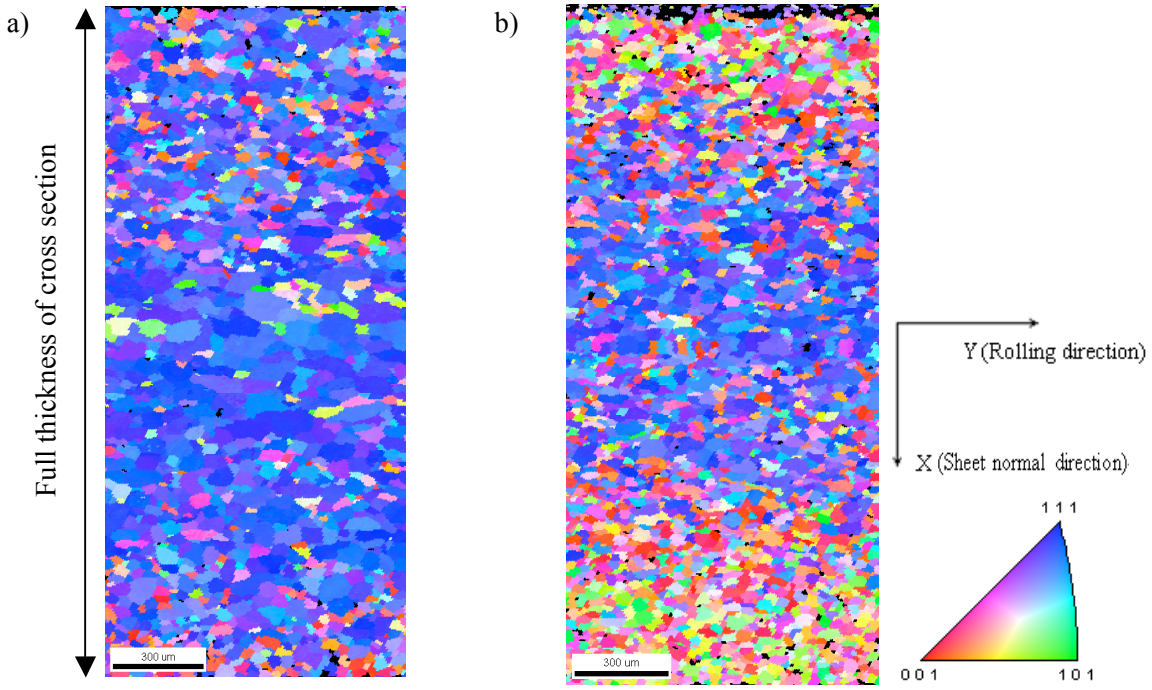

Figure D. 14: IPF maps of niobium sheet a) 991101 and b) 993401 from left to right respectively with thickness 2mm.

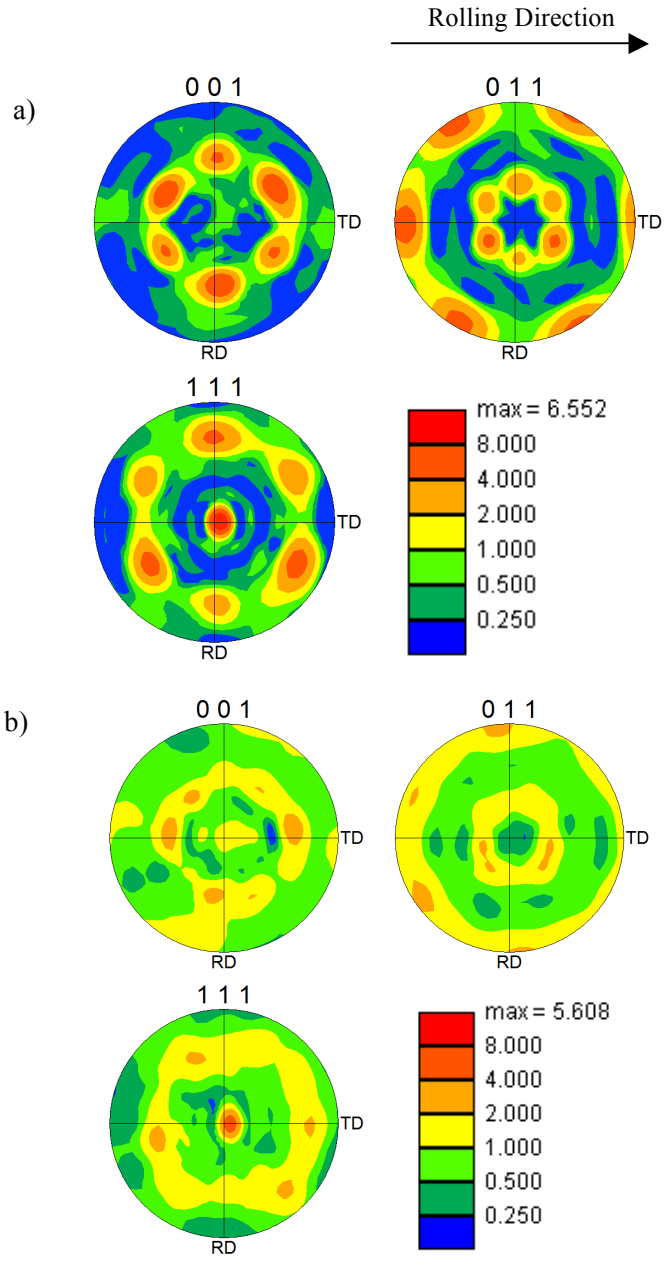

Figure D. 15: PFs of niobium sheet a) 991101 and b) 993401 from top to bottom respectively with thickness 2mm

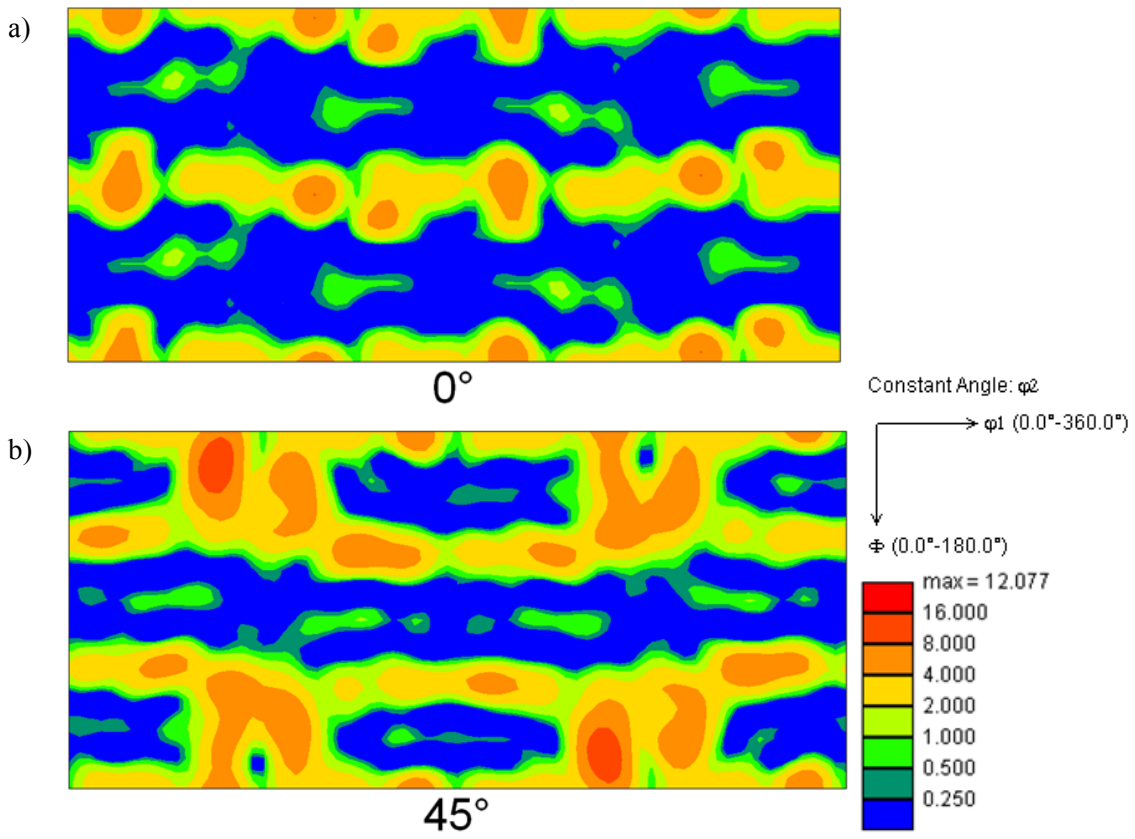

Figure D. 16: ODF plots when ϕ_2 equals a) 0° and b) 45° for niobium sheet 130202-25-02 #6 with thickness 2mm.

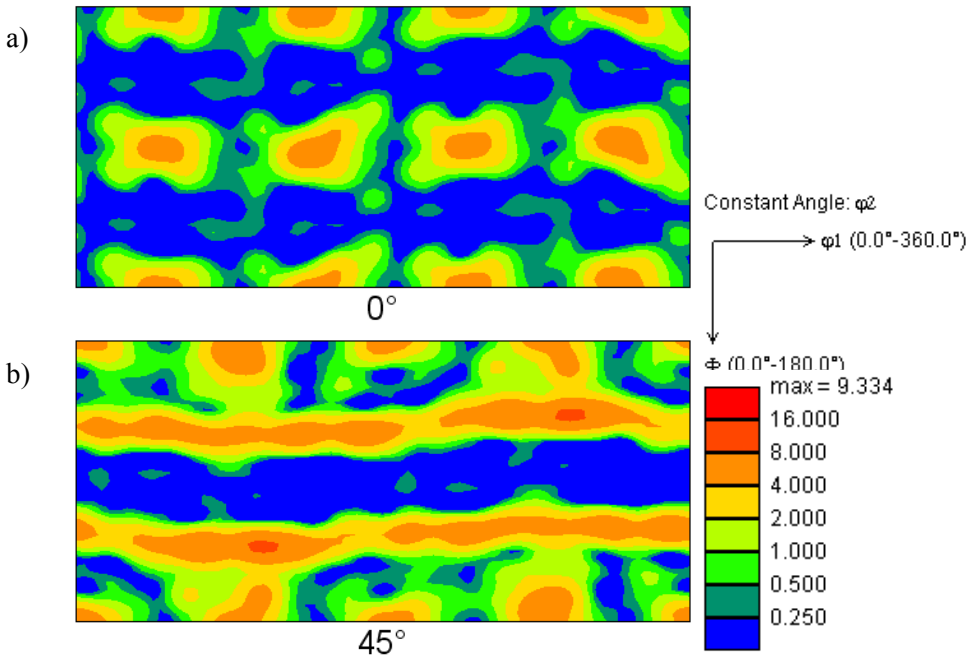

Figure D. 17: ODF plots when ϕ_2 equals a) 0° and b) 45° for niobium sheet 130517-FW501-02 #2 with thickness 2mm.

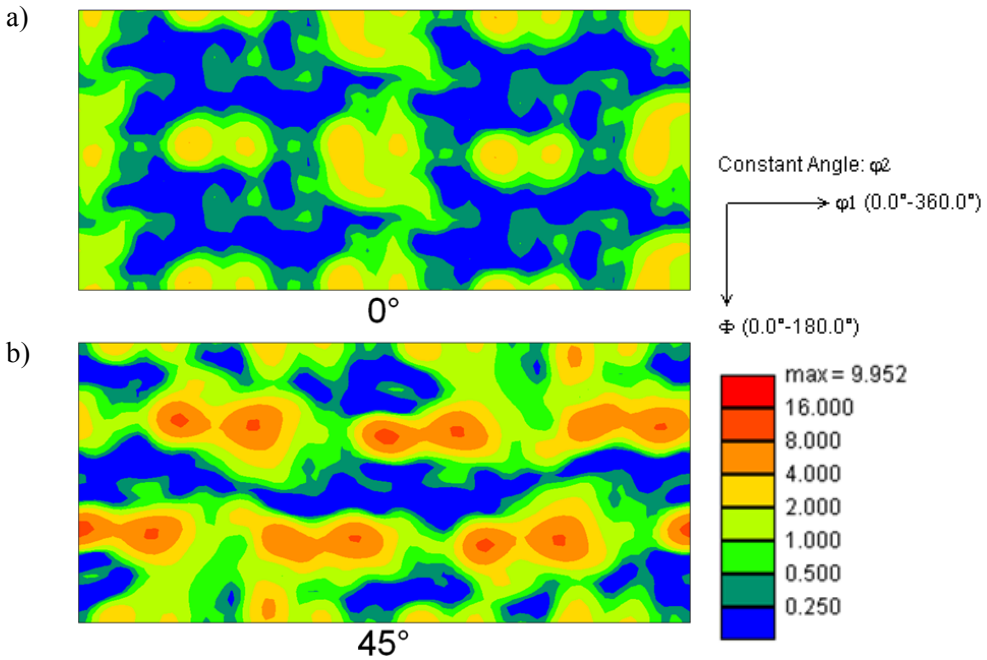

Figure D. 18: ODF plots when ϕ_2 equals a) 0° and b) 45° for niobium sheet 130517-FW501-02 #3 with thickness 2mm.

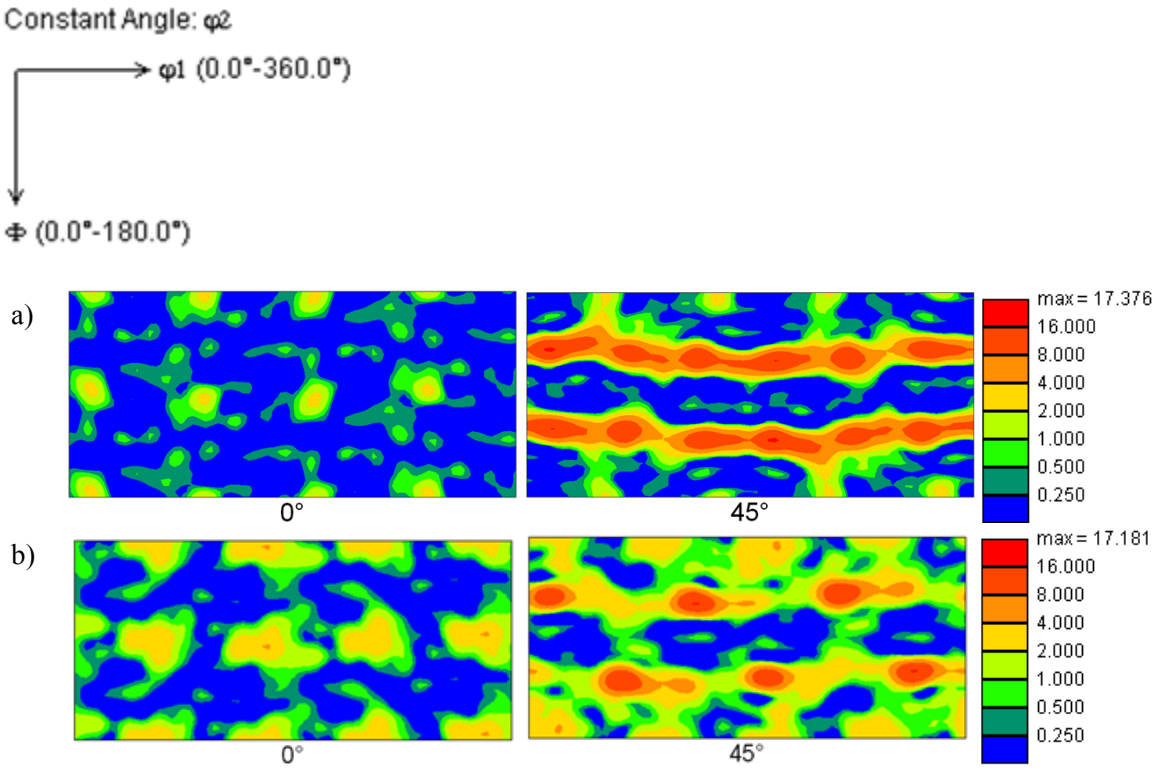

Figure D. 19: ODF plots when ϕ_2 equals 0° and 45° for niobium sheet NT02 a) A-5 and b) A-26 with thickness 2mm.from top to bottom respectively.

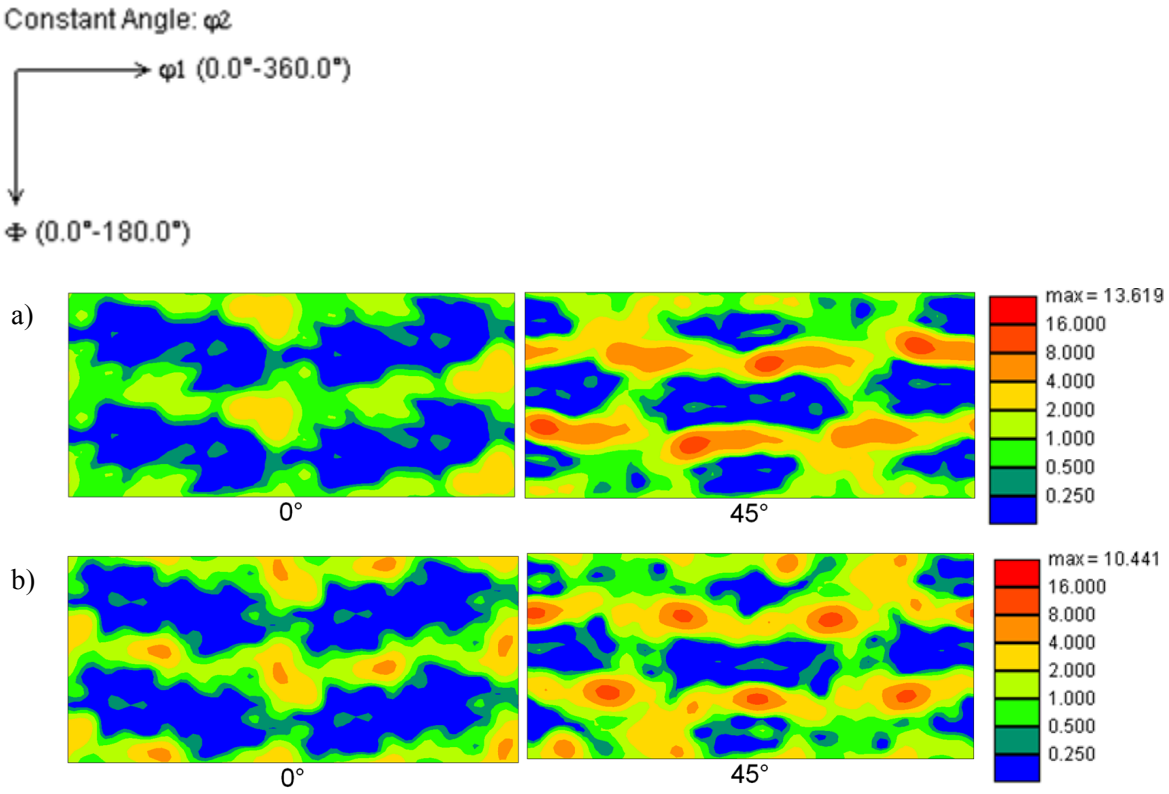

Figure D. 20: ODF plots when ϕ_2 equals 0° and 45° for niobium sheet NT02 a) B-1 and b) B-7 with thickness 2mm from top to bottom respectively.

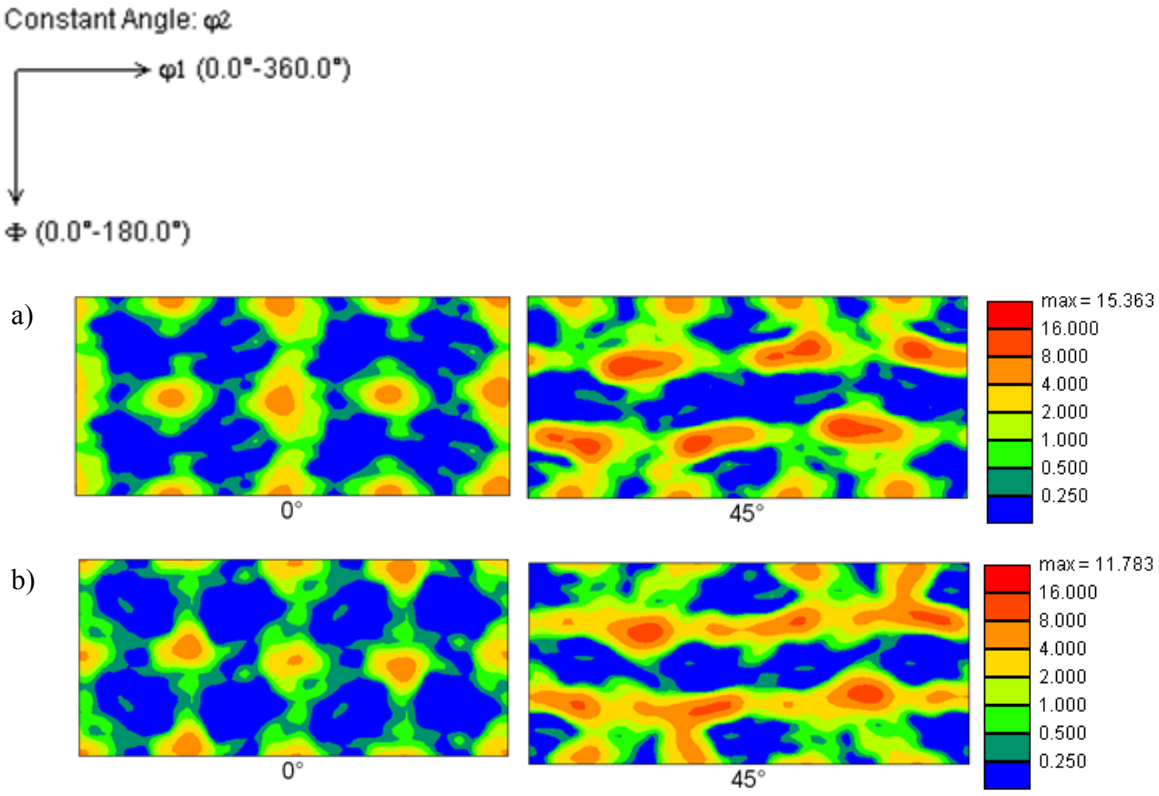

Figure D. 21: ODF plots when ϕ_2 equals 0° and 45° for sheet NT02 a) C-11 and b) C-17 with thickness 2 mm from top to bottom respectively.

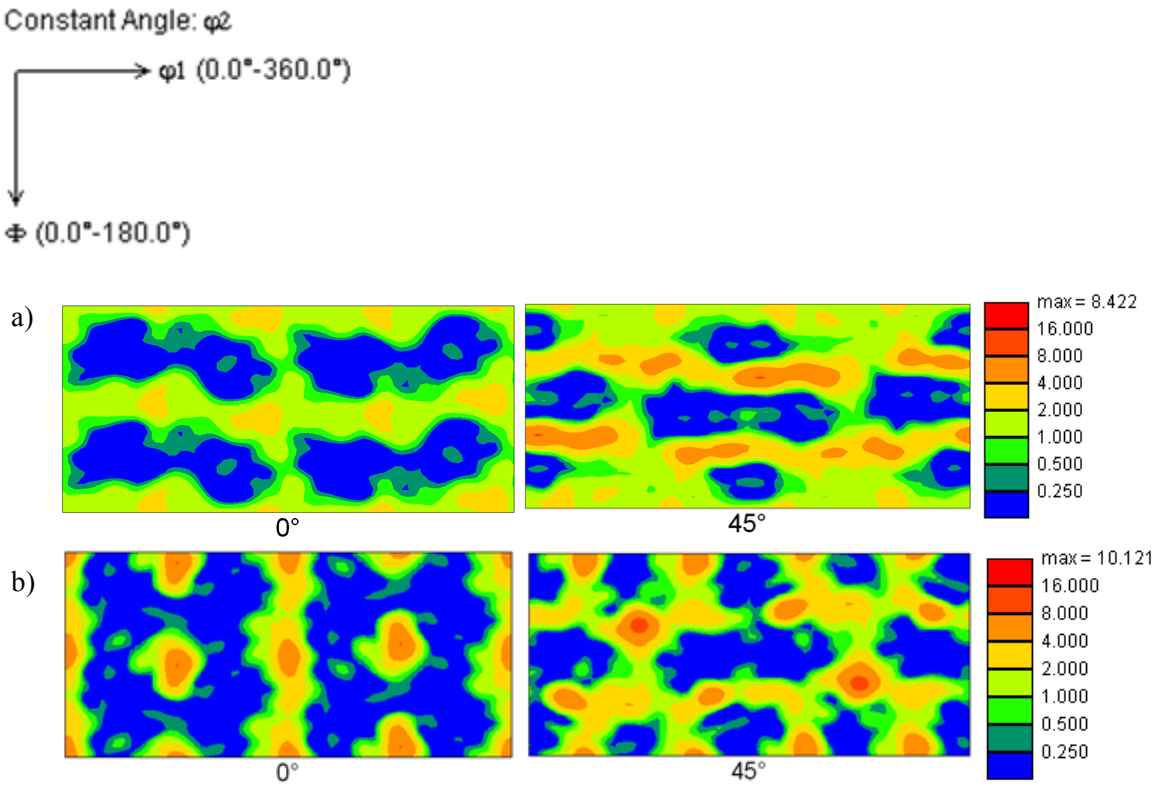

Figure D. 22: ODF plots when ϕ_2 equals 0° and 45° for niobium sheet NT02 a) D-25 and b) D-27 with thickness 2 mm from top to bottom respectively.

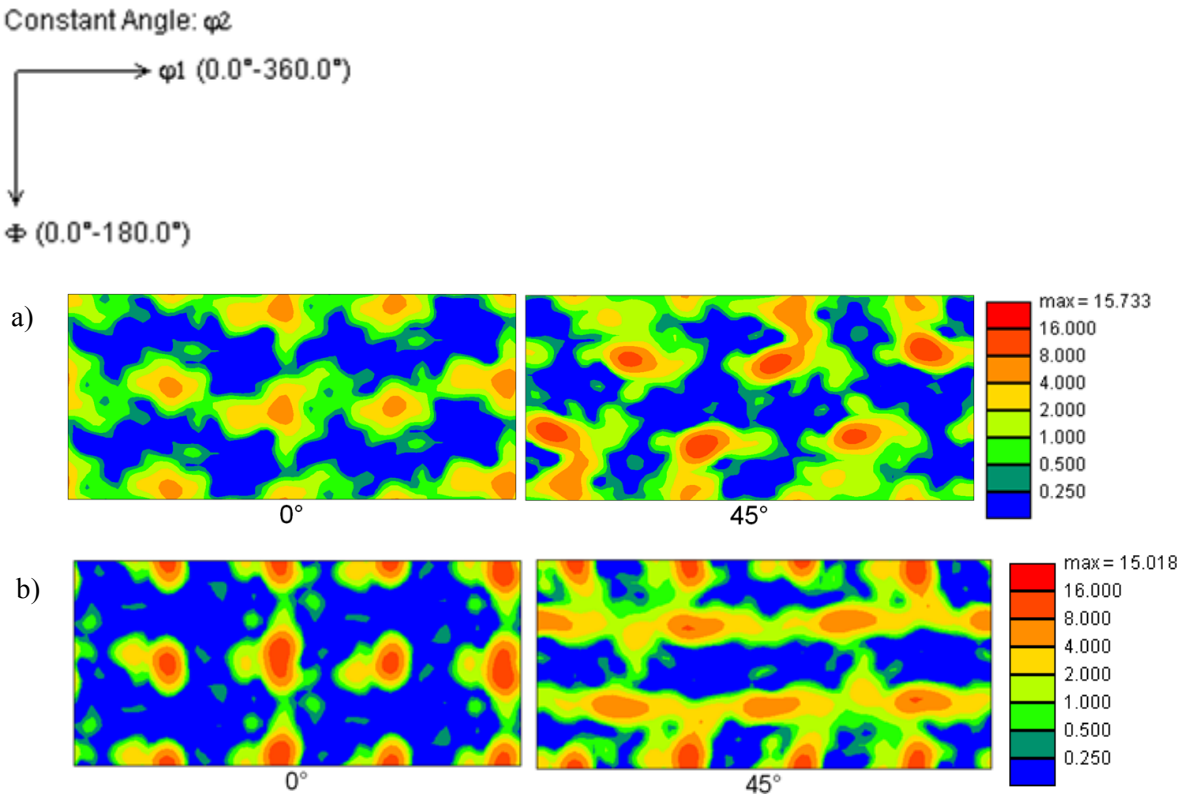

Figure D. 23: ODF plots when ϕ_2 equals 0° and 45° for niobium sheet NT02 a) E-37 and b) E-38 with thickness 2 mm from top to bottom respectively.

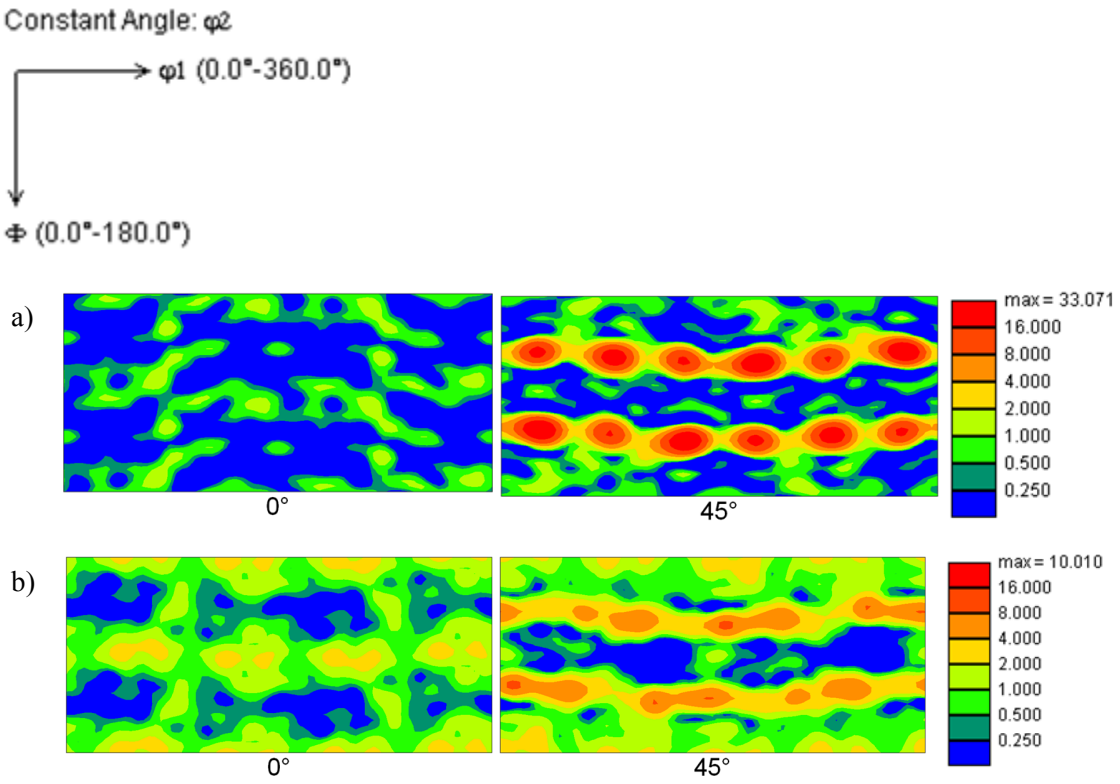

Figure D. 24: ODF plots when ϕ_2 equals 0° and 45° for niobium sheet a) 991101 and b) 993401 with thickness 2 mm from top to bottom respectively.

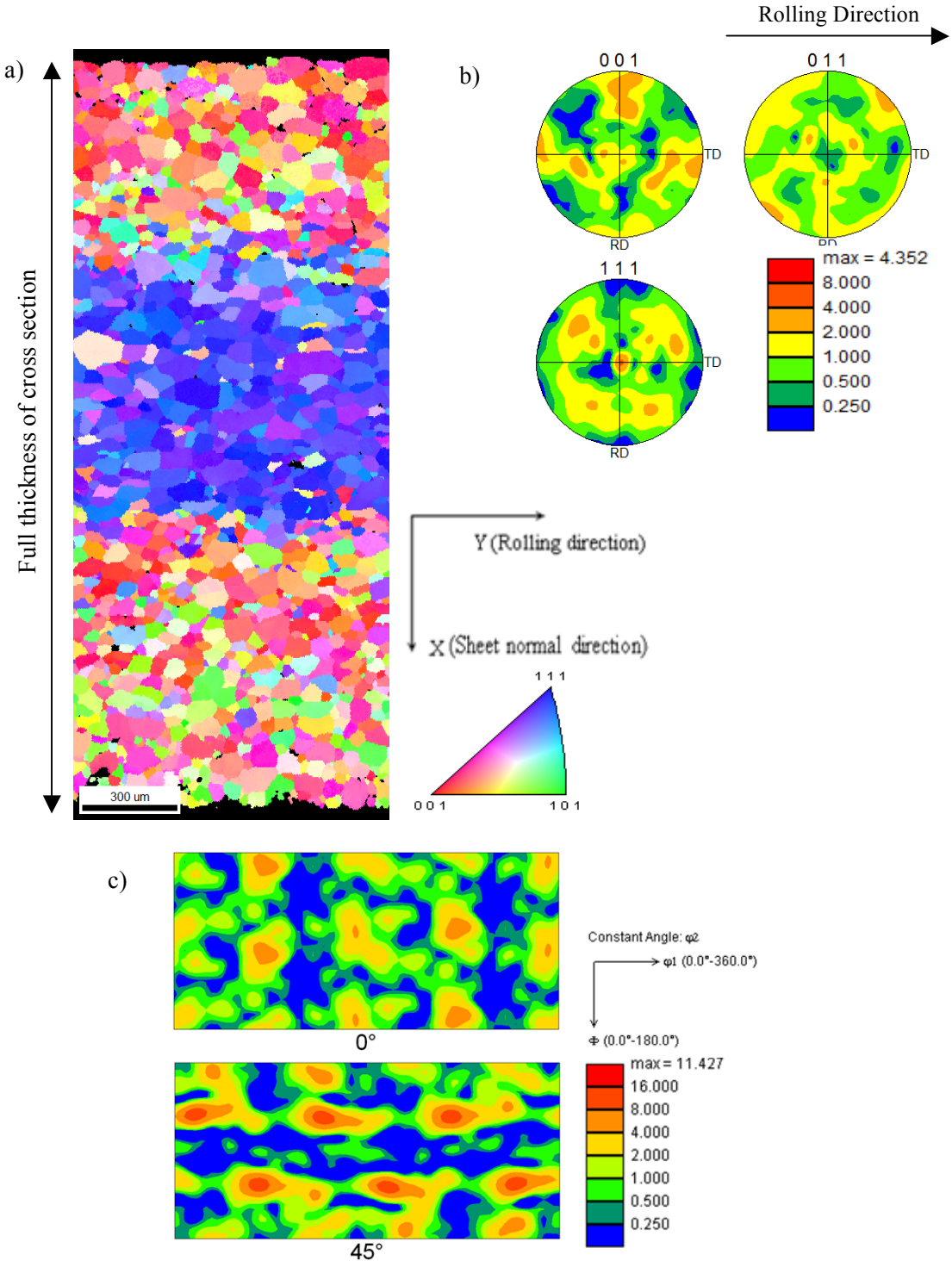

Figure D. 25: a) IPF map, b) PF and c) ODF plots when ϕ_2 equals 0° and 45° of niobium sheet A.

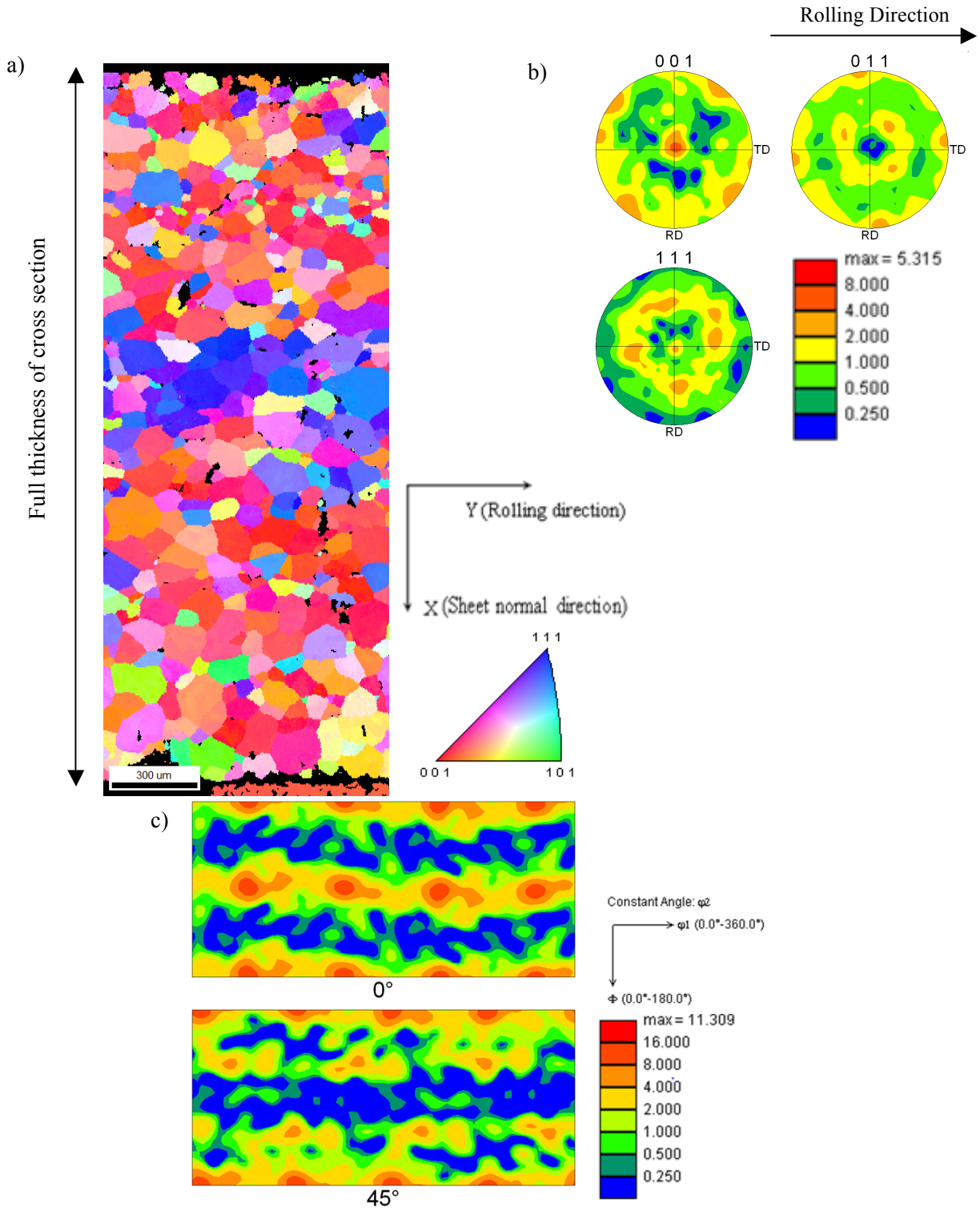

Figure D. 26: a) IPF map, b) PF and c) ODF plots when ϕ_2 equals 0° and 45° of niobium sheet B.

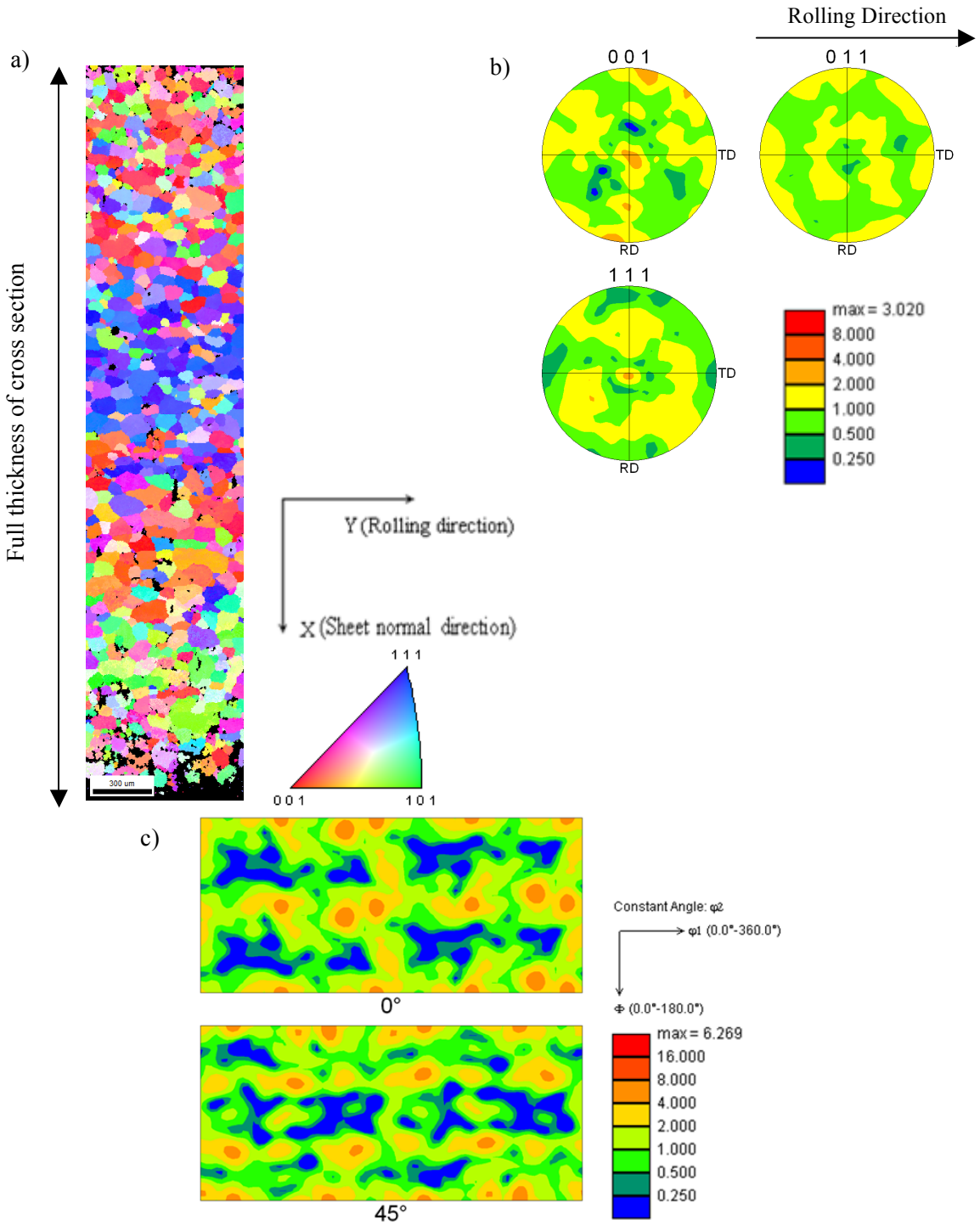

Figure D. 27: a) IPF map, b) PF and c) ODF plots when ϕ_2 equals 0° and 45° of niobium sheet C.

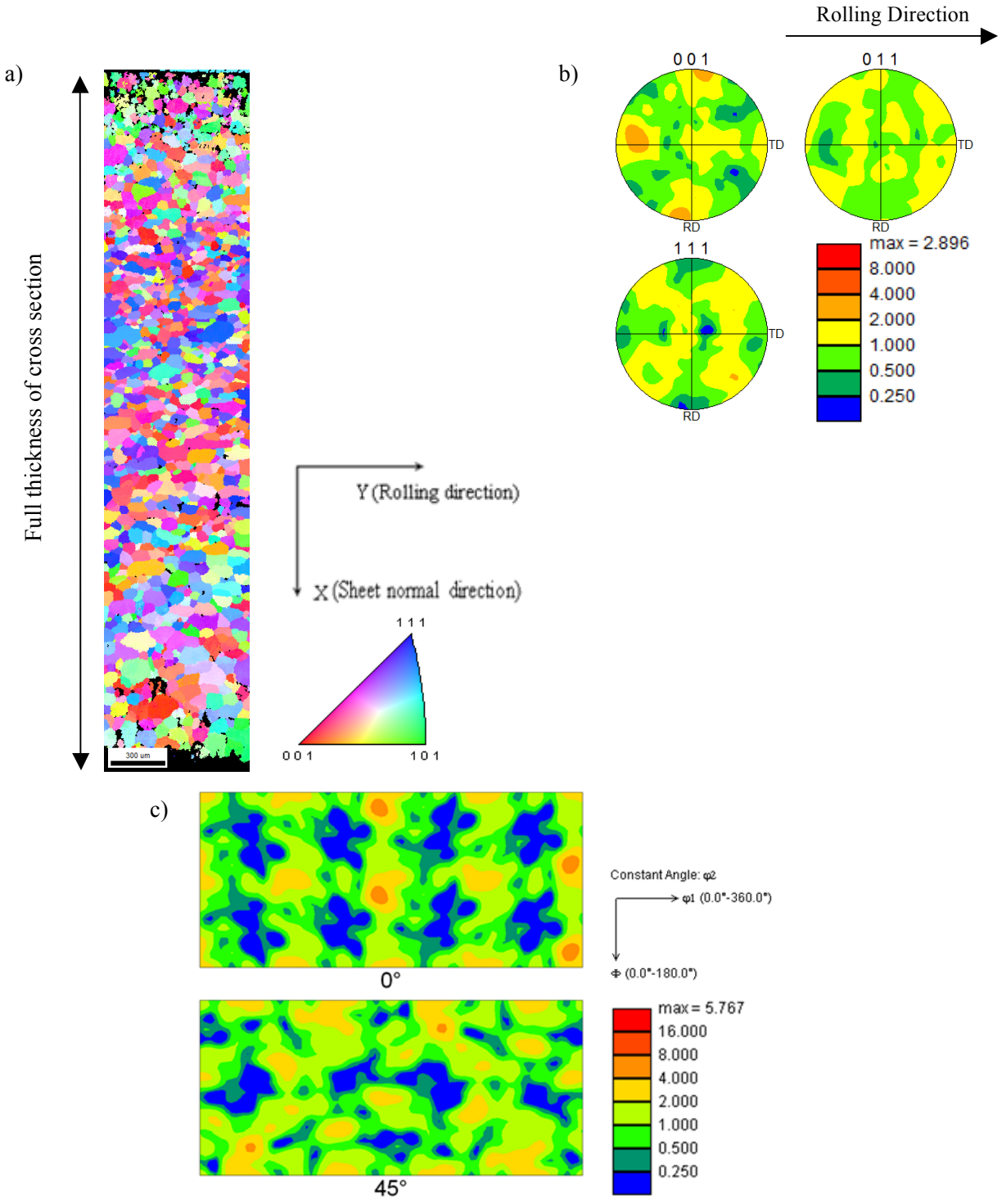

Figure D. 28: a) IPF map, b) PF and c) ODF plots when ϕ_2 equals 0° and 45° of niobium sheet D.

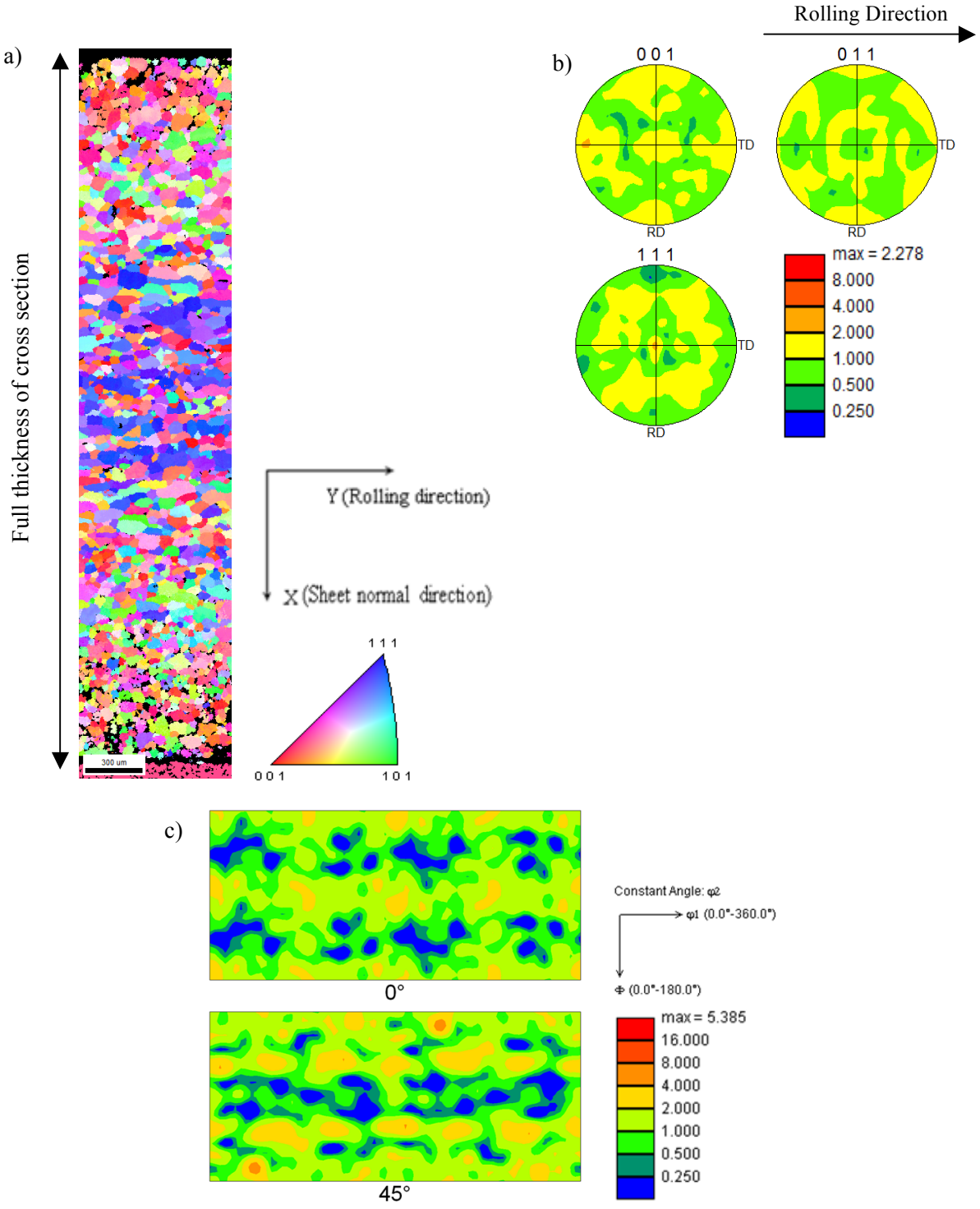

Figure D. 29: a) IPF map, b) PF and c) ODF plots when ϕ_2 equals 0° and 45° of niobium sheet E.

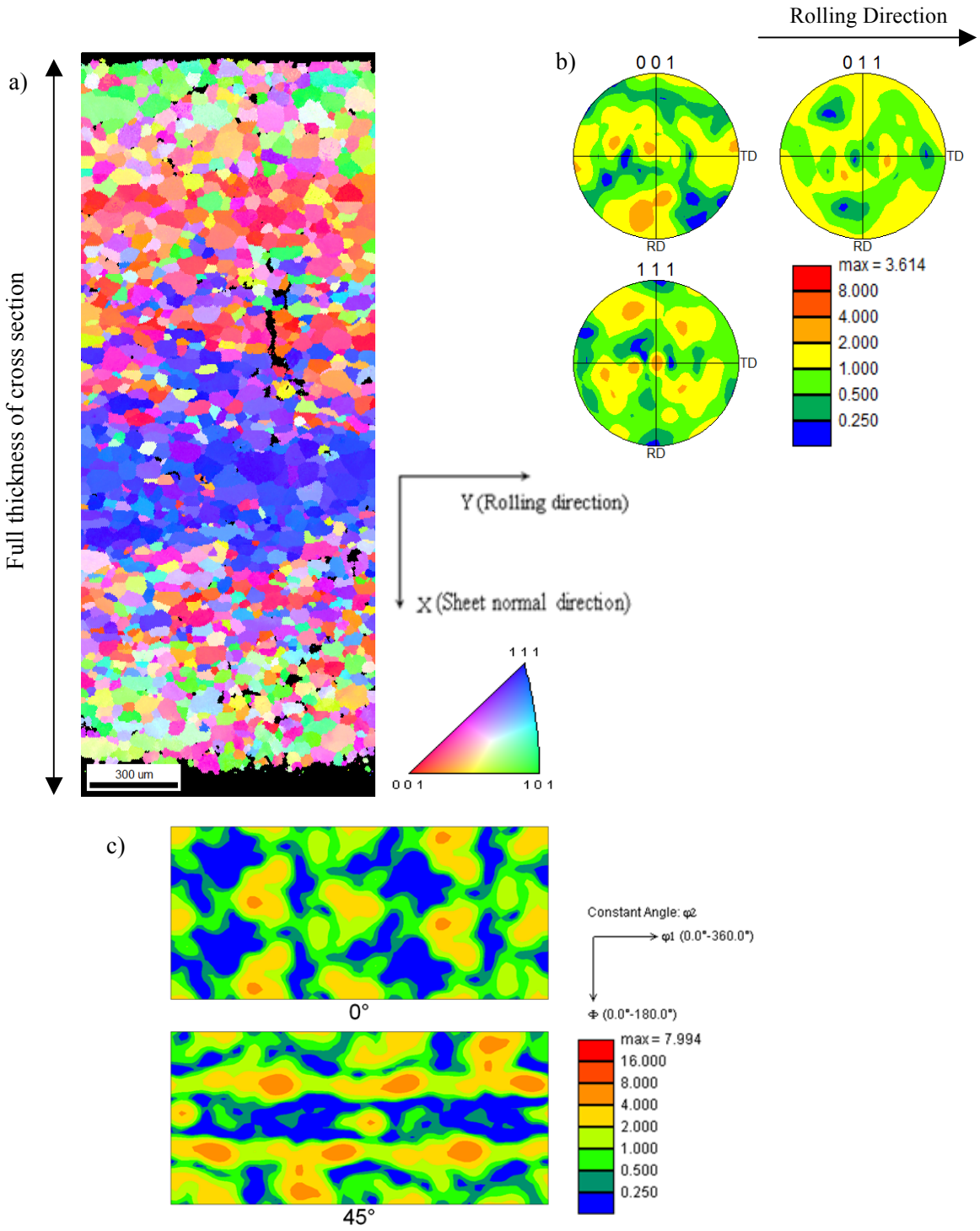

Figure D. 30: a) IPF map, b) PF and c) ODF plots when ϕ_2 equals 0° and 45° of niobium sheet F.

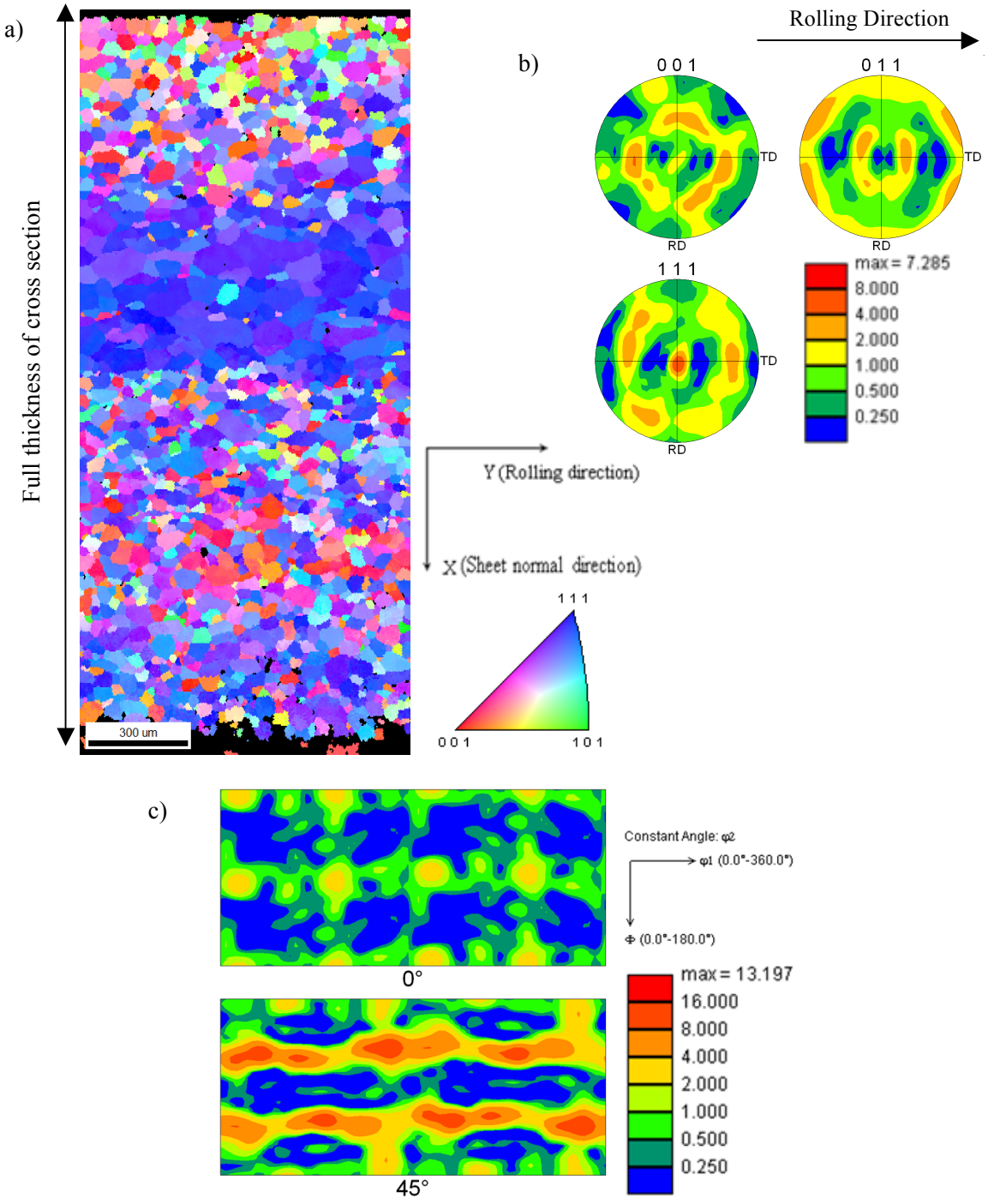

Figure D. 31: a) IPF map, b) PF and c) ODF plots when ϕ_2 equals 0° and 45° of niobium sheet G.

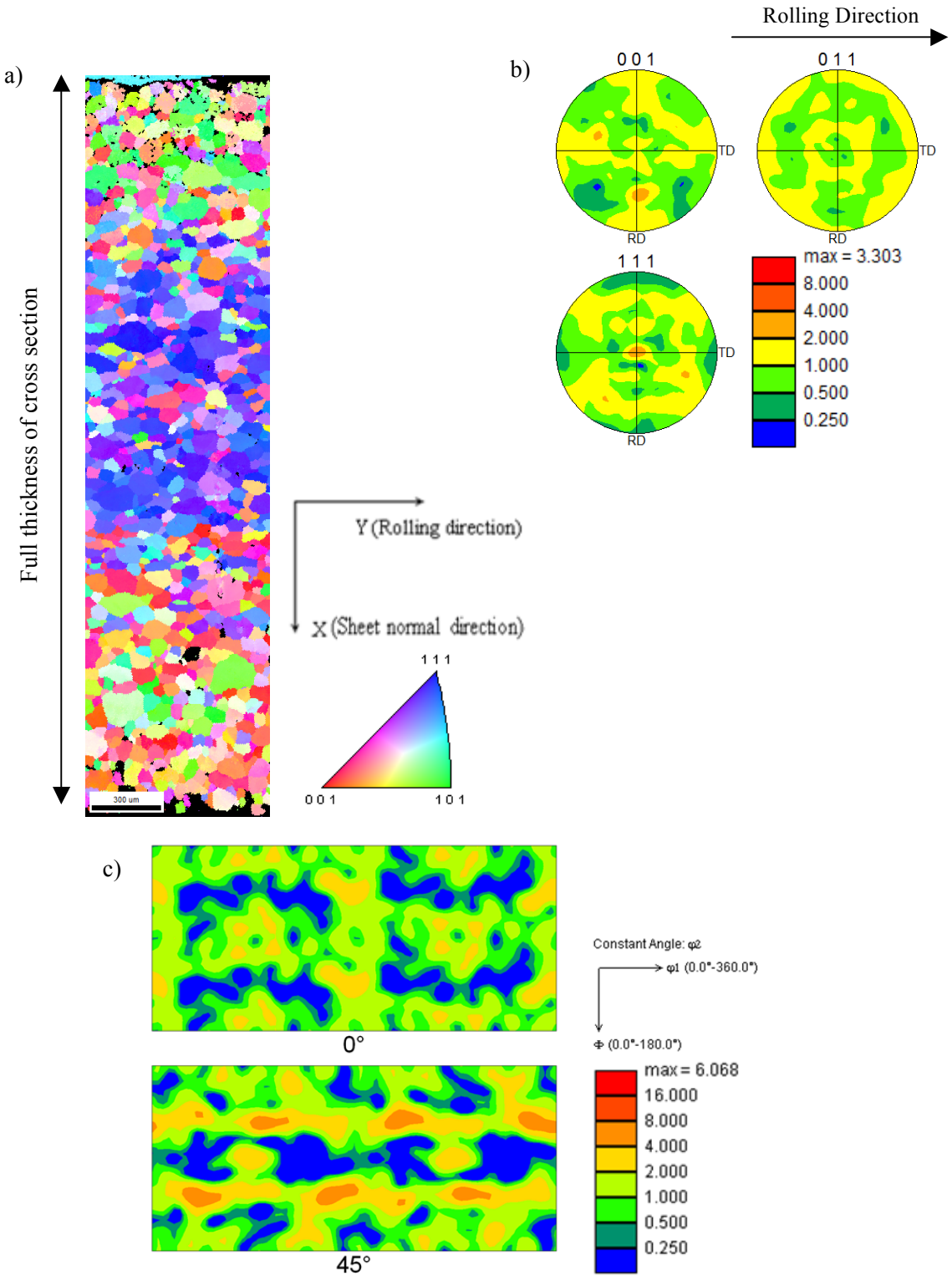

Figure D. 32: a) IPF map, b) PF and c) ODF plots when ϕ_2 equals 0° and 45° of niobium sheet H.

BIBLIOGRAPHY

BIBLIOGRAPHY

1. Padamsee H, Knobloch J, Hays T. RF Superconductivity for Accelerators. Wiley, John & Sons, Incorporated, 1998.

2. Cook C, Harms E. Testing and Analysis of 'Bare' Superconducting Radio-Frequency Cavities. University of Wisconsin-Eau Claire, 2011.

3. Zamiri A. Effect of strain path on deformation texture of superconducting niobium sheet. *arXiv preprint arXiv:1403.7689*, 2014.

4. Suwas S, Gurao NP. Crystallographic texture in Materials. *Journal of the Institute of Science*, Vol. 88, pp. 2, 2008.

5. Compton C, Bieler T, Chandrasekaran S, Kang D, Miller D, Wright N. Quality assurance and acceptance testing of niobium material for use in the construction of the facility for rare isotope beams (FRIB) at Michigan State University (MSU). *MOP033*, these proceedings.

6. Maitland T, Sitzman S. Electron Backscatter Diffraction (EBSD) Technique and Materials Characterization Examples. Vol. 14, pp.522, Berlin: Springer, 2007.

7. Singer W, SRF Cavity Fabrication and Materials. 2014.

8. Ding X, Boucher S. A method for establishing Q-factors of RF cavities. 2010.

9. Wenk HR, Houtte PV. Texture and anisotropy. *Reports on Progress in Physics*. 67, no. 8, pp. 1367-1428, 2004.

10. EBSD Explained from data acquisition to advanced analysis, Web. 2015. < http://www.oxford-instruments.com/OxfordInstruments/media/nanoanalysis/EBSD/EBSD%20Explained/EBSD-Explained_web.pdf?width=0&height=0&ext=.pdf&returnurl=%2Fproducts%2Fmicroanalysis> Oxford Instruments.

11. Brewer LN, Field DP, Merriman CC. Mapping and assessing plastic deformation using EBSD. Electron backscatter diffraction in materials science. pp. 251-265, Springer US, 2009.

12. Bieler TR, Wright NT, Pourboghrat F, Compton C, Hartwig KT, Baars D, Zamiri A, Chandrasekaran S, Darbandi P, Jiang H, Skoug E, Balachandran S, Lee GE, Liu W. Physical and mechanical metallurgy of high purity Nb for accelerator cavities. Phys. Rev. ST Accel. Beams, Vol 13 (03), pp.031002,2010

13. Saraf L. Kernel Average Misorientation Confidence Index Correlation from FRIB Sliced Ni-Fe-Cr alloy Surface. *Microscopy and Microanalysis*, 17. S2, pp. 424-425, 2011.

14. Wright SI, Nowell MM, Field DP. A Review of Strain Analysis Using Electron Backscatter Diffraction. *Microscopy and Microanalysis*, 17. 03 pp. 316-329, 2011.

15. Graphs and charts, Web. <http://web.anglia.ac.uk/numbers/graphsCharts.html>

16. Preston C, Grimm T, Compton C, Sanborn N. Etching of Niobium in Buffered Chemical Polish in a small Ventilated Room. Web. 2000. < https://people.nscl.msu.edu/~hartung/phptry/srf/pdf/EtchRoomReport.pdf>